Linking observations and modelling to advance our understanding of spatio-temporal variations in structure and productivity of Arctic protist plankton

Dissertation

zur Erlangung des Doktorgrades
der Mathematisch-Naturwissenschaftlichen-Fakultät
der Christian-Albrechts-Universität zu Kiel

vorgelegt von
Vanessa Lampe, M.Sc.

Kiel, April 2024

Abgabe der Dissertation: 12.04.2024
Tag der mündlichen Prüfung: 03.07.2024

....
Prof. Dr. Eric Achterberg, Vorsitz der Prüfungskomission

....
Prof. Dr. Andreas Oschlies, Erster Gutachter

....
Prof. Dr. Anja Engel, Zweite Gutachterin

....
Prof. Dr. Natascha Oppelt, Mitglied Prüfungskomission

Summary

The Arctic Ocean's significance for the global climate is well established, and there is broad evidence that the Arctic represents an important and unique ecosystem. Besides their global importance, Arctic regions exhibit high degrees of variability in physical, chemical, and biological processes. The variability observed in the Arctic is substantial, in both temporal and spatial dimensions, especially in comparison with warmer and more oligotrophic ocean regions of lower latitudes. Spatially, it encompasses diverse subregions, each with its unique characteristics. Temporally, the Arctic experiences variability at seasonal, inter-annual, and longer time scales, with significant implications for its ecosystems and global climate dynamics. The warming effects of anthropogenically induced climate change are amplified in the Arctic, leading to a rapid decline in sea ice extent and thickness. These documented changes in temperature and sea ice cover are expected to affect Arctic ecosystems and their biogeochemical functioning. Potential impacts include shifts in plankton community composition, changes in productivity, or mismatches in timing between primary producers and their grazers, with consequences for higher trophic levels such as fish, marine birds, and mammals.

Despite efforts to understand climate change impacts in the Arctic, isolating trends remains challenging, given the strong seasonal and spatial variability in the observational data. The primary objective of my thesis is to advance our understanding of the connections between the microbial pelagic ecosystem and organic matter cycling in the Arctic Ocean, while explicitly accounting for the variability seen in observational data. My main goal is to unravel the complex dynamics that drive temporal and spatial variations in protist plankton composition and to identify the key spatial regions important for discerning the underlying growth dynamics. Understanding the ranges and drivers of seasonal and inter-annual variability in these processes is critical for reliable projections of future climate change impacts on Arctic ecosystems. The limited availability of ocean data from this region poses a challenge to creating a comprehensive synthesis of the interdependent ecological and biogeochemical processes. To bridge this gap, I adopted an approach where I was able to combine highly resolved ecological data derived from microscopic measurements with a size-based plankton ecosystem model. By following a Lagrangian approach, I could track the specific physical forcing histories that plankton communities experience during their transit through the Fram Strait, which helped to disentangle great parts of the variability seen in tracer concentrations and phytoplankton biomass. Additionally, I employed a machine learning technique that allowed relating the seasonal and inter-annual variability of phytoplankton standing stocks to the Fram Strait's variable hydrographic conditions.

The community size structure of Arctic protist plankton and its variability is the focus of Chapter 2 (Manuscript 1). Continuous size spectra were derived using the Kernel Density Estimation method from microscopic data of the protist plankton collected in the Fram Strait between 2016 and 2018. These plankton size spectra provide insight into the size distribution of cell abundance and biovolume, revealing specific size intervals that indicate size-selective predation and omnivory, and ‘loopholes’ caused by reduced grazing pressure, improved growth conditions, or both. This analysis furthermore revealed that the decline in total biovolume from summer to autumn is accompanied by a clear shift towards larger plankton cell size. Such highly resolved size spectra contain detailed ecological information and provide an excellent basis for constraining results of size-based model applications.

With a size-based Lagrangian modelling approach, as described in Chapter 3 (Manuscript 2), it is possible to analyse the dynamical links between the changes in biogeochemistry, which include productivity and export of organic matter, and the development of the size structure of the plankton community. This plankton ecosystem model resolves nine distinct size classes of phyto- and zooplankton and considers the size-dependency of crucial ecological and physiological processes by applying allometric scaling relationships to simulate standing stocks and fluxes of carbon and nitrogen with the nutrient, phyto-, zooplankton and detritus pools. The 1D ecosystem model is forced with 4 ensembles of trajectories that trace the physical conditions along the major currents through the Fram Strait. Overall, estimates of biogeochemical tracer standing stocks and fluxes in the model compare well with *in-situ* and climatological data. Furthermore, simulations of the plankton size structure are in reasonable agreement with the size spectra presented in Chapter 2. Of the variability observed locally at HAUSGARTEN LTER stations, 10–72 % can be attributed to the differences in origin and temporal development of the environmental conditions along the individual trajectories. The model-estimated maxima in productivity and vertical export suggest that these occurred earlier and thus at some distance from the sampling sites of the Fram Strait.

Finally, in Chapter 4, the separation (sectorisation) of surface water mass properties in the Fram Strait with a machine learning (k-means clustering) technique could be further elaborated. With this clustering approach, the variability in remote sensing chlorophyll-*a* data could be disentangled, revealing similar characteristic and robust features within the resolved sectors (regional clusters). Instead of differentiating only between the warmer West Spitsbergen Current (WSC) and the colder East Greenland Current (EGC) influenced regions, a third sector was explicitly resolved to account for the highly variable frontal system in the Fram Strait. The timing and intensity of plankton blooms in remote sensing surface chlorophyll-*a* concentrations differ within the three hydrographical subsections of the Fram Strait, with earlier blooms starting in May in the EGC sector, and later blooms in July in the WSC sector. While the chlorophyll-*a* variability generally correlates with the total chlorophyll-*a* concentration, the normalised variability revealed a significantly higher baseline variability in the EGC sector compared to the WSC and front sectors, which is linked to the highly variable sea ice dynamics.

By integrating observational data, modelling approaches, and machine learning techniques, this thesis highlights the impact of variations in the water mass characteristics on the seasonal plankton phenology and productivity patterns. This thesis provides new insights into the spatial and temporal variability of Arctic protist plankton in the Fram Strait, its causes, and interrelationships that should help drive future research in this critical region.

Zusammenfassung

Die Bedeutung des Arktischen Ozeans für das globale Klima ist wohlbekannt, und es gibt viele Hinweise darauf, dass die Arktis ein wichtiges und einzigartiges Ökosystem darstellt. Neben ihrer globalen Bedeutung weisen die arktischen Regionen ein hohes Maß an Variabilität bei physikalischen, chemischen und biologischen Prozessen auf. Die in der Arktis beobachtete Variabilität ist sowohl in zeitlicher als auch in räumlicher Hinsicht beträchtlich, insbesondere im Vergleich zu den wärmeren und oligotrophen Ozeanregionen der niedrigeren Breitengrade. Räumliche Variabilität spiegelt sich in den verschiedenen arktischen Subregionen wieder, von denen jede ihre eigenen Merkmale aufweist. In zeitlicher Hinsicht verzeichnet die Arktis Variabilität auf saisonalen, zwischenjährlichen und längerfristigen Skalen, mit erhebliche Auswirkungen auf ihre Ökosysteme und die globale Klimadynamik. Die Erwärmung durch den anthropogenen Klimawandel wird in der Arktis noch verstäkt, was zu einem raschen Rückgang der Ausdehung und Dicke des Meereises führt. Es ist zu erwarten, dass diese dokumentierten Veränderungen der Temperatur und der Meereisbedeckung die arktischen Ökosysteme und ihre biogeochemischen Funktionen beeinträchtigen werden. Zu den möglichen Auswirkungen gehören Verschiebungen in der Zusammensetzung der Planktongemeinschaft, Veränderungen in der Produktivität oder zeitliche Diskrepanzen zwischen den Primärproduzenten und ihren Fressfeinden, mit Konsequenzen für höhere trophische Ebenen wie Fische, Meeresvögel und Säugetiere.

Trotz der Bemühungen die Auswirkungen des Klimawandels in der Arktis zu verstehen, bleibt die Isolierung von Trends angesichts der starken saisonalen und räumlichen Variabilität der Beobachtungsdaten eine Herausforderung. Das Hauptziel meiner Dissertation ist es, unser Verständnis für die Zusammenhänge zwischen dem mikrobiellen pelagischen Ökosystem und dem Kreislauf der organischen Materie im Arktischen Ozean zu verbessern und dabei die Variabilität der Beobachtungsdaten explizit zu berücksichtigen. Ich möchte die komplexe Dynamik entschlüsseln, die die zeitlichen und räumlichen Schwankungen in der Zusammensetzung des Protistenplanktons bewirkt, und die räumlichen Schlüsselregionen identifizieren, die für die Erkennung der zugrunde liegenden Wachstumsdynamik wichtig sind. Das Verständnis der Bandbreite und der Triebkräfte der saisonalen und zwischenjährlichen Variabilität dieser Prozesse ist von entscheidender Bedeutung für zuverlässige Projektionen der künftigen Auswirkungen des Klimawandels auf die arktischen Ökosysteme. Die begrenzte Verfügbarkeit von Meeresdaten aus dieser Region stellt jedoch eine Herausforderung für die Erstellung einer umfassenden Synthese der zusammenhängenden ökologischen und biogeochemischen Prozesse dar. Um diese Lücke zu schließen habe ich einen Ansatz gewählt, bei dem ich hoch aufgelöste ökologische Daten, abgeleitet aus mikroskopischen Messungen, mit einem größenbasierten Plankton-Ökosystemmodell kombinieren konnte. Mit Hilfe eines Lagrange-Ansatzes konnte ich die Geschichte der unterschiedlichen physikalischen Einflüsse verfolgen, denen die Planktongemeinschaften während ihrer Durchquerung der Framstraße ausgesetzt sind, und so einen großen Teil der Variabilität der Tracerkonzentrationen und der Phytoplanktonbiomasse entschlüsseln. Darüber hinaus habe ich eine Maschine-Learning-Technik eingesetzt, die es ermöglichte, die saisonale und interannuelle Variabilität der Phytoplanktonbestände mit den variablen hydrographischen Bedingungen in der Framstraße in Beziehung zu setzen.

Die Größenstruktur der Gemeinschaft des arktischen Protistenplanktons und ihre Variabilität ist der Schwerpunkt von Kapitel 2 (Manuskript 1). Aus mikroskopischen Daten, welche zwischen 2016 und 2018 in der Framstraße gesammelt wurden, wurden mit der Methode der Kerndichtenschätzung kontinuierliche Größenspektren des Protistenplanktons abgeleitet. Diese Plankton-Größenspektren geben Aufschluss über die Größenverteilung der Zellhäufigkeit und des Biovolumens und enthüllen spezifische Größenintervalle, die auf größenselektive Prädation und Omnivorie sowie auf 'Schlupflöcher' hinweisen, die durch verringerten Weidedruck, verbesserte Wachstumsbedingungen, oder beides verursacht werden. Diese Analyse ergab außerdem, dass der Rückgang des Gesamtbiovolumens vom Sommer bis zum Herbst mit einer deutlichen Verschiebung zu größeren Planktonzellen einhergeht. Solche hochaufgelösten Größenspektren enthalten detaillierte ökologische Informationen und bieten eine hervorragende Grundlage für die Überprüfung der Ergebnisse von größenbasierten Modellanwendungen.

Ein größenbasierter Lagrangescher Modellierungsansatz, wie er in Kapitel 3 (Manuskript 2) beschrieben wird, ermöglicht es, die dynamischen Zusammenhänge zwischen Veränderungen in der Biogeochemie, einschließlich der Produktivität und des Exports von organischem Material, mit der Entwicklung der Größenstruktur der Planktongemeinschaft zu analysieren. Dieses Plankton-Ökosystemmodell löst neun verschiedene Größenklassen von Phyto- und Zooplankton auf und berücksichtigt die Größenabhängigkeit entscheidender ökologischer und physiologischer Prozesse durch die Anwendung allometrischer Skalierungsbeziehungen, um die Bestände und Flüsse von Kohlenstoff und Stickstoff innerhalb der Nährstoff-, Phyto-, Zooplankton- und Detritus-Pools zu simulieren. Das 1D-Ökosystemmodell wird mit vier Trajektorienensembles angetrieben, mit denen die physikalischen Bedingungen entlang der Hauptströmungen in der Framstraße nachgezeichnet werden. Insgesamt stimmen die Schätzungen der biogeochemischen Tracerbestände und -flüsse im Modell gut mit den *in-situ*- und Klimadaten überein. Außerdem stimmen die simulierten Größenverteilungen des Planktons gut mit den in Kapitel 2 vorgestellten Größenspektren überein. Von der lokal an den HAUSGARTEN LTER-Stationen beobachteten Variabilität können 10–72 % auf die unterschiedliche Herkunft und zeitliche Entwicklung der Umweltbedingungen entlang der einzelnen Trajektorien zurückgeführt werden. Die modellgeschätzten Maxima in Produktivität und vertikalem Export organischen Materials lassen vermuten, dass diese früher und damit in einiger Entfernung von den Probenahmestellen in der Framstraße auftraten.

Abschließend wird in Kapitel 4 die Trennung (Sektorisierung) der Oberflächenwassermasseneigenschaften in der Framstraße mit einer Machine Learning Technik (k-means clustering) weiter ausgearbeitet. Mit diesem Clustering-Ansatz könnte die Variabilität der Fernerkundungs-Chlorophyll-a-Daten entflochten werden, wodurch ähnliche charakteristische und robuste Merkmale innerhalb der aufgelösten Sektoren (regionale Cluster) sichtbar werden. Anstatt nur zwischen den wärmeren, vom Westspitzbergenstrom (WSC) und den kälteren, vom Ostgrönlandstrom (EGC) beeinflussten Regionen zu unterscheiden, wurde hier ein dritter Sektor explizit aufgelöst, um dem hochvariablen Frontensystem in der Framstraße Rechnung zu tragen. Der Zeitpunkt und die Intensität der Planktonblüte in den Fernerkundungsdaten der Chlorophyll-a-Oberflächenkonzentrationen unterscheiden sich innerhalb der drei hydrographischen Sektoren der Framstraße, wobei die Blüte im EGC-Sektor früher im Mai beginnt und im WSC-Sektor später im Juli. Während die Chlorophyll-a-Variabilität im Allgemeinen mit der Gesamtchlorophyll-a-Konzentration korreliert, zeigte die normalisierte Variabilität im EGC-Sektor eine signifikant höhere Basisvariabilität als im WSC- und im Front-Sektor, was mit der sehr variablen Meereisdynamik zusammenhängt.

Durch die Integration von Beobachtungsdaten, Modellierungsansätzen und Machine Learning Techniken werden in dieser Arbeit die Auswirkungen von Variationen der Wassermasseneigenschaften auf die saisonale Planktonphänologie und Produktivitätsmuster aufgezeigt. Diese Arbeit bietet neue Einblicke in die räumliche und zeitliche Variabilität des arktischen Protistenplanktons in der Framstraße, ihre Ursachen und Zusammenhänge, welche die zukünftige Forschung in dieser kritischen Region anregen sollen.

Contents

Chapter 1

Introduction

1.1 Variability in the Arctic

The Arctic Ocean is a key player in the global climate system due to its role in water mass transformation and the freshwater budget (Rudels and Friedrich, 2000). Moreover, its ice cover is crucial for the cooling regulation because of the albedo effect (e.g. Perovich et al., 2007; Stroeve et al., 2012). However, the ecosystems within the Arctic Ocean are facing unprecedented challenges, including the impacts of climate change, intensified fishing pressure, and pollution (e.g. Wassmann, 2011; Arrigo, 2013; Townhill et al., 2022). Characterized by pronounced variability across various spatial and temporal scales (e.g. Wilson et al., 2021), the Arctic Ocean stands as a dynamic and critical component of the Earth's climate system.

Spatial variability can be expressed by the larger-scale differences in the Arctic subregions. For example, the influence of the freshwater system plays different roles in the Arctic subregions, such as the coastal shelf regions and the major basins of the Arctic Ocean. While waters entering the central Arctic from the Nordic Seas are temperature-stratified, those entering from the Bering Strait are salinity-stratified, which leads to differences in the winter mixed layer depths between the Eurasian and Amerasian Basins (Brown et al., 2020). The coastal shelf regions, however, are subject to seasonally varying riverine input of terrestrial matter (nutrients, particulate organic and inorganic matter, with limited transport into the deep basins) and seasonally varying sea ice cover (Brown et al., 2020). Spatial variability can also be expressed on finer scales, such as the mesoscale variability in the physical conditions introduced by eddies (extending up to 100 km), that modify the sea ice conditions and thereby impact primary productivity (e.g. Von Appen et al., 2022). On even finer scales, variability can be observed in the form of plankton patches (usually extending over 2–5 km), where the chlorophyll-a concentration within a patch can exceed outside concentrations by a factor of 3–17 (e.g. Trudnowska et al., 2016).

Temporal variability can also be observed on various levels. For example, seasonal variability in primary productivity in the Arctic Ocean is predominantly shaped by extreme gradients in light availability, ranging from complete darkness during the polar night in winter to 24h of light exposure during the polar day in summer, and the seasonal cycle of melting and freezing of the sea ice cover that modulates the stratification of the water column and the water column light field (e.g. Castellani et al., 2022). Furthermore, inter-annual variations can be reflected in biological variables, such as plankton bloom dynamics and the impact on higher trophic levels like fish recruitment, as documented e.g. in the Oscillating Control Hypothesis for the eastern Bering Sea (Hunt et al., 2011). The OCH describes how the timing of seasonal ice retreat impacts the timing of plankton blooms and thus the copepod composition and distribution, which in turn affects pollock recruitment and stock sizes. Early retreat favors smaller copepods and leads to reduced pollock stocks, while late retreat supports larger copepods and increased pollock populations in the following year (Hunt et al., 2011). On multi-annual (i.e. decadal or multi-decadal) scales, observations have shown how atmospheric oscillatory processes, such as the Arctic Oscillation and the Low Frequency Oscillation, influence atmospheric sea level pressure and surface air temperatures and drive a large amplitude of atmospheric variability in the Arctic (Polyakov and Johnson, 2000).

On longer time scales, the Arctic Ocean is under serious transformation due to anthropogenically induced climate change (e.g. Wassmann and Reigstad, 2011; Stroeve et al., 2012). The Arctic shows considerably stronger warming than other regions on the globe, a phenomenon often referred to as Arctic Amplification. (Manabe and Stouffer, 1980) have shown with a relatively simple model that when atmospheric carbon dioxide (CO_2) is quadrupled, warming is amplified in the Arctic, and that this warming is stronger in winter than in summer, which considerably decreases the seasonal amplitude. Responsible for this amplification are feedback processes associated with temperature, water vapour, clouds, and surface albedo (Holland and Bitz, 2003). The sea-ice albedo feedback is often considered the most important contributor, although Pithan and Mauritsen (2014) have found that the amplification occurs also in models that simulate no change in sea ice cover, indicating that the temperature feedback is even stronger. Newer research by Jenkins and Dai (2021) however contradicts this view and identifies sea ice loss and the resulting changes in surface warming and surface albedo as the drivers of Artic Amplification, concluding that sea ice loss enhances the heat release during winter, which in summer leads to a positive albedo effect and in winter to a moderate positive cloud feedback, that both contribute to the Arctic Amplification. Between 1979 and 2021, temperatures in the Arctic have risen four times faster than the global average, as demonstrated by Rantanen et al. (2022) using a combination of several sets of different types of observations. The authors conclude that when the observed four-fold warming is compared to the results of various models, it qualifies as an extremely unlikely event and may indicate how current models underestimate polar amplification. In absolute numbers, this corresponds to an increase in sea and sea-ice surface temperature by 4.5°C between 1982 and 2021 averaged over the Arctic, with considerable regional variability and a peak increase of 10°C in the north-eastern Barents Sea (Nielsen-Englyst et al., 2023). The temperature increase has led to a substantial decline in sea ice extent and thickness (Stroeve et al., 2012; Hansen et al., 2013; Renner et al., 2014; Spreen et al., 2020).

The documented changes in temperature and ice cover are expected to have considerable impacts on Arctic ecosystems and their biogeochemical functioning (Wassmann and Reigstad, 2011). The effects range from changes in the composition of the planktonic communities with smaller picoplankton (< 2 µm) replacing the larger nanoplankton (2–20 µm) (Li et al., 2009) to changes in productivity due to the longer ice-free periods, where estimates range between an increase of ca. 30 % for the period 1998–2012 (Arrigo and van Dijken, 2015) to a smaller increase of 4.5 % for the period 1998–2018 (Kulk et al., 2020). Phytoplankton and ice algae (growing attached to the underside of sea ice) serve as a food source for higher trophic levels, e.g. copepods. However, the earlier timing of bloom initiation may cause mismatches between the abundance of nutrition and the established reproduction and life cycles of metazoan grazers (Søreide et al., 2010).

Given the strong seasonal and spatial variability, isolating trends associated with climate-change-induced warming is a difficult task and requires confident knowledge of the ranges of natural variability in this remote and heterogeneous region.

1.1.1 General plankton dynamics in the European Arctic

The seasonal dynamics in water column stability (stratification and vertical mixing) that are largely determined by the freeze-melt cycle (e.g. Brown et al., 2020), along with the changes in the photosynthetically available radiation (PAR) during the annual light cycle (e.g. Castellani et al., 2022), drive the seasonal phenology of primary producers in the water column of the Arctic seasonal ice zone.

The Arctic plankton community is subject to strong seasonal and spatial variations in nutrient and light availability, which was comprehensively described in overview figures by Wassmann and Reigstad (2011) shown in Fig. 1.1. In the marginal ice zone (Fig. 1.1 a)), a zone of pronounced productivity (e.g. Smith et al., 1987), the thick sea ice and its snow cover begin to melt in spring. A first bloom occurs in the bottom layer of the sea ice, triggered once light levels are sufficient for the low-light adapted ice-algal species (Leu et al., 2015). In the following, increased stratification of the upper water column and further increasing light availability trigger brief and intensive pelagic plankton blooms. These ice-edge associated blooms form belts of 20–100 km width along the ice-edge (Sakshaug, 2004). The positive buoyancy of the upper water column prevents deep mixing, e.g. by wind, and separates the euphotic zone and seasonal mixed layer from the permanent nutricline (Brown et al., 2020). Autotrophic growth exceeds heterotrophic degradation during this phase, which leads to the rapid accumulation of biomass. However, this primary production quickly depletes dissolved nutrients from the surface down to increasingly greater depths, and heterotrophic processes gradually take over, initiating the decline of the bloom. During this time, new production is small and a subsurface chlorophyll maximum forms above the nutricline (Brown et al., 2020). During summer, export to depth is highest and consists mostly of biogenic matter that originates from phytoplankton. As this vertical organic matter (OM) export gradually declines throughout late summer and autumn, the composition of the exported OM becomes progressively dominated by more degraded biogenic matter that stems from heterotrophic micro- and mesoplankton (Wassmann and Reigstad, 2011). Nutrient limitation and decreasing light availability due to the decreasing day length and the onset of sea ice formation limit further photoautotrophic growth, which deprives the heterotrophic community of their resources. Consequently, heterotrophic biomass declines and the remaining organic matter is either exported to depth or remineralised in the surface layer. However, when sea ice formation in autumn releases brine again and erodes the summer halocline down to the permanent halocline, autumn blooms may occur (Brown et al., 2020). During winter, biomass and export remain low and nutrients in the upper water column are replenished through diffusion and vertical mixing until the next spring (Wassmann and Reigstad, 2011). Ice-edge blooms are constantly on the move while sea ice breaks up

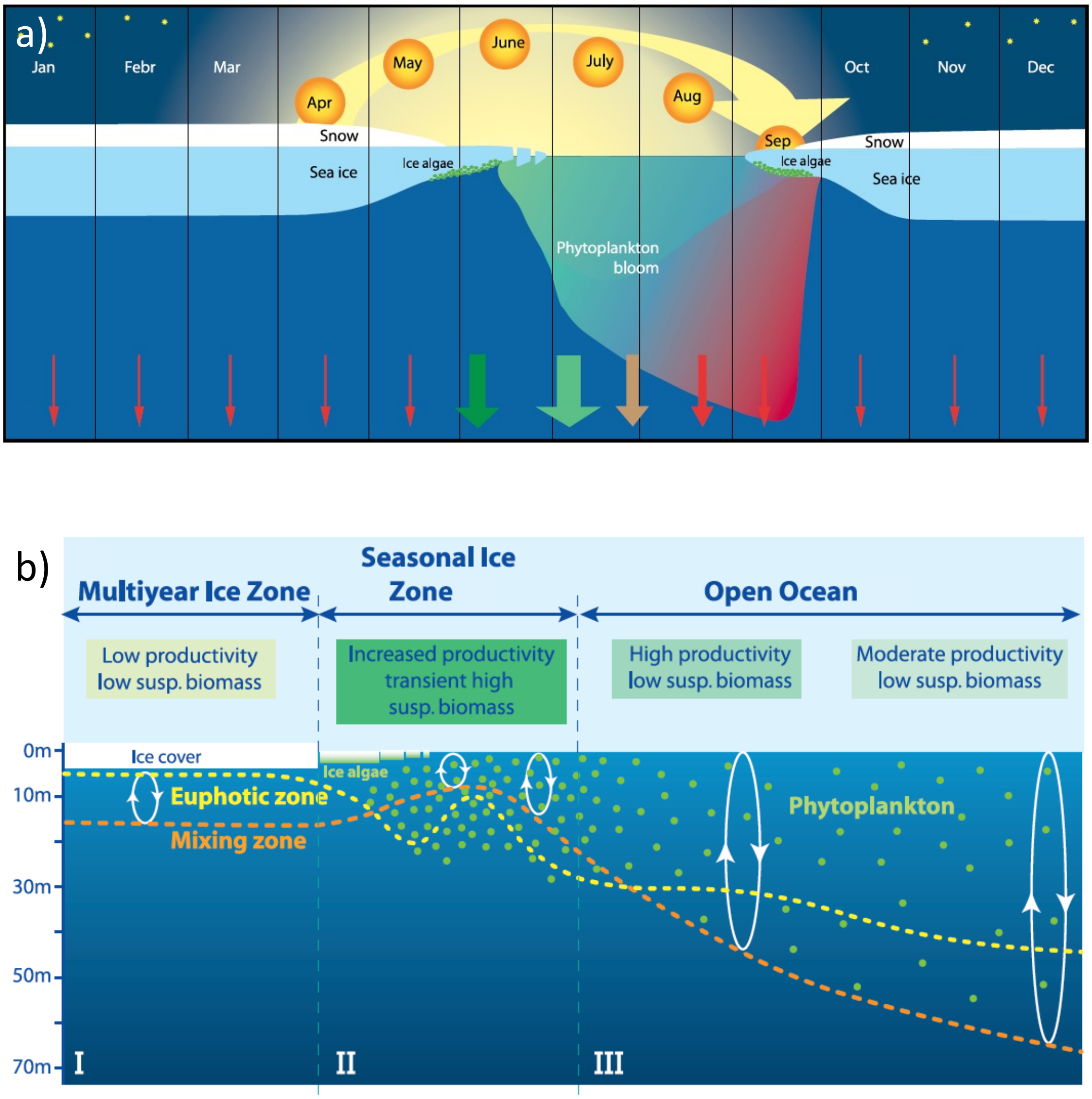

Figure 1.1: Seasonal and spatial variability in phytoplankton bloom dynamics, as conceptualised and described by Wassmann and Reigstad (2011, Figs. 2 and 3, combined and simplified). The seasonality in bloom development of protist phyto- and zooplankton in the seasonal ice zone is shown in **a)**. During the dark period, vertical export of organic matter (shown semi-quantitatively as arrows) is low. In spring, light availability increases as the ice cover thins, allowing the growth of ice algae (shown as green dots). As the ice retreat continues, meltwater stabilises the water column and a pelagic phytoplankton bloom forms (shown in green). The proportion of heterotrophic plankton increases during the open water period (indicated by the green-to-red gradient). The key source of exported matter changes during the growth period (colour of arrows; ice algae = dark green, phytoplankton = light green, orange to red = increasing proportion of detritus). The spatial variability in relation to sea ice is shown in **b)**. In the multiyear ice zone, thick ice cover prevents light from reaching the water column, and primary productivity and suspended biomass are low. Productivity is increased in the marginal ice zone, leading to transient high suspended biomass, as light can enter the water column. Meltwater stratification stabilises the water column preventing the phytoplankton from mixing out of the euphotic zone. The depth of the mixed layer increases with increasing distance to the ice edge. Here, productivity is high but suspended biomass is low.

and exposes nutrient rich water, with the bloom following the retracting ice edge, being youngest close to the edge, and in the culmination phase in some distance (Sakshaug, 2004).

The dynamics of plankton productivity in the ice-covered regions differ from those in the open sea. In general, the large-scale variability in polar phytoplankton is driven by how much mixed-layer conditions allow for increasing and decreasing cell division rates. The interplay of the division and loss rates, which are highly correlated with loss rates lagging behind division rates by a few days, creates boom-bust cycles of biomass (Behrenfeld et al., 2017). While productivity and its variability are most pronounced in the marginal ice zone, photosynthetic activity in the multi-year ice zone is limited by low under-ice light availability and is mainly associated with ice-algae (Leu et al., 2015). In the open ocean zone, the water column is subject to a weaker, thermal stratification. Here, productivity decreases with increasing distance to the ice edge, and suspended biomass concentrations are considerably lower than in the marginal ice zone (see Fig. 1.1 b)). Periodic mixing, e.g. due to strong winds or upwelling at the shelf breaks, partly replenishes the upper water column with fresh nutrients and triggers occasional small pulsed bloom events (Wassmann and Reigstad, 2011).

In the European Arctic, the phenology of blooms is highly variable in terms of intensity and onset. For example, along the Greenland coast, the date of bloom initiation shows a strong north-to-south gradient with earlier onset starting in April in the south and later, by the end of June north off Greenland (Vernet et al., 2021). Furthermore, along this S–N gradient, productivity is affected by the sea ice, its formation and melting, with higher rates and earlier onset offshore, moving closer to the coast during summer (Vernet et al., 2021). A long-term analysis of satellite-derived estimates of sea-surface chlorophyll *a* (Chl-*a*) concentrations between 1998 and 2012 revealed high intra and inter-annual variability and showed that Chl-*a* maxima were typically reached around May or June (bloom duration 73–128 days) in the western Fram Strait off Greenland and in June or July (duration 112–142 days) in the eastern Fram Strait off Spitsbergen (Nöthig et al., 2015).

Apart from the differences in timing and duration of blooms, the total (integrated) primary productivity differs within the Fram Strait. The estimated annual net primary production in the western part of the Fram Strait is estimated around 49.5 to 53.2 $\mathrm{g\,C\,m^{-2}\,yr^{-1}}$ from ocean color remote sensing and 23.9 to 34.5 $\mathrm{g\,C\,m^{-2}\,yr^{-1}}$ from SINMOD model simulations, with its maximum of 0.6 $\mathrm{g\,C\,m^{-2}\,d^{-1}}$ in June or July (Vernet et al., 2021). The f-ratio (fraction of new production and total production) around 0.7 indicates that a large amount (ca. 70 %) of total primary production is available for export to depth or higher trophic levels (Vernet et al., 2021) and therefore a potentially less effective influence of the microbial loop. The eastern part of the Fram Strait shows higher productivity during the productive season (April to September). Similarly to the western part, Vernet et al. (2019) observed a strong south-to-north gradient in gross primary production (GPP) from SINMOD model results, ranging from 120 $\mathrm{g\,C\,m^{-2}\,6mo^{-1}}$ west of Spitsbergen to 60 $\mathrm{g\,C\,m^{-2}\,6mo^{-1}}$ north of Svalbard, of which 15 $\mathrm{g\,C\,m^{-2}\,6mo^{-1}}$ are available for export each year. In this region of Atlantic water inflow, advected plankton account for 30 times the *in-situ* annual production. While the contribution of advected plankton to the total biomass is intermediate (10 to 20 times) at

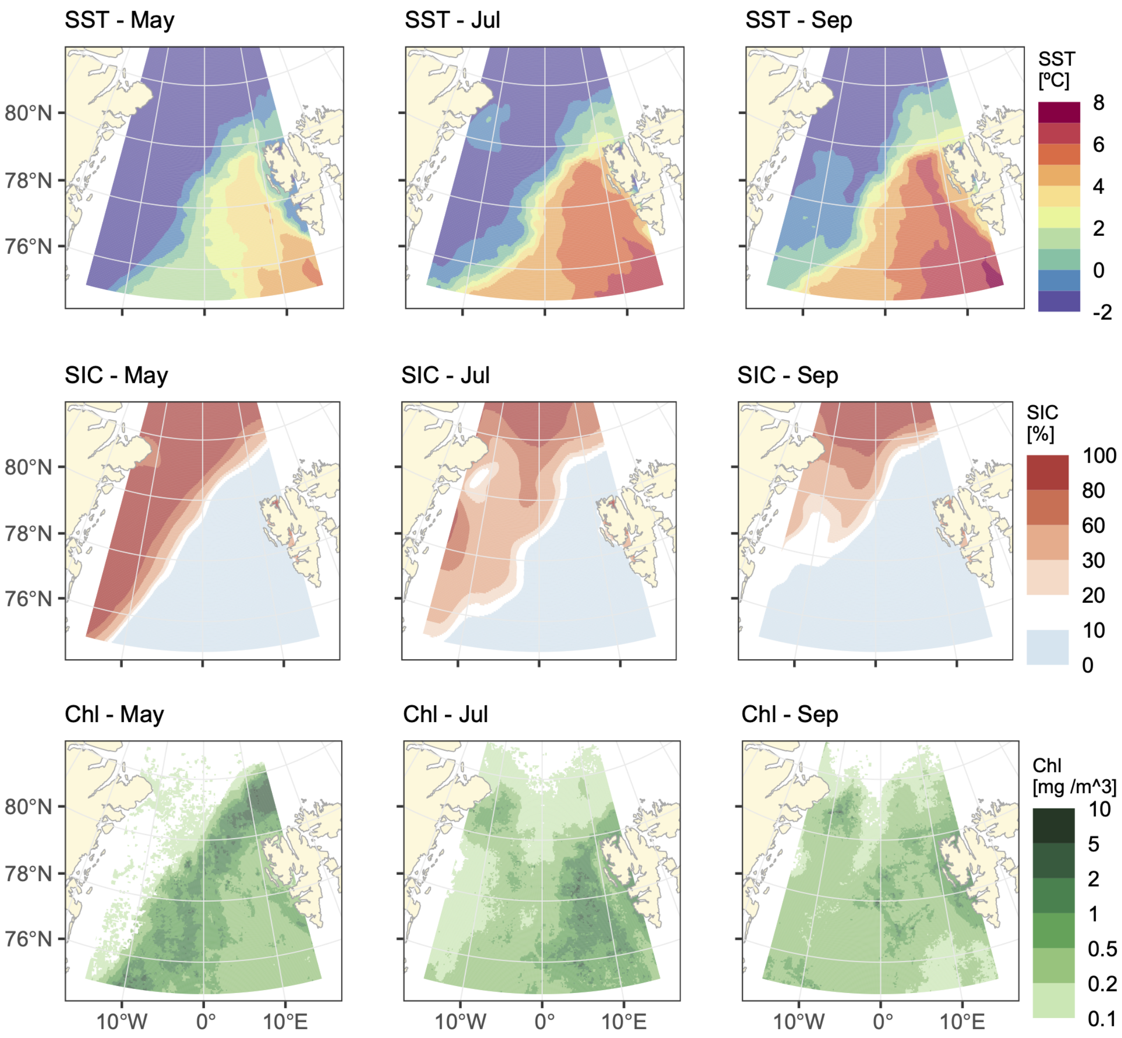

Figure 1.2: Remote sensing observations of sea surface temperature (SST), sea ice cover (SIC), and chlorophyll-*a* concentration (Chl) in the Fram Strait. Shown here are monthly aggregates of daily data products (mean) for May, July and September in 2018. SST and SIC data were provided by GHRSST, Met Office and CMEMS (Good et al., 2020), Chl data are sourced from CMEMS and ACRI (2023).

the beginning and the end of the growth season, the ratio is especially small (5 times) when *in-situ* GPP is high, i.e. during the spring bloom, and maximum (50 times) in August (Vernet et al., 2019).

Another example of the temporal and spatial variability in chlorophyll-*a* standing stocks and its relationship with sea ice cover and sea surface temperature (as a proxy for water mass type) can best be analysed with available data derived from remote sensing, as exemplified for 2018 in Fig. 1.2. In the Fram Strait, sea surface temperatures (SST) reveal highly variable horizontal patterns, with lower temperatures in the northwest (ca. -2–0°C) and higher temperatures in the southeast (> 4°C). SST is intermediate between the two regions. The regional extent of the warmer, colder, and intermediate zones however changes over time, with the intermediate and warmer zones progressively gaining in size from May to September. High spatial and temporal variability is also apparent in the ice cover (sea ice concentration). The cold region in the northwest is fully covered with sea ice, while open ocean conditions occur in the southwest. The extent of the ice cover decreases from May to September, retracting northwards and opening a polynya off Greenland in July, that is connected to the open ocean by September. The remote sensing data show well how the high variability in the hydrographic conditions and sea ice cover is reflected in the standing stocks of phytoplankton. In May, the concentration of chlorophyll is highest along the margin of the ice sheet and lowest where SST is high, with sparse observations of low concentrations in the region of high ice cover. In July, elevated chlorophyll concentrations occur in the polynya off Greenland and the region of warmer SST off Spitsbergen. In regions of intermediate ice cover (approx. > 60 %), chlorophyll concentration is markedly low. In large parts of the Fram Strait, chlorophyll concentrations are low in September, with occasional small patches of higher concentration and elevated chlorophyll in a strip off the western coast of Spitsbergen.

1.1.2 Scales of variability in data

For unravelling variability in time and space, it is hardly possible to rely on a single type of observational data. Different data types reveal different scales of variability in terms of their spatial and temporal resolution. Spatial variability on coarser scales can be captured well with data retrieved from remote sensing satellites. The spatial resolution depends on the satellite and sensors used and on the data processing, for example, the SST and SIC data displayed in Fig. 1.2 are available on a 0.05x0.05° grid (Good et al., 2020) (approx. 5.5x4.5 km in this latitude range), and the chlorophyll data on a 4x4 km grid (CMEMS and ACRI, 2023). Although data collected with novel measurement devices on modern satellites, such as Maxars WorldView-3 (launched in 2014), have a resolution of 0.3–30 m depending on sensor type (ESA, 2024), the processed final data products are usually available in coarser resolutions. Since this type of ocean data product is often available daily, they can be combined or aggregated over time for analysing the temporal variability over the timescales of days to decades back to the 1980ies (Comiso, 1995). However, despite the potential high resolution of remote sensing estimations of ocean color with optical sensors, observations in the Arctic are often obscured by aerosols, clouds, and seasonally sun glint, low illumination, and sea ice cover (e.g. Cole et al., 2012; Cherkasheva et al., 2014; Kuhn et al., 2023).

On somewhat coarser scales, valuable information can be derived from climatological data products such as the World Ocean Atlas (Garcia et al., 2019a), which entail long-term average data of various variables, e.g., sea surface temperatures, salinity, or nutrient concentrations, collected over multiple years or decades often combining measurements from ships, autonomous samplers, buoys, and satellites. These data are vertically resolved and can thus inform about depth gradients and may resolve major seasonal changes on local, regional to global scales.

In-situ sampling from research vessels allows for a finer spatial resolution of surface observations, but a considerably smaller spatial coverage, i.e., along the track of the ship or at discrete sampling stations. However, in contrast to remote sensing observations that may only penetrate the upper water column, *in-situ* sampling at discrete stations makes it possible to depict the depth dimension at a specified resolution down to defined depths.

Repeated sampling at discrete stations permits the creation of time series. The repeated sampling over years or decades provides highly valuable data that capture the local variability in time. However, their temporal resolution is defined by the interval stations are sampled. For example, the Isfjorden Adventfjorden time series in Isfjorden (Svalbard) is sampled on a weekly to monthly basis (The University Centre in Svalbard UNIS, 2024). More offshore locations, such as the HAUSGARTEN location in the Fram Strait, are usually sampled yearly, as the remote and harsh conditions in the region require extensive logistics. HAUSGARTEN comprises a network of sampling stations (described in the following Sect. 1.2) and thereby additionally allows resolving the spatial variability between the discrete locations within the area. The *in-situ* sampling furthermore allows the detailed investigation of important biological variables such as the composition of plankton communities and organic matter, in addition to observations of their bulk concentrations. For example, with microscopic measurements, samples of the plankton community can be analysed in terms of abundance, species composition, and size structure. Such highly resolved optical measurements provide important details of the plankton ecosystem.

1.2 The Fram Strait

The Fram Strait, shown in Fig. 1.3, is considered one of the main gateways to the Arctic Ocean, connecting the central Arctic to the Atlantic Ocean between Greenland and Svalbard. With a sill depth of 2600 m, it is the only deep water connection, and its width at the narrowest point is approximately 450 km. The region is characterised by a highly variable hydrography and sea ice situation (Soltwedel et al., 2016).

Waters in the eastern Fram Strait are dominated by the inflow of Atlantic water that carries relatively warm and nutrient-rich water from the North Atlantic into the central Arctic Ocean with the West Spitsbergen Current (WSC, red arrow in Fig. 1.3) (Beszczynska-Möller et al., 2012). In the west, the East Greenland Current (EGC, blue arrow in Fig. 1.3) transports colder, fresher Polar Water (PW) southwards, exiting the Arctic Ocean and carrying sea ice into the North Atlantic (de Steur et al., 2009). Between the two major currents, a frontal system separates the water masses. The East Greenland Polar Front (EGPF) is affected by sea ice dynamics and shows high seasonal variability in its intensity and extent (Liu et al., 2022). Eddies are frequent in this region and add to the mesoscale variability (e.g. Von Appen et al., 2022). The complex hydrographic situation results in a highly variable sea ice cover, with a permanently ice-free southeast, predominantly ice-covered northwest, and seasonally varying conditions in the central and northeastern parts (Soltwedel et al., 2016).

Since 1999, the Fram Strait has been home to the Long Term Ecological Research (LTER) observatory HAUSGARTEN, making it the longest multidisciplinary open-ocean site time-series study in polar regions (Soltwedel et al., 2016). Sampling stations follow a bathymetric transect along the 79°N latitude from 250 m to 5500 m depth, extending from Kongsfjorden to the Molloy Deep and covering the WSC branch. Stations that are located further to the west in the EGC, were added in 2014. In addition to the transect, three sites are located in the northeastern Fram Strait (79°30'–80°N), close to the ice edge, and another site in the permanently

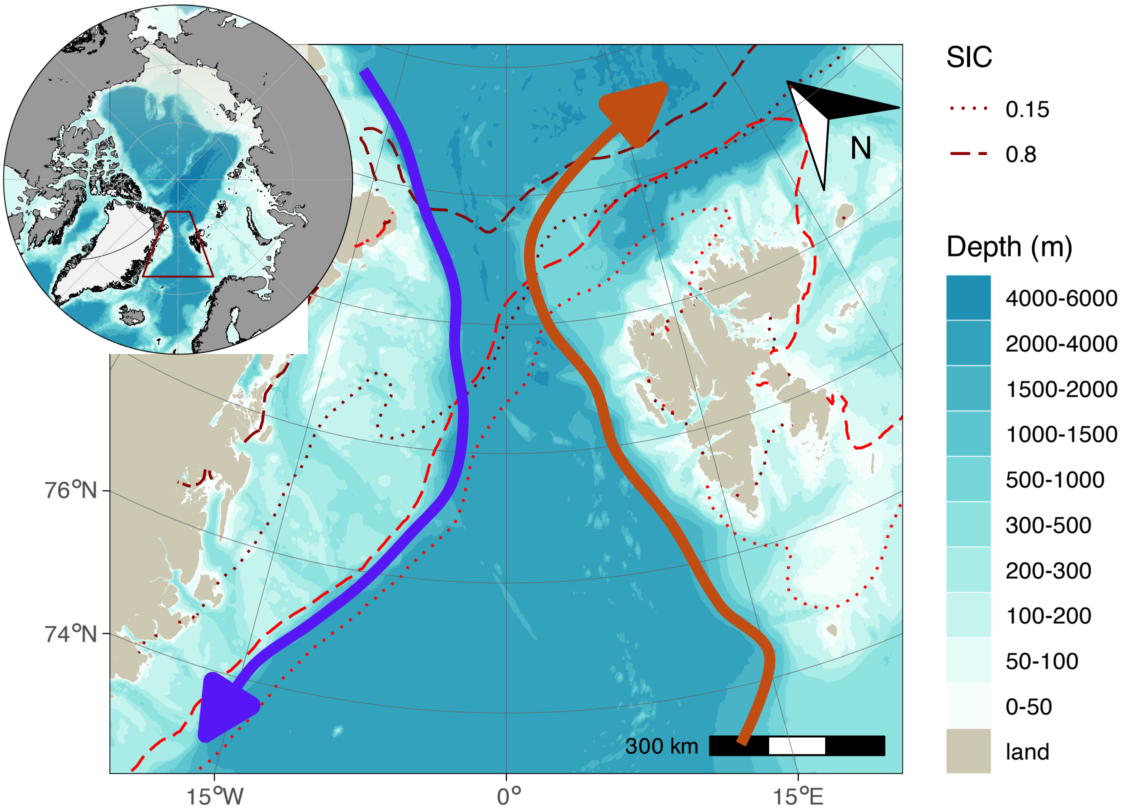

Figure 1.3: Location and bathymetric features of the Fram Strait. The red polygon in the panarctic map (top left) indicates the location of the FS. The Fram Strait detail map shows the 15 % (dotted) and 80 % (dashed) sea ice contours for April (light red) and September (dark red). The arrows indicate the major currents (blue = EGC, orange = WSC). The panarctic map was created with the ggOceanMaps R package (Vihtakari, 2024), detailed bathymetry data for the FS map was provided by IBCAO (2023), sea ice data by Good et al. (2020), arrows were drawn after Beszczynska-Möller et al. (2012).

ice-free region at 78°30' N.

Yearly expeditions, predominantly during summer, head for the HAUSGARTEN site and allow for the repeated sampling of the water column and sea floor. Furthermore, autonomous devices and moorings perform year-round sampling. In the multidisciplinary investigations at HAUSGARTEN, biologists, geochemists, sedimentologists, and physical oceanographers collaborate to describe and understand the physical, chemical, and biological variations and interdependencies, including changes in plankton communities and organic matter fluxes (Soltwedel et al., 2016).

1.3 Modelling pelagic Arctic ecosystems

For accurate model representations of plankton ecosystem dynamics in the Arctic, it is crucial to understand the stoichiometric coupling between carbon and limiting nutrients in both autotrophic and heterotrophic processes, as highlighted by Thingstad et al. (2008). This understanding is fundamental for precise representations of the current and future carbon cycle dynamics in the Arctic.

A key component of marine food webs is the microbial loop, as described by Azam et al. (1983), which outlines the microbial recycling of organic matter. In the ‘classical’ food chain, primary producers (phytoplankton) produce organic matter from inorganic substances through photosynthesis, and small zooplankton feed on the phytoplankton. Small zooplankton serve as a food source for larger zooplankton, which in turn are grazed on by fish, and thus energy and matter are gradually transferred up to higher trophic levels. According to Sheldon et al. (1972), the biomass is distributed approximately equally among logarithmic size classes from bacteria to whales, and organisms predominantly rely on prey that is smaller than themselves by one order of magnitude. Detritus accumulating along this food chain is either exported to depth or remineralised by bacteria. The microbial loop extends this concept by considering loop pathways, in which dissolved organic matter (DOM), predominantly released by phytoplankton, is not only remineralised by heterotrophic bacteria but channelled back to the main food chain as the DOM-consuming bacteria are grazed on by heterotrophic flagellates, and autotrophic and heterotrophic flagellates are preyed on by microzooplankton (Azam et al., 1983; Pomeroy et al., 2007).

A sufficient representation of the microbial loop dynamics is difficult to achieve. This has been addressed by Thingstad et al. (2008) and Thingstad and Cuevas (2010), who proposed a minimum food web model. This model describes three pathways in which nutrients are acquired by osmotrophs. Osmothrophs are organisms, that feed on dissolved compounds absorbed through osmosis and include bacteria and phytoplankton. In contrast, phagotrophic organisms, such as heterotrophic nanoflagellates, ciliates, and mesozooplankton engulf their prey. The first pathway is the ‘bacterial’ pathway, where heterotrophic bacteria absorb inorganic nutrients and bioavailable organic matter and are in turn preyed on by heterotrophic nanoflagellates. In the second, ‘autotrophic flagellate’ pathway, inorganic nutrients are utilised by autotrophic flagellates. Flagellates, both heterotrophic and autotrophic, serve as a food source for ciliates. The third, ‘diatom’ pathway describes the transfer of nutrients via diatoms to the mesozooplankton (copepods) who also feed on ciliates. Therefore, this food web model resolves three vertical food chains, where nutrients are transferred via osmotrophs to their phagotrophic predators and a horizontal food chain connecting the phagotrophs (heterotrophic flagellates > ciliates > copepods).

Larsen et al. (2015) have extended the concept of Thingstad and Cuevas with a fourth pathway based on experiments in an Arctic mesocosm study. Here, a distinction between small and large diatoms is made, with ciliates being able to additionally graze on small diatoms. This food web model has shown to be sensitive to changes in the abundance of mesozooplankton (i.e. copepods), underlining the potential role of top-down control in shaping Arctic microbial food webs. Although practical, the distinction between autotrophic and heterotrophic organisms is often blurry, suggesting that the dichotomy is over-simplifying (Flynn et al., 2013). Many planktonic organisms display both feeding strategies, to a variable extent, and e.g. *Micromonas* and *Dynobrion*, traditionally classified as phytoplankton, account for a significant amount of bacteriovory in the Arctic (Stoecker and Lavrentyev, 2018). In a global model, the consideration of mixotrophy has shown to increase the trophic transfer efficiency and vertical carbon flux (Ward and Follows, 2016).

Ecosystem functions are very sensitive to changes in the community composition and the dominant linkages, depending on the underlying structure of the food web (Prowe et al., 2022), and in reality, food webs are more complex than the idealised relationships between their components assumed in the previously described food web configurations. For example, allowing intra-guild predation (the grazing of predators on prey that shares the same resources; e.g. ciliates on ciliates), a pathway not commonly resolved in models, reduces the energy transfer to higher trophic levels and increases net primary productivity and recycling (Prowe et al., 2022). A key challenge is to impose constraints that allow deriving unique model solutions of plankton interactions, which remains difficult even in cases when data of excellent quality seem to resolve all major state variables of the minimum food web model. Therefore, research on plankton ecosystem model design is an active field, focussing on how the reduce the problems caused by imposed structures while considering established principles and rules. Here, also the availability of data should be taken into account so that a clear or at least representative model solution can be identified with the help of observations (Schartau et al., 2017).

Instead of structuring microbial food webs by functional types, a promising approach is to structure the communities and their grazing interactions by organism size. Cell size is a 'master trait' that controls many aspects of plankton dynamics, from cellular to community level (e.g. Marañón, 2015; Andersen et al., 2016; Blanchard et al., 2017). For example, physiological processes such as nutrient assimilation can be described with allometric relationships (e.g. Moloney and Field, 1989; Litchman et al., 2007; Edwards et al., 2012). Also, interactions between predators and prey are size dependent, with most predators showing size selectivity with a relatively constant predator:prey size ratios (Hansen et al., 1994). Size-based models are built on allometric relationships and can be used for explaining changes in the plankton community structure and implications for biogeochemical functioning (Moloney and Field, 1991; Banas, 2011; Ward et al., 2012). Models that resolve the size structure of the plankton community can be tested or calibrated with observational data, for example in the form of plankton size spectra.

When studying the variability of the plankton community structure, it is important to adequately resolve the small-scale variability in physical forcing and biological interactions a plankton community is subject to over time. This is especially the case in the Fram Strait, where the major currents carry the communities through the region, exposing them to extreme gradients for example in light and temperature regimes along their journey. The ocean model SINMOD (Slagstad and McClimans, 2005; Wassmann et al., 2006) is commonly used to simulate physical, chemical, and biological processes in the Nordic and Arctic Seas. This regional coupled 3D model has a horizontal resolution of 20 km with 25 vertical layers and encompasses hydrodynamic, sea ice, and ecological components. Although the food web configuration is rather simple, SINMOD successfully reproduces observations of suspended biomass in the Barents Sea in space and time, finding substantial differences in the seasonal variability in the ice-covered Arctic waters and the Atlantic waters, but underestimates the vertical export (Wassmann et al., 2006). Similarly, as described in Sect. 1.1.1, Vernet et al. (2019) and Vernet et al. (2021) have applied SINMOD to investigate the spatial and temporal variability of primary productivity in the western and eastern parts of the Fram Strait.

SINMOD is an Eulerian model, i.e., it describes the flow of water through a fixed grid system, capturing the large-scale circulation patterns. Although local model solutions at specific sites may be similar in terms of biomass, the underlying community structure and resulting plankton interactions may differ due to differences in their experienced physical forcing. However, for relating local results to the processes that occurred previous to reaching the location, outside the specific grid cell, further analyses are often necessary. Using a Lagrangian approach, where an observer follows a water parcel as it is carried along the currents, allows for resolving the small-scale temporal and spatial variability in a computationally efficient way. Thereby, it is possible to relate the specific histories of plankton communities to their observed variability at a given time or location. For example, using a Lagrangian approach, Banas et al. (2016) show that the bloom timing and magnitude are controlled by ice cover, mixing, and advection in the east Bering Strait. Although chlorophyll variability is generally similar in Eulerian and Lagrangian global model approaches, Kuhn et al. (2023) highlight that a Lagrangian approach captures more variability in regions with strong boundary currents, while Eulerian variability is larger in upwelling regions. For comparing and calibrating size-based models with observational data from specific sites in the Fram Strait, it therefore appears meaningful to consider the pronounced variations in the physical forcing and the response within the community structure along the transit pathways, as variations prior to reaching discrete sites are likely responsible for variations in the community size structure observed at these sites. For this task, combining a size-based ecosystem model with a Lagrangian forcing appears a promising approach.

1.4 Scope of the thesis

1.4.1 Objectives

The main goal of my thesis is to contribute to a better understanding of the links between the microbial pelagic ecosystem and the cycling of organic matter in the Arctic Ocean while deciphering some of the variability found in the observational data. My main interest is to elucidate some of the complex dynamics responsible for temporal variations in protist plankton composition and to identify key spatial domains whose distinctions are essential for identifying differences and similarities in the underlying growth dynamics. Understanding the ranges and drivers of the seasonal and inter-annual variability of the involved processes is crucial for estimating how future climate change will affect the Arctic.

Although the region is becoming increasingly accessible due to better ships, the application of autonomous devices, and not least because of the retracting sea ice cover, the region remains remote, harsh, and undersampled. It remains a challenge to provide a comprehensive synthesis that explains the complex relationships between ecological and biogeochemical processes, mainly due to the limited data resolution. Model applications that reconcile model results with observations may help bridge this gap. Although not perfect, such an approach has the advantage that dynamically consistent mass fluxes can be related to ecological changes in plankton composition under well-defined model assumptions.

The approach I followed was to combine highly resolved ecological data, which were derived from microscopic measurements, with a size-based plankton ecosystem model. I chose a Lagrangian modelling approach that allows tracking the specific histories of physical forcing plankton communities are subject to on their transit through the Fram Strait. Furthermore, I employed a machine learning approach to investigate the seasonal and inter-annual variability of phytoplankton standing stocks and their relationship to the variable hydrographic conditions that prevail within the Fram Strait. The overarching topics of the three chapters of this thesis and their overlap are illustrated as a Venn diagram in Fig. 1.4.

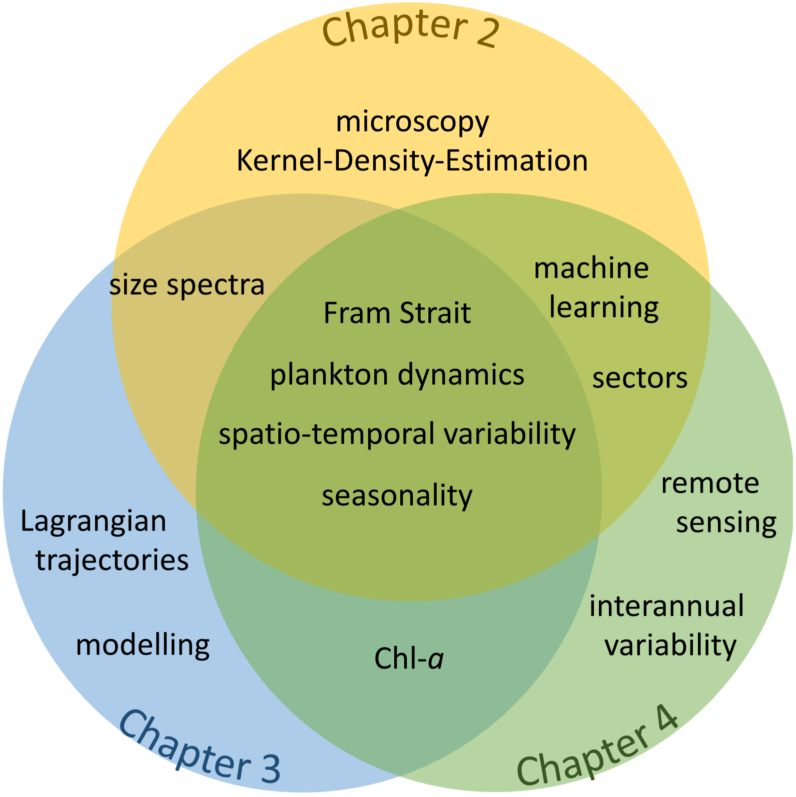

Figure 1.4: Topics and their overlap within the chapters of this thesis.

1.4.2 List of manuscripts and author contributions

Chapter 2 focuses on the derivation of detailed information about the size structure of Arctic pelagic protist plankton and its variability. Our analysis of microscopic data of unicellular plankton collected in the Fram Strait from 2016 to 2018 reveals variations in the size structure of the microbial community. Utilising the Kernel Density Estimation method, we obtained continuous size spectra (ranging from 1 µm to $\approx$ 200 µm Equivalent Spherical Diameter, ESD) that provide insights into cell abundance and biovolume. Specific size intervals indicate size-selective predation and omnivory, while also loopholes with elevated cell abundance are observed. The analysis incorporates remote sensing data to differentiate between polar Arctic and Atlantic water, linking size spectra to seasonal changes in chlorophyll-a concentration. The results highlight a decline in total biovolume from summer to autumn, with a notable shift towards larger cell sizes ($>$ 30 µm) in phytoplankton biovolume size spectra during October. The derived detailed size spectral data contribute valuable information that can be used for constraining the results of subsequent size-based model applications.

This chapter is published in Frontiers in Marine Science as:
Vanessa Lampe, Eva-Maria Nöthig, Markus Schartau: **Spatio-Temporal Variations in Community Size Structure of Arctic Protist Plankton in the Fram Strait**. Frontiers in Marine Science (7) 2021, DOI: 10.3389/fmars.2020.579880
Author contribution:
VL generated and analysed the size spectra and produced all figures and tables. She conceptualised and structured the manuscript and prepared the first draft.
EMN provided microscopic measurements and guided the analysis in terms of discriminating taxonomic groups and trophic strategies.
MS initiated the study and guided the analysis with respect to statistics.
All authors contributed in writing this manuscript.

In Chapter 2, the Kernel Density Estimator was based on a Gaussian Kernel. Over the course of my doctoral project, this method has been developed further by Maria-Theresia Pelz, as part of her doctoral thesis, into a diffusion-based Kernel Density Estimator (diffKDE), which was published in Pelz et al. (2023) (manuscript not included in this thesis). I contributed to this publication and conducted comparison experiments based on the plankton spectra published in Lampe et al. (2021). In turn, I used the diffKDE in my subsequent studies.

Chapter 3 investigates plankton variability in the Fram Strait with a size-based Lagrangian modelling approach. Employing a plankton ecosystem model with nine distinct size classes of phyto- and zooplankton ranging from 1 to 200 µm, we simulate standing stocks and fluxes of carbon and nitrogen within the nutrient, phytoplankton, zooplankton, and detritus pools, while considering the allometric scaling of crucial ecological and physiological processes. The physical forcing of the 1D model is given by 4 ensembles of trajectories that were extracted from SINMOD simulation results and trace the WSC and EGC through the Fram Strait. Generally, the model results of the plankton size structure are in reasonable agreement with the observations described in Chapter 2, and our estimates of standing stocks and fluxes of biogeochemical tracers are consistent with *in-situ* and climatological data. We find distinct temporal developments in plankton size composition, growth, and export within and between the ensembles, with 10–72 % of the variability observed locally at HAUSGARTEN stations attributable to differences in the origin and temporal development of environmental conditions along the individual trajectories.

This chapter is submitted for publication in Journal of Geophysical Research: Oceans as:
Vanessa Lampe, Aidan Hunter, Ben Andrew Ward, Eva-Maria Nöthig, Anja Engel, Ingrid Helene Ellingsen, Markus Schartau: **A Lagrangian model-based analysis of protist plankton variability and its impact on organic matter dynamics along transit pathways through the Fram Strait**
Author contribution:
VL ran the simulations and calibration of the model and prepared the figures and tables. She conceptualised this study and prepared the first draft.
AH and BW conceptualised and programmed the model. AH ran the numerical optimisation.
EMN provided observational data and expertise on plankton and biogeochemical parameters.
IE provided the SINMOD simulation results.
AE provided *in-situ* data and expertise on biogeochemical observations.
MS initiated and guided the study and revised the model regarding the representation of light-limited growth.
All authors contributed in writing this manuscript.

Chapter 4 takes up the topic of sectorisation of the Fram Strait based on surface water mass properties discussed in Chapter 2 and employs this technique for the analysis of chlorophyll-*a* (Chl-*a*) variability. Here, three (instead of two, as previously resolved) hydrographic sectors describing the EGC-, WSC- and front-influenced regions of the Fram Strait are identified using the unsupervised machine learning algorithm k-means clustering on remote sensing observations of sea surface temperature. Differences in the development of blooms in terms of timing and intensity are observed in remote sensing Chl-*a* concentrations within the hydrographical subregions. Blooms form earlier, around May, in the ice-influenced EGC sector and typically in July in the WSC sector. Overall, the Chl-*a* variability correlates with Chl-*a* concentration, but even when normalised, significantly higher variability is observed in the EGC sector compared to the other sectors and linked to the highly variable sea ice dynamics.

This chapter is in preparation for submission as: **Distinguishable variations in chlorophyll-*a* concentration in the Fram Strait based on hydrographic features resolved by a machine learning approach**
Author contribution:
VL drafted this manuscript.

Chapter 2

Spatio-temporal variations in community size structure of Arctic protist plankton in the Fram Strait

This chapter is based on the paper 'Spatio-temporal variations in community size structure of Arctic protist plankton in the Fram Strait'

Citation:
Vanessa Lampe, Eva-Maria Nöthig, Markus Schartau: Spatio-Temporal Variations in Community Size Structure of Arctic Protist Plankton in the Fram Strait. Frontiers in Marine Science (7) 2021, DOI: 10.3389/fmars.2020.579880

Abstract

The Arctic Ocean is subject to severe environmental changes, including the massive decline in sea ice due to continuous warming in many regions. Along with these changes, the Arctic Ocean's ecosystem is affected on various scales. The pelagic microbial food web of the Arctic is of particular interest, because it determines mass transfer to higher trophic levels. In this regard, variations in the size structure of the microbial community reflect changes in size-dependent bottom-up and top-down processes. Here we present analyses of microscopic data that resolve details on composition and cell size of unicellular plankton, based on samples collected between 2016 and 2018 in the Fram Strait. Using the Kernel Density Estimation method, we derived continuous size spectra (from 1 µm to $\approx$ 200 µm Equivalent Spherical Diameter, ESD) of cell abundance and biovolume. Specific size intervals (3–4, 8–10, 25–40, and 70–100 µm ESD) indicate size-selective predation as well as omnivory. In-between size ranges include loopholes with elevated cell abundance. By considering remote sensing data we could discriminate between polar Arctic- and Atlantic water within the Fram Strait and could relate our size spectra to the seasonal change in chlorophyll-*a* concentration. Our size spectra disclose the decline in total biovolume from summer to autumn. In October the phytoplankton biovolume size-spectra reveal a clear relative shift towards larger cell sizes ($>$ 30 µm). Our analysis highlights details in size spectra that may help refining allometric relationships and predator-prey dependencies for size-based plankton ecosystem model applications.

2.1 Introduction

Noticeable oceanographic, biogeochemical and ecological transformations have been documented for the Arctic Ocean. Along with trends in declining sea ice thickness and extent (Stroeve et al., 2012) and increasing sea surface temperature (SST) (Comiso and Hall, 2014), various changes in the marine Arctic ecosystem were recorded. These transformations include shifts in range, behaviour, phenology, and abundance of marine mammals, birds, fish, plankton, and benthos (Wassmann et al., 2011). Therefore, describing and understanding plankton ecology and the underlying ecosystem dynamics involved in a changing Arctic Ocean has become a research focus for many marine scientists.

Regions of particular interest are the Barents Sea and the Fram Strait, because they are important gateways for warmer seawater entering the northern polar ocean, where cold Arctic Water meets warmer Atlantic Water. Long-term SST trends are difficult to ascertain in these regions, but observations indicate a warming and salinification due to an increased influence of Atlantic Water, which was reported for the Barents Sea by Barton et al. (2018). In the Fram Strait, the mean temperature of Atlantic Water increased linearly between 1997–2010, although no significant trend in volume transport was reported (Beszczynska-Möller et al., 2012). For more recent years, a study by Wang et al. (2020) indicates an increase in volume transport. The separation between Arctic Water and Atlantic Water in the Fram Strait is characterised by the northward flowing West Spitsbergen Current (WSC) and the East Greenland Current (EGC) that transports Polar water towards the south. The Fram Strait has been subject of various research in many disciplines over the past decades, as reviewed by Soltwedel et al. (2005, 2016). Of particular interest are variations in plankton composition in response to a changing influence of Atlantic Water in the Fram Strait, as they may entail subsequent effects on higher trophic levels and the biogeochemistry in Arctic regions north of Spitsbergen, e.g. the availability of fatty acids in large diatoms preyed by Arctic *Calanus* species (e.g. Falk-Petersen et al., 2009). For disclosing trophic interdependencies and eventually unravelling pathways of mass transfer to copepods, it is important to resolve changes in the community size structure of the microbial food web.

Cell size is regarded as key determinant of phytoplankton biology and it is interpreted as the master functional trait that affects plankton dynamics on cellular, population, and community levels (Chisholm, 1992; Raven, 1998; Litchman and Klausmeier, 2008; Finkel et al., 2010; Marañón, 2015). Size dependencies of bottom-up and top-down regulatory processes that determine size diversity can be subject to important trade-offs, e.g. between nutrient uptake and the vulnerability to grazing (Acevedo-Trejos et al., 2018). Ecosystem functioning and biogeochemical element cycling are known to be sensitive to the plankton community size structure (Falkowski et al., 1998). Understanding the major mechanisms that describe the coupling between autotrophic and heterotrophic activity within the microbial food web is critical for projecting future changes in biogeochemistry and trophic transfer in the Arctic (Thingstad et al., 2008). Three possible main pathways were discussed by Thingstad and Cuevas (2010), that describe how mineral nutrients can enter the plankton ecosystem and eventually determine the mass transfer to higher trophic levels, e.g. to copepods. The entry points are associated with osmotrophs of three distinct size ranges (i.e. heterotrophic bacteria, autotrophic flagellates, diatoms). A fourth pathway was investigated by Larsen et al. (2015), who introduced an additional size range by discriminating between large and small diatoms. Since all these pathways are size-dependent, temporal changes in autotrophic and heterotrophic plankton size spectra can be expected to disclose size ranges that inform about predator-prey interdependencies.

Is it important that we trace detailed changes in the plankton community structure, because some size ranges can be subject to predation, while yet other size ranges may act as 'loopholes' (Bakun and Broad, 2003), with improved growth conditions and by escaping high predation rates (Irigoien et al., 2005). The size structure of a plankton community is commonly described as biomass spectrum (e.g. Rodriguez and Mullin, 1986; Sprules and Munawar, 1986) or size-abundance spectrum (y=logarithmic number of individuals vs. x=logarithmic size (e.g. Reul et al., 2005; Huete-Ortega et al., 2010, 2012). The y-intercept is ascribed to reflect total biomass, whereas the slope is interpreted as a measure of trophic efficiency. The slope is usually negative and it informs whether a community is dominated by larger (less negative) or smaller cells (more negative). It differs between coastal regions (-0.96, Huete-Ortega et al., 2010) and the open ocean (-1.15, Huete-Ortega et al., 2012), also increasing with latitude from -1.2 in the oligotrophic subtropical gyres to -0.6 in the North Atlantic (Barton et al., 2013). Deriving the y-intercept and the slope from abundance and cell size data can be ambiguous (Moreno-Ostos et al., 2015), because estimates of these two parameters can be collinear. Of potential interest are those size ranges that deviate from log-linear plankton size spectra, because they may reveal ecological details like distinctive size intervals of extensive predation as well as size ranges of reduced grazing pressure that can foster algal growth (loopholes) within the microbial food web.

Here we analyse plankton size spectra of the unicellular plankton community in the Fram Strait (Arctic Ocean) collected between 2016 and 2018. Rather than introducing individual size classes and imposing a linear (parametric) dependency between logarithmic cell concentration and logarithmic size, we derived non-parametric size spectra as Kernel Density Estimates (KDEs). Confidence intervals for the respective size spectra were determined by stochastic resampling, elaborating the KDE method as proposed by Schartau et al. (2010). The purpose of our extensive approach is to have details of the laborious microscopic measurements transferred to continuous size spectra of autotrophic and heterotrophic plankton in the size range between ≈ 1 µm (*Micromonas*) and ≈ 200 µm (large diatoms and tintinnids). We aim at identifying specific and robust patterns in the plankton community size structure of the microbial food web in the Arctic.

2.2 Material and methods

2.2.1 Description of the sampling site

The Fram Strait is considered a gateway to the Arctic Ocean. In the eastern part of the Fram Strait, warm and nutrient-rich water from the North-Atlantic is transported northwards with the West-Spitzbergen Current (WSC) (e.g. Beszczynska-Möller et al., 2012). The East-Greenland Current (EGC) transports colder and fresher water southwards in the western part (e.g. de Steur et al., 2009). Sea-ice cover in this region is variable. The western part is predominantly ice-covered throughout the year, the ice-cover in the north-eastern area varies seasonally while the south-eastern part remains permanently ice-free (Soltwedel et al., 2016). The sampling was conducted at the Fram Strait Long Term Ecological Research (LTER) observatory HAUSGARTEN (Fig. 2.1) between 78°N – 81°N and 5°W – 11°E, a region that is characterised by the highly productive Marginal Ice Zone (Soltwedel et al., 2016). The sampling sites encompass cold Polar water of the EGC as well as of the warmer WSC.

2.2.2 Ship-board sampling

Plankton samples were collected during four cruises to the Fram Strait LTER Observatory (Table 2.1). Sea water samples were collected with a rosette sampler with 24 Niskin bottles (12 L). An attached CTD system (SEA-BIRD Instruments) recorded depth profiles for conductivity, temperature and density. Respective plankton samples were fixed with 0.5–1% hexamine neutralised formaldehyde (final concentration) in brown glass bottles (200–250 mL) and stored in the dark until microscopic analyses (Edler, 1979). A total number of 60 samples were analysed and cell sizes were measured in great detail.

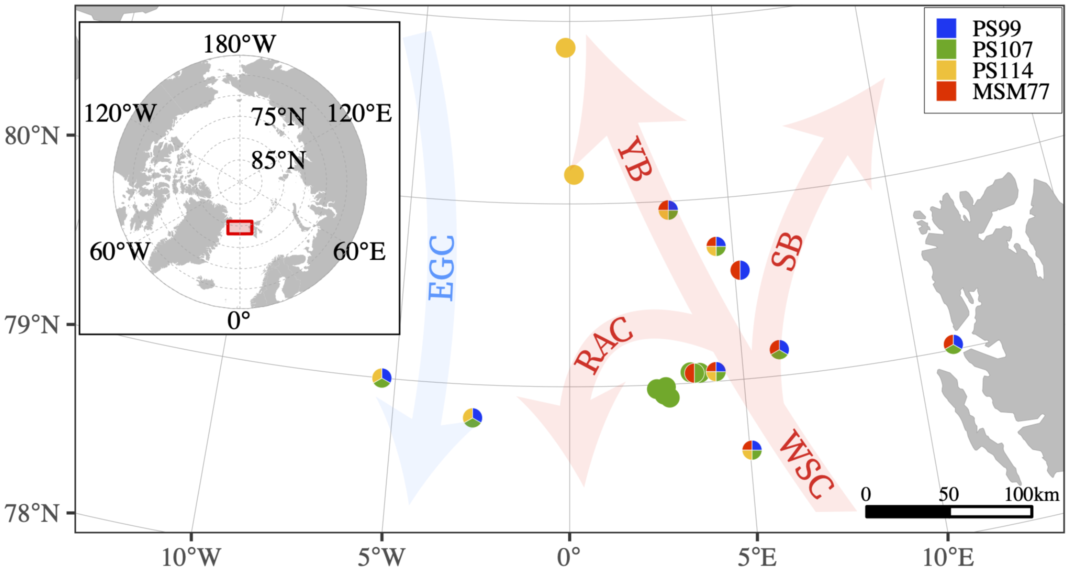

Figure 2.1: Location of the sampling site in the Fram Strait. Sampling stations are shown as dots, colour-coded by the respective campaigns (Table 2.1 shows sampling time and depth ranges). Arrows show the main currents from the North-Atlantic (warm, red; WSC: West-Spitsbergen Current, RAC: Return Atlantic Current, YB: Yermak Branch, SB: Svalbard Branch) and the Arctic Ocean (cold, blue; EGC: East-Greenland Current), after Soltwedel et al. (2016).

2.2.3 Microscopic community composition and size measurements

Microscopic counting of phytoplankton and protozooplankton were conducted for 50 mL aliquots of each sample, following Utermöhl (1958) and Olenina et al. (2006). After a sedimentation period of at least 48 h, cells were identified and counted using an Utermöhl chamber and an inverted microscope (Axiovert 40 C) under 63x, 100x, 160x, 250x, and 400x magnification. Especially smaller species were only identified to genera. The corresponding cell lengths and widths were measured with a calibrated ocular micrometer (Zeiss). For further analyses, species were grouped by their trophic strategies, distinguishing between photo-autotrophy (phytoplankton) and heterotrophy (zooplankton).

Table 2.1: Sampling campaigns to the HAUSGARTEN area in the Fram Strait (Arctic Ocean) during the years 2016–2018 recovered varying numbers of samples for microscopic community analyses.

Cruise	Ship	Dates	No. of samples	Depth range [m]
PS99.2	*RV POLARSTERN*	06-23 – 07-16-2016	10	10 – 30
PS107	*RV POLARSTERN*	07-23 – 08-19-2017	24	10 – 40
PS114	*RV POLARSTERN*	07-10 – 08-03-2018	14	5 – 43
MSM77	*RV MARIA S. MERIAN*	09-16 – 10-12-2018	12	5 – 34

The sample fixation can discolour chloroplasts, which hinders the determination of a cell's trophic strategy, when a precise identification is not available. Although common among protist plankton, mixotrophic cells could not be explicitly resolved. Green dinoflagellates were assigned to the group of photoautotrophs while their colourless counterparts were regarded as heterotrophic. A small fraction of micro- and nanoflagellates could not be unambiguously identified microscopically (mostly for cells with sizes smaller than 6 µm), which happened on average in 7.3 % of all counts (resulting in 10.4 % of the total cell concentration). Subject to these limitations, 50 % of these cells were grouped as being photoautotrophic, and the remaining were assigned to the heterotrophic group. This assumption is based on our experience from previous measurements of samples taken in the Fram Strait, where the relative fractions between photoautrophs and heterotrophs in nanoflagellates varied between 30 and 70 %. A study by Sherr et al. (2003) supports our assumption. In general, during spring more photoautotrophic forms were observed, whereas in summer we had found heterotrophic forms that prevailed. In our samples, most of the small flagellates were identifiable such as the often dominating autotrophic *Phaeocystis* spp. single cells with cell sizes between 2 and 6 µm.

2.2.4 Resampling of cell counts and size measurements

When comparing individual size spectra, the consideration of inherent methodological uncertainties is helpful. This includes uncertainties in counts, as well as the precision of microscopic measurements of cell length and width. The former involves the sample volume and the microscopic area (field of view) scanned for counting, whereas the latter depends on the microscopic magnification. To account for such uncertainties, we followed the bootstrapping approach described in Schartau et al. (2010), by analysing ensembles of resample datasets. The generation of resample datasets was done in two consecutive steps. First, we resampled cell counts. In a second step, we assigned resampled cell lengths and widths to the respectively resampled counts.

Resample cell counts were obtained by randomly drawing from a Poisson probability distribution with an expected value λ that was equal to the observed number of cell counts, which had been summarised before according to cell taxonomy and size. This way we considered uncertainties in counting, which becomes particularly relevant in cases of finding few counts of a specific species/taxon of one particular size. Furthermore, a single count in a sub sample of 50 mL was regarded as a *rare event* and it is associated with a large uncertainty when upscaling it to a concentration (abundance in units cells L^{-1}). The consideration of a Poisson probability distribution for resampling counts is meaningful in this respect. For example, the probability of resampling an observed single count ($\lambda = 1$) as $P(k = 1) = P(k = 0) \approx 0.37$, meaning that the probability of finding or missing such *rare event* is equal. Capturing two counts of identical size is also possible, although the probability reduces to $P(k = 2) \approx 0.18$. The probability of finding three or more counts decreases further accordingly. Resampled cell counts were eventually extrapolated to cell concentrations [cells L^{-1}] while considering the magnification and field of view of the original observations.

In a second step, we resampled lengths and widths while accounting for the varying precision limits that depend on the microscopic magnification as shown

Table 2.2: Precision limits of microscopic size measurements are derived from the distance between two graduation marks of the ocular micrometer used, and therefore dependent on the microscopic magnification.

Microscopic magnification (x)	Precision limit $\frac{\Delta s_{\text{grad}}}{6}$ [µm]
63	2.5
100	1.6
160	1.0
250	0.6
400	0.4

in Table 2.2. The precision limits have been derived according to the division of the ocular micrometer (distance between two graduation marks, Δs_{grad}). To ensure that at least 99.7 % of the resampled size values (lengths and widths) laid in an interval of [observed size $\pm\Delta s_{\text{grad}}/2$], we drew from a Gaussian (normal) probability distribution. As mean values we imposed the observed sizes and the second moments were chosen to account for the varying precision limits, so that representative standard deviations became equal to $\Delta s_{\text{grad}}/6$. For every original data set, we computed an ensemble of 100 resample-datasets using the described resampling approach.

2.2.5 Derivation of continuous size spectra

We applied a Kernel Density Estimation method (e.g. Silverman, 1986) for the derivation of continuous size spectra from discrete microscopic measurements. A Kernel Density Estimate (KDE) was derived for each of the 100 resample datasets. Final size spectra were calculated as means of the ensembles' KDEs together with their respective 95 % confidence intervals.

As a first step, the cell volumes were determined based on simple geometric shapes (Edler, 1979; Olenina et al., 2006) and the Equivalent Spherical Diameters (ESD) were calculated. Phytoplankton and protozooplankton have a wide range of geometric shapes, so the volume-dependent ESD was used as a normalised size proxy rather than the length or width dimension of a cell. The length dimension can span from 1 µm in small *Micromonas* to 1000 µm in long *Rhizosolenia* cells. In terms of ESD, the range still covers cells from 1 µm–200 µm. The ESD values were log-transformed and normalised by 1 µm:

$$S = \log_{10}\left(\frac{ESD}{1\mu\text{m}}\right) \tag{2.1}$$

A KDE is the normalised sum of individual kernels that are themselves probability density functions (pdfs) centred around every data point S_i. The width of the kernels is determined by the bandwidth h (also referred to as smoothing parameter). As a kernel, we applied a Gaussian function, which means that S_i is equal to the first moment (mean) and the bandwidth h is similar to the second moment (standard deviation; see following paragraphs for the selection of h) of a normal probability density function. When a KDE is not normalised with respect to the total number of cells C_j^{tot} (total number of kernels), it readily represents a plankton size spectrum:

$$KDE_j(s,h_j) = \frac{1}{h_j}\sum_{i=1}^{C_j^{\text{tot}}} \frac{1}{\sqrt{2\pi}} \exp\left[-\frac{1}{2}\left(\frac{s-S_i}{h_j}\right)^2\right] \tag{2.2}$$

with j being an index of selected data (e.g. split up according to individual taxa or grouped by trophic strategy). The enumerator in the exponent $(s - S_i)$ describes the distance from data point S_i. Since the KDEs have not been normalised we note that they do not represent pdfs, but the following is applicable:

$$\frac{1}{C_j^{\text{tot}}} \times \int_{\log_{10}(0.5)}^{\log_{10}(500)} \text{KDE}_j(s,h_j)\; ds \approx \int_{\log_{10}(0.5)}^{\log_{10}(500)} pdf_j(s)\; ds = 1 \tag{2.3}$$

From the ensemble (KDEs of the 100 resample-datasets), we calculated a mean KDE_j and its standard error (SE). The confidence interval is the mean $\overline{\text{KDE}}_j(s) \pm 1.96 \times \text{SE}_j(s)$. Despite small confidence intervals, we assume high uncertainty in the cell concentration density estimates for ESDs smaller than $\approx 2\,\mu\text{m}$ that arises out of the limitations in light microscopy (see Table 2.2). We indicated this uncertainty as dotted lines in the following size spectra.

As described previously, j is an index of selected data. When j is a combined subset of all phytoplankton cells or all zooplankton cells (per sample), the combined size spectrum for all phytoplankton or zooplankton in a dataset is the average of the sample-specific size spectra of phyto- and zooplankton:

$$\text{KDE}_{\text{phy/zoo}}^{\text{combined}}(s) = \overline{\text{KDE}}(s, h_{\text{phy/zoo}}) \tag{2.4}$$

The bandwidth parameter h controls the degree of smoothing. As described in Schartau et al. (2010), we used a simple rule-of-thumb approach proposed by Silverman (1986). In this plug-in method, an optimal h is estimated from a measure of spread inherent in s, expressed as the standard deviation σ. Since σ is sensitive to outliers, the interquartile range $(s_{[0.75n]} - s_{[0.25n]})$ can serve as a more robust estimator of spread. The optimal estimation for h is:

$$\hat{h}_{opt} = 1.06 \min\left\{\sigma, \frac{s_{[0.75n]} - s_{[0.25n]}}{1.34}\right\} n^{-\frac{1}{5}} \tag{2.5}$$

The number of selected data subsets (indexed j) can be increased to the total number of taxonomic groups resolved by the microscopic measurements, which allows us to construct composite size spectra with a maximum in resolution. Doing so we learned that the apparent gain in resolution impaired an ascertaining of predominant structural changes, because many additional details were associated with considerable uncertainties. For this reason we resorted to simpler subsets, distinguishing between autotrophic and heterotrophic cells and separating according to sampling periods and locations. Examples of high resolution composite size spectra of phyto- and microzooplankton are provided in the supplementary material. We note that the taxonomic precision affects details resolved in composite spectra, because bandwidths ($\hat{h}_{opt}$, Equation 2.5) are then obtained for taxonomic groups individually. In contrast, the combined spectra do not depend on taxonomic precision other than the separation between photoautotrophs and heterotrophs.

2.2.6 Spatial and temporal separation of observational data

The Fram Strait's throughflow is characterized by the cold EGC flowing southward, and the warmer WSC flowing northward. In between is a frontal zone of pronounced spatial variability. Some sampling sites were differently affected by one or the other of the two currents. At dates of sampling, these sites were thus subject to a plankton signal that originated either from northern parts of the Fram Strait or from the South. At first we analysed salinity, density and temperature data, as obtained from the CTD sensors attached to the sampling rosette. We identified individual water masses according to Amon et al. (2003), but distinguishing between Polar Water, Intermediate Water, and Atlantic Water turned out to be vague in certain cases. A sole spatial separation between cold (Polar) and warm (Atlantic) seawater seemed less ambiguous, which we approached by analysing sea surface temperature (SST) data.

We used the High Resolution SST dataset provided by NOAA/OAR/ESRL PSL, Boulder, Colorado, USA[1]. We determined daily maps that comprise two distinct spatial areas within the region 10°W – 12°E and 77°N – 81°N, a "warm" cluster and another that embraces seawater of cold SST. The two spatial clusters were derived with the iterative k-means-clustering method of Hartigan and Wong (1979), as implemented in R (version 3.5.2 R Core Team (2018)). Within a cluster the SST values were alike and horizontal variability remained low. Based on the date and geographical location of sampling, we could eventually assign every sample to either the cold or to the warm SST cluster.

For temporal differences we distinguished between summer and autumn data. Samples from PS99, PS107, and PS114 covered periods in summer, and samples from MSM77 were collected during a cruise in autumn. For putting the spatio-temporal distinguished data into the context of general bloom development, we also compiled a time-series of chlorophyll concentrations for the years 2016–2018 between 10°W – 12°E and 77°N – 81°N. We used daily chlorophyll-a remote sensing estimates (Level-3 Standard Mapped Image (SMI), Global, 4km, Chlorophyll, Daily composite data from the Visible and Infrared Imager/Radiometer Suite (VIIRS)), provided by NOAA CoastWatch/OceanWatch[2]. The satellite data were assigned to the SST (cold Polar/warm Atlantic) clusters that had been determined before. A moving average was calculated, with a window width of 15 days, weighed by the number of respective observations for each of the two SST clusters. With the constructed chlorophyll-a time series we could trace the initial build-up, maximum, and decay of the phytoplankton bloom for the three sampling years for both spatial clusters respectively.

---

[1] https://psl.noaa.gov/data/gridded/data.noaa.oisst.v2.highres.html, last accessed 02-21-2019

[2] https://coastwatch.noaa.gov/cw/satellite-data-products/ocean-color/science-quality/viirs-snpp.html, last accessed 07-31-2019

Table 2.3: Mean [minimum value, maximum value] total cell concentrations and total biovolumes, averaged for all samples and by individual sampling campaigns.

Cruise	Type	Cell conc. $[\times 10^6 \frac{\text{cells}}{\text{L}}]$	Biovol. $[\frac{\text{mm}^3}{\text{L}}]$
average	autotroph	24.9 [0.02, 92.14]	3.02 [0.03, 14.3]
average	heterotroph	3.7 [0.01, 54.32]	2.30 [0.03, 10.34]
PS99	autotroph	3.4 [0.30, 9.55]	0.32 [0.04, 1.16]
PS99	heterotroph	0.2 [0.07, 0.43]	0.22 [0.05, 0.48]
PS107	autotroph	44.8 [0.02, 92.14]	5.33 [0.04, 12.19]
PS107	heterotroph	6.8 [0.02, 54.32]	4.21 [0.09, 10.34]
PS114	autotroph	23.6 [0.12, 91.70]	2.68 [0.04, 14.34]
PS114	heterotroph	2.4 [0.01, 0.22]	1.70 [0.04, 4.94]
MSM77	autotroph	4.9 [0.08, 26.68]	1.03 [0.03, 3.95]
MSM77	heterotroph	1.1 [0.02, 6.94]	0.95 [0.03, 3.26]

2.3 Results

2.3.1 Composition and abundance of phyto- and protozooplankton

We grouped organisms into 61 different identifiable groups (species or higher taxonomic levels) with ESDs ranging from 1 to 196 µm (Fig. 2.2). The smallest of the 42 photo-autotrophic cells were *Micromonas* sp. (ESD ≈ 1 µm), *Rhizosolenia* spp. were the largest (ESD > 150 µm). Of the 17 heterotrophic species we found small choanoflagellates (ESD ≈ 1 µm), while the largest heterotrophic dinoflagellate had an ESD of 196 µm. The groups of nano- and microflagellates could not be identified further (in average 10.4% of the total cell concentration), and three cell types were not identifiable at all so only size measurements were taken.

The mean total cell concentration as well as mean total biovolume were generally higher for autotrophic cells (3.02 mm^3 L^{-1}; 24.9 × 10^6 cells L^{-1}) than for heterotrophs, although values differed notably between the cruises (Table 2.3). The highest cell concentrations were observed in PS107 (44.8 × 10^6 cells L^{-1}; 5.33 mm^3 L^{-1}), followed by PS114 (23.6 × 10^6 cells L^{-1}; 2.68 mm^3 L^{-1}). Phytoplankton concentration was similar in PS99 (3.4 × 10^6 cells L^{-1}; 0.32 mm^3 L^{-1}) and the autumn-cruise MSM77 (4.9 × 10^6 cells L^{-1}; 1.03 mm^3 L^{-1}). Heterotrophic biovolume was 2.30 mm^3 L^{-1} in average, and the mean cell concentration 3.7 × 10^6 cells L^{-1}, but also varied between the cruises.

As Fig. 2.2 illustrates, the location of the median cell size varied considerably among species and taxonomic groups. The spread of ESD within species was also highly variable. Variations in cell size were often smaller for precisely identified species than for groups of higher taxonomic level (e.g. flagellates or tintinnids), with exceptions. For most taxa the median ESD laid between 9 µm and 50 µm.

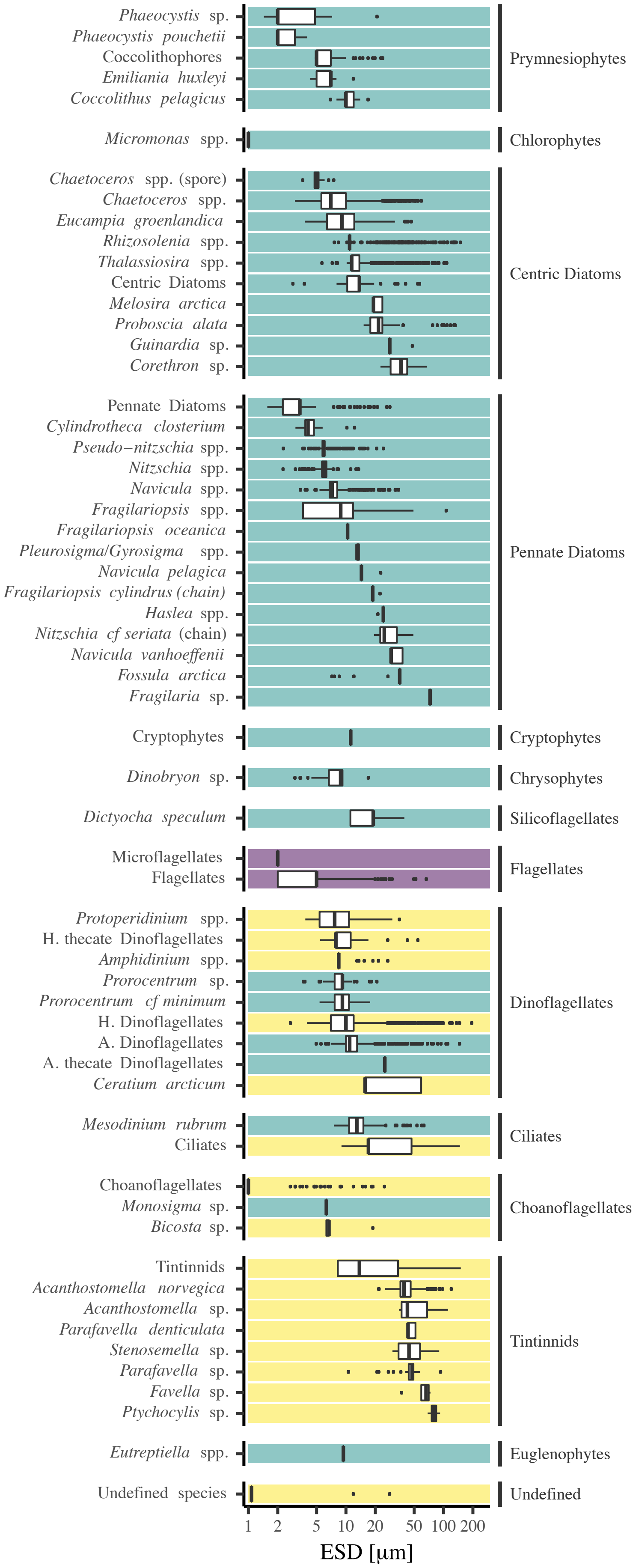

Figure 2.2: Grouping of all identified species or species groups and their respective size ranges (equivalent spherical diameter (ESD) in µm) on a logarithmic scale. Turquoise species are autotrophic (A.), yellow species are heterotrophic (H.). For purple species, a clear distinction was not possible (in average 10.4% of the total cell concentration), therefore 50 % of the cells were treated as autotrophic, and 50 % as heterotrophic.

2.3.2 Spatial separation of cold and warm surface temperature regimes

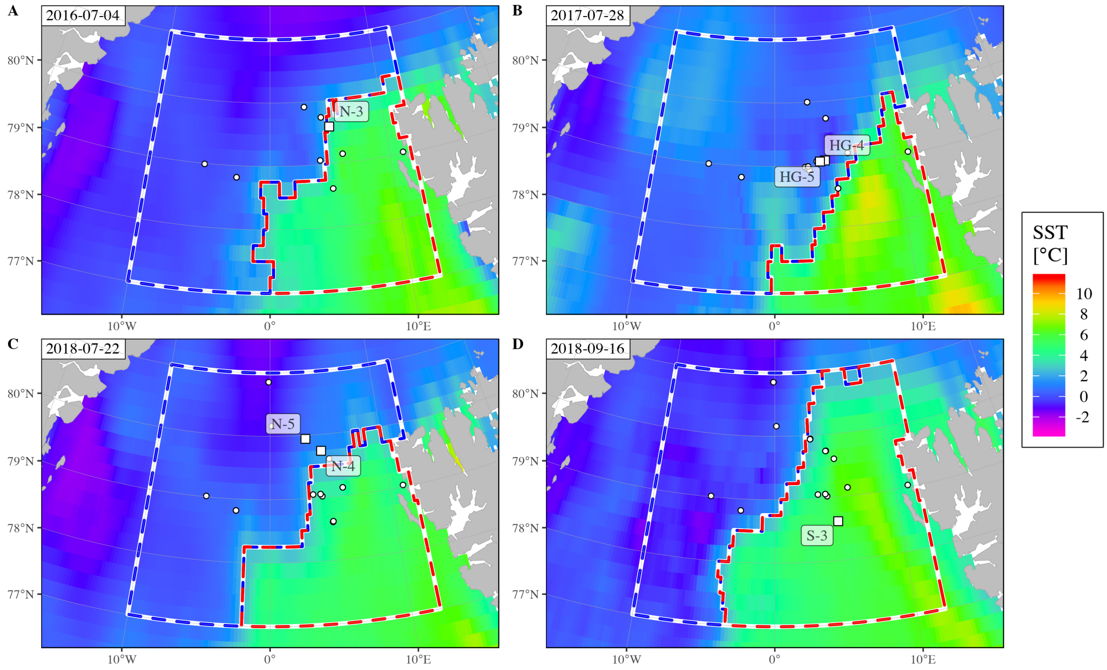

Figure 2.3: Distinction of Polar (cold, blue dashed line) and Atlantic (warm, red) sections of the study site during the four sampling campaigns. The four snapshots (2016-07-04, PS99 (**A**), 2017-07-28, PS107 (**B**), 2018-07-22, PS114 (**C**), 2018-09-06, MSM77 (**D**)) illustrate the horizontal variability of the front system. Labelled white squares mark stations sampled on the respective days, remaining stations are indicated as white dots.

With our analyses of SST remote sensing data we were able to separate the water surface of the sampling area (77 – 81°N, 10°W – 12°E) into cold (Polar) and warm (Atlantic) regions for each day of the years 2016–2018. The location of the frontal zone was somewhat variable and changed within days, and we traced how its meandering affected individual sampling sites. Some sites remained within either of the warm or cold clusters at all samplings (e.g. sites EG-1, EG-2, and N-5 within cold; site HG-1 and SV-1 within warm; for a complete list of all stations see Table S1 in the supplemental material). Especially the central stations, for example sites HG-4 and HG-6, were either subject to cold or to warm waters, depending on the time of sampling. Therefore, the separation was helpful when unravelling differences between the size spectra. An illustration of the variable location of the front relative to the sampling stations is given in Fig. 2.3, displaying four situations during PS99 (**A**), PS107 (**B**), PS114 (**C**), and MSM77 (**D**). Mean SST increased in both regions over the course of the year, reaching their maxima in July (Atlantic section in 2016) or August (Polar section in 2016, both sections in 2017–2018). In the Atlantic region, maximum mean temperatures were between 5.85°C in 2018 and 6.99°C in 2016, whereas the minimum mean temperature was reached between February and April (1.70°C in 2016 and 0.86°C in 2018). The maximum mean temperature in the Polar region was between 0.81°C in 2016 and 1.65°C in 2017. The coldest mean temperature was observed in January 2016 (-1.22°C), and April 2017+2018

(-1.40°C). In the defined area, the Polar region always was in the North-West and the Atlantic in the South-East.

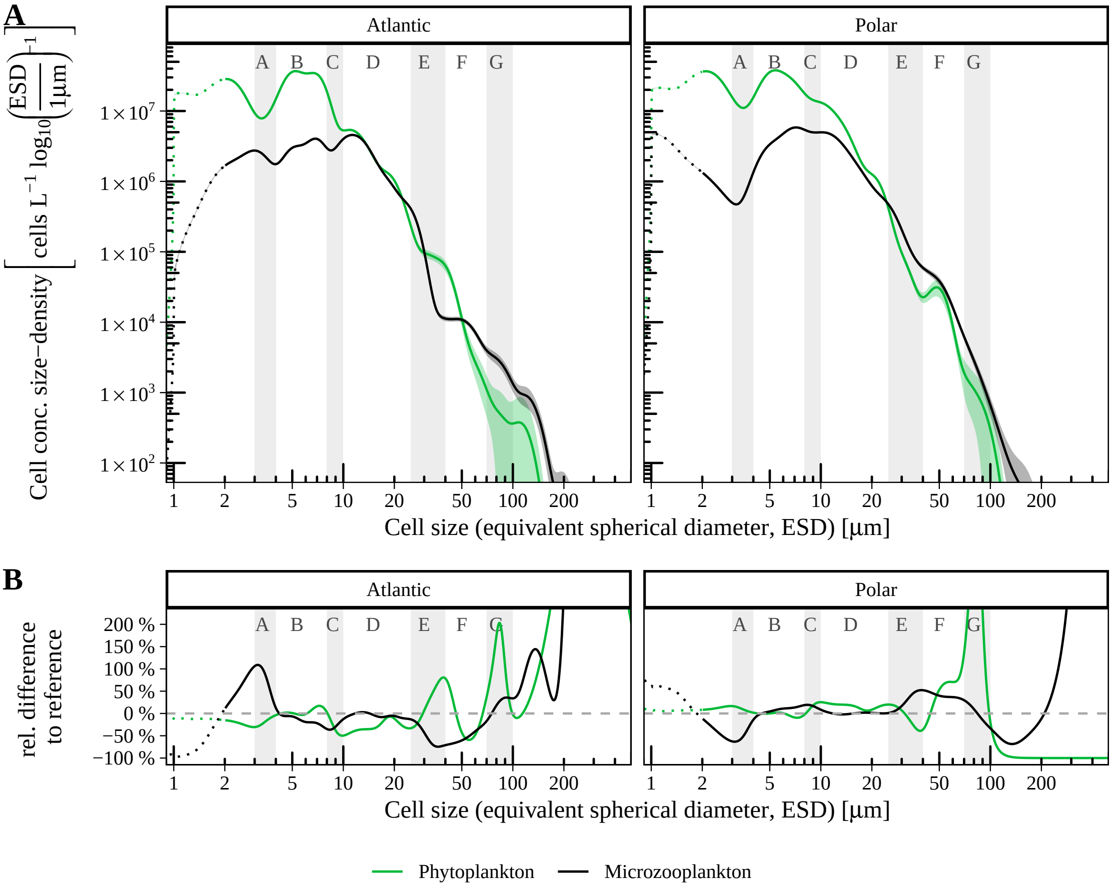

Figure 2.4: Size spectra for autotrophic phyto- (green) and heterotrophic microzooplankton (black) in samples from the Atlantic (left) and Polar (right) section of the study site (**A**). Shaded areas indicate the confidence interval (95 % CI), dotted lines indicate reduced reliability of size measurements for cells with ESD < 2 μm. Relative differences between the Polar and Atlantic size spectra to the reference (combined spectrum of all samples, see supplemental material) in percent (**B**).

Mean total cell concentrations were slightly higher in Polar water samples for both, autotrophs and heterotrophs (26.4 [0.02, 92.14] × 10^6 cells L^{-1} and 4.0 [0.01, 54.32] × 10^6 cells L^{-1}), than in Atlantic water samples (22.1 [0.08, 91.70] × 10^6 cells L^{-1} and 3.1 [0.03, 9.22] × 10^6 cells L^{-1}). While also autotrophic mean total biovolume was higher in Polar samples (3.17 [0.03, 12.19] mm^3 L^{-1} vs. 2.73 [0.03, 14.34] mm^3 L^{-1} in Atlantic samples), heterotrophic biovolume was similar (2.30 [0.04, 9.30] and 2.32 [0.03, 10.34] mm^3 L^{-1}). While in the Polar waters autotrophic total biovolume exceeded the heterotrophic total biovolume, similar biovolumes of autotrophs and heterotrophs may indicate a higher activity of the microbial loop in the Atlantic waters.

The size spectra for autotrophs and heterotrophs, separating between Atlantic and Polar samples in Fig. 2.4**A**, show clear deviations in certain size ranges, in spite of total abundance being similar. Deviations are more pronounced in Fig. 2.4**B**, where we show the relative difference of the Atlantic (left) and Polar (right) size spectra to the reference (combined-spectra from all samples, see supplemental material). Autotrophic cell abundance between 10 and 25 µm (size range D) was higher in the Polar spectrum, as diatoms and chrysophyceans in this size range were more abundant than in Atlantic samples. The high abundance of silicoflagellates and undefined cells around ESD = 40 µm caused an elevated cell concentration density in the Atlantic spectrum relative to the Polar. Large diatoms and autotrophic dinoflagellates around ESD = 110 µm contributed to a local peak, which was missing in the Polar spectrum. Differences between Atlantic and Polar spectra were more noticeable for heterotrophic plankton. Despite high uncertainty, the abundance of cells with ESD < 2 µm was considerably smaller in the Atlantic subset compared to the Polar subset, where small (1 µm) choanoflagellates were common. Interestingly, ciliates in this size range were only observed in Polar samples. However, a high abundance of choanoflagellates, with an ESD around 3 µm, in Atlantic samples lead to a local peak in the Atlantic spectrum in size range A, which was supplemented by ciliates. Since both groups were considerably less abundant in Polar samples, a local minimum could be identified in the size spectrum. The cell concentration density minimum in size range E of the Atlantic spectrum could be attributed to dinoflagellates and flagellates being less abundant relative to the Polar spectrum. The cell concentration density distribution was shifted towards larger ESDs in Atlantic samples, and as a result the Atlantic spectrum exceeded the Polar samples for ESD > 80 µm.

2.3.3 Spatio-temporal distinction of community size spectra

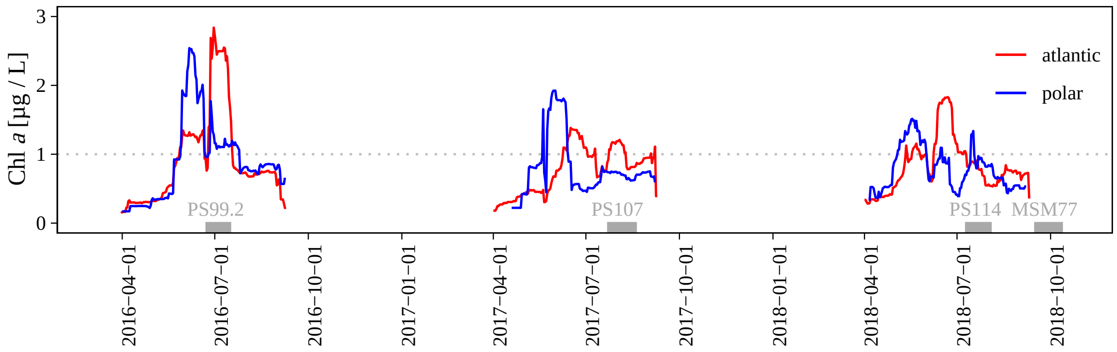

Figure 2.5: Time series of satellite derived chlorophyll-a concentration estimates. The distinction of Polar and Atlantic areas is described in the materials and methods section. We used daily chlorophyll-a estimates and applied a 15 d moving average, weighed by the number of available data points. Grey bars indicate the duration of sampling campaigns and the dotted grey line indicates the threshold chlorophyll concentration we imposed for classifying as a ”bloom” (Wu et al., 2007; Nöthig et al., 2015).

As Fig. 2.5 shows, chlorophyll-a concentration derived through satellite imagery differed over time in the three observed years (temporally) and in the two regions (spatially). From these results we conclude that the development and progression of phytoplankton blooms in the Atlantic and Polar regions of the study site were different. During the four sampling campaigns, protist plankton communities were therefore observed in different growth phases.

The algal blooms were more intense in the Polar region than the corresponding blooms in the Atlantic region, and started earlier in 2017 and 2018. In the

Table 2.4: Average and [minimum value, maximum value] total cell concentrations and total biovolumes for a spatio-temporally separated dataset.

Season	Region	Type	Cell conc. [$\times 10^6 \frac{\text{cells}}{\text{L}}$]	Biovol. [$\frac{\text{mm}^3}{\text{L}}$]
autumn	cold	autotroph	0.21 [0.19, 0.24]	0.09 [0.07, 0.12]
autumn	cold	heterotroph	0.08 [0.02, 0.14]	0.07 [0.06, 0.08]
autumn	warm	autotroph	5.89 [0.08, 28.68]	1.22 [0.03, 3.95]
autumn	warm	heterotroph	2.45 [0.03, 6.94]	1.12 [0.03, 3.26]
summer	cold	autotroph	27.84 [0.02, 92.14]	3.34 [0.04, 12.19]
summer	cold	heterotroph	4.22 [0.01, 54.32]	2.42 [0.04, 9.30]
summer	warm	autotroph	36.95 [0.30, 91.70]	4.09 [0.04, 14.34]
summer	warm	heterotroph	3.71 [0.18, 9.22]	3.41 [0.09, 10.34]

Atlantic region, we observed two pronounced and distinct blooms, with a denser second bloom (2016+2018). The second bloom in the Polar region was hardly expressed. PS99 captured the second bloom of the season in both regions, but while PS107 catched the end of the second bloom in the Atlantic region, the bloom ended already six weeks earlier in the Polar region. Chlorophyll-*a* concentration showed a narrow peak among otherwise moderate values in the Polar region during PS114, and a bloom in the Atlantic region has recently faded. Because of the Polar Night, no satellite observations were available for the autumn cruise MSM77, but in-situ HPLC measurements (data not shown) indicated no further bloom in 2018. A remarkable feature was the increase in variability in autumn. As total cell numbers declined we found certain size ranges with vastly reduced cell numbers (amplified reduction). Size spectra of autotrophs differed greatly in terms of abundance of cells with an ESD $< 2\,\mu\text{m}$. The small chlorophyte *Micromonas* sp. (ESD $\approx 1\,\mu\text{m}$) was abundant in summer, but not in autumn. Furthermore, diatoms and the prymnesiophyte *Phaeocystis* spp., in the size range between 2 and 7 µm, were highly abundant in summer.

By further dividing summer and autumn samples into Polar and Atlantic samples, we could account for spatio-temporal changes in size spectra for autotrophic and heterotrophic plankton (Fig. 2.6). Mean total biovolume was larger in the Atlantic region both in summer and in autumn (Table 2.4). Furthermore, more autotrophic than heterotrophic biovolume was observed within the investigated size range. In the Polar region, the ratio of autotrophic to heterotrophic biovolume was higher (in summer and autumn) than in the Atlantic region. Autotrophic cell concentration was higher in Atlantic than in Polar samples in summer, and reversed for heterotrophs. In autumn, both autotrophic and heterotrophic cell concentrations were higher in the Atlantic region than in the Polar region.

As Fig. 2.6 (upper panels) shows, Atlantic (left) and Polar (right) size spectra aligned relatively well in summer. However, autotrophic cell concentration density for Atlantic samples was slightly elevated in section B, because even though less diatoms were observed, substantially more prymnesiophytes of this size range were found compared to Polar samples. Mismatches in sections E and > G related to higher dinoflagellate and diatom concentrations in Atlantic samples. Differences in the size distribution of choanoflagellates caused the contrary course of Polar and Atlantic heterotrophic size spectra. Furthermore, less flagellates and dinoflagellates

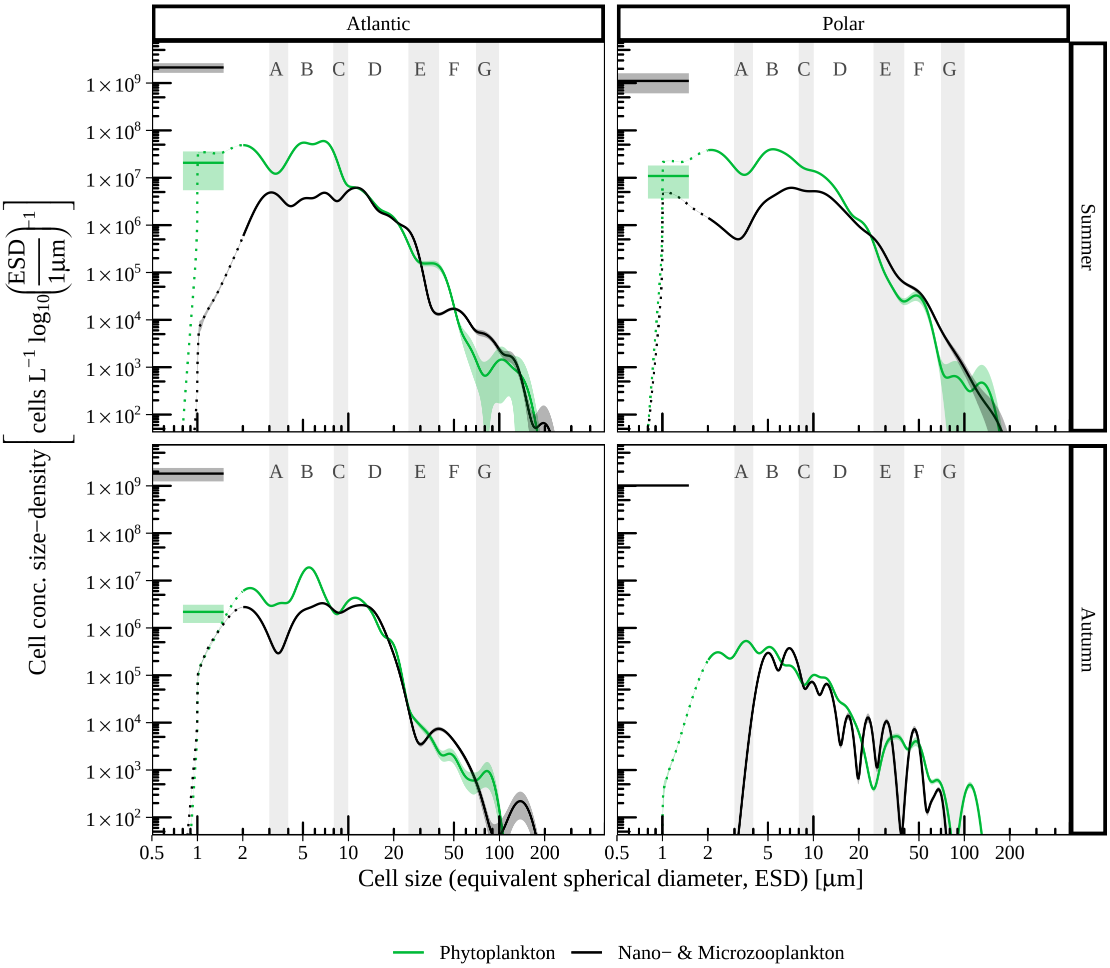

Figure 2.6: Abundance size spectra for phyto- (green) and microzooplankton (black) of temporally (summer, top panels; autumn, bottom panels) and spatially (Atlantic, left panels; Polar, right panels) separated data. Coloured shaded areas indicate the 95 % confidence intervals, dotted lines indicate reduced reliability of size measurements for cells with ESD $< 2\,\mu m$. For comparison, cell concentration densities derived from Flow Cytometry measurements are shown for bacteria (black line, 0.5 – 1.5 µm, data from corresponding samples in von Jackowski et al. (2020a) and for *Synechococcus* (green line, 0.8 – 1.5 µm, data from Paulsen et al. (2016); August-south $\triangleq$ Summer-Atlantic, August-north $\triangleq$ Summer-Polar, November $\triangleq$ Autumn-Atlantic).

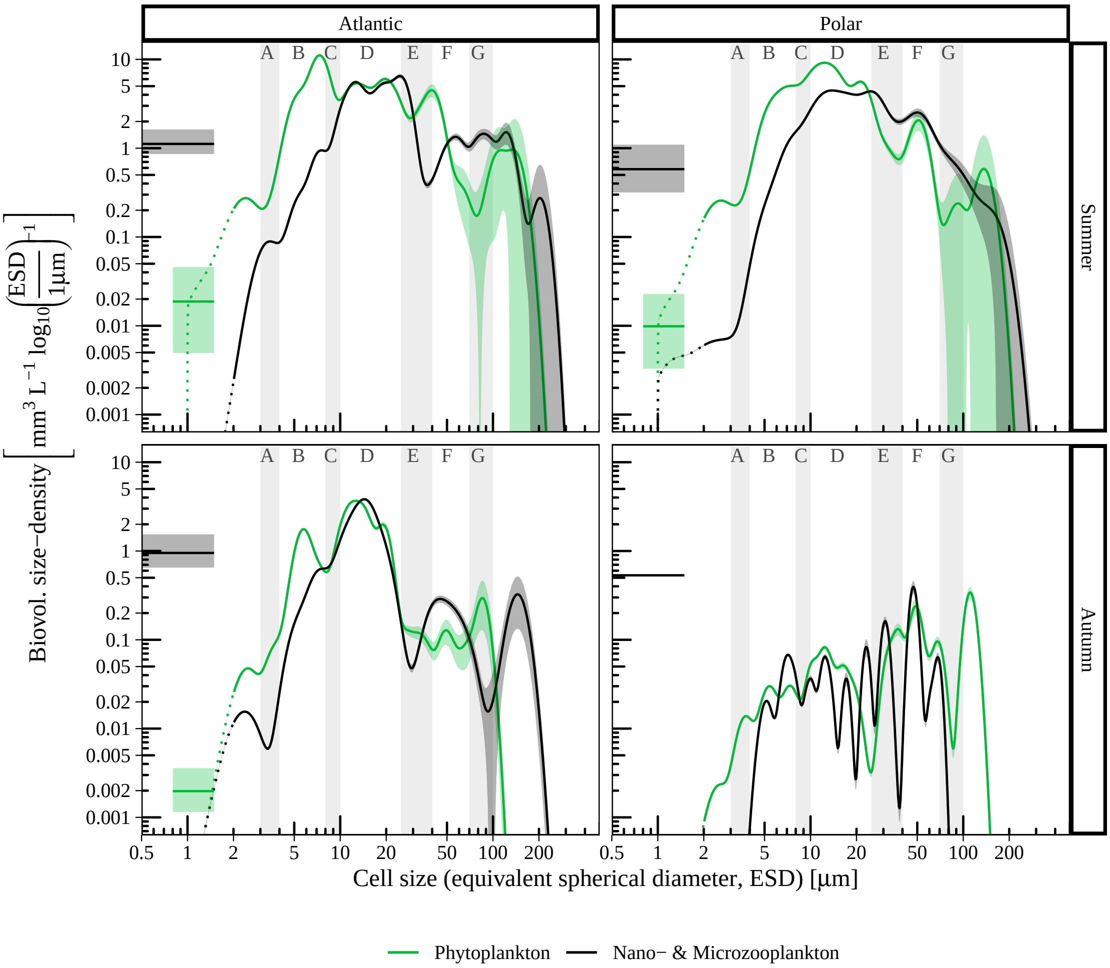

Figure 2.7: Biovolume size spectra for phyto- (green) and microzooplankton (black) of temporally (summer, top panels; autumn, bottom panels) and spatially (Atlantic, left panels; Polar, right panels) separated data. Coloured shaded areas indicate the 95 % confidence intervals, dotted lines indicate reduced reliability of size measurements for cells with ESD < 2 µm. For comparison, biovolume concentration densities derived from Flow Cytometry cell count measurements are shown for bacteria (black line, 0.5 – 1.5 µm, assuming mean ESD = 1 µm, data from corresponding samples in von Jackowski et al. (2020a) and for *Synechococcus* (green line, 0.8 – 1.5 µm, assuming mean ESD = 1.2 µm, data from Paulsen et al. (2016)).

in section E caused a local minimum in the Atlantic spectrum around 40 µm.

In autumn (Fig. 2.6, lower panels), differences between Polar and Atlantic spectra were considerably more pronounced. Autotrophic and heterotrophic cell concentration densities were smaller for ESD $< 30\,\mu m$, and converged for larger cells. No chlorophytes were observed in autumn, and the cell concentration density of small prymnesiophytes and diatoms was lower in the Polar than in the Atlantic spectrum. In sections A–D, the autotrophic spectra ran relatively parallel, with reduced cell concentration densities in the Polar spectrum (less diatoms and dinoflagellates), and then converged. In contrast to smaller size ranges, diatoms with ESD $\approx 120\,\mu m$ were more common in the Polar samples. While the Atlantic size spectrum for heterotrophic cells in autumn covered a size range of 1–180 µm, the Polar spectrum only covered 3–80 µm.

The Atlantic and Polar biovolume size spectra shown in Fig. 2.7 likewise showed less deviation in summer, compared to autumn. In the size ranges 3–4 and 8–10 µm the biovolume size density was consistently reduced relative to its neighbouring size ranges in all spatio-temporally separated spectra. Furthermore, the size ranges 35–40 and 70–100 µm frequently contained local minima and generally expressed high variability.

2.4 Discussion

2.4.1 Changes in plankton community structure in the Arctic

A long-term gradual increase in phytoplankton biomass was reported for the West Spitsbergen Current (WSC) in the Fram Strait by Nöthig et al. (2015). According to an analysis of satellite-derived chlorophyll-a data of the period between 1991 and 2012, this temporal trend is evident for the warmer Atlantic waters entering the Arctic ocean through the Fram Strait but not for the southward moving colder Polar waters (Nöthig et al., 2020). Following a warm water anomaly between the years 2005 and 2007, Nöthig et al. (2015) also observed a shift in species composition, from a domination of diatoms towards smaller sized cells of haptophyte *Phaeocystis* and other nanoflagellates in the Atlantic waters of the WSC during the summer months. Our data from 2016, 2017, and 2018 include measurements of *Phaeocystis*, whose abundance and biovolume decreased from summer to autumn. In both seasons, abundance and biovolume were always higher in Atlantic than in Polar waters.

Changes in plankton composition in the Arctic also involve shifts in the abundance of picophytoplankton, like *Micromonas* and *Synechococcus*. Significantly high cell numbers of picophytoplankton were found within the WSC northwest of Spitsbergen, of *Synechococcus* (Paulsen et al., 2016) as well as of *Micromonas* (Kilias et al., 2014). The presence of autotrophic picoplankton in northern polar regions was emphasized by Li et al. (2009), who discovered an increase in the abundance of small picoplankton ($< 2\,\mu m$) in the Canada Basin between 2004 and 2008. This finding was linked to a freshening of surface waters. Likewise, Comeau et al. (2011) stressed the tendency towards observing higher abundance of small plankton cells like haptophytes and *Micromonas* in the Canadian Beaufort region, which they attributed to enhanced stratification and thus general decrease in nitrate availability. Paulsen et al. (2016) highlighted the high abundance of *Synechococcus* in August 2014, which was similar to the abundance of *Micromonas* resolved by our summer microscopic data from the years 2016, 2017, and 2018. In October *Micromonas* was nearly absent, while significant numbers of *Synechococcus* can be found even in November within the Atlantic water (Paulsen et al., 2016). On the one hand, the biovolume of *Synechococcus* reported for November 2014 in Paulsen et al. (2016) is a small fraction relative to our total biovolume estimates of October (see Figs. 2.6 and 2.7). On the other hand, the abundance of *Synechococcus* might have been higher during October in that year than in November. Paulsen et al. (2016) explained the presence of *Synechococcus* could be associated with a reduced grazing pressure by heterotrophic nanoflagellates. Our spectra support their interpretation, as we could reveal a drastic decline in heterotrophic nanoflagellate abundance (between 3 and 4 µm) already in the Polar water's summer spectrum and even more so in the autumn spectrum of the Atlantic water (Figs. 2.6 and 2.7). In the Polar water we did not find a significant number of heterotrophic nanoflagellates in October. We here recall the differences between the Polar- and Atlantic water with respect to the timing of the bloom and the successional plankton development, as shown in Fig. 2.5. This indicates that the plankton signal in the Atlantic water was lagged by several weeks compared to the Polar water, and *Synechococcus* might have been present at higher abundance in October in the Polar water as well, which remained unresolved in our measurements.

Overall, recent observations substantiate the appearance of autotrophic picoplankton in the Arctic, with potential consequences for the functioning of the microbial loop dynamics. However, we learned that great care has to be taken when making inferences about a general trend with respect to heterotrophic bacteria and autotrophic picoplankton in a changing Arctic. Given the high variability in the abundance of the picoplankton it remains difficult to assess whether shifts towards higher abundance of smaller cells can be attributed to variations in timing of the seasonal succession or is a general phenomenon. In this context, it becomes meaningful to relate the here observed spectra to the seasonal bloom development, which will be further addressed in Section 2.4.3.

2.4.2 Specific patterns in plankton size spectra

Based on our size spectra we identified distinctive size ranges of local maxima and minima. Four size ranges of high variability at 3–4, 8–10, 25–40, and 70–100 µm indicate size-selective grazing. These patterns cannot be explained by allometric physiological processes of the phytoplankton, because they appeared in size spectra for both, autotrophic and heterotrophic cells. Rather, the variability within these specific size intervals accentuate variations between bottom-up effects and top-down control through grazing. Furthermore, the distinctive size ranges denote the importance of prey size, with no clear discrimination according to the trophic status (omnivory). In contrast, interjacent size ranges showed noticeably less variability, suggesting that these size ranges were less influenced by variations in grazing. Similar size specific patterns had been observed in other studies. For example, Schartau et al. (2010) used a similar approach to generate size-spectra from epi-fluorescence microscopic plankton counts and size measurements from equatorial Pacific samples (Landry et al., 2000). They observed a clear minimum around 4 µm ESD, and a step-like decrease between 30 and 50 µm ESD, which became even more pronounced in samples of a fertilised patch where algal growth was stimulated by the addition of iron. The depression in the proximity of 4 µm ESD of the plankton community size structure was so prominent that it could readily be identified by histogram representations of fixed size classes, with lowered cell abundance in the 2–5 µm size class of the original data set described in Landry et al. (2000). Mainly heterotrophic flagellates, dinoflagellates, prymnesiophytes, and small diatoms were subject to this size-specific grazing impact. Rodríguez et al. (1998) compiled size-abundance spectra for samples from the deep fluorescence maxima at different locations in the Alboran Sea (Mediterranean), combining flow cytometry and microscopy data. Consistently, the abundance of cells between 5 and 6 µm ESD was reduced relative to smaller and larger cells. In a size spectrum compiled by Marañón (2015), log(cell abundance) deviates notably from the linearly decreasing relationship with log(cell volume), especially in a cell size range around 4 µm. Similarly, in size spectra derived by Quinones et al. (2003) from image analyses of samples from the North-West Atlantic, anomalies in biovolume (deviations from a log-linear relationship) are traceable at sizes 3–4 µm and at approximately 30–40 µm. Volume size spectra derived from Laser In-Situ Scattering and Transmissometry (LISST) measurements in the Fram Strait by Trudnowska et al. (2018) show maxima in phytoplankton biovolume between 4–5 µm, with much lower values for sizes greater than 10 µm. Their spectral measurements represent conditions found in the middle of July 2013. In contrast to their LISST data, our spectra exhibit a substantial fraction of phytoplankton biovolume also in the size range greater than 10 µm not only in summer but also in autumn. Interestingly, the total particle spectra (of the phyto- and other- types of particles) resolved by LISST in Trudnowska et al. (2018) disclose minima between 20 and 30 µm, most noticeably for measurements in the WSC.

Moreno-Ostos et al. (2015) derived a series of size abundance spectra from samples collected in the subtropical Atlantic (south and north of the equator). They concluded that the spectral slope of a log-linear size-abundance relationship of the phytoplankton is not a good indicator for total biovolume, in particular within oligotrophic waters. This was attributed to considerable variability within specific size ranges so that slope and intercept may not become ultimately constrained by the size and abundance data. Amongst size ranges of large variations in their study were those in the vicinity of 4 µm (volume $\approx 10^{1.5}$ µm^3), as well as between 27 µm and 50 µm (volume ranges of $\approx 10^4$–$10^{4.8}$ µm^3). Clearly, some of the prominent size ranges with pronounced variations revealed in our study for the Arctic microbial plankton community seem to be generic rather than site-specific.

2.4.3 Spatial and temporal separation

In the study of Trudnowska et al. (2016), spatial variability in the Fram Strait was investigated in July 2012. They could resolve patches of high plankton abundance that occupied between 2 to 17 % of the Fram Strait region. According to their analysis, major differences in normalised biovolume size-spectra could be mainly attributed to differences in oceanographic conditions. For example, consistent with our observations, phytoplankton in the WSC region were larger (higher abundance in the size range larger than 100 µm) than in the Polar water. Based on our analyses of remote sensing chlorophyll-a concentrations, we showed that the temporal development of chlorophyll-a differed between the Polar and Atlantic water masses. The spring blooms in Polar waters appeared earlier than the pronounced blooms of the Atlantic waters, which is consistent with the results of Nöthig et al. (2015), who revealed differences in the variability, trends and bloom duration between EGC and WSC in the period 1991–2012.

Because our samples covered the Polar and Atlantic water masses as well as two different seasons (summer and autumn), we may interpret the spatio-temporally separated size spectra (section 2.3.3) as independent size spectra that represent four different points in time, relative to the progression of the plankton community succession: Scenario 1–4 (S1–S4, approximately 0, 1–8, 9–11, and 15–17 weeks after the bloom maximum, Fig. 2.8). During the summer cruises (PS99, PS107, PS114), remote sensing indicated high chlorophyll-a averages in the Atlantic section of the sampling site. We therefore interpret size spectra from Atlantic summer samples as Scenario 1 (S1), as they originate from mid to end of bloom situations. Mean chlorophyll-a concentration had decreased already in the Polar section during the summer cruises, and the peak bloom had passed approximately 1–8 weeks ago (S2). In 2018, chlorophyll-a concentration in the Atlantic section peaked approximately 9–11 weeks before MSM77-sampling was undertaken, hence we interpret Atlantic autumn spectra as S3. Mean chlorophyll-a concentration peaked earlier, throughout May in 2018, in the Polar section, so 15–17 weeks passed between the end of the bloom in early June until sampling during MSM77. Polar autumn size spectra therefore represent S4.

With this approach we could resolve changes in plankton size structure, revealing that while mean total cell concentration and total biovolume decreased (see Fig. S3 in the supplemental file), major patterns strengthened, diminished, or even reversed. For example, the maximum around 3 µm in the heterotrophic spectrum at S1 turned to a local minimum at S3–S4. During the decline of the phytoplankton community, the relative abundance of smaller sized cells (ESD < 30 µm) decreased more than the number of larger cells. If interpreted in terms of a log-linear relationship between abundance and ESD, this corresponds to a reduction of the slope. The gradual reduction of the abundance of small cells eventually induced a sign-change in the slope of phytoplankton biovolume spectrum (see Fig. 2.8B), with the biovolume being dominated by cells of ESD > 10 µm. During S4, the maximum abundance of autotrophs was at ESD ≈ 3 µm, which is a size range of noticeable grazing pressure, appearing as a local trough at other times. This inversion suggests some potential for recovery of the standing stocks in this size range. Interestingly, Marañón et al. (2013) showed experimentally that the size-dependent maximum growth rate $\mu_{\max}$ has an optimum in the vicinity of this size range, likely as a result of a trade-off between the ability to replenish internal nutrient cell quota and the ability to synthesise new biomass (Ward et al., 2017).

According to our spectra, the size-selective grazing showed clear signs of omnivory, but also of intraguild predation within the microbial community. Ciliates are often regarded as a single functional group (guild) in models of the microbial loop (e.g. Thingstad and Cuevas, 2010). Stoecker and Evans (1985) have shown experimentally that while both, the large tintinnid *Favella* sp. and the smaller ciliate *Balanion* sp. fed on the dinoflagellate *Heterocapsa triquetra*, the large tintinnid could also prey on the smaller ciliate. In their model, ecosystem structure was shaped by the relative efficiencies of the one-step and the two-step pathway of this triangular trophic relationship. The results of our analysis agree with their findings. In our spectra the ciliates occupied a broad size range, from 7 µm small undefined

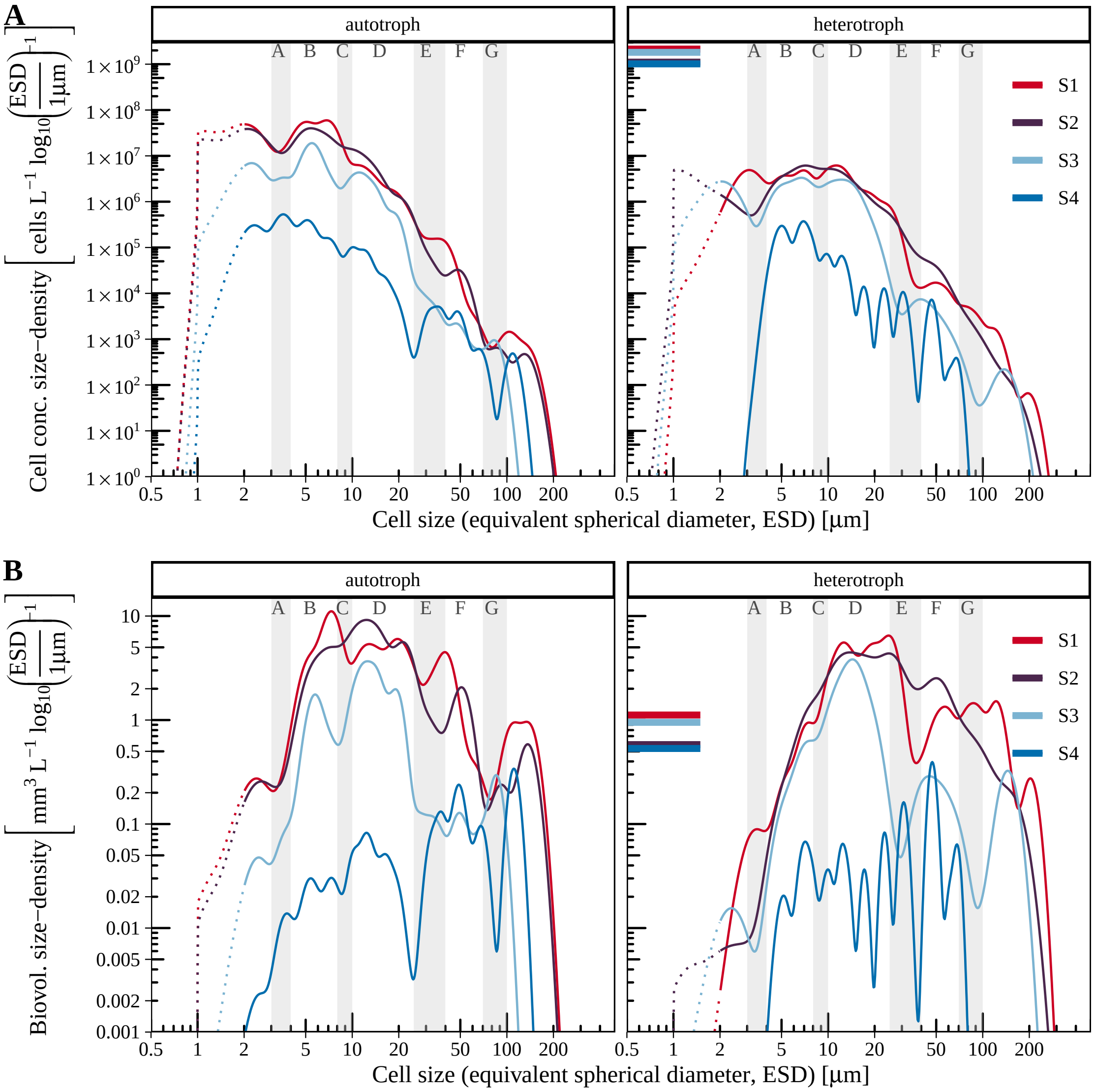

Figure 2.8: Spectra at different times relative to the progression of plankton succession (S1-S4). During the summer cruises, the Atlantic waters were subject to bloom conditions (S1 ≈ 0 weeks after bloom), while in the Polar waters the peak bloom had already passed (S2 ≈ 1–8 weeks after bloom). The spatio-temporal separation of the autumn spectra was done likewise (S3 ≈ 9–11, and S4 ≈ 15–17 weeks after bloom). Abundance spectra are shown in (**A**), biovolume spectra in (**B**). Dotted lines indicate reduced reliability of size measurements for cells with ESD < 2 µm. For comparison, abundance and biovolume concentration densities derived from Flow Cytometry cell count measurements are shown for bacteria as horizontal lines (0.5 − 1.5 µm, assuming mean ESD = 1 µm, data from corresponding samples in von Jackowski et al. (2020a).

ciliates to the tintinnid *Acanthostomella norvegica* with ESD = 120 µm, while the majority of ciliates were larger than 10 µm. Heterotrophic cells in the 25–40 µm size range (section E) were composed mainly from dinoflagellates, tintinnids, and other ciliates in slightly varying proportions between S1 and S3, but the absence of ciliates and tintinnids < 40 µm caused a prominent trough at S4. The density of larger tintinnids between 35–90 µm however stayed relatively constant, which could indicate a transition from mainly herbivory on phytoplankton to increasing carnivory on smaller ciliates, their former competitors, as total phytoplankton declines. The consideration of larger ciliates grazing on smaller ones increases the length of the food chain and thus the number of loops, which could be approached by considering the theory and size-based model of multiple food chains suggested by Armstrong (1994) For every additional loop cycle within the microbial food web the efficiency of matter transfer to the copepods is reduced, while more organic matter is released and becomes available for bacterial consumption (Azam et al., 1983), with potential consequences for nutrient recycling and organic matter export (Steele, 1998). Although unresolved by our spectra, the loss of the largest microzooplankton (tintinnids and heterotrophic dinoflagellates $> 80\,\mu m$) at S4 and the decrease of large diatoms were likely associated with copepod grazing and aggregation.

2.4.4 ESD and *effective prey size* of plankton

When comparing plankton size spectra, certain aspects of how cell size was measured and normalised have to be considered. For unicellular nano- and microplankton we could demonstrate that the ESD can be a robust measure of size, otherwise our spectra would have become more blurred because of the various cell shapes and thus distinct patterns would not have been identifiable. Our ESD values are based on cell volumes that were derived from length and width measurements, thereby considering differences in the plankton cell's geometric shapes described in Edler (1979) and Olenina et al. (2006). This approach is more advanced than assuming ellipsoids, but with respect to biovolume, the ESD is likely a less accurate proxy than the area-based diameter (ABD), a normalised measure based on the entire area of a single cell or organism of various shapes. The ABD is a valuable approximation of the biovolume, which would be a good measure for investigating allometric physiological dependencies, e.g. size dependent variations in nutrient affinity (e.g. Aksnes and Egge, 1991). In our plankton size spectra we could identify recurrent patterns but did not find a perfect match in ESD of the distinctive minima due to size-selective grazing. This is likely because of morphological differences. The ESD of a prey cell does not necessarily reflect the actual dimension that a predator might face. For example, the star-shaped *Dictyocha speculum* has a relatively small cell volume and a small ESD accordingly, but appears bulky due to its spines. Care has to be taken when elaborating predator-prey interactions from changes in ESD based size spectra. In other words, while ESD might work well for explaining bottom-up allometric effects we do not expect that ESD is equally representative as prey size. Identical ESDs can be assigned to cells of very different morphology. Bearing this in mind, we recommend the consideration of an *effective prey size* when looking at predator-prey dependencies, while using ESD for biovolume dependent processes. In this manner, the formation of colonies impacts the *effective prey size*, with ecological implications.

We treated cells that were part of colonies as single cells, because the sample fixation with hexamine neutralised formaldehyde may have an impact on the durability of cell colonies. The prymenesiophyte *Phaeocystis* sp. can reach high abundance in the Marginal Ice Zone (Gradinger and Baumann, 1991; Nöthig et al., 2015) and is known to occur in form of small flagellated cells or to grow to large colonies (Rousseau et al., 2007). We observed mostly free living, flagellate single cells of *P. pouchetii* with an average diameter of $2.4\,\mu m$, while spherical colonies can reach 0.1 mm and cloud-shaped colonies may reach 2 mm, as reviewed in Rousseau et al. (2007). Interestingly, with the formation of colonies, the *P. pouchetii* cells can overrun the 8–10 µm and 25–40 µm size ranges of definite grazing pressure, generating a loophole for their growth and reaching the size range of large chain forming diatoms. Such an effect could not be resolved with our measurements, but should be better addressed in future studies. The formation of colonies is hypothesised to be a defence mechanism against microzooplankton grazers, with the consequence of entering the size range of prey for copepods (Nejstgaard et al., 2007). Furthermore, some diatom species are known to form chains to escape size ranges of high grazing pressure (Bjærke et al., 2015). In our study we indeed observed colonial assemblages of *Chaetoceros* sp., *Pseudo-nitzschia* spp., *Eucampia groenlandica*, *Navicula vanhoeffenii*, *Navicula pelagica*, *Navicula* sp., *Fragilariopsis* spp., *Fossula arctica*, and other undefined pennate diatoms.

2.4.5 Limitations and outlook

Microscopic measurements depend on the experience of the observer. Therefore, comparisons between data or their combination need to made with caution. We respected uncertainties in plankton counts and in size measurements by introducing a resampling approach, but some uncertainties in taxonomic identification may still exist. A study by Jakobsen et al. (2015) has shown large variations not only between different taxonomists, but also for repeated measurements of the same taxonomists. The purpose of grouping and averaging size-spectra of individual samples was to eliminate potential biases and compensate for major methodological variations. The mixotrophic lifestyle may be common or even predominant among protist plankton (Flynn et al., 2013), however we could not resolve this microscopically. Instead, all dinoflagellates containing chloroplasts were regarded as photo-autotrophic, and the colourless as heterotrophic. We furthermore assigned half of the flagellates an autotrophic and half a heterotrophic nutrition, which contributes to further blur in the trophic identifications. Our classifications of autotrophic and heterotrophic feeding modes therefore do not refer to strict trophic strategies, but rather indicate a tendency towards one or the other, without resolving all intermediate lifestyles.

All samples considered in our analysis were collected during four cruises within a three years period, covering different times of the natural plankton succession in the Fram Strait. Each of the cruises span a three week period, being ‘snapshots’ of the protist plankton community. In spite of these short term observations, the specific size ranges discussed above were distinctive within all size spectra, which implies that the trophic dynamics of the microbial community in the Fram Strait are well reflected in our size spectra within the size range between 2 and 200 µm. Considerable uncertainties exist in our spectra for sizes smaller than 2 µm. With our microscopic measurements we could not resolve the abundance of picoplanktonic cyanobacteria and of heterotrophic bacteria. However, for comparison we considered picoplankton data from the studies of von Jackowski et al. (2020a) (bacteria) and Paulsen et al. (2016) (*Synechococcus*). These data are typically available as measurements of a different type, e.g. flow cytometry. Likewise, the consideration of copepod data would provide a more complete picture of the microbial loop dynamics, including mass transfer. A synthesis of our derived size spectra with complementary ecological and biochemical data appears as constructive objective for future studies.

The here presented size spectra are particularly valuable for constraining solutions obtained by size-based model applications. Only by modelling we could disentangle some of the complex interdependencies between the phyto- and the microzooplankton. Our spectra reflect the state of the microbial community structure at times after the bloom maximum, a period when the microbial dynamics is critical for regenerated production. The identified size ranges of high grazing pressure and size niches that favour autotrophic growth impose strong constraints on model solutions, in particular with respect to resolving variations between bottom-up and top-down regulatory effects and trophic efficiency. The latter is of vital importance for estimating mass transfer to higher trophic levels in model applications, i.e. prey availability for copepods.

2.5 Conclusion

The primary aim of our study was to gain insight to the plankton community size structure within the Arctic environment of the Fram Strait. The employed KDE method for analysing the size structure (as equivalent spherical diameter, ESD) of the nano- and microplankton community was shown to reveal details that may become masked by introducing individual size classes. In conclusion, with our extensive approach we documented how laborious and thus valuable microscopic measurements can be well transferred to continuous size spectra of autotrophic and heterotrophic plankton of ESD between 1 µm and ≈ 200 µm. With this approach we could accentuate details that show distinct deviations from any log-linear dependency between plankton size, abundance, and biovolume.

From our remote sensing data analyses we learned that the plankton community within the polar Arctic Water lead the seasonal succession by approximately two to three weeks relative to the plankton observed in the Atlantic Water. Our plankton size spectra document the decline in total biovolume during the post bloom period as well as a substantial shift in the phytoplankton's relative biovolume towards larger cell sizes (> 30 µm) in autumn. We conclude that the spatial separation between Arctic and Atlantic waters within the Fram Strait was crucial, as both water masses contained plankton and likely a biogeochemical signal that differed with respect to the timing in seasonal succession.

Amongst the most interesting details are four specific size ranges (3–4 µm, 8–10 µm, 25–40 µm, 70–100 µm). The four size ranges induce pronounced deviations from a log-linear dependency between plankton size, abundance and biovolume. Thus, these specific size ranges appear to be valuable indicators for temporal changes between bottom-up and top-down regulatory processes within the microbial food web.

The identified size ranges disclose size-selective grazing impacts on the Arctic nano- and microplankton community, regardless of the trophic status. Since autotrophs and heterotrophs seemed to be subject to similar grazing pressures within specific size ranges, we conclude that the conjecture of phytoplankton and heterotrophic nanoflagellates being the only prey for ciliates is inappropriate. Instead, omnivory and intraguild predation seem to be vital pathways within the pelagic microbial food web in the Arctic. Whether the identified grazing-sensitive size ranges are specific for the Arctic or generic for the microbial food webs remained unresolved here, but comparisons with other spectra clearly indicated similar grazing impacts, at least within the size ranges 3–4 µm and 25–40 µm.

Conflict of Interest Statement

The authors declare that the research was conducted in the absence of any commercial or financial relationships that could be construed as a potential conflict of interest.

Author Contributions

VL generated and analysed the size spectra and produced all figures and tables. EN provided the microscopic measurements, based on samples collected during four cruises to the Fram Strait. She guided the analysis with respect to discrimination between taxonomic groups and trophic strategies. MS initiated this study and guided the analyses with respect to the statistical methods applied. All authors contributed in writing the manuscript.

Funding

This study was funded by the Helmholtz Association and the German Federal Ministry of Education and Research (BMBF) as a contribution to the microARC project (03F0802A), part of the Changing Arctic Ocean programme, jointly funded by the UKRI Natural Environment Research Council (NERC) and BMBF.

Acknowledgments

Data were obtained during four *POLARSTERN* and *MARIA S. MERIAN* cruises and we thank the captains and crews. Special gratitude is owed to the student helpers Malte Schmidt and Lisa Zacharski for their tedious hours of plankton counting. We thank Ben Ward, whose comments helped improving the manuscript. Fruitful discussions about the Arctic plankton community with Neil Banas and Friederike Prowe are much appreciated. We are grateful for constructive comments by the two anonymous reviewers.

Data Availability Statement

R-scripts used to compile the here presented size spectra and for the separation of Polar and Atlantic sea surface temperature regions, as well as the generated size spectra will be shared upon request by the authors.

Chapter 3

A Lagrangian model-based analysis of protist plankton variability and its impact on organic matter dynamics along transit pathways through the Fram Strait

This chapter is based on the paper 'A Lagrangian model-based analysis of protist plankton variability and its impact on organic matter dynamics along transit pathways through the Fram Strait'

Citation:
Vanessa Lampe, Aidan Hunter, Ben Andrew Ward, Eva-Maria Nöthig, Anja Engel, Ingrid Helene Ellingsen, Markus Schartau: A Lagrangian model-based analysis of protist plankton variability and its impact on organic matter dynamics along transit pathways through the Fram Strait.
Submitted to Journal of Geophysical Research: Oceans in April 2024

Abstract

The Arctic Ocean is characterised by substantial seasonal and inter-annual variability, of which the sources and impacts are not yet fully understood. Employing a plankton ecosystem model with nine distinct size classes of phyto- and zooplankton ranging from 1 to 200 µm, we simulate standing stocks and fluxes within the nutrient, phytoplankton, zooplankton, and detritus pools. Crucially, some integral physiological and ecological parameters scale with size. The model is driven by data of the physical environment extracted along trajectories derived from the ocean model SINMOD, tracing the opposing East-Greenland and West-Spitsbergen currents through the Fram Strait. Our approach involves four ensembles of trajectories, yielding multiple solutions conditioned by the trajectories' origins and specific pathways. Model results, when compared to *in situ* observations of biogeochemical tracers and plankton size measurements, as well as climatological data of dissolved inorganic nitrogen and remote sensing chlorophyll, are largely in accordance with the data. At the times of sampling in the Fram Strait, we found the maxima of net primary production and vertical exports had already occurred. Distinct temporal developments in plankton size composition, growth, and export are evident from individual trajectories between and within the ensembles. We find that 10–72 % of locally observed variability in tracer concentrations, within the upper 100 m of the water column in the Fram Strait, can be attributed to differences in water parcel trajectories. These deviations stem from differences in origin and temporal development of environmental conditions along their voyage. A substantial portion of variability remains unexplained, underscoring the necessity for further research. Key areas include resolving processes like sea ice associated bloom dynamics, and refining allometric relationships and predator-prey interactions to enhance our understanding of plankton dynamics in this critical region.

Plain Language Summary

This study uses a particle-tracking model to estimate sources of variability in the Fram Strait region of the Arctic Ocean. In this perspective, an observer follows a water parcel along the currents and investigates physical, chemical, and biological changes within. The model simulates the growth of plankton populations, their influence on nutrient concentrations and the production of dead, dissolved and decaying organic matter, as water is transported northwards from the Atlantic Ocean and southwards from the Arctic Ocean into the Fram Strait. By simulating a number of different pathways, the model provides estimates of how variability in the environmental conditions along those pathways contributes to variability of the plankton ecosystem in the upper water column of the Fram Strait. When compared to measurements of the ecosystem taken from ships and observed by satellites, we find that the model is successful in reproducing changes in the plankton size structure observed in the Fram Strait and yields estimates of productivity and export that are close to observations from the region. Our study finds that a substantial portion (10–72 %) of the observed variability in biogeochemical tracers can be explained by differences in the histories (origins and pathways) of water parcels. Nonetheless, there is still a large amount of variability that remains unexplained, indicating the

need for further research to better understand essential processes. This research is important because it helps unravel the various sources of variability in the Fram Strait. Accurate models that consider detailed processes enable us to make better predictions about elemental cycling, productivity and export, especially in the face of climate change. In particular, by identifying the ranges of natural variability, we will be more able to identify and predict exceptional events that are occurring more frequently under climate change.

3.1 Introduction

The Arctic Ocean has changed significantly in recent decades as sea surface temperatures have risen (Comiso and Hall, 2014; Nielsen-Englyst et al., 2023) and the extent and thickness of sea ice has declined (Stroeve et al., 2012; Hansen et al., 2013; Renner et al., 2014; Spreen et al., 2020). These changes in the environment may substantially modify biogeochemical processes and alter the functioning of marine ecosystems.

The Fram Strait, between Greenland and Spitsbergen, is one of the main gateways to the Arctic Ocean and has been the subject of numerous repeated studies in the fields of biological, chemical and physical oceanography. A target area in the Fram Strait covers the Long-Term Ecological Research (LTER) observatory HAUSGARTEN (e.g., Soltwedel et al., 2005, 2016), where warmer waters enter from the North Atlantic in the East (West-Spitsbergen current, WSC) and colder, seasonally ice-covered waters exit the Arctic Ocean southwards in the West (East-Greenland Current, EGC). With the WSC and the EGC passing through the HAUSGARTEN area, the observations at different sampling sites capture biological and chemical signals that are influenced by dynamical changes that have already taken place outside the study area, for which data with comparable details are not available.

Most *in situ* investigations conducted in the Fram Strait focused on the summer conditions (e.g., Nöthig et al., 2020), as the region is seasonally covered with sea ice or close to the ice edge. More recent studies also covered periods in autumn or spring (e.g., von Jackowski et al., 2020a, 2022). Observations from the dark winter months are still rare (e.g., Błachowiak-Samołyk et al., 2015; Wietz et al., 2021). Detecting longer-term trends from annually repeated observations in summer and autumn within the Fram Strait is difficult given the strong spatial and temporal variability in ice cover and hydrographic conditions and usually requires many years, if not decades, of data collection. Helpful in this respect is to disentangle the range and causes of the observed variability within such regions, which contributes to our understanding of the processes involved.

In principle, variability in organic matter (OM) observations is conditioned by a combination of external factors, which are variations in physical and chemical conditions such as light, nutrient availability, and temperature, as well as of internal factors that are associated with the plankton dynamics. Overall, in the context of this study, we are concerned with several sources of variability that are linked to each other and become ultimately expressed in regions of observations:

I. Spatio-temporal variations in environmental conditions
   - differences in the horizontal transport of water masses (pathways)
   - differences in vertical mixing

II. Temporal variations in plankton dynamics
   - differences in plankton physiology, community structure, and interaction
   - differences in pre-conditioning, spatial origin and growth history of the plankton community

Apart from purely stochastically driven (random) processes, and disregarding methodological uncertainties, individual *in situ* measurements are subject to, and a combination of, these major sources of variability, that create differences between nearby but distinct sampling sites.

The horizontal heterogeneity, variance in space, as observed during a limited period of ship-board sampling (usually 2–3 weeks) in the HAUSGARTEN can, to some extent, be attributed to differences in the prior history along different pathways of water parcels passing through that region. These pathways can be investigated with a Lagrangian modelling approach, allowing dynamically consistent solutions of a one-dimensional (1D) marine ecosystem model to be derived along trajectories of individual water parcels (e.g., Banas et al., 2009). This approach facilitates the identification of optimised model solutions due to its computational efficiency (Banas et al., 2016), as model calibration requires multiple simulation runs. In a recent study by Kuhn et al. (2023) it is shown that the variability in Chl-*a* concentration is similarly described by an Eulerian and a Lagrangian approach on timescales of 30 days (approximately two times the characteristic timescale of plankton growth). Only in some ocean areas, with boundary currents or in upwelling regions, can differences between the two approaches become significant. With regard to plankton ecosystems in ocean regions that include frontal systems like in the Fram Strait, the findings of Kuhn et al. (2023) suggest suitable descriptions when a Lagrangian perspective is chosen. To investigate the spatial heterogeneity found in the HAUSGARTEN data the Langrangian approach is particularly useful, as it allows us to connect detailed local observations, e.g., plankton community structure, to spatio-temporal variations in tracer concentrations, primary production and carbon export outside of the target region.

Many aspects of plankton dynamics, from cellular to community level, are controlled by cell size, which can be regarded as a ‘master trait’ (Marañón, 2015; Andersen et al., 2016; Blanchard et al., 2017). Physiological processes such as nutrient assimilation and photosynthetic rates are size dependent (e.g., Litchman et al., 2007; Edwards et al., 2012), as are predator-prey interactions (e.g., Hansen et al., 1994). Size based ecosystem models make use of these allometric features to explain structural changes of the plankton community (e.g., Moloney and Field, 1991; Banas, 2011; Ward et al., 2012; Ward and Follows, 2016). Litchman et al. (2007) have shown that trade-offs between ecophysiological and morphological traits arise from fundamental allometric relationships that describe diverse plankton interactions and can explain variations in community composition along environmental gradients. Similarly, Ward et al. (2012) have shown that their size-structured ecosystem model was able to reproduce global patterns in biogeography and community structure of marine plankton, demonstrating the utility of size-based modelling.

Our primary objective is to investigate to what extent the differences between the environmental conditions (histories) of horizontally advected water parcels (trajectories) may contribute to the spatial heterogeneity of particulate and dissolved organic matter (POM and DOM) concentrations in the Fram Strait, as observed during summer and autumn of 2018 respectively. Along four ensembles of Lagrangian trajectories, which differ with respect to their origins and times passing the observational HAUSGARTEN area in the Fram Strait, a 1D size-based plankton ecosystem model is applied. We assess the model's ability to reproduce changes in the community size spectra observed in Lampe et al. (2021), where the plankton community showed a shift towards larger cell size during the summer-autumn transition in 2018. While stoichiometric variations in carbon-to-nitrogen and Chl-a-to-carbon ratios are explicitly resolved, we provide insight to differences in simulated rates of net primary production and export before, during, and after the sampling periods along trajectories that originate either from northern Arctic or from southern North Atlantic regions.

3.2 Methods

For our analyses we used observational data collected in the Fram Strait (FS), which comprise tracer concentration measurements (Torres-Valdés et al., 2019; Engel et al., 2019; von Jackowski et al., 2020b) as well as microscopic measurements of cell abundance and cell size (Lampe et al., 2021). In addition, remote sensing Chl-a data Sathyendranath et al. (2021), and climatological data of the World Ocean Atlas 2018 (WOA18, Boyer et al., 2018) were considered. We apply a one-dimensional (1D), vertically resolved ecosystem model, forced with data along trajectories that were extracted from SINMOD (Slagstad and McClimans, 2005; Wassmann et al., 2006) model results. For the 1D model we obtain multiple solutions, depending on the origins and pathways of individual trajectories. Results are based on four different ensembles of Lagrangian trajectories, as described in Sect. 3.2.2. The oceanographic conditions of respective trajectories provide the physical framework for our plankton ecosystem model. The ecosystem model is a nutrient-phytoplankton-zooplankton-detritus (NPZD) model with nine size classes for phytoplankton and zooplankton. Some model parameters, important for physiology and ecological interactions (e.g. regulating cell quota, nutrient uptake, growth, mortality, and grazing) are dependent on cell size and scale exponentially with cell volume ($x = a \cdot \mathrm{Vol}^b$). We fit the model to observations (*in situ*, remote sensing, and climatological data) by adjusting the model parameters.

3.2.1 Observational data

Observational data used for model evaluation were collected at the HAUSGARTEN Long Term Ecological Research observatory (LTER) site in the Fram Strait, located between Greenland and Spitsbergen (see Fig. 3.1). This region is commonly referred to as a main gateway to the Arctic Ocean (e.g., Nöthig et al., 2015) and is characterised by the convergence of two hydrographic regimes. While the eastern part of the Fram Strait is dominated by the northward flowing West-Spitsbergen-Current (WSC) that transports warm water from the North Atlantic into the Arctic Ocean (e.g., Beszczynska-Möller et al., 2012), the East-Greenland-Current (EGC) carries cold Arctic water into the Atlantic through the western Fram Strait (e.g., de Steur et al., 2009). The western region of the Fram Strait remains covered with sea ice for most of the year. More seasonal variability in sea ice cover is observed in the north-eastern, WSC dominated, part while the south-eastern region stays ice free throughout the year Soltwedel et al. (2016). The HAUSGARTEN LTER is located in the central Fram Strait between 78°N–81°N and 5°W–11°E and includes sampling stations in the colder EGC waters, as well as in the warmer WSC waters. The Marginal Ice Zone is a highly productive region (Soltwedel et al., 2016).

The data consist of *in situ* concentration measurements of inorganic nitrogen (nitrite and nitrate) (Torres-Valdés et al., 2019), and chlorophyll-a (Chl-a), particulate organic carbon (POC) and nitrogen (PON) (Engel et al., 2019; von Jackowski et al., 2020b), collected between July 16th and July 27th 2018 during the PS114 expedition of research vessel RV *Polarstern*. Additionally to the observational data recorded during summer time, we also consider data from a research cruise in autumn. Autumn samples were collected on MSM77 research cruise on RV *Maria S. Merian* between September 16th and October 4th 2018 and include measurements of Chl-a and POC. Unfortunately, no measurements of DIN and PON were conducted during this expedition. To complement the biogeochemical tracers, we also considered ecological data to evaluate the model. For this, we used plankton size data in the

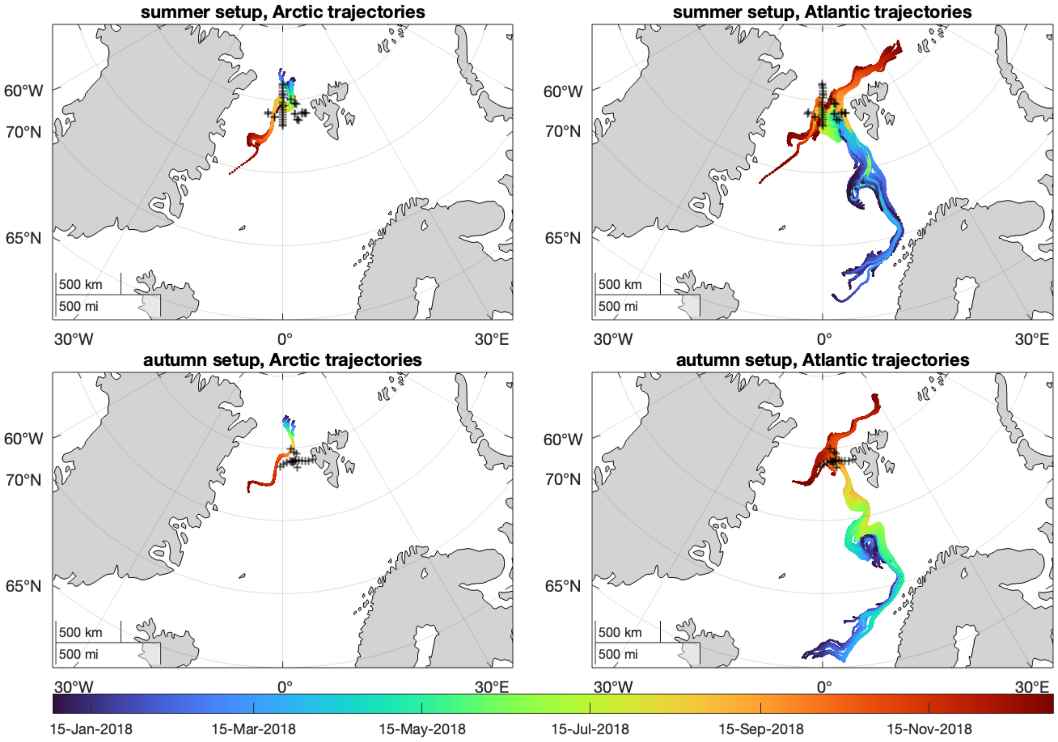

Figure 3.1: Particle trajectories for the physical model forcing. The starting point at day=1 is indicated in dark blue. Black crosses mark the sampling stations of observational *in situ* data used for model evaluation. Trajectories of the summer setup pass the stations during the summer sampling period (July 16th – July 27th 2018), those of the autumn setup during the autumn sampling period (September 16th – October 4th 2018).

form of size spectra of the protist plankton community, as described in Lampe et al. (2021), where size spectra of 60 samples from summer (PS99, PS107, PS114) and autumn (MSM77) and both the WSC and ESC influenced HAUSGARTEN stations were used.

3.2.2 Model setup and forcing

The 1D-NPZD model resolves n=9 size classes of phytoplankton and zooplankton with variable stoichiometry (carbon-to-nitrogen, C:N ratio), similar to the size-based models of Ward et al. (2012) and Ward and Follows (2016). In this model, 10 important parameters controlling the physiology (e.g. nutrient uptake rates, biosynthesis rates) and ecology (e.g. grazing) are dependent on organism size (see Tab. 3.1). We chose a Lagrangian approach to simulate lateral dispersal of the plankton along with the water currents (flow field). Along these trajectories the plankton experience changing environmental conditions, including variations in vertical mixing and exposure to light. The target region is the HAUSGARTEN observatory in the Fram Strait, to be reached at times that cover the two sampling periods, in summer and autumn. The Lagrangian approach appears especially appropriate for simulating observations in the Fram Strait, where most of the differences seen between sampling sites are associated with variations between and within two opposing currents (WGC and ESC), as well as the formation of small eddies and recirculation patterns (von Appen et al., 2015; Nöthig et al., 2020).

Physical forcing

The physical forcing data were extracted from the ocean model SINMOD (Slagstad and McClimans, 2005; Wassmann et al., 2006), a regional coupled 3D model system encompassing physical, chemical, and biological domains. Configured for the Nordic and Arctic Seas, it operates at a horizontal resolution of 20 km and with 25 vertical layers. The hydrodynamic component, responsible for calculating fundamental oceanic properties such as velocity, water temperature, and pressure, is based on the primitive Navier-Stokes equations, implemented on a z-grid (Slagstad and McClimans, 2005; Slagstad et al., 2015). The ice model incorporates two state variables: ice thickness and concentration, shaping ice interaction dynamics (Hibler, 1979). This model integrates the ice momentum equation and an equation for ice internal stress, utilizing the elastic-viscous-plastic (EVP) dynamical model proposed by (Hunke and Dukowicz, 1997). Vertical turbulent diffusivity is calculated based on a Richardson number based scheme described in Sundfjord et al. (2008). Surface irradiance is calculated based on solar elevation, cloud cover and light attenuation through sea ice. Cloud cover is obtained from ERA-Interim reanalysis data from the ECMWF (Europen Centre for Medium-Range Weather Forecasts). Details regarding the model runs including atmospheric, freshwater and tidal forcing utilised in this study can be found in Vernet et al. (2021). The data extraction was achieved by applying the *particulator* MatLab tool (Banas, 2018) (Fabian Grosse and Neil Banas, personal communication). The extracted data include surface irradiance ($I_{\mathrm{surf}}(t)$), water temperature ($T(z,t)$) and vertical (turbulent) diffusivity ($K(z,t)$) for times t (day) and depths z (m). The spatio-temporal development of $I_{\mathrm{surf}}(t)$ and surface temperature are shown in Fig. 3.2. Irradiance attenuates exponentially with depth ($I(z,t)$), assuming a seawater attenuation coefficient of $\kappa_{\text{SW}} = 0.04\ \text{m}^{-1}$ together with a light attenuation by Chl-a, which is $\kappa_{\text{P}} = 0.0149\ \text{m}^2\,(\text{mg Chl})^{-1}$ (Krause-Jensen and Sand-Jensen, 1998), see Eqs. B.10 and B.11 in the Supplemental Information file (SI, Chapter B.1). The pathways of these model trajectories are shown in Fig. 3.1.

The model is applied in two setups. In the first 'summer' setup, we isolated particle trajectories that passed through the HAUSGARTEN region during the July 2018 sampling period by defining 'catchment areas' at the location of each *in situ* sample. Trajectories within 25 km from a sample location at the time of sampling were retained, and all other trajectories passing through Fram Strait were omitted. Observational samples were usually taken in regions with no or thin ice cover. We therefore excluded trajectories of Arctic origin with high ice cover (ice cover > 50 % in July) from the pool of forcing trajectories. In total, 139 trajectories

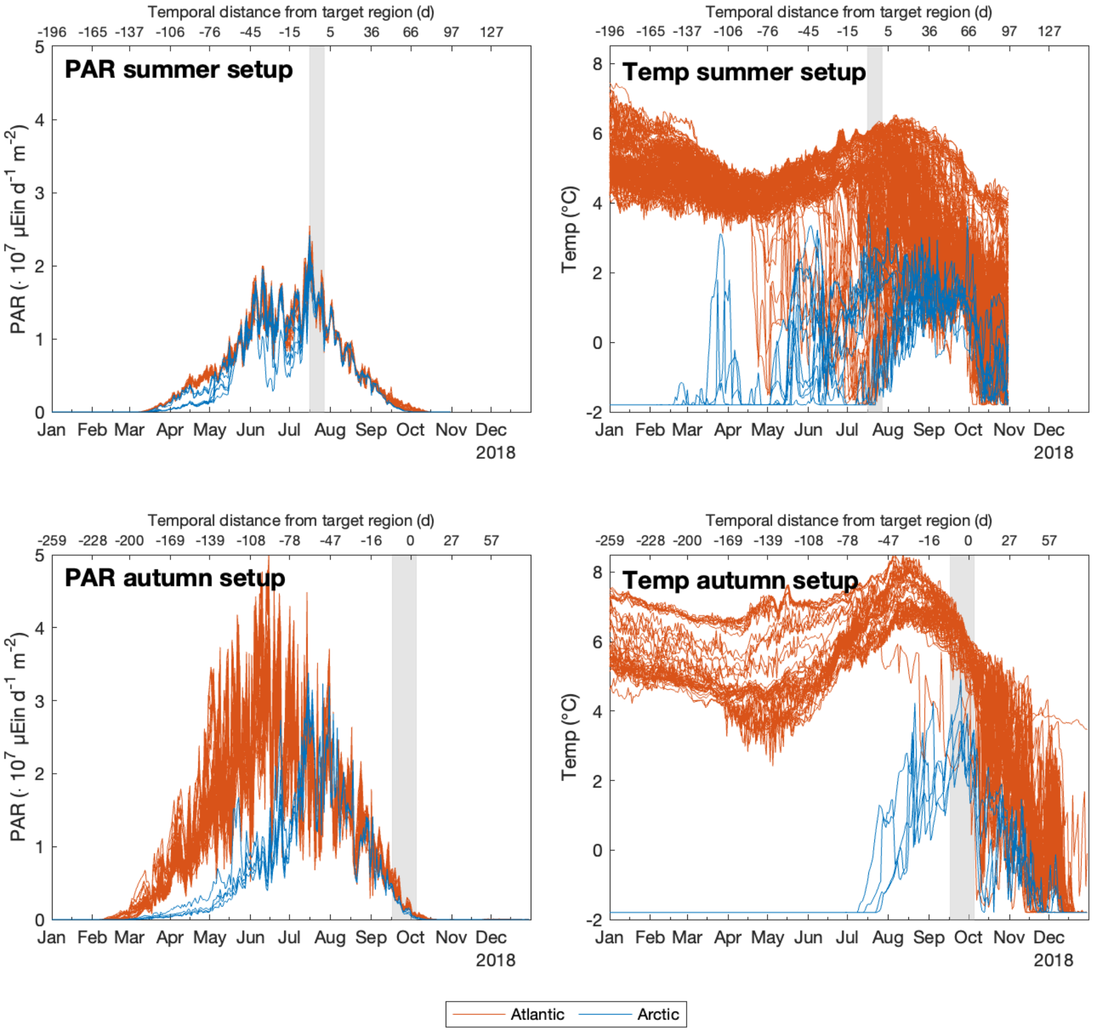

Figure 3.2: Physical forcing of the model trajectories. The left column shows surface PAR ($= I_{\text{surf}}(t)$) for the summer (upper) and autumn (lower) setup, the right column shows the sea surface temperature. Line colours indicate the trajectory origins (Arctic = blue or Atlantic = orange). Grey shaded areas exhibit the periods trajectories pass the HAUSGARTEN stations (Jul. 16th – Jul. 27th 2018 for summer setup, Sep. 16th – Oct. 4th 2018 for autumn setup).

of Atlantic origin and 10 trajectories of Arctic origin have been applied to force the model in the summer setup.

In a second ‘autumn’ setup, we isolated trajectories that passed through the HAUSGARTEN region during the September to October 2018 sampling period. In order to arrive in the target region later in the year, trajectories of Atlantic and Arctic origin start their voyage further south and north, respectively, than their counterparts in the summer setup. Eventually, five trajectories of Arctic origin and 50 of Atlantic origin could be considered for the autumn setups. The catchment area radius for trajectories had to be increased to 100 km for the autumn setup, due to low number of available SINMOD particle trajectories and sampling stations from the field campaigns. If a 25 km catchment area radius was used like for the summer setup, no Arctic trajectories would remain for the autumn setup.

Plankton ecosystem dynamics

The dynamical plankton ecosystem model is described by a set of differential equations that describe the mass flux of nitrogen and carbon. The phytoplankton and zooplankton are structured according to cell size (9 size classes: 1.12 – 2.00; 2.00 – 3.56; 3.56 – 6.33; 6.33 – 11.25; 11.25 – 20.00; 20.00 – 35.57; 35.57 – 63.25; 63.25 – 112.48; 112.48 – 200 µm equivalent spherical diameter, ESD), applying allometric rates that determine autotrophic growth within the respective size classes, as well as size-specific grazing by heterotrophs. While some parameters are independent of organism size, others are dependent on the cell size, e.g. maximum cell nutrient quota, nutrient uptake, and linear mortality. The model’s parameter values are listed in Tab. 3.1. The differential equations are adapted from Ward et al. (2012) and Ward et al. (2017), but modified to represent a 1D water column and with some minor changes to parameterisation:

$$\frac{\partial N}{\partial t} = \frac{\partial}{\partial z} K \frac{\partial N}{\partial z} - \sum_j V_{\mathrm{N},j} B_{\mathrm{C},j} + \sum_k r_{\mathrm{N},k} M_{\mathrm{N},k} \tag{3.1}$$

$$\begin{aligned}\frac{\partial B_{i,j}}{\partial t} =& \frac{\partial}{\partial z} K \frac{\partial B_{i,j}}{\partial z} + V_{i,j} B_{\mathrm{C},j} - \sum_{j_z} G_{i,j_z,j} B_{\mathrm{C},j_z} \\ &+ \sum_j \lambda_{i,j_z} G_{i,j_z,j} B_{\mathrm{C},j_z} - (m_j + m_2 B_{i,j}) B_{i,j}\end{aligned} \tag{3.2}$$

$$\begin{aligned}\frac{\partial D_{i,k}}{\partial t} =& \frac{\partial}{\partial z} K \frac{\partial D_{i,k}}{\partial z} - w_k \frac{\partial D_{i,k}}{\partial z} - r_{i,k} D_{i,k} \\ &+ \sum_j \beta_{j,k} (m_j + m_2 B_{i,j}) B_{i,j} + \sum_{j_z} B_{\mathrm{C},j_z} \sum_j \beta_{j,k} (1 - \lambda_{i,j_z}) G_{i,j_z,j}\end{aligned} \tag{3.3}$$

Here, the state variables are concentrations of N (dissolved inorganic nitrogen, DIN), $B_{i,j}$ (phytoplankton and zooplankton biomass, a stacked matrix $B_{i,j} = [P_{i,j_p}, Z_{i,j_z}]$) and $D_{i,k}$ (dissolved and detrital particulate organic matter, DOM and detritus respectively). Subscripts index nutrients ($i \in \{\mathrm{C, N, Chl}\}$), plankton size classes ($j = [j_p, j_z] \in \{1, \dots, n_p + n_z\}$), and type of detrital organic matter ($k \in \{\mathrm{DOM, detritus}\}$). Chlorophyll is relevant only for phytoplankton, so the zooplankton and organic matter matrix rows where $i = \mathrm{Chl}$ are zeroed.

Table 3.1: Model parameters: the first 17 parameters are independent of cell size, while 7 parameters are described according to an allometric relationship $\left(x = a \cdot (\frac{\text{Vol}}{1\ \mu\text{m}})^b\right)$. Two estimates of the originally assumed size-dependent parameters turned out best when treated without a size dependency ($b = 0$)

#) Notation	Values	Unit	Description (Equation)
1) T^{ref}	20	°C	reference temperature (B.5)
2) A	0.05	–	temperature sensitivity (B.5)
3) h	10	–	uptake quota regulation (B.4)
4) m_2	$0.05^{\dagger}$	m^3 mmol C^{-1} d^{-1}	quadratic mortality (B.24)
5) a_P^*	$3.83 \cdot 10^{-7}$	mol C m^{-2} (g Chl a μEin$)^{-1}$	initial slope of P-I curve (B.8, B.14)
6) θ	4.2	mg Chl-a (mmol N$)^{-1}$	maximum Chl-a:N ratio (B.14)
7) ξ	2.33	mol C (mol N$)^{-1}$	cost of biosynthesis (B.12)
8) $a_G{}^*$	4	m^3 (day mmol C$)^{-1}$	grazing clearance rate (B.16)
9) k_G	2.75	mmol C $(\text{m}^3)^{-1}$	total prey half saturation (B.15, B.16)
10) δ_{opt}	10	–	optimum predator-prey size ratio (B.18)
11) σ^*	2	–	width of grazing kernel (B.18)
12) Λ	-1	–	prey refuge parameter (B.15)
13) λ^{max}	0.7	–	max. assimilation efficiency (B.21, B.22)
14) m_{min}	0.01	d^{-1}	summand to prevent m_j approaching 0 (B.23)
15) $r_{i,k}{}^*$	0.04	d^{-1}	remineralisation rate (3.1, 3.3)
16) β	$b_1 = 0.9$, $b_2 = 0.2222$, $b_3 = 2$	-	detritus and DOM partitioning (B.25, B.26, B.27)
17) $w_{\text{det}}{}^*$	10	m d^{-1}	sinking velocity of detritus (3.3)
	$(x = a \cdot \text{Vol}^b)$	(Unit of x)	
18) Q_N^{min}	$a^* = 0.035$, $b = 0$	mol N (mol C$)^{-1}$	minimum N:C quota (B.2, B.3, B.4)
19) m	$a^* = 0.05$, $b = 0$	d^{-1}	mortality rate (3.2, B.23, B.24, B.27)
20) $\tilde{s}_N^{\text{max}}$	a^*=0.6166, $b^* = -0.09$	–	scaling of maximum N:C quota (B.2)
21) v^{max}	$a^* = 0.1008$, $b^* = 0.09$	mol N (mol C$)^{-1}$ d^{-1}	maximum uptake rate (B.6)
22) α	$a^* = 0.5933$, $b^* = -0.18$	m^3 (mmol C) $^{-1}$ d^{-1}	nutrient affinity (B.6)
23) P^{max}	$a^* = 2.5$, $b^* = -0.08$	d^{-1}	maximum photosynthetic rate (B.7)
24) G^{max}	$a^* = 11$, $b^* = -0.16$	d^{-1}	maximum prey capture rate (B.15, B.16)

†For the largest size class, otherwise 0.
*Parameter was considered in numerical optimisation, see Sect. 3.2.4

The rate of change in DIN is the sum of change due to vertical diffusion and replenishment via remineralisation minus the uptake by autotrophs. The rate of change in biomass is the sum of changes due to vertical mixing, autotrophic uptake (phytoplankton), uptake through grazing (zooplankton) minus changes due to grazing and mortality. The rate of change in D (DOM and detrital, particulate OM) is the sum of change due to vertical diffusion, mortality and messy feeding minus sinking and remineralisation. Because the model only resolves the labile–semi-labile fraction of DOC, we refer to it as $\mathrm{DOC_{SL}}$. The detailed terms of model equations 3.1–3.3 are described in Sect. 1 in the SI.

The efficiency at which the primary production is exported to depth is diagnosed from the model results as the pe-ratio, and is calculated as the fraction of total export flux at 100 m (combining the sinking of detritus ($w_{\mathrm{det}} \cdot [D_{i,\mathrm{POM}}]_z$) and the net flux induced from the turbulent vertical diffusion of POM (detritus + zooplankton + phytoplankton)) divided by the depth-integrated (100 m) net primary production (NPP) (e.g., Serra-Pompei et al., 2022). The pe-ratio is therefore calculated as:

$$pe = \frac{\text{export}}{\text{NPP}} \tag{3.4}$$

In this study, we considered instant, daily pe-ratios and time integrated pe-ratios over the productive period. For the time integrated pe-ratios, we integrated export and NPP over April–September prior to calculation of the ratios.

Initial conditions

The initial conditions were to some extent directly adopted from SINMOD simulation results. With regard to initial DIN profiles (at the origins on 1st January) of the Arctic trajectories, the SINMOD results exhibit surface concentrations around 6–7 $\mathrm{mmol\,m^{-3}}$, which are lower than those derived in the WOA18 (10–11 $\mathrm{mmol\,m^{-3}}$). For these Arctic trajectories we adjusted the initial conditions to agree with the profiles of the WOA18 data. Plankton N biomass was initialised by splitting SINMOD's small and large phytoplankton N biomass evenly across the respective model size classes. For the initial plankton C biomass a constant C:N factor of 6.625 is imposed. We assume Chl-a:N = 0.75 to be a reasonable ratio for model initialisation on Jan 1st, and therefore calculated initial Chl-a biomass as $B_{\mathrm{Chl},j_p} = 0.75 \cdot B_{\mathrm{N},j_p} \cdot \theta$, with θ being the maximum Chl-a:N ratio (Tab. 3.1).

Initial detritus was derived from initial plankton. We assume that detrital organic matter equals a small fraction of plankton organic matter, and therefore derive $\sum_k M_{i,k} = 0.05 * \sum_j B_{i,j}$. Of the total detrital organic matter, $\sum_k M_{i,k}$, half is assumed dissolved, and the other half particulate. We stress that the sensitivity of the simulated phytoplankton and zooplankton biomass in spring, summer and autumn to variations of the initial conditions turned out to be extremely small. This is because of the prolonged period of darkness during the first months of the year; long enough to cause respective biomass to converge towards negligible concentrations in the range of $1 \cdot 10^{-8}$ $\mathrm{mmol\,C\,m^{-3}}$, which is given after approximately 40 days.

3.2.3 Model assessment

Monthly mean climatological DIN concentrations of WOA18 (Boyer et al., 2018; Garcia et al., 2019b) are considered for evaluating the model's performance with regard to spatio-temporal changes in nutrient acquisition along the pathways of the trajectories. On local scales, the ensembles of model solutions are assessed against the *in situ* measured DIN, Chl-*a*, POC, and PON concentrations of the respective sampling periods in the Fram Strait. The corresponding biovolume-size spectra derived from microscopic measurements are considered for an evaluation of the size-specific structural changes resolved by the model. In principle two different metrics are applied, the Root Mean Square Deviation (RMSD) for the tracer concentrations and a divergence function for the plankton size spectra.

Root Mean Square Deviation and Coefficient of Variation

In order to quantify the model's ability to reproduce the *in situ* observational data collected during the cruises, we calculated the Root Mean Square Deviation (RMSD) for DIN (nitrate + nitrite), Chl-*a*, POC and PON. We deliberately choose the notation RMSD instead of Root Mean Square Error, as it is not exclusively a model error, but also includes the variation between individual model trajectories. Accordingly, a wide spread of solutions of all trajectories will yield a RMSD that is higher than for cases where these solutions are very similar.

$$\mathrm{RMSD} = \sqrt{\frac{1}{N}\sum_{p}^{n_p}\sum_{t}^{n_t}\sum_{z}^{n_z}(\mathrm{mod}_{p,t,z} - \mathrm{obs}^*_z)^2} \tag{3.5}$$

with $\mathrm{obs}^*_z = \mathit{median}(\mathrm{obs})_z$ being the median of all individual samples at depth z across all days and $N = n_p + n_t + n_z$. The indices represent model trajectory (p), day-of-year (Julian day) (t), and depth (z). Model results were interpolated to depths where data are available. For both model setups (summer and autumn), we distinguish between trajectories according to their origins (Arctic and Atlantic).

Furthermore, we derived a measure that relates the RMSD to the corresponding mean of obs^*_z, similar to a coefficient of variation (CV):

$$\mathrm{CV} = \frac{\mathrm{RMSD}}{\mathit{mean}(\mathrm{obs}^*)} \tag{3.6}$$

The calculated RMSD and CV, as defined in Eqs. 3.5 and 3.6 include deviations from observations of every trajectory (ensemble member).

For the assessment of DIN profiles of the model, we additionally evaluate RMSD against the monthly mean climatological WOA18 data along the ensembles' mean of trajectories. The monthly WOA18 data are representative for the model trajectories with a 20 km radius. Here, the RMSD are calculated as:

$$\mathrm{RMSD} = \sqrt{\frac{1}{n_m}\frac{1}{n_z}\sum_{z}^{n_m}\sum_{z}^{n_z}(\mathrm{mod}_{z,m} - \mathrm{WOA}_{z,m})^2} \tag{3.7}$$

where $\mathrm{mod}_{z,m}$ and $\mathrm{WOA}_{z,m}$ are monthly averages over trajectories for model results and WOA data, respectively.

Integrated Quadratic Distance

The simulated plankton size spectra are evaluated against those derived from microscopic measurements by applying a non-parametric distance metric. We use the Integrated Quadratic Distance (IQD) (e.g., Thorarinsdottir et al., 2013). In our case it represents a divergence function that describes the difference between the cumulative distribution of normalized biovolumes of all size classes resolved by the model (F_{mod}) and observations (G_{obs}) derived from the normalized, continuous biovolume-size spectra (f_{mod} and g_{obs}):

$$\text{IQD}(F_{\text{mod}_{x,y}}, G_{\text{obs}}) = \int_s \left(F_{\text{mod}_{x,y}}(s) - G_{\text{obs}}(s)\right)^2 \, \mathrm{d}s \tag{3.8}$$

with s being the log-transformed equivalent spherical diameter ($s = \log_{10}(\frac{\text{ESD}}{1\mu\text{m}})$. The IQD is separately calculated for the phytoplankton and zooplankton spectra, distinguishing between the summer and autumn set ups as well as between the trajectories origins (Arctic and Atlantic). We note that this metric accounts for relative changes in the community size structure. Changes in biomass are exclusively assessed as RMSD described before, based on the Chl-a, POC, and PON data.

3.2.4 Model calibration

Model calibration was performed in two successive parameter estimation steps. In a first step, the sum of residuals between transformed data and model results was minimised, using a genetic algorithm for optimising parameter values. The transformation was determined by a linear mixed model, based on log-transformed, depth-resolved measurements of different types. We estimated a total of 17 parameters (indicated with * in Tab. 3.1) in the numerical optimisation, of which 12 parameters determine size dependencies in the model. This initial numerical optimisation produced unsatisfactory results with respect to cross-comparisons with monthly WOA18 data along the trajectories, which were not included in the cost function. Also, the simulated plankton size spectra poorly matched their observational counterparts. Perhaps crucially, as we later realised, the cost function was under-constrained by not imposing non-linear restrictions on combinations of the size-dependent parameters representing minimum nutrient quota, nutrient uptake rate, and photosynthetic rate, as described by Ward et al. (2017).

From a subsequent parameter sensitivity analysis we could identify six model parameters (described below) whose refined values significantly improved the model's ability to reproduce observational data. Therefore, in a second step, we used the parameter estimates from the initial optimisation and adjusted the values of these six parameters, such that the final model solutions show much better agreement with all four different data types, using the RMSD and IQD (Eqs. 3.5, 3.7, and 3.8) for assessing the model results of: the i) local tracer concentrations, ii) Chl-a remote sensing data, iii) monthly WOA18 climatology, and iv) the plankton size spectra.

For three of the six parameters, we have introduced values that further improve the model solutions in terms of comparability with the observed tracer concentrations: The minimum nitrogen quota of the autotrophs is set to $Q_{N,a}^{\text{min}} = 0.035$ $\text{mol N (mol C)}^{-1}$, the sinking velocity of detritus is adjusted to be $w_{\text{det}} = 10\ \text{m d}^{-1}$, and a single remineralisation rate of $r_{i,\text{DOM}} = 0.04\ \text{d}^{-1}$ is assigned to the hydrolysis and remineralisation of DOC and DON. Furthermore, the size dependency of photosynthesis is modified by refining the exponent of the maximum photosynthetic rate ($P_b^{\text{max}} = \text{-}0.08$). A quadratic mortality is introduced with a value of $m_2 = 0.05$

$\mathrm{m^3\,mmol\,C^{-1}\,d^{-1}}$ for the largest size class ($j = 9$). Finally, the impact of grazing is refined with a maximum potential prey capture rate $G_a^{\max}$ of 11 $\mathrm{d^{-1}}$.

This manual 'hand-tuning' of model parameters should be unnecessary, indeed, repeating the first optimisation step while including greater constraint upon parameters (based on Ward et al., 2017) may be all that is required to achieve satisfactory model outputs from a purely automated method. Alternatively, there may be need to include the WOA18 data into a single meaningful cost function, alongside the *in situ* measurements, or to perform a multi-objective optimisation with three or even four different metrics for the respective data types. The former of these two options would require additional research efforts while the latter would demand optimisation algorithms to be tested according to their usefulness for our special case. Improvement to the numerical optimisation routine continues, but goes beyond the scope of this study, so we therefore restrict our analysis to the model solutions identified with the two-step calibration approach.

3.3 Results

First, we consider the model solutions along the trajectories. The results are compared with the climatological monthly WOA18 data and with monthly Chl-a concentrations derived from satellite measurements. We then focus on comparisons of the local patterns between the HAUSGARTEN data and our model results, distinguishing between variations in vertical tracer distributions and horizontal heterogeneity. The simulated plankton size spectra in the Fram Strait are compared with the spectra derived from microscopic measurements. Finally, the temporal developments in the plankton community size structure, of net primary production and export are presented as they occur before, during and after the observation periods. In general, all model solutions are obtained with an identical set of parameter values and any differences between these solutions are due to variations in origin and pathway of the individual trajectories. Accordingly, these differences are largest between the four ensembles (summer Arctic, summer Atlantic, autumn Arctic, and autumn Atlantic) and smaller between individual members of an ensemble.

3.3.1 Data-model comparison: seasonal patterns of DIN and Chl-*a* concentrations along trajectories

By averaging over all members (trajectories) of an ensemble, we find major differences between the ensembles with respect to the timing and intensity of plankton growth and nutrient utilization. This can be well illustrated by comparing seasonal changes in monthly mean DIN concentration, which can also be assessed against the climatological nitrate concentrations derived from WOA18 data along the trajectories' pathways (Fig. 3.3). When compared with the WOA18 monthly means, the simulated profiles reproduce the vertical distribution and temporal development of DIN concentration in a similar manner. The major discrepancy is a delayed but then more rapid decline in DIN concentration during late spring/early summer in the model solutions. The timing of the DIN decline fits best in Atlantic trajectories of the autumn setup. While minimum concentrations in the WOA18 data sporadically fall below 1 $\mathrm{mmol\,m^{-3}}$ in all subsets, similarly low DIN concentrations are

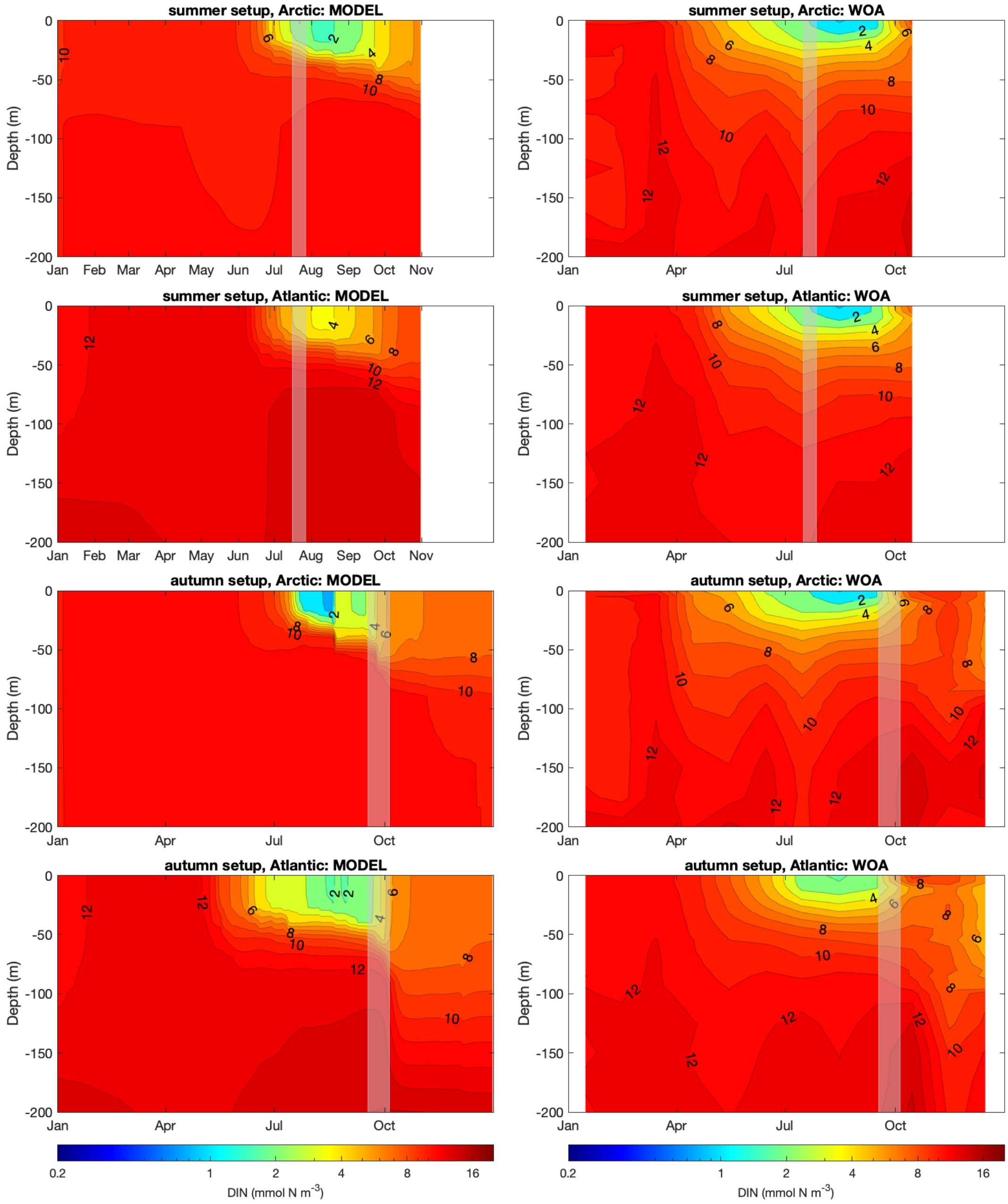

Figure 3.3: Fit of simulated DIN to corresponding World Ocean Atlas data. Model results (left column) were averaged over trajectories, discriminating between their Arctic and Atlantic origins. World Ocean Atlas data (right column, Boyer et al. (2018); Garcia et al. (2019b)) was extracted along the model trajectories for each day with a 20 km radius, then averaged over trajectories.

only reproduced in model solutions of the autumn setup simulations of the Arctic trajectories.

We furthermore compared simulated Chl-a to monthly mean concentrations derived from remote sensing along the model trajectories (20 km radius, limited to 2018) in Fig. 3.4. Although similar in magnitude, the timing of the spring bloom along the Arctic trajectories could not be resolved by our simulations. Model solutions of some individual trajectories exhibit a somewhat earlier bloom development, e.g. starting by the end of May. The overall delayed bloom development in the simulated Arctic trajectories leads to an overestimation of Chl-a concentration in June and July. These discrepancies in Chl-a decrease with time, without major deviations occurring in the late summer and early autumn months, when the simulated Chl-a concentrations become similar to the remote sensing data. We note that re-

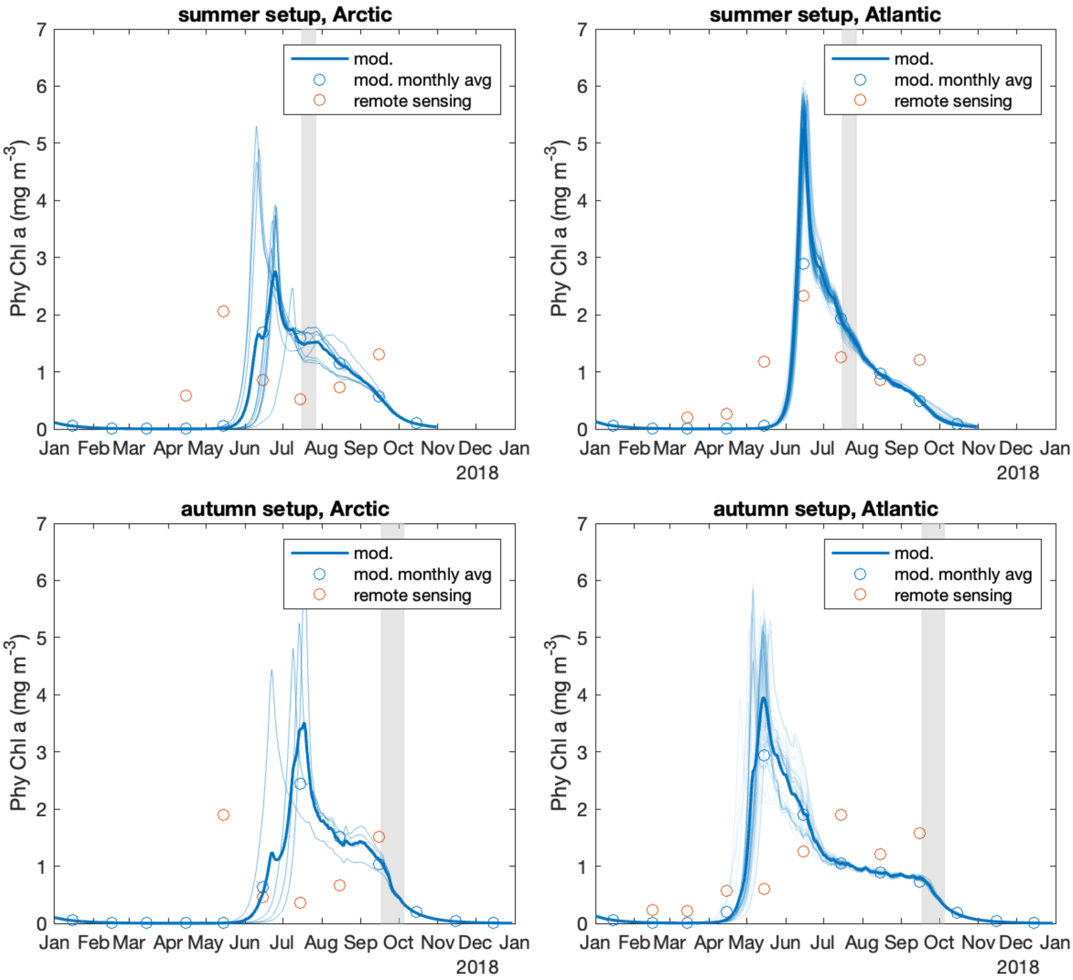

Figure 3.4: Comparison between simulated Chl-a with corresponding remote sensing data. Remote sensing data (red circles, monthly means (Sathyendranath et al., 2021)) were extracted along the model trajectories with a 20 km radius. Faint blue lines represent daily average chlorophyll concentrations over the upper 46 m for individual model trajectories and indicate the variability across trajectories. Solid blue lines represent their respective average over trajectories. Blue circles represent the monthly averages of the (depth and trajectory averaged) simulation results.

mote sensing estimates for April and May along the Arctic trajectories come with large uncertainties, as ice cover is still extensive during this period, which allows only few observations. These few observations may be biased as they stem from locations with thinner ice cover and therefore more light exposure.

For the Atlantic trajectories, the model solutions are in better agreement with the data. The monthly mean Chl-a concentrations in June compare well, with similarly good matches during the post bloom period in summer and during the autumn period. The best model representation can be assigned to the solutions of the summer setup of the Atlantic trajectories, as they also provide the best fit to the monthly mean WOA18 nitrate concentration data (Fig. (3.3)). Daily concentrations of simulated Chl-a can exceed the monthly averages by a factor up to two, with some considerable variations between trajectories during the exponential growth phase in June and July (Atlantic summer trajectories), and in May and June in the Atlantic autumn trajectories. We note that the earlier bloom development in the Atlantic autumn ensemble is due to the more southern positions of these trajectories in May, with higher light levels compared to the trajectories of the Atlantic summer setup. The remote sensing Chl-a data reveal a small but distinctive bloom in September that is less accentuated in the simulation results. The simulated Chl-a concentrations in September are rather a prolongation of the summer conditions. In November the simulated Chl-a concentrations of all trajectories, of all four ensembles, drop below 0.05 $\mathrm{mg\,m^{-3}}$. With the onset of the dark Arctic winter period all photoautotrophic growth becomes inhibited in our simulations.

3.3.2 Data-model comparison: local patterns in the Fram Strait

The ensembles of model solutions of the individual trajectories allow us to analyse the range of simulated biogeochemical tracer concentrations within the region of the HAUSGARTEN observatory in the Fram Strait during the periods of sampling in 2018.

Local vertical distributions

Within the target region, the model reveals greater variability in concentrations of DIN and Chl-a than in POC and PON (Fig. 3.5). In particular, the variations in POC and PON observed during the sampling campaigns (summer: 16-07–27-07.2018; autumn: 16-09–04-10-2018) are larger than those explained by the ensembles of model solutions.

We calculated the root mean squared deviation and coefficient of variation (Sect. 3.2.3) as a metric for model fit. Averaged values for the seasonal model setups are summarised in Tab. B1 in the SI. The model (in summer setup; no observational nitrogen data for autumn sampling campaign) slightly overestimated DIN concentrations in the upper 100 m. For the *in situ* comparison, smaller RMSDs and CVs indicate a slightly better fit in the Arctic trajectories than in those coming from the Atlantic. Simulated chlorophyll values in the summer setup in the upper 26 m seem overestimated, however several depth layers with single measurements (the single

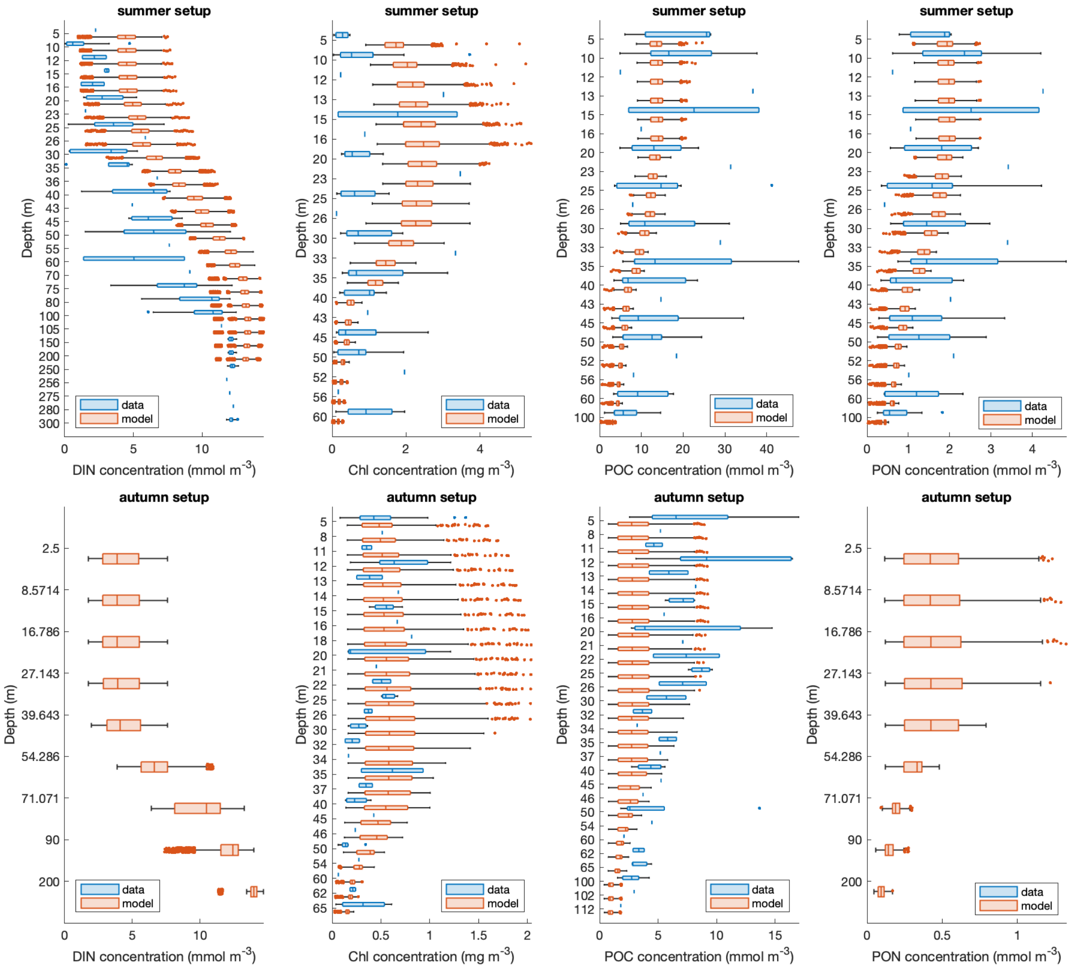

Figure 3.5: Fit of observed and simulated concentration depth profiles (without water mass distinction; data from Engel et al. (2019) and Torres-Valdés et al. (2019)). Model results were interpolated to corresponding observation depths and limited to the time frame when sampling was conducted (summer: 16-07–27-07.2018; autumn: 16-09–04-10-2018) ± 7 d. No DIN and PON observational data were available for the autumn period. In this boxplot representation, a box represents the interquartile range, the line in the box is the median, and whiskers represent the 99.3% confidence interval (assuming normally distributed data). Single vertical lines with missing boxes are drawn where only individual measurements were available.

vertical blue lines in the figure indicate a single observation at the respective depth) are occasionally well above the interquartile range of simulated Chl-a concentrations. The fit between 30–40 m matches well, and simulated concentrations for depths below 40 m are slightly underestimated. Model-data-fit of Chl-a concentrations in the autumn setup is particularly good, although the model produces outliers well above observed concentrations. Both, in summer and autumn, smaller RMSEs and CVs indicate a better fit for Atlantic trajectories. Concentrations of POC in summer and their simulated counterparts fit well, although simulated concentrations below 30 m are rather on the lower end of the observed range. Noticeably, the interquartile ranges of simulated values are smaller then of the observations. The POC data are consistently underestimated during the autumn setup. Simulated PON concentrations were in good agreement with observations in the summer setup (no data for autumn setup).

Horizontal heterogeneity in local tracers

Here we examine the statistical properties of our model solutions and put them into context of the observed horizontal variability (disparities in the measurements between sampling sites in the HAUSGARTEN), using local depth-averaged (upper 100 m) data and model results. The resolved spatial differences are mainly representative for the horizontal heterogeneity, although to some small extent they include short-term temporal variations during the sampling periods, in summer (12 days) and in autumn (19 days). Tab. 3.2 documents measures of central tendency as well as 95% confidence intervals (CI95) of concentrations of DIN, Chl-a, POC, PON, POC:PON, and $\mathrm{DOC_{SL}}$. The limits of the CI95 represent 2.5 % and 97.5 % quantiles ($Q_{0.025}$ and $Q_{0.975}$) derived from cumulative Kernel density estimates of the respective data, estimated using a diffusion based diffKDE (Pelz et al., 2023). Accordingly, the width of the interval is $\Delta\mathrm{CI95} = Q_{0.975}$ - $Q_{0.025}$.

In general, the medians and means of the model results fall into the 95 % confidence intervals of the observations. Comparisons between the simulated and observed mean concentrations reveal biases that correspond with the differences already seen in the vertical profiles (Fig. 3.5); the model's tendency to underestimate measured PON and POC concentrations while the means of the simulated DIN concentrations (between 8.2 and 9.8 $\mathrm{mmol\,N\,m^{-3}}$) are higher than the observational means (between 7.4 and 7.7 $\mathrm{mmol\,N\,m^{-3}}$). The simulated means of the POC:PON ratio are generally lower than observed, between 7.1 and 8.1 in the model results and 9.3 and 10.2 in the observations. With regard to the $\mathrm{DOC_{SL}}$ accumulation in summer and the subsequent drawdown until autumn, the model results compare well with the observed concentrations.

When comparing the 95 % confidence intervals, and as indicated by the upper CI95 limits ($Q_{0.975}$), a noticeable finding is that only in the solutions of the autumn-Arctic trajectories the simulated maxima in $\mathrm{DOC_{SL}}$ concentration ($Q_{0.975}$ = 4.7 $\mathrm{mmol\,C\,m^{-3}}$) exceed the observed range ($Q_{0.975}$ = 3.1 $\mathrm{mmol\,C\,m^{-3}}$). In all other cases, the $Q_{0.975}$ limits of the observations are higher than in the model solutions, which is even true in the case of DIN, although the model overestimates the observational means. Ultimately, the concentration range of simulated DIN, Chl-a, POC and PON, as well as the variations in POC:PON ratio, do not cover the full range ($\Delta\mathrm{CI95} = Q_{0.975}$ - $Q_{0.025}$) derived from the depth-averaged observational data. Thus, the model's ensemble solutions of the trajectories can explain only a portion of the observed horizontal variability of the HAUSGARTEN data.

To put the variability of the model solutions in relation to the variations found in the observations, we set the widths of the respective confidence intervals in relation to each other ($\Delta\mathrm{CI95_{mod}}/\Delta\mathrm{CI95_{obs}} \times 100$), see Tab. 3.2. For the summer period, the model trajectories approaching the Fram Strait from the north (Arctic) describe a greater portion of the observed horizontal variability (18–41%) than those of the Atlantic entering from the south (6–17 %). The relative portions are generally larger in autumn (39–76 %), in addition to the higher than observed $Q_{0.975}$ in the simulated $\mathrm{DOC_{SL}}$ concentration of the Arctic trajectories (254 %) mentioned before. There are two reasons why a larger portion of the horizontal variability within the target region can be explained by the model trajectories arriving in autumn. On the one

Table 3.2: Measures of central tendency and 95 % confidence limits of tracer concentrations, averaged over the upper 100 m, covering periods of observation. Median and the limits of the 95 % confidence interval (CI95) were calculated as quantiles (Q) from cumulative probability densities derived from Kernel density estimates: Median = $Q_{0.5}$, lower ($Q_{0.025}$) and upper ($Q_{0.975}$) limits of the CI95, and ΔCI95 = $Q_{0.975}$ - $Q_{0.025}$.

Variable / unit, subset	type	median	mean	$Q_{0.025}$	$Q_{0.975}$	$\Delta \mathrm{CI95}_{\mathrm{mod}} / \Delta \mathrm{CI95}_{\mathrm{obs}} \times 100$
DIN / mmol N m^{-3}						
- **summer** Atlantic	**observed**	**7.2**	**7.4**	**2.4**	**13.2**	
	simulated	9.8	9.8	8.8	10.6	17
- **summer** Arctic	**observed**	**7.3**	**7.7**	**3.6**	**13.5**	
	simulated	8.2	8.2	7.5	9.4	19
- **autumn** Atlantic	**observed**	–	–	–	–	
	simulated	7.2	7.1	6.3	7.8	–
- **autumn** Arctic	**observed**	–	–	–	–	
	simulated	8.0	8.0	7.6	8.3	–
Chl-*a* / mg Chl m^{-3}						
- **summer** Atlantic	**observed**	**1.4**	**1.5**	**0.1**	**3.3**	
	simulated	0.8	0.8	0.7	1.0	9
- **summer** Arctic	**observed**	**0.4**	**0.5**	**0.1**	**1.0**	
	simulated	0.8	0.7	0.5	0.9	33
- **autumn** Atlantic	**observed**	**0.4**	**0.4**	**0.3**	**0.6**	
	simulated	0.3	0.3	0.2	0.4	50
- **autumn** Arctic	**observed**	**0.4**	**0.4**	**0.1**	**1.0**	
	simulated	0.3	0.3	0.2	0.6	44
POC / mmol C m^{-3}						
- **summer** Atlantic	**observed**	**16.2**	**16.4**	**5.5**	**27.8**	
	simulated	7.6	7.5	6.8	8.1	6
- **summer** Arctic	**observed**	**7.1**	**7.9**	**1.7**	**15.0**	
	simulated	6.9	6.7	5.4	7.7	18
- **autumn** Atlantic	**observed**	**4.3**	**4.5**	**3.0**	**6.9**	
	simulated	2.0	2.1	1.2	3.0	46
- **autumn** Arctic	**observed**	**4.0**	**4.7**	**2.7**	**9.3**	
	simulated	2.3	2.3	1.1	3.8	39
PON / mmol N m^{-3}						
- **summer** Atlantic	**observed**	**1.8**	**1.8**	**0.6**	**2.9**	
	simulated	1.1	1.1	1.0	1.2	9
- **summer** Arctic	**observed**	**0.7**	**0.9**	**0.1**	**2.2**	
	simulated	0.9	0.8	0.6	1.0	19
- **autumn** Atlantic	**observed**	–	–	–	–	
	simulated	0.3	0.3	0.2	0.4	–
- **autumn** Arctic	**observed**	–	–	–	–	
	simulated	0.3	0.3	0.2	0.5	–
POC:PON / mol mol^{-1}						
- **summer** Atlantic	**observed**	**9.3**	**9.3**	**6.9**	**11.4**	
	simulated	7.0	7.1	7.0	7.3	9
- **summer** Arctic	**observed**	**10.4**	**10.2**	**5.0**	**14.9**	
	simulated	7.8	8.1	7.6	10.5	29
- **autumn** Atlantic	**observed**	–	–	–	–	
	simulated	6.6	6.6	6.4	6.8	–
- **autumn** Arctic	**observed**	–	–	–	–	
	simulated	6.7	6.7	6.5	7.0	–
$\mathrm{DOC}_{\mathrm{SL}}$ / mmol C m^{-3}						
- **summer** Atlantic/Arctic	**observed**[1]	–	**6.2**	**2.8**	**9.7**	
Atlantic	simulated	5.5	5.5	5.1	5.9	12
Arctic	simulated	5.9	5.7	4.2	7.0	41
- **autumn** Atlantic/Arctic	**observed**[1]	–	**2.5**	**1.9**	**3.1**	
Atlantic	simulated	1.9	1.9	1.4	2.3	76
Arctic	simulated	3.0	3.1	1.7	4.7	254

[1]: For the 95 % confidence limits we use the z-score together with the standard deviations published in von Jackowski et al. (2020b)

hand, the observed and simulated OM concentrations are generally lower in autumn than in summer and the widths of the CI95 become narrower. On the other hand, the model trajectories that arrive in autumn are associated with longer pathways, and thus more divergent histories of plankton growth, than the summer trajectories. This is consistent with the finding that the confidence intervals of the autumn data of Chl-a and POC in the WSC and the corresponding model results (Atlantic trajectories) are narrower than those associated with the EGC (Arctic trajectories). The autumn Atlantic trajectories expand over greater distances, covering a larger latitudinal range.

When comparing the horizontal heterogeneity observed with the spread of depth-averaged solutions obtained with the ensembles of trajectories, some additional insight can be gained by simple comparisons of the non-parametric probability densities (PD) obtained by Kernel density estimation, see Fig. B5 in the SI. These PDs illustrate the results presented above, particularly with regard to the different widths of the confidence intervals. However, they also show details such as bimodalities and the skewness in the PDs.

Local plankton community size structure

To evaluate how well the model resolves the size composition of the plankton community, we compare simulated plankton size spectra to continuous size spectra derived from microscopic counts and size measurements (expressed as equivalent spherical diameter, ESD), as described in Lampe et al. (2021), based on samples collected during summer and autumn. Fig. 3.6 shows that the overall slopes of simulated size-abundance spectra around the time of *in situ* sampling are in agreement with observations. Spectra of total biovolume by size are shown in Fig. B1 in the SI. Despite this satisfactory general characteristic, the observations in the size range between 4 and 40 µm clearly differ from the simulated almost log-linear relationship (with a nearly constant slope). The solutions of the autumn setup of the Arctic trajectories are the only exception, which instead show a higher abundance of cells with ESD below 2 µm in the simulations. This is all the more interesting because it is this setup in which the total abundance of phytoplankton (sum of all size classes) agrees well with the observations. In all other cases, total abundance is generally underestimated by our model solutions at times of the sampling period. Within the mentioned size range between 4 and 40 µm, the deviations can be as high as a factor of 10 in the trajectories of the summer setup, and even higher (almost factor 20) in the autumn setup of the Arctic trajectories. We note that the deviations in the size spectra are not accompanied by serious discrepancies compared to the PON and POC data shown before; data that were used as constraints for the total biomass.

3.3.3 Temporal variations in community size structure of the plankton

The relative size distributions and the corresponding total phytoplankton biomass of our model solutions resolve distinctive seasonal patterns (Fig. 3.7). The simulated blooms in the Arctic trajectories reveal two distinct peaks associated with the spring bloom. Some minor first peaks occur in early June (summer setup with 3 $\mathrm{g\,C\,m^{-2}}$) and mid-June, with approximately 2.5 $\mathrm{g\,C\,m^{-2}}$ in the autumn setup. These first peaks are followed by stronger peaks, only three and four weeks later in the summer and autumn setups of the Arctic trajectories respectively. Both maxima differ in their magnitude. Those trajectories that approach the Fram Strait in autumn yield maxima of around 8.5 $\mathrm{g\,C\,m^{-2}}$. In the summer setup, the total phytoplankton biomass reaches 6 $\mathrm{g\,C\,m^{-2}}$ during the bloom. According to our model results, the blooms along the EGC are later but more intense the further north they are, away from the HAUSGARTEN region. Apart from the double peaks, we obtain a characteristic that is consistent with this result for the Atlantic trajectories coming from the south. The difference is that the Atlantic trajectories starting further south show the earlier bloom, which is the case for the autumn setup with a maximum of almost 8 $\mathrm{g\,C\,m^{-2}}$.

Here, too, the later bloom in the Atlantic trajectories of the summer setup is accompanied by a higher intensity, reaching almost 10 $\mathrm{g\,C\,m^{-2}}$ in mid-June. These trajectories approach the Fram Strait in summer and therefore originate further

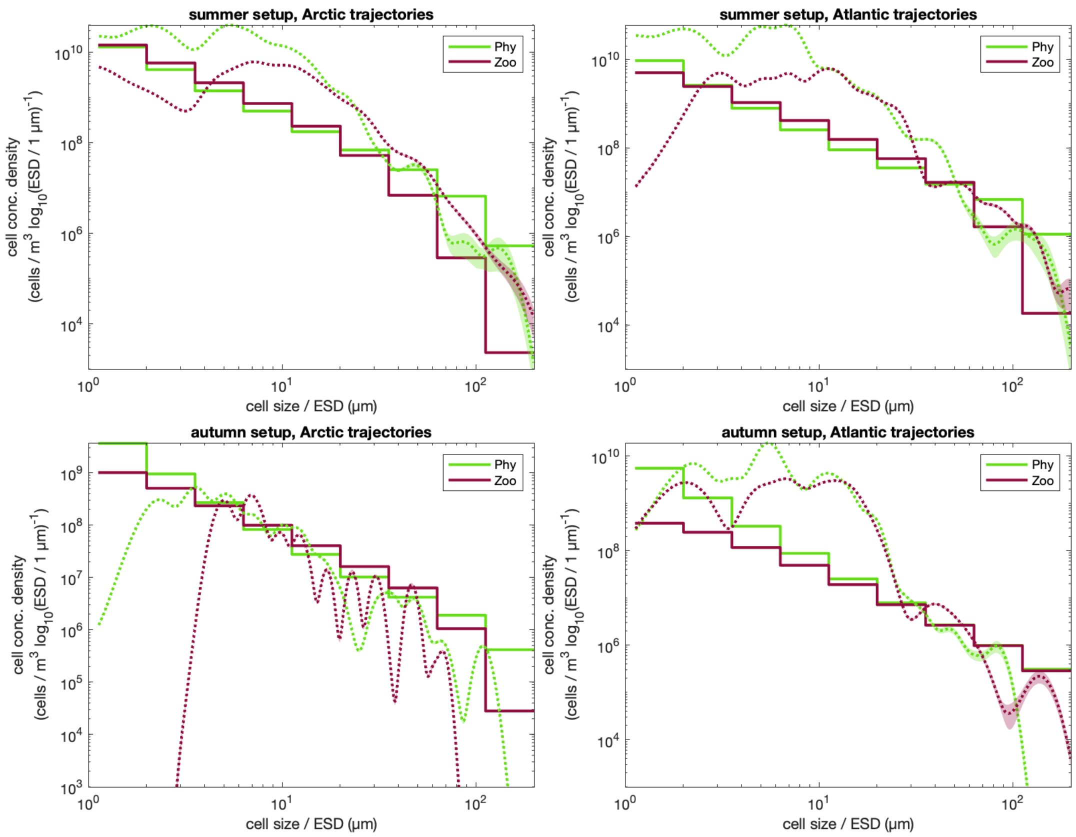

Figure 3.6: Comparison of simulated plankton size spectra (during sampling period) and observations Lampe et al. (2021). Model results were extracted for the sampling period ± 7 d and averaged over the upper 46 m. Cell concentrations were derived from C-biomass per size class divided by the respective carbon quota (cell conc. $[\mathrm{cells\,m^{-3}}] = B_{\mathrm{C},j}[\mathrm{mmol\,C\,m^{-3}}]/Q_{\mathrm{C}}[\mathrm{mmol\,C\,cell^{-1}}]$). Shown here are the mean cell concentration densities (over model trajectories or *in situ* samples) of phyto- and zooplankton, respectively, with shaded areas indicating the standard error. The dotted graphs represent the observations, the solid lines represent the simulated (size binned) spectra.

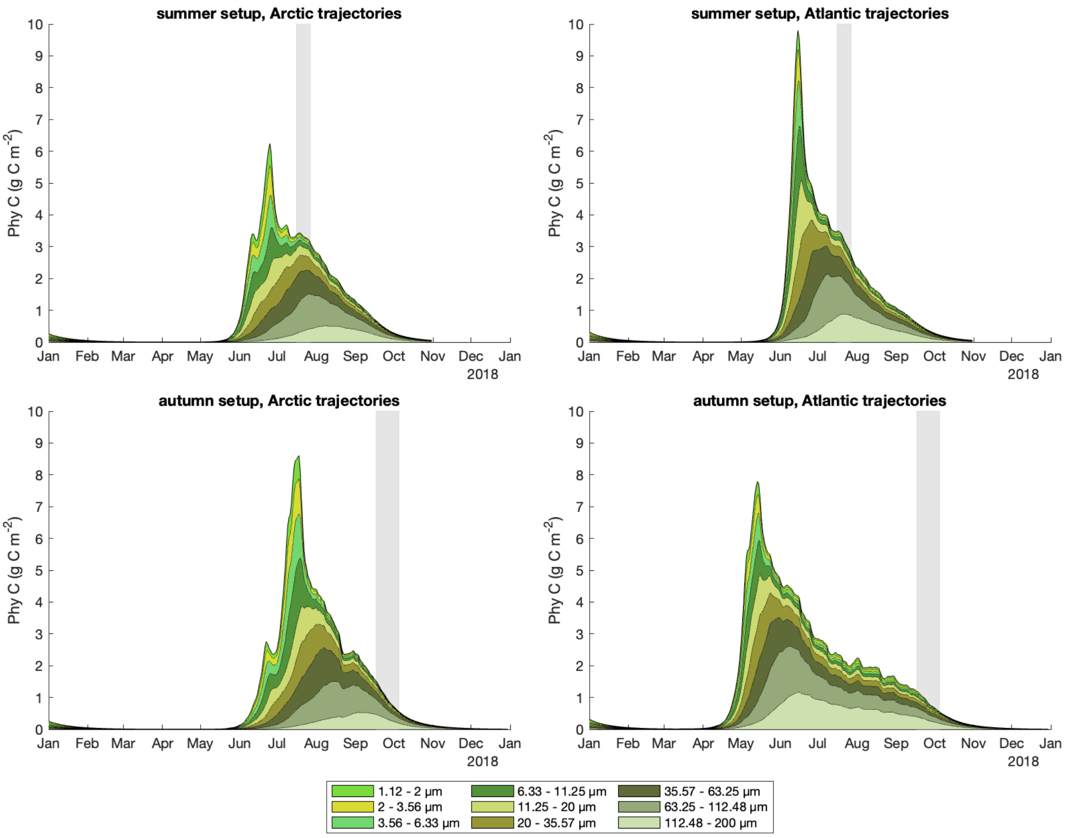

Figure 3.7: Integrated phytoplankton biomass per size class over time. C-biomass was integrated to 100 m depth and averaged by trajectory origin. Phytoplankton size classes are represented by green colours, and their respective sum equals total phytoplankton biomass.

north than the trajectories that do not arrive there until autumn. Thus, the summer Atlantic trajectories are always north of the corresponding autumn trajectories and they are thus exposed to lower light levels during the spring period. Overall, all the results together make it clear that it is predominantly the availability of light within the mixed layer that determines the temporal bloom development in these high latitudes in these simulations. We note that short-term (e.g. diurnal) stratification events remain unresolved in this model; a process that could counteract light-limitation of phytoplankton growth. Considering the predominant role of light exposure in the presence of short-term stratification (e.g. within ice and snow covered regions), this could explain why the simulated blooms are delayed in the Arctic trajectories, as previously described (Fig. 3.4).

The shift of plankton biomass towards larger size can be well demonstrated by depicting the temporal variations of the most dominant class (Fig. 3.8). The figure shows the size class that comprises the maximum carbon concentration of all 9 size classes, of the phytoplankton and the zooplankton respectively. In general, temporal changes in dominant size class show greater similarities between trajectories that share the same origin than between the different seasonal model setups. A common feature to all is that the early shift towards larger phytoplankton cells during the initial growth phase occurs under low light conditions, at times when the total biomass is still very small. According to the model's solution, the larger

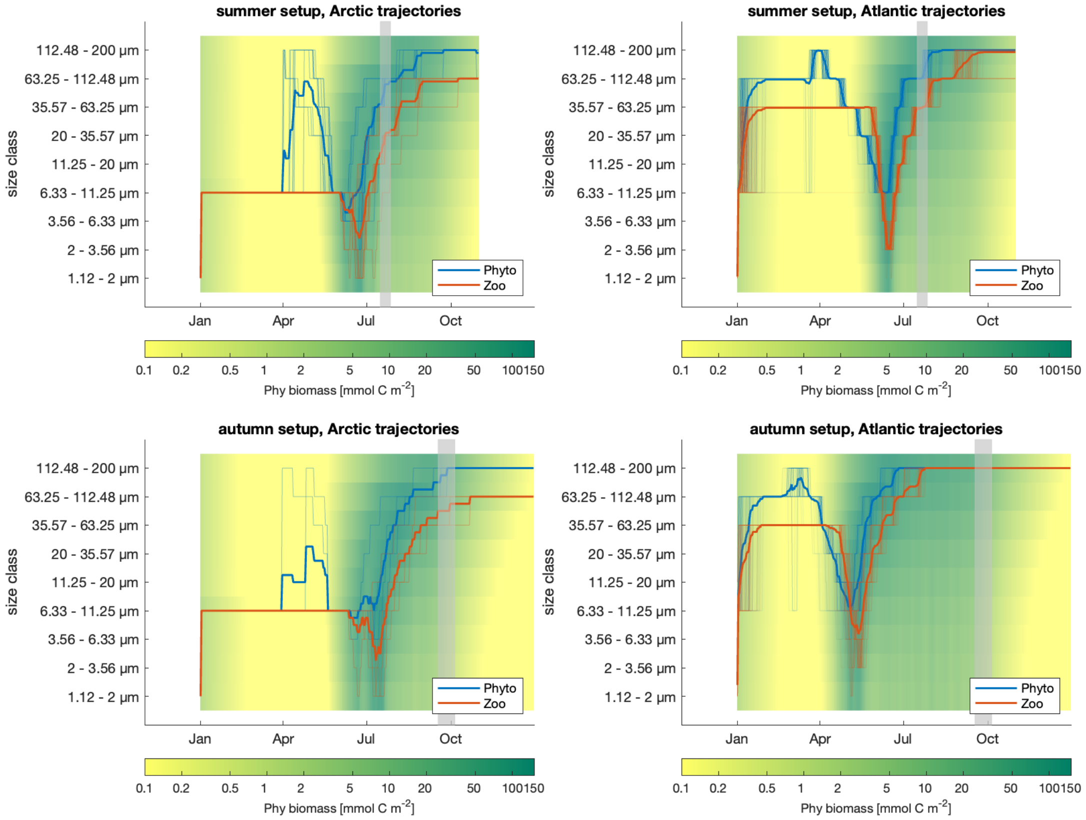

Figure 3.8: Size classes with maximum biomass for phytoplankton (blue) and zooplankton (orange) over time, integrated over the upper 46 m. Translucent lines represent single trajectories, solid lines the trajectory-mean (calculated from the respective size class indices). Background colours indicate the depth-integrated phytoplankton biomass per size class.

cells are more efficient than the smaller sized phytoplankton during this early prebloom period, because of a higher rate of nitrogen uptake per carbon fixed through photosynthesis (the maximum uptake rate $v^{\max}$ scales positively with size). This feature is of short duration, and as soon as light limitation becomes reduced, the advantage of larger cells vanishes. When total phytoplankton biomass increases in May, the biomass rapidly becomes dominated by phytoplankton of smaller size.

In the Arctic and the Atlantic trajectories, the zooplankton respond to the food availability in the smaller size range. Clearly, the temporal fluctuations in the predominant size class of zooplankton are a delayed response signal that follows the predominant size class of phytoplankton after about one to three weeks. Once zooplankton stocks sufficiently increased, the grazing progressively depletes populations of small phytoplankton. Following the peak in total biomass, more and more biomass shifted to larger size classes as total biomass declined. Most biomass end in the largest size class (112-200 µm), at times when total biomass has decreased below 2-3 mg C m^2. Apart from the Arctic autumn trajectories, most zooplankton biomass is found in the largest size class, roughly one month after phytoplankton have reached their maximum size class in the Atlantic trajectories. In the Arctic trajectories, the largest dominant sizes of the zooplankton range within the 8th size class (63 - 112 µm). This size class becomes dominant in September in the summer

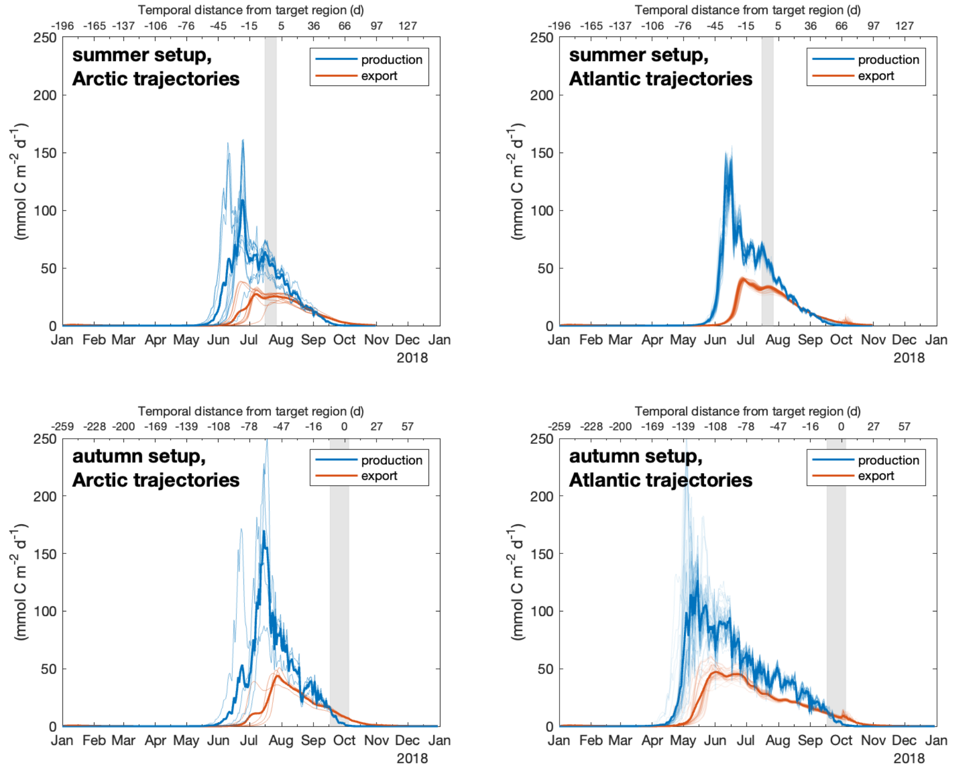

Figure 3.9: Depth-integrated carbon production (blue) and export (orange) at depth (100 m). Solid lines show the mean between all Arctic (left panels) and Atlantic (right) model trajectories. Translucent lines show the values of individual trajectories. Upper panels show the results from the summer model setup, lower panels from autumn setup. In situ sampling was conducted during timespans highlighted in grey.

setup and in October in the autumn setup.

3.3.4 Temporal variations in net primary production and export of Carbon and Nitrogen

Our analyses of the annual, depth-integrated net primary production (NPP), the POM export at 100 m, and the corresponding export efficiency along the model trajectories reveal clear differences between the ensembles (Tab. 3.3). The temporal variations are more pronounced in NPP than in export, also revealing greater variability in the Arctic than in the Atlantic trajectories (Fig. 3.9).

With 101 $\mathrm{g\,C\,m^{-2}\,yr^{-1}}$ we find the highest productivity in the Atlantic trajectories of the summer setup, where light availability is highest. Compared to the Arctic trajectories, the NPP in the trajectories of Atlantic origin is generally higher (Tab. 3.3). Despite the overall lower NPP, the spatio-temporal variability in NPP is higher along the Arctic trajectories, in particular at times when the bloom begins, which is due to extensive fluctuations in temperature rather than in surface irradiance (see Fig. 3.2). Generally, our model results yield lower C:N ratios in yearly production rates in the Atlantic ensembles (summer: 7.9; autumn: 7.8) than in the Arctic ensembles (summer: 8.7; autumn: 9.3). Surprisingly, and despite the previously mentioned differences, the ensemble mean values of NPP appear to have converged during the observation periods and show similar values between the Atlantic and Arctic trajectories: Arctic (NPP = 54 ± 11 and 5 ± 4 mmol $\mathrm{C\,m^{-2}\,d^{-1}}$, summer and autumn respectively), Atlantic (NPP = 56 ± 8 and 6 ± 4 mmol $\mathrm{C\,m^{-2}\,d^{-1}}$).

Generally, export is closely related to NPP and follows it with a lag of 2–3 weeks. The rapid increase in productivity in spring is not immediately reflected in exports, suggesting that much of the spring production remains in the upper ocean and is recycled rather than being rapidly exported to depth. The high temporal variability in the export in Arctic trajectories is linked to the high variability in NPP. Furthermore, the spatial variability in NPP, that is strongly expressed in Atlantic trajectories of the summer setup, propagates to export. During September, export begins to exceed local production. The productivity is always higher in the Atlantic than in the Arctic trajectories, which translates into higher annual export accordingly, with a maximum of 50 g $\mathrm{C\,m^{-2}\,yr^{-1}}$ in the Atlantic summer setup. As for the NPP, the C:N ratios of the yearly export rates are lower for the Atlantic ensembles (7.4 for both, summer and autumn setups) than in the Arctic counterparts (summer: 7.9; autumn: 8.4). Although not as striking as in case of NPP, during the sampling periods, the export flux at 100 m do not differ much in Arctic (Export = 24.8 ± 3.6 and 10.4 ± 2.8 mmol $\mathrm{C\,m^{-2}\,d^{-1}}$ in summer and autumn respectively) and Atlantic (Export = 32.5 ± 1.5 and 9.1 ± 1.8 mmol $\mathrm{C\,m^{-2}\,d^{-1}}$) trajectories. These differences are small despite the preceding developments in export flux exhibit larger differences (Fig. 3.9).

The efficiency of export integrated over the productive period is slightly higher in the solutions of the Atlantic ensembles, indicating less efficient export and thus more retention and recycling takes place in Arctic trajectories. Differences in the pe-ratio of C and N are, albeit small, caused by the variable stoichiometry in the model. The model solutions indicate some marginally more efficient export of N than of C. We note that the rates assigned to remineralisation in our model are identical for C and N, which means that the difference here only reflects the higher C:N ratio of the OM that is remineralised. Instant, daily pe-ratios show a considerable temporal and spatial variability (Fig. B4 in the SI). While in the beginning of the productive period pe-ratios are close to 0, they increase to 0.4–0.6 in Arctic trajectories and 0.4–0.8 in Atlantic trajectories during the summer sampling period and eventually exceed 1 during the autumn sampling period. An instant pe-ratio greater than one

Table 3.3: Time and depth-integrated (100 m) net primary production, export of carbon (C) and nitrogen (N) at 100 m, and export efficiency (pe-ratio). Values are the model ensemble means ± standard deviation.

Data subset (ensemble)	Production [$\mathrm{g\,m^{-2}\,yr^{-1}}$] C	N	Export [$\mathrm{g\,m^{-2}\,yr^{-1}}$] C	N	pe-ratio C	N
summer/Arctic	53.14±6.34	7.11±0.87	22.16±3.17	3.23±0.46	0.42±0.01	0.45±0.01
summer/Atlantic	61.04±0.93	9.01±0.19	28.02±0.65	4.40±0.14	0.46±0.01	0.49±0.01
autumn/Arctic	69.04±1.39	8.69±0.44	27.37±2.38	3.79±0.38	0.40±0.03	0.44±0.02
autumn/Atlantic	100.96±5.67	15.04±0.77	50.15±2.73	7.85±0.43	0.50±0.01	0.52±0.01

is due to the continuation of export, here at 100 m, of POM that has already been produced before, while at the same time the actual productivity gradually ceases.

3.4 Discussion

As water parcels move through space over time, they are subject to varying environmental conditions, such as light availability, temperature, and water column stratification. Studies in the HAUSGARTEN observatory that present time series of biogeochemical measurements (e.g., Nöthig et al., 2015; Engel et al., 2019; Nöthig et al., 2020) reveal substantial variability in the data, differences between individual sampling sites during limited periods of observation. Some part of the variability seen in the local observations can be attributed to water masses that are passing by the sampling stations and are thus 'snapshots' of the current situation. To relate observed changes, e.g. in plankton composition, to changes in local physical and biogeochemical conditions is difficult, since the specific conditions to which the communities were exposed before their arrival in the observation region remain unresolved. The Lagrangian modelling approach allowed us to investigate bottom-up and top-down processes that determine seasonal changes along trajectories. With our simulations of distinct ensembles of trajectories we could analyse a large suite of model solutions (with different histories in space and time) and examine how these can contribute to the variability seen in the pelagic ecosystem at HAUSGARTEN in the Fram Strait at times of observation. Furthermore, we determined the spatio-temporal variations along the major trajectories passing the Fram Strait.

This section discusses the representativeness and usefulness of our model solutions. We address the insights gained on the different distributions (spatial and temporal) of the trajectories, focusing on NPP and POC export. We further elucidate aspects of the compositional variations of the plankton. The differences in DOM and POM, as resolved by our simulations, are discussed in relation to the concentrations typically observed in the Fram Strait. Finally, we explain the limitations of the model as well as potential improvements.

3.4.1 Influence of trajectory origin and evolution on NPP and POC at HAUSGARTEN sites

Trajectories emanating from the North Atlantic cover a wide latitudinal range of 15°or up to 1930 km in summer and as much as 17°(2100 km) in autumn. The Arctic trajectories cover only a range between 5.5°(650 km) and 6.7°(830 km) latitude (autumn and summer setup respectively, see Fig. 3.1. In Sect. 3.3.2 we show that a significant part (6–17 % in Atlantic and 18–41 % in Arctic trajectories of the summer setup; 46–76 % in Atlantic and 39–44 (254) % in Arctic trajectories of the autumn setup) of the variability in tracer concentrations observed locally at HAUSGARTEN is caused by differences in the pathways of water parcels passing the HAUSGARTEN sampling sites. Here we discuss how our estimated rates of NPP and export in the Fram Strait compare with those derived from observations and other modelling studies, and document how these rates change along the trajectories resolved in our model.

Our model results of annual NPP are within the range of rates reported for the Fram Strait from observations and modelling studies. The ensemble means of NPP in the Fram Strait of the Atlantic trajectories are 61.0±0.9 (summer setup) and 101.0±5.7 (autumn setup) $\mathrm{g\,C\,m^{-2}\,yr^{-1}}$ (Tab. 3.3). The corresponding Arctic trajectories (along the EGC) yield mean rates that are slightly lower, 53.1±6.3 (summer setup) and 69.0±1.4 (autumn setup) $\mathrm{g\,C\,m^{-2}\,yr^{-1}}$. Arrigo and Van Dijken (2011) derived an average NPP for the Greenland Sea of 86.0±6.5 $\mathrm{g\,C\,m^{-2}\,yr^{-1}}$ from long-term remote sensing analysis between 1998 and 2009, while Hop et al. (2006) reported an average rate of 80 $\mathrm{g\,C\,m^{-2}\,yr^{-1}}$ for the Fram Strait. Similar to our results, Wassmann et al. (2010) found GPP to be higher in the eastern than in the western part of the Fram Strait in their SINMOD simulations (east: GPP ≈ 130

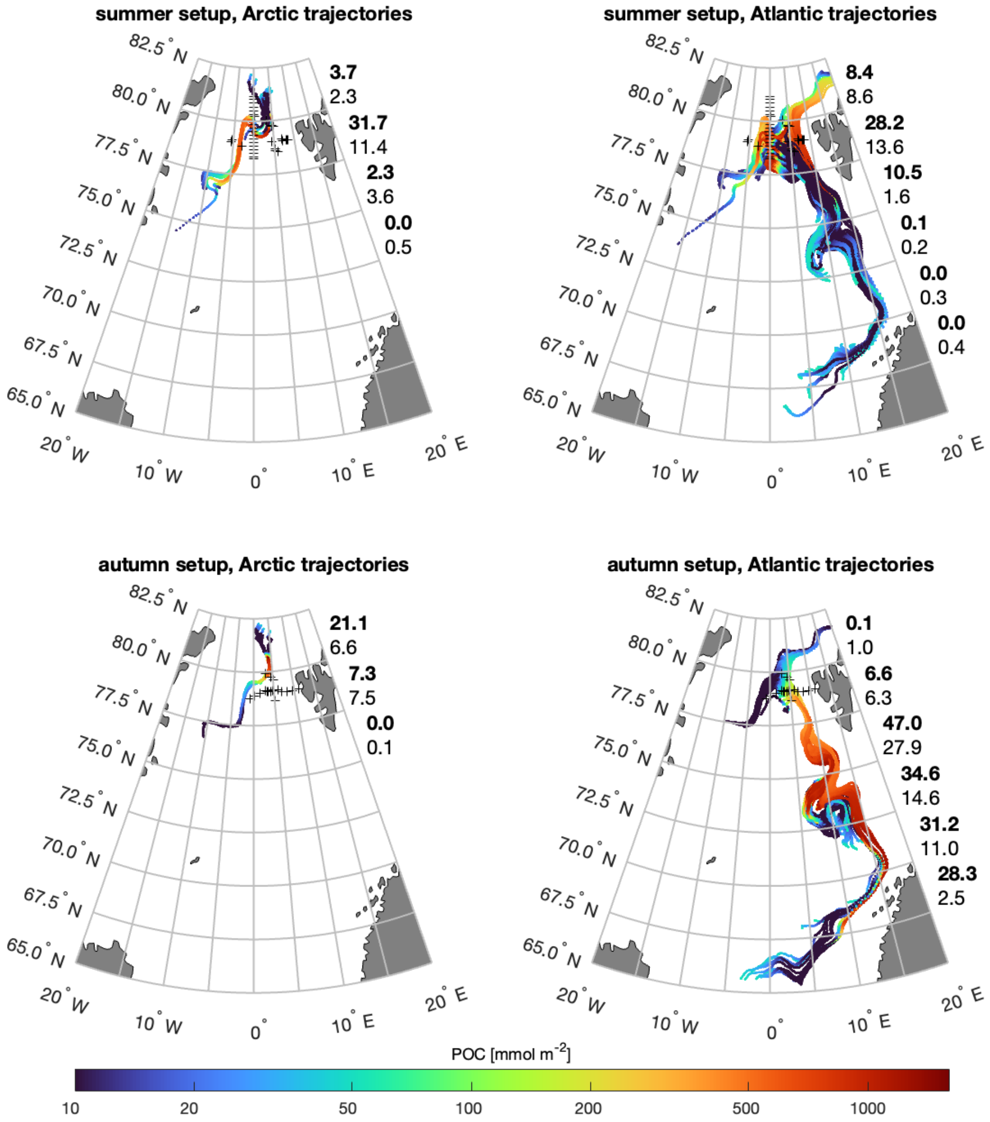

Figure 3.10: Depth-integrated (100 m) POC concentrations along model trajectories. Numbers in bold font on the right sides represent average Carbon NPP (integrated over upper 100 m [$\mathrm{mmol\,C\,m^{-2}\,d^{-1}}$]) fluxes within latitude bins of 2.5°, numbers in regular font represent carbon export at 100 m depth [$\mathrm{mmol\,C\,m^{-2}\,d^{-1}}$]. *In situ* sampling locations at HAUSGARTEN are marked with '+' symbols.

$\mathrm{g\,C\,m^{-2}\,yr^{-1}}$, and west: 50 $\mathrm{g\,C\,m^{-2}\,yr^{-1}}$). NPP estimates obtained in SINMOD simulations were considerably lower, as documented in Vernet et al. (2021), and yield an NPP of 33.2 $\mathrm{g\,C\,m^{-2}\,yr^{-1}}$ in the EGC dominated region of the Fram Strait. For the same region, even lower rates of NPP (11 $\mathrm{g\,C\,m^{-2}\,yr^{-1}}$) were derived from their remote sensing data analysis, which is roughly equivalent to only 18 % of NPP in our results.

Peaks in productivity occur well before the trajectories reach HAUSGARTEN, as shown in Sect. 3.3.4. The time difference is shorter for the summer setup (20–40 days for Arctic; 30–40 days for Atlantic trajectories) than the autumn setup (ca. 70 days for Arctic and 130–140 days for Atlantic trajectories). During these productivity peaks, our model estimates the maximum daily NPP (integrated to 100 m) around 150–250 $\mathrm{mmol\,C\,m^{-2}\,d^{-1}}$, which is within the range reported by Forest et al. (2010) (maximum GPP: 1.5–2.3 $\mathrm{g\,C\,m^{-2}\,d^{-1}}$, thus ca. 125–190 $\mathrm{mmol\,C\,m^{-2}\,d^{-1}}$), but considerably higher than estimations around 0.6 $\mathrm{g\,C\,m^{-2}\,d^{-1}}$ (thus 50 $\mathrm{mmol\,C\,m^{-2}\,d^{-1}}$) for the EGC-influenced sector (Vernet et al., 2021). While the timing of the productivity increase is relatively homogeneous within Atlantic trajectories, it is much more variable for Arctic trajectories. Although the average of Arctic trajectories has a slightly later maximum than in the Atlantic trajectories, productivity peaks already in early June in few Arctic trajectories (Fig. 3.9). Arctic trajectories are subject to variations in sea ice cover, while Atlantic trajectories remain ice free throughout the simulated period. Sea ice strongly influences the light available in the water column, which is reflected in the high variability in the start date of the spring bloom in Arctic trajectories in the summer setup. Similarly, Banas et al. (2016) found that in the East Bering Strait, bloom timing was controlled mainly by light availability and the light availability was in turn controlled by ice cover in regions under high ice influence, whereas in the ice-free regions, a composite of surface light availability and diffusivity correlated to the bloom timing. Long-term remote sensing observations of Chl-*a* concentrations between 1998 and 2012 typically show maxima around May or June in the EGC and around June or July in the WSC influenced region of the Fram Strait (Nöthig et al., 2015). Furthermore, Vernet et al. (2021) report the initiation of the bloom between late May and mid-June for the North-East region off Greenland, which is similar to our simulations.

The temporal delay in NPP and export signals leads to the accumulation of POC at different times and distances from the target region, as shown in Fig. 3.10. In the summer ensembles, POC concentrations reach their highest levels just before entering the HAUSGARTEN region (*in situ* sampling stations are marked with black '+' signs). During this time, within the 77.5°–80°N latitude bin, NPP (31.7 $\mathrm{mmol\,C\,m^{-2}\,d^{-1}}$ in Arctic and 28.2 $\mathrm{mmol\,C\,m^{-2}\,d^{-1}}$ in Atlantic trajectories) and export (11.4 and 13.6 $\mathrm{mmol\,C\,m^{-2}\,d^{-1}}$) average fluxes are highest. Export exceeds NPP once the Atlantic trajectories leave the target region. In contrast, in the autumn setup the maxima in POC concentration, NPP, and export occur before the Atlantic trajectories enter the target region. In the Atlantic-autumn ensemble, we observe the highest POC concentrations about 5° south of HAUSGARTEN, and the concentrations have decreased considerably by the time the trajectories reach the region. Similarly, in the Arctic-autumn ensemble, NPP and POC reach their highest values before the trajectories approach the HAUSGARTEN region, but the distance is shorter than in the Atlantic counterparts and export is highest in the 77.5°–80°N latitude bin.

Although our estimations of NPP and tracers (see Sect. 3.3.2 and 3.4.3) are within the range of observations, our model considerably overestimates export. The annual average of POC export fluxes at HAUSGARTEN between 2000 and 2013, as observed with sediment traps in 200 m depth, ranged from 0.16–0.18 $\mathrm{mol\,C\,m^{-2}\,yr^{-1}}$Salter et al. (2023), which is equivalent to 1.92–2.16 $\mathrm{g\,C\,m^{-2}\,yr^{-1}}$. Bauerfeind et al. (2009) reported similar values, with POC fluxes between 1.6–2.5 $\mathrm{g\,C\,m^{-2}\,yr^{-1}}$ measured with sediment traps in 200–300 m depth. However, our model estimations at the 100 m depth horizon are 10–20 times higher than these observations. Our estimations for POC export at 300 m depth are about half of those simulated at 100 m (Summer Arctic: 12, Atlantic: 16; Autumn Arctic: 15, Atlantic: 28 $\mathrm{g\,C\,m^{-2}\,yr^{-1}}$) and still significantly higher than the sediment trap observations. Considerably higher values, around 24–34.5 $\mathrm{g\,C\,m^{-2}\,yr^{-1}}$, have been reported from short-term sediment trap deployments in the seasonal ice zone North off Svalbard (Dybwad et al., 2021), being closer to our estimates. Maximum export rates in our simulations of 30–40 $\mathrm{mmol\,C\,m^{-2}\,d^{-1}}$ occur 10–20 days before Arctic and Atlantic trajectories reach HAUSGARTEN in the summer setup. For the autumn setup, maxima were higher (ca. 50 $\mathrm{mmol\,C\,m^{-2}\,d^{-1}}$) and at a greater temporal distance from the sampling region (50 d for Arctic, 110 d for Atlantic trajectories). These rates are again considerably higher than export rates observed during high carbon export events, which range between 20–50 $\mathrm{mg\,C\,m^{-2}\,d^{-1}}$(Cardozo-Mino et al., 2023), i.e. 2.4–4.2 $\mathrm{mmol\,C\,m^{-2}\,d^{-1}}$.

We note that the apparent overestimation of POC export by our model occurs even though productivity rates and tracer concentrations lay within the ranges we expect from observations, and even though we assume a sinking velocity for detritus of 10 $\mathrm{m\,d^{-1}}$. Using a larger detritus sinking velocity of 100 $\mathrm{m\,d^{-1}}$, as is often assumed in the literature (e.g., Bauerfeind et al., 2009; Iversen, 2023), leads to further general overestimation of vertical POC export and underestimation of POC concentrations in the water column during the sampling period, as shown in Fig. B6 in the SI.

3.4.2 Variations in plankton community structure

The Lagarangian ecosystem model outlined above divides the phytoplankton and zooplankton populations into a number of discrete size-classes, with plankton ecophysiological traits determined by organism size, in line with observed allometric relationships (e.g., Edwards et al., 2012). In line with previous size-structured plankton ecosystem models, our Lagrangian model captures the observed equivalence of phytoplankton biomass in logarithmically-spaced size classes (e.g., Schartau et al., 2010; Brewin et al., 2014). This behaviour is a robust feature of size-based marine ecosystem models that include coupled phytoplankton and zooplankton size classes (Ward et al., 2014), and occurs because the biomass within each phytoplankton size class is restricted by top-down grazing pressure from their respective zooplankton predators (Armstrong, 1994).

In-situ observations of spring bloom and summer phytoplankton populations in Arctic waters have been described in several publications but are either limited to certain species or limited to specific periods (e.g., Eilertsen et al., 1989; Gradinger and Baumann, 1991; Hasle and Heimdal, 1998; Degerlund and Eilertsen, 2010; Nöthig et al., 2015; Kubiszyn et al., 2017). In the Fram Strait bloom biomass is usually dominated by either colony-forming *Phaeocystis* (0.1–2 mm, Rousseau et al.

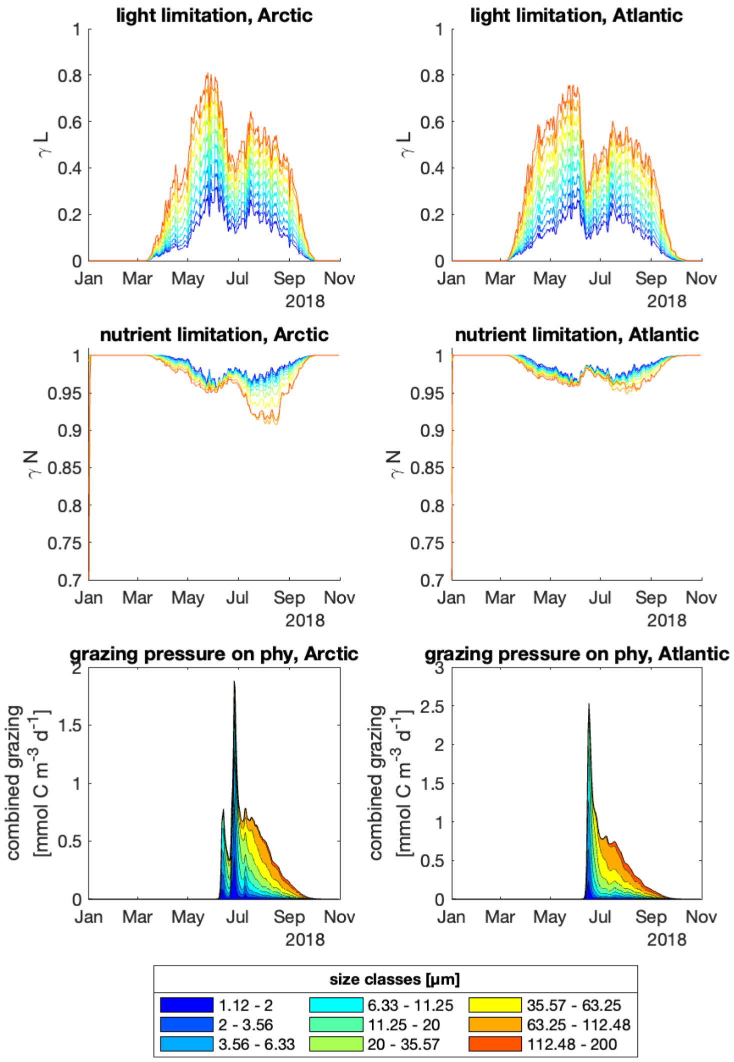

Figure 3.11: Factors controlling the size composition of phytoplankton stocks in the summer model setup. The photosynthetic rate is limited with a light limitation term γL (Eqs. B.8, B.11). The nutrient limitation term γN limits the light saturated photosynthesis rate P_j^{sat} (Eq. B.7). Grazing pressure describes the combined grazing of all zooplankton on each phytoplankton size class.

(2007)), also occurring as small flagellates (ca. 2.5 µm), or/and diatom species of the genus *Thalassisira* (ca. 20 µm) or *Chaetoceros* (ca. 7 µm), accompanied by varying amounts of pennate diatoms (ca. 5–15 µm) such as *Nitzschia*, *Navicula*, and *Fragilariopsis*. Dinoflagellates (ca. 5–20 µm) and other flagellate species (ca. 2–5 µm) are a minor contributing group during spring. In the course of the late summer to autumn a variety of flagellates become more prominent, for instance Hegseth and Sundfjord (2008) found a bloom of *Emiliania huxleyi* (ca. 4–7 µm). In the Fram Strait very large cells (up to ca. 180 µm) of the genera *Rhisosolenia* and *Proboscia* were also found during autumn together with small flagellates (Menge, 2019).

Although our model underestimates abundance and biovolume of small - intermediate size classes compared to observations, it resolves the relative shift of biomass from smaller to larger size from summer to autumn observed in Lampe et al. (2021). We can link the variability in plankton size structure to bottom-up and top-down controls that have varying effects throughout the productive season, as seen in Fig. 3.11.

Early in the productive season, when nutrient concentrations are high but light availability is low, bottom-up processes dominate. The light limitation term γ_{L} limits the photosynthetic rate P_j (P_j is the product of the light saturated photosynthetic rate P_j^{sat} and γ_{L}). This allows for growth of large phytoplankton at low light levels, but only for inefficient growth of small phytoplankton, leading to the pre-bloom peak in phytoplankton size seen in Fig. 3.8. By the beginning of May, when surface irradiance (I^{surf}) exceeds $5 \cdot 10^6\ \mu\mathrm{Ein}\,\mathrm{d}^{-1}\,\mathrm{m}^{-2}$ in the summer setup, the photosynthetic rate reaches 40% (Arctic) to 60% (Atlantic) of P_j^{sat} in larger phytoplankton, but only below 10% in the smallest size class. As the light availability increases, the effects of light limitation decrease. Since the maximum photosynthetic rate P_j^{max} decreases exponentially with cell size, this gradually cancels out the effect of fading size dependent light limitation, allowing rapid growth of small phytoplankton and causing a relative shift of biomass to smaller sizes until the peak of the bloom is reached.

The light saturated photosynthetic rate P_j^{sat} is controlled by a nutrient limitation term $\gamma_{\mathrm{N},j}$, which affects larger cells stronger than smaller cells. However, $\gamma_{\mathrm{N},j}$ never decreases below 0.9, meaning P_j^{sat} is never down-regulated to less than 90% of the maximum photosynthetic rate P_j^{max} due to lack of nutrients. This fits to DIN concentrations in our simulations not falling below 2 $\mathrm{mmol\,m^{-3}}$ in the summer setup, never fully exhausting nutrient supply.

Once sufficient zooplankton stocks form, the plankton size structure becomes subject to increasing top-down control through zooplankton grazing. Increasing phytoplankton stocks allow the growth of zooplankton, who graze on phyto- and zooplankton. As soon as zooplankton biomass increases, the phytoplankton biomass peak collapses due to the now increasing loss though grazing. Zooplankton grazing is size dependent with an optimum predator:prey size ratio (δ_{opt}) of 1:10. When the phytoplankton bloom peaks, most biomass is fixed in small size classes. These size classes are then preferentially grazed upon by zooplankton, as grazing on the larger size classes is less efficient. This exhausts smaller phytoplankton faster than larger phytoplankton, despite the larger P^{max}, causing a relative shift towards larger size classes again. As the phytoplankton stocks decrease and the relative size structure shifts towards larger sizes, zooplankton size follows due to the grazing preferences.

The size structure of the protist planktonic community is an important indicator whether retention or export of accumulated OM is dominant in a system. Communities dominated by large diatoms with silica frustules tend to have high export rates as upon being grazed, they form larger fecal pellets that sink faster (Cael et al., 2021) and are relatively dense and less accessible to microbial degradation (Hansen et al., 1996). More recycling as opposed to export is observed in systems that are dominated by picoplankton (Azam et al., 1983). Therefore, unravelling dynamics in the microbial food web is essential to understand mass transfer of organic matter to higher trophic levels and subsequent recycling or export in the Fram Strait.

3.4.3 Variability in OM pools

We can link the spatial variability in observed organic matter pools in the HAUSGARTEN region during summer and autumn to the different Lagrangian pathways (histories) in physical conditions (predominantly light) and ecological dynamics (plankton interaction) each of the simulated trajectories experienced during their voyage.

In our model, the partitioning of organic carbon (C_{org}) into living biomass, detritus and DOC is largely controlled by the size structure of the plankton community. Total POC increases in spring until the peak of the bloom, and is mainly made up from phytoplankton biomass. In the following weeks, this leads to an increase in both, detritus and DOC_{SL}. Since the partitioning of C_{org} (generated through background mortality and sloppy feeding) into the dissolved or particulate phase is size dependent (see equations B.25, B.26), small cells are partitioned roughly 80:20 into DOC:detritus, while the largest 20:80. As the plankton biomass is dominated by smaller size classes during the spring bloom, the DOC to detritus production is at similar levels at this time. With the increase in phytoplankton biomass, zooplankton stocks increase, and their grazing controls phytoplankton stocks. Grazing leads to further increase in detritus (in addition to background mortality), again with a size-dependent partitioning of DOC and detritus. Furthermore, grazing changes the size structure of the plankton, as the smaller plankton are preferentially grazed (the optimal size ratio between predator and prey δ_{opt} is 10:1), which increases carbon allocation into detritus. As a consequence, export of organic matter increases, since only detritus can be exported via sinking. Compared to the model results, observations in the HAUSGARTEN area for summer and autumn 2018 showed roughly two times higher concentrations for POC but similar ones for DOC_{SL} (Tab. 3.2). One process not resolved in the model is the partitioning of DOC into POC due to bacterial uptake and the formation of gel-like particles by aggregation processes, e.g. transparent exopolymere particles (TEP). TEP contributed on average 1.78 $\mathrm{mmol\,C\,L^{-3}}$ in summer (von Jackowski et al., 2020a), which would constitute an 25 % increase of modelled POC. In autumn TEP-C contributions were lower, i.e. 0.59 $\mathrm{mmol\,C\,L^{-3}}$, equivalent to 30 % of modelled POC. Bacterial production drives the microbial food web and is an important sink for DOC (5.47–27.4 $\mathrm{g\,L^{-1}\,yr^{-1}}$).

DOC concentration in the upper 100 m of the water column varies over the productive season in Fram Strait and ranged between ca. 40 and 170 $\mathrm{\mu mol\,L^{-1}}$ µmol L-1 during the period 2009–2017 (Engel et al., 2019). Thereby, the highest concentrations were observed in the upper 20 m, decreasing slightly to 30 m. Considerable variability was still observed at 100 m, ranging between 40 and 95 $\mathrm{\mu mol\,L^{-1}}$. Below 250 m, DOC concentration is relatively stable, indicating a refractory pool of 52±2 $\mathrm{\mu mol\,L^{-1}}$. Estimates for the production of fresh DOC by Arctic phytoplankton vary around 15 % of NPP (Codispoti et al., 2013; Engel et al., 2013). For the Arctic, few measurements of NPP exist; most PP estimates are based on satellite data, where subsurface, marginal or under-ice blooms are not well represented. Primary productivity in June and July 1984, with an average daily integrated productivity of 35 $\mathrm{mmol\,C\,m^{-2}\,d^{-1}}$, was also highest at the ice margin in Fram Strait during a study by Smith et al. (1987). However, an increase in primary production has been estimated for the pan-Arctic region over the last decades as a consequence of climate change (Ardyna and Arrigo, 2020). Due to the loss of sea ice, the duration of the phytoplankton growing season and the total extent of open water have increased significantly and could explain an estimated 30 % increase in net primary production (NPP) between 1998 and 2012, yet largest changes are attributed with ice melting on the shelves (Laptev, Kara and East Siberian).

3.4.4 Limitations and perspectives

The Lagrangian approach allows us to take a different look at the biogeochemical state of a particular region as it is found within a limited period of observations. Even in analyses using three-dimensional coupled physical-biogeochemical ocean models, where the state changes in an area can be resolved in time, supplementary analyses are needed to relate local results to the processes that took place before and outside the region. This is achieved in our study, but is also accompanied by certain disadvantages and limitations.

By using ensembles of trajectories, where a one-dimensional model can be solved in a computationally efficient way, the individual trajectory solutions of the plankton model are independent of each other, even if they are spatially in close proximity to each other. Apart from the identical dynamical equations, the only other connection between some (spatially adjacent) trajectories of an ensemble is the similarity of the physical conditions, since they are based on the same results of a particular circulation model. Horizontal gradients transverse to the trajectories, e.g. of Chl-a, are not taken into account, while the lateral horizontal mixing remains unresolved, with lateral diffusivities being typically in the order of 10^2 - 10^3 $\mathrm{m}^2\,\mathrm{s}^{-1}$ (10 - 10^2 $\mathrm{km}^2\,\mathrm{d}^{-1}$) (e.g., Zhurbas et al., 2014). Lateral mixing may dilute and thus dampen peak concentrations seen in our results, and it likely reduces the variability explained by our approach. In the study of Ser-Giacomi et al. (2023) a Lagrangian approach is proposed where a water patch is subject to strain (changing its shape and size) and diffusion (changing its concentration due to dilution or entrainment of surrounding waters). These explicit considerations provide a more elaborate representation of spatial variability. In principle, such patch dynamics may also be applicable to approaches similar to ours, but it would require additional assumptions with respect to the connectivity, distances and concentration differences, between the individual trajectories.

A special feature of our model runs is that we consider solutions that are all based on an identical set of parameter values. In the case of the Arctic trajectories coming from the north, the model provides a delayed onset of bloom (late May - early June) compared to the remote sensing data (late April) (Fig. 3.4). We note that the earlier bloom detection derived from satellite data is associated with large uncertainties, mainly because of the low sun angle and the smaller number of pixels that are free of clouds and ice. Our simulated raise in Chl-a in late May and early June compare well with the times of bloom initiation in SINMOD simulations analysed by Vernet et al. (2021); therein the western Fram Strait is referred to as NorthEast (NE) region of Greenland. With some adjustment of the value assigned to the photosynthetic efficiency (a_P) only in the Arctic trajectories we can obtain a much improved match with respect to the remote sensing data (Fig. B7 in the SI). However, such apparent improvement, achieved by adjusting the value of a single model parameter, leads to a misfit in the depth profile of Chl-a, which is associated with Chl-a maxima that are deeper than observed. Instead of considering different parameter values for the Atlantic and the Arctic trajectories, our findings rather indicate that some mechanisms remain unresolved by the model, e.g. growth of ice algae or short-term (diurnal) stratifications that keep some phytoplankton within the upper layers while increasing their exposure to light.

In the end, improvements should be achieved if the model is further revised with regard to specific size ranges of the grazing, as well as a division of the detritus into fast and slow sinking particles, as discussed before. Furthermore, trajectories derived from a higher spatial resolution model could also help to increase the simulated variability in the target area. An improved representation of the ice edge blooms along the Arctic trajectories would likely bring the timing of bloom initiation into better agreement with the remote sensing data.

3.5 Conclusions

In this study, our primary objective was to unravel the extent to which the spatial variability observed in local measurements of dissolved and particulate organic matter concentrations, productivity, and export rates in the HAUSGARTEN Long-Term Ecological Research site could be explained by divergent environmental conditions encountered by water parcels during their transit through the Fram Strait. To achieve this, we employed a 1D size-based NPZD plankton ecosystem model with variable stoichiometry, forced by four ensembles of Lagrangian trajectories passing the LTER at different times (summer or autumn) and from distinct directions (originating in the North Atlantic or Arctic Ocean). These trajectories presented diverse sets of physical conditions that plankton within a water parcel may experience along their journey.

Overall, our model has shown that it can generate solutions that are broadly in agreement with data from very different types of observations, comprising tracer concentration measurements, protist plankton spectra derived from microscopy, remote sensing products and climatological data.

Temporal developments in plankton growth, size composition, and organic matter export varied among trajectory ensembles, despite using identical model parameter values. Light availability discrepancies influenced the timing of plankton blooms and the size composition of primary producers and thus their grazers, subsequently impacting organic matter export. During local *in situ* observations in the Fram Strait, maxima in productivity and export had already occurred.

While our model solutions can explain between 10–72 % of the observed variability, due to the diverse physical conditions of the individual trajectories, a substantial portion of variability remains unexplained. Whether models of higher spatial resolution can overcome such disparities remains unclear, but it certainly underscores the necessity for future research to advance our knowledge of the spatio-temporal variations in plankton dynamics.

Open Research Section

The code to generate model simulations and figures, and data used for calibration and validation of the model can be found in https://github.com/vlampe/microARC/.

Acknowledgments

We thank Fabian Grosse for extracting and providing the particle trajectories from SINMOD model results.
The remote sensing Chl-*a* data was provided through the Ocean Color CCI data product (V5, http://dx.doi.org/10.5285/1dbe7a109c0244aaad713e078fd3059a).
This study was funded by the Helmholtz Association and the German Federal Ministry of Education and Research (BMBF) as a contribution to the microARC project (03F0802A), part of the Changing Arctic Ocean programme, jointly funded by the UKRI Natural Environment Research Council (NERC) and BMBF.

Chapter 4

Distinguishable variations in chlorophyll-*a* concentration in the Fram Strait based on hydrographic features resolved by a machine learning approach

This chapter is based on the paper 'Distinguishable variations in chlorophyll-a concentration in the Fram Strait based on hydrographic features resolved by a machine learning approach' by Vanessa Lampe and in preparation for submission.

Abstract

The Fram Strait (FS), an important gateway to the Arctic Ocean, exhibits pronounced variability in chlorophyll-a (Chl-a) concentration on both intra- and interannual scales. This variability is intricately linked to the complex hydrography of the region, marked by two opposing currents divided by a frontal system.

Given the challenges of sparse temporal and spatial coverage of *in-situ* data, remote sensing satellite data provide valuable insights, particularly when studying larger regions and trends over time. Therefore, I propose a machine learning approach to separate the FS into three hydrographical sectors based on sea surface temperature, the main property for water mass identification besides salinity. The sectors resolve the cold Arctic-influenced, the warm Atlantic-influenced, and the intermediate front-influenced regions. This sectorisation allows for a nuanced analysis of variability, accounting for the dynamic behaviour of the currents and frontal system.

This study reveals distinct differences in bloom initiation and bloom development that are reflected by the Chl-a concentrations within these hydrographical subregions. Blooms tend to occur in May in the Arctic-influenced sector and may appear later, in July, in the Atlantic-influenced sector. Overall, the magnitude of Chl-a variability is related to its average concentration. Importantly, when normalised with concentration, the variability seen in the remote sensing data is notably higher in the Arctic-influenced sector, emphasising the impact of environmental differences within the hydrographical regimes on phytoplankton dynamics. The analysis of a short time series from 2016 to 2021 does not reveal any discernible trends in Chl-a average concentration or variability.

The here proposed methodology not only enhances the understanding of hydrographic characteristics in the FS but also provides a valuable tool for analysing large geospatial data sets, especially in the absence of *in-situ* measurements that resolve the physical properties of the water column. This research contributes to a broader comprehension of the expected variability ranges of Chl-a in the Fram Strait, highlighting the efficacy of machine learning techniques in unravelling the complex dynamics of hydrographic variability.

4.1 Introduction

Global annual primary production (PP) by marine phytoplankton is estimated to be between 47.8 to 52.2 $\mathrm{Gt\,C\,yr^{-1}}$, one of the largest carbon fluxes on the planet (Kulk et al., 2020). While this formation of carbon serves as the basis of marine food webs, approximately one-third of the total production is exported from the upper ocean and retained in the ocean interior for centuries to millennia (Falkowski et al., 1998). These estimates of biogenic carbon fluxes are derived from changes in organic carbon concentration over large spatial distances and over long periods of time. On shorter time scales and smaller spatial scales, however, primary production shows strong variability that is largely reflected in changes in chlorophyll-a concentrations, from significant seasonal variations to interannual differences.

The Arctic is a unique system with pronounced inter- and inter-annual variations. The gradient in light availability ranges from complete darkness during the polar night in winter to permanent daylight during the polar day in summer, and sea ice cover varies in thickness and extent spatially, seasonally, and inter-annually. Furthermore, Climate Change is amplified in the Arctic compared to other regions, predominantly due to temperature and albedo feedbacks (Pithan and Mauritsen, 2014). Rising sea surface temperatures (Comiso and Hall, 2014; Nielsen-Englyst et al., 2023) and declining extent and thickness of the sea ice (Stroeve et al., 2012; Hansen et al., 2013; Renner et al., 2014; Spreen et al., 2020) may fundamentally change the functioning of marine ecosystems and biogeochemical processes. The increase in the duration of ice-free open water phases of 45 days led to an increase in Arctic-wide primary production by 20 % between 1998–2008, as estimated from remote sensing imagery (Arrigo and Van Dijken, 2011). If this time series is extended further until the year 2012, Arrigo and van Dijken (2015) report an even stronger raise of 30 %, predominantly associated with reductions in sea ice extent and potentially also due to an enhanced influx of terrestrial nutrients. A smaller increase in Arctic PP of 4.5 % is reported by Kulk et al. (2020) for the period 1998–2018. However, available time series of remote sensing Chl-a and PP may still be too short to reliably detect climate change signals, as Henson et al. (2010) estimate a time series covering approximately 40 years would be required.

The Fram Strait connects the central Arctic Ocean to the Atlantic, serving as an important gateway for water exchange and sea ice export. This highly dynamic region is characterised by two opposing currents. In the East, the West Spitsbergen Current (WSC) transports warm and saline Atlantic waters northwards into the Arctic Ocean (Beszczynska-Möller et al., 2012). In the west, Polar waters exit the Arctic Ocean in the ice-covered western Fram Strait with the East Greenland Current (EGC) (de Steur et al., 2009). In between, separating the water masses, lies the East Greenland Polar Front which is affected by sea ice dynamics and exhibits strong seasonal variation in terms of both area and intensity (Liu et al., 2022). In addition, this region is rich in eddies, that further contribute to the observed high mesoscale variability (Von Appen et al., 2022).

Given the complex hydrographic nature of the Fram Strait, it is likely that ranges of variability differ in the subregions. The identification and thus distinction of subregions however is complicated, as their geographic extent changes within short time scales. In a study by Nöthig et al. (2015), the distinction of the Fram Strait into a Western and an Eastern region was made along the prime meridian (0°, Greenwich Meridian), a division that has already resulted in noticeable differences in variability and trends in the remote sensing Chl-a concentrations between 1998 and 2012. While in the western EGC region Chl-a peaks usually occurred in May and June, peaks in the eastern WSC region were observed in June or July between 2002–2009, but also in May or June before and after this period. While the authors do not report a significant trend for the EGC, the variability increased, and in the WSC the trend of $+0.54\ \mathrm{mg\,Chl\,m^{-3}}$ was found to be significant. Although the distinction along the prime meridian was meaningful and practical, it may overly simplify the dynamic and complex hydrography in this region. Lampe et al. (2021) have proposed using a machine learning approach to classify the subregions only based on remote sensing sea surface temperature (SST) and found distinct phenological patterns in remote sensing Chl-a in the EGC and WSC regions of the Fram Strait between 2016–2018.

Estimating trends in productivity in this highly variable region is an important but difficult task since the distinction of trends from natural variability is only possible if the ranges of natural variability are known (Soltwedel et al., 2016). This study aims to derive credible ranges of Chl-a variability within the distinct hydrographic subregions of the Fram Strait. First, I extend the machine learning clustering approach presented in Lampe et al. (2021) to resolve three clusters: 1) the cold, EGC-influenced, 2) the warm, WSC-influenced, and 3) the intermediate front region for the year 2018 and evaluate the validity of the identified SST clusters. Within these clusters, I then compare the seasonal cycle of Chl-a concentration from remote sensing estimates and their variability. Finally, extending the analysis to the period of 2016–2021, I analyse whether the patterns observed in 2018 are robust and thus representative and also found in the adjacent years. Furthermore, I investigate whether trends in average concentration, timing, or variability are detectable.

4.2 Methods

First, I briefly describe the remote sensing data products. Then, I explain the machine learning procedure to derive distinct hydrographic subregions based on sea surface temperature (SST). Finally, I summarise the methods applied for the statistical analysis of chlorophyll-a variability.

4.2.1 Remote sensing data

Remote sensing data for sea surface temperature (SST) and sea ice coverage (SIC) are provided by GHRSST, Met Office, and CMEMS (Good et al., 2020), which contains reprocessed daily satellite and *in-situ* data on an 0.05°x 0.05°grid.

Concentrations of chlorophyll-a derived from ocean colour are available daily on a 4 km x 4 km grid (CMEMS and ACRI, 2023, L3 product, daily) for 2018. For this data product, the Chl-a concentration estimates were merged from SeaWiFS, MODIS, MERIS, VIIRS-SNPP & JPSS1, and OLCI-S3A & S3B. This dataset furthermore contains Chl-a concentrations by plankton functional types (PFT) and binned by size.

For the longer 2016–2021 time series, I used the OC-CCI 8-day mean Chl-a data set (Sathyendranath et al., 2021, Version 5.0), which contains globally merged MERIS, Aqua-MODIS, SeaWiFS, VIIRS and Sentinel3A-OLCI observations. Due to the 8-day aggregation, the file size of the data product is smaller compared to the daily data, making the computation of the six-year time series more computationally efficient. Furthermore, using a second, independent, data product offers the opportunity of cross-validating the seasonal patterns in both data products.

4.2.2 Clustering of SST sectors

In Lampe et al. (2021) a k-means clustering algorithm was applied to partition the Fram Strait into regional clusters. The clustering was based on SST and intended to characterise the sampling stations of the HAUSGARTEN observatory to be either Arctic or Atlantic influenced. This approach was chosen because the water mass classification based on salinity, temperature, and density profiles collected by CTD samplers after Amon et al. (2003) yielded ambiguous classifications of Polar Water, Intermediate Water, and Atlantic water and, therefore, the authors decided to focus on distinguishing between cold (Arctic-influenced) and warm (Atlantic-influenced) SST regions. The main advantage of this approach is that SST data from remote sensing is available on a daily and global basis, whereas *in-situ* measurements of temperature and density are available on a much more limited spatial and temporal resolution.

The k-means clustering is an unsupervised machine learning algorithm that groups values into k clusters so that within-cluster variances (sums of squares) are minimised (Hartigan and Wong, 1979). For this analysis, I chose to resolve three SST clusters ($k = 3$), to represent 1) the cold, Arctic-influenced parts of the Fram Strait, 2) the warm, Atlantic-influenced part, and 3) a cluster of intermediate SST to represent the front between the cold and warm clusters.

For each day, I extracted the remote sensing SST values between 75°–85°N and 15°W–15°E. Each value is associated with a coordinate (latitude and longitude). Using k-means clustering, I assigned each SST value to one of the three clusters, yielding a vector of class labels (i.e. cluster IDs), which I reassigned to their respective coordinates. This means that the clustering is solely performed on the SST values, regardless of the geographic location of the respective values. For each cluster, I then created a spatial polygon spanning its outer edges. An example of the clusters' extent is shown in Fig. 4.2 (lower left panel), where the polygons derived for an exemplary day (27th July 2018) are plotted on top of the remotely sensed SST. These spatial polygons were then used as 'clipping masks' to extract ice coverage or Chl-a concentrations within the respective regional clusters, as shown in the centre and right lower panels of the same figure.

4.2.3 Variability analysis

Within each of the clusters, I calculated daily statistics of SST, SIC and Chl-a concentrations. The statistics included measures of central tendency (arithmetic mean, median, and mode) and spread (minimum, maximum, standard deviation (SD), 1st and 3rd quartiles (Q1 and Q3), interquartile range (IQR), 95 % confidence interval (CI95), and the width of CI95, ΔCI95). I calculated minimum, maximum, mean, and standard deviation using the pre-implemented functions in R (R Core Team, 2018). The remaining statistics (median, mode, Q1, Q3, and the edges of the 95 % CI) were derived from nonparametric probability density estimates, expressed as probability density functions (pdf). I estimated the pdf(x) using the diffusion Kernel Density Estimator (diffKDE) by Pelz et al. (2023). p-Quantiles are statistics below which a proportion p of all values in a probability distribution ($f(x)$) fall. A real number x_p is called the p-quantile of a random variable X, when:

$$P((-\infty, x_p]) \geq p \tag{4.1}$$

and

$$P([x_p, +\infty)) \geq 1 - p \tag{4.2}$$

or, expressed as the probability density function f:

$$\int_{-\infty}^{x_p} f(x)dx \geq p \tag{4.3}$$

For example, the Q1 or 25 % quantile is therefore:

$$P((-\infty, x_{0.25}]) = \int_{-\infty}^{x_{0.25}} f(x)dx \geq 0.25 \tag{4.4}$$

Using the cumulative density function F we can then easily find x_p:

$$F(x_p) \geq p \tag{4.5}$$

This way, I derived the Q1, Q2 (= median) and Q3 quantiles. I furthermore calculated the confidence interval to include 95 % of all values (CI95):

$$F(\mathrm{CI95}_{\mathrm{lower}}) \geq 0.025 \tag{4.6}$$

$$F(\mathrm{CI95}_{\mathrm{upper}}) \geq 0.975 \tag{4.7}$$

The (global) mode is the value where the probability density function $f(x)$ is at its maximum.
The interquartile range is the distance between Q1 and Q3:

$$\mathrm{IQR} = Q3 - Q1 \tag{4.8}$$

and the width of CI95 (ΔCI95) is calculated as:

$$\Delta\mathrm{CI95} = \mathrm{CI95}_{\mathrm{upper}} - \mathrm{CI95}_{\mathrm{lower}} \tag{4.9}$$

4.3 Results

In this section, I first analyse the intra-annual variability in Chl-a concentrations in the Fram Strait, without distinguishing between any subregions. I then investigate the ability of the machine learning approach to identify distinct subregions in the Fram Strait and analyse the variability of Chl-a within these derived subregions for the year 2018. Finally, I compare the inter-annual Chl-a variability in an extended time series from 2016 to 2021.

4.3.1 Intra-annual variability of Chl-a concentrations in the Fram Strait

Here, I focus on the intra-annual variability of remote sensing Chl-a observations in the 75°–85°N and 15°W–15°E region within the Fram Strait with a focus on bloom development, without distinguishing between hydrographic clusters (sectors) and thereby disregarding the spatial variability. A time series of Chl-a concentrations and their variability (mean, median, [Q1, Q3] interval, and 95 %-CI) is shown in Fig. 4.1. The outcome of this analysis serves as a simple and basic reference that represents only the overall temporal development in chlorophyll-a concentration in the Fram Strait.

In the entire region of interest, Chl-a observations from remote sensing cover the second half of March until the end of September. Throughout this period, the

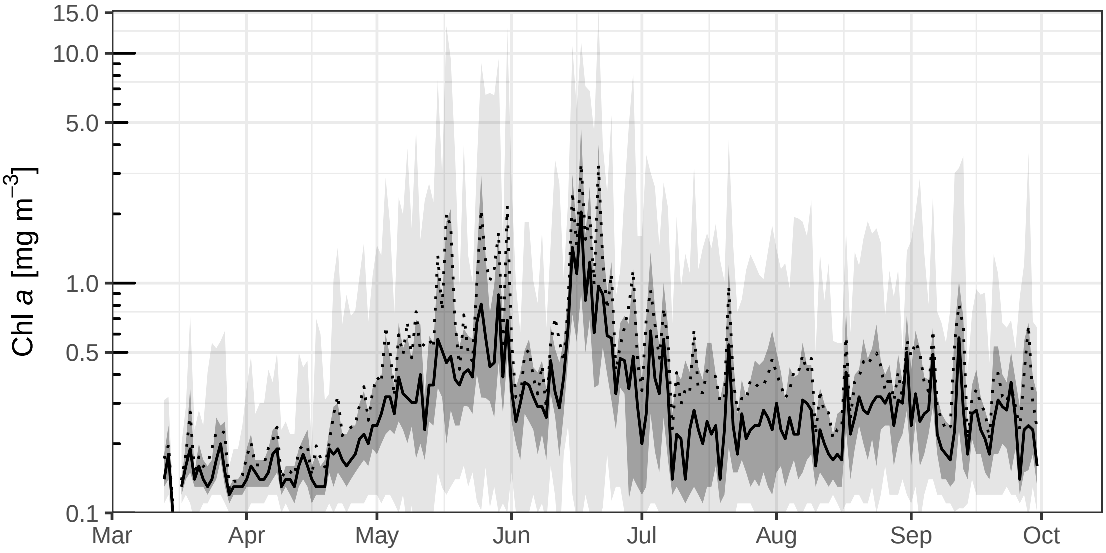

Figure 4.1: Daily remote sensing Chl-a concentrations and their variability. Solid lines represent the median, and dotted lines the mean. Darker shaded areas represent the [Q1, Q3] interval, and the lighter shaded areas indicate the 95 % confidence interval.

median is always smaller than the mean, indicating that daily distributions of Chl-a concentrations are right-skewed. Furthermore, the mean is close to the Q3 most of the time. Since the arithmetic mean is influenced by data points with high values that appear regularly in this time series, the median appears to present a better estimate of central tendency for Chl-a concentrations.

When disregarding any spatial differentiation, two distinct bloom events stand out in this time series. Mean and median Chl-a concentrations begin to increase in the second half of April, eventually reaching a first peak by the end of May. During this time, median values reach about 0.5 mg Chl m^{-3} and the mean exceeds the bloom threshold of 1 mg Chl m^{-3}(e.g. Wu et al., 2007), occasionally reaching up to 2 mg Chl m^{-3}. During the first two weeks of June, concentrations drop again to mean values around 0.4 mg Chl m^{-3} and median values around 0.3 mg Chl m^{-3}. A second bloom peak that reaches global maxima within this time series occurs in the second half of June, where median values reach up to 2 mg Chl m^{-3} and mean values up to 3 mg Chl m^{-3}. Following this peak, Chl-a concentrations decrease again and median concentrations fluctuate in the range of 0.2–0.3 mg Chl m^{-3} until the end of the observational period. Overall, the variability observed here is substantial, especially at times when mean and median Chl-a concentration is high. During the bloom peaks, the CI95 spans from 0.1 to 12 mg Chl m^{-3}, thus covering three orders of magnitude.

4.3.2 Distinction of hydrographic regimes in the Fram Strait using SST clustering

In the following, I assess the ability of the k-means algorithm to distinguish three separate clusters of sea surface temperature (SST) in the highly heterogeneous realm of the Fram Strait and how the distinction is also reflected in other variables, such

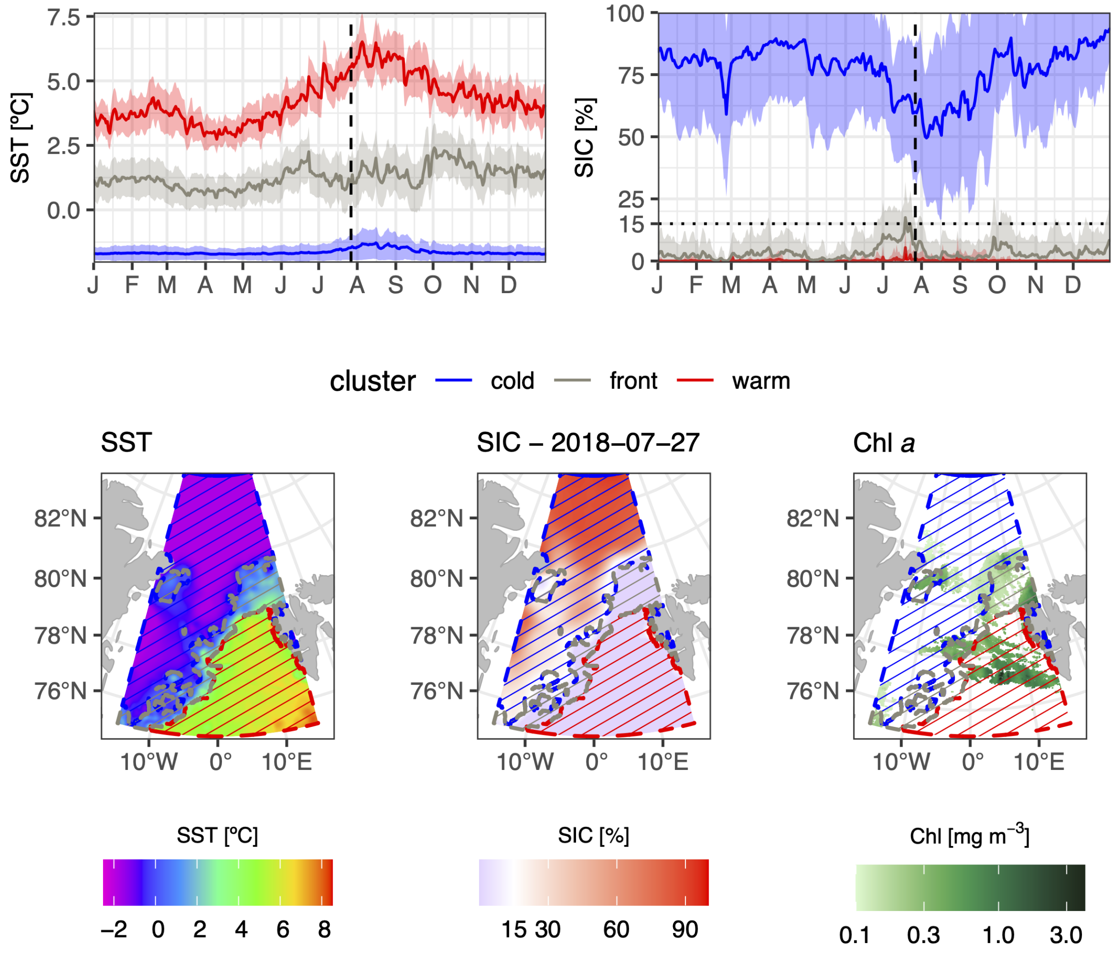

Figure 4.2: Upper panels show the average ± standard deviation of Sea Surface Temperature (SST, left) and Sea Ice Cover (SIC, right) within the distinct SST clusters in 2018. For an exemplary day (27th July 2018, marked with a dashed line in the time series plots), the lower panels show the remotely sensed SST (left), SIC (centre), and Chl-a concentrations (right) together with the spatial clipping masks of the identified clusters.

as sea ice cover and Chl-a concentration. Time series of daily averages and standard deviations derived from the daily remote sensing products within the clusters are shown in Fig. 4.2 for SST (top left) and SIC (top right) and reveal clear differences between the clusters.

SSTs are well distinguishable between the clusters throughout the time series with no overlaps of the mean±SD confidence intervals. In the SIC time series, however, the confidence intervals between the front and warm clusters do overlap, although mean SIC in the front cluster is notably higher than in the warm cluster, especially during July. The SIC in the cold cluster remains on average greater than 75 % for the majority of the year, dropping to around 50 % in August. Although the confidence intervals of this cluster are larger, there is no overlap with those of the other clusters.

The distribution of SST in the Fram Strait for an exemplary summer day (27th July 2018) is captured well by the identified clusters, as shown in Fig. 4.2 (lower left panel). Here, the warm, Atlantic cluster (outlined in red) contains all pixels with SST $\gtrsim$ 3℃ and the cold, Arctic cluster (outlined in blue) contains pixels with SST

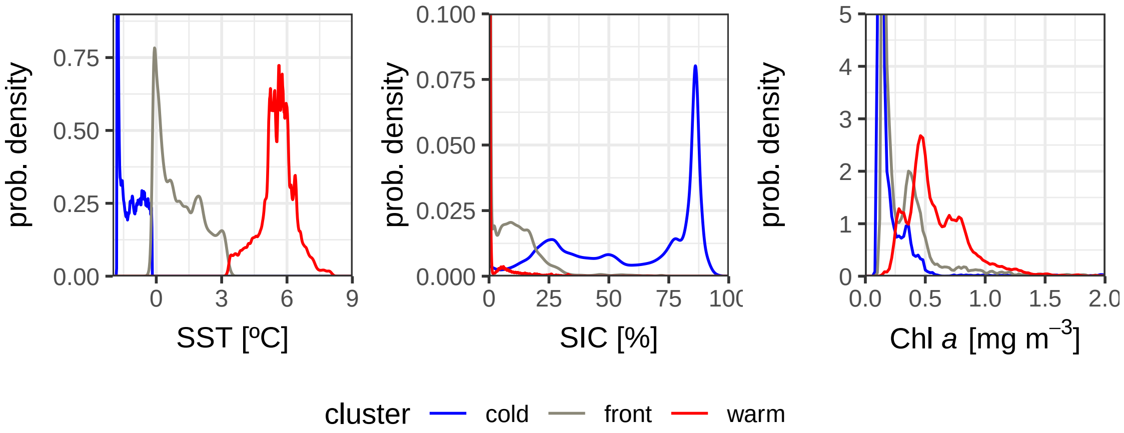

Figure 4.3: Probability distributions of SST (left), SIC (centre), and Chl-a concentration (right) within the identified clusters on the 27th July 2018. The PDFs were estimated using the diffKDE package.

$\lessapprox$ 0°C. SST in between are categorised to the intermediate, front cluster, outlined in grey. The probability density distributions (estimated using the diffKDE package) of SST values for each cluster on this day shown in Fig. 4.3 (left) confirm the credibility of the regional separation according to the SST-based k-means clustering. The temperature boundaries of the clusters vary throughout the year, as does the observed average SST, with the highest values in August.

The clusters are also apparent in SIC on the 27th July 2018, where sea ice is restricted to the cold sector (lower centre panel, Fig. 4.2). While the warm, Atlantic cluster is entirely ice-free, the cold, Arctic cluster is covered with 15–100 % sea ice. Apart from the polynya East off Greenland, where SIC is around 15 %, the intermediate "front" cluster is mostly ice-free. The ice edge, defined as the 15 % SIC contour (e.g. Meier and Stroeve, 2008), roughly follows the boundary of the cold and intermediate clusters, but is predominantly located in the cold cluster. This leads to a less clear distinction of the clusters in the probability distribution of SIC values shown in Fig. 4.3 (centre). Although the modes clearly differ between the clusters (warm: 0 %, front: 8 %, cold: 85 %) the distributions have long tails to the right (warm and front) and to the left (cold), that overlap. The ice edge is located either entirely or at least in its majority within the cold cluster on most days of 2018, leading to the apparent low sea ice cover in the front sector in the SIC time series previously mentioned.

Remote sensing observations of Chl-a concentrations are sparse in the region, due to cloud masking or contamination of the signal by sea ice (e.g. Comiso, 1995), which is apparent in the lower right panel in Fig. 4.2, where observations are not available for large areas in the region of interest on 27th July 2018. Still, differences in Chl-a concentrations are noticeable, with concentrations around 0.1 mg Chl m^{-3} in the cold cluster and concentrations reaching up to 3 mg Chl m^{-3} or higher in the warm cluster on this day. The probability distributions of Chl-a concentrations for this day shown in Fig. 4.3 are right-skewed and the modes are clearly distinguishable between the cold and warm clusters. The front cluster however appears bimodal, with both modes corresponding approximately to the modes of either the cold and the warm clusters, respectively, suggesting that the front cluster has signals of both

Table 4.1: Measures of variability for the entire observational region (75° – 85°N; 15°W–15°E; 'total') and the identified clusters. The values were averaged over the observational period (ca. mid-March – October) and express the standard deviation (STD), interquartile range (IQR), width of the 95 % confidence interval (ΔCI95) and the ΔCI95 normalised by the average daily Chl-a concentration (norm. ΔCI95)

cluster	STD [$\mathrm{mg\,m^{-3}}$]	IQR [$\mathrm{mg\,m^{-3}}$]	ΔCI95 [$\mathrm{mg\,m^{-3}}$]	norm. ΔCI95 [%]
total	0.60	0.37	1.89	300.40
cold	0.44	0.25	1.41	312.04
front	0.58	0.38	1.90	269.42
warm	0.42	0.33	1.35	208.07

clusters on this day.

4.3.3 Intra-annual spatially decoupled chlorophyll variability in the Fram Strait

Here, I investigate whether the patterns of inter-annual Chl-a variability differ between the distinguished hydrographical subsections. I furthermore analyse whether the distinction reduced the overall variational range compared to the entire observational region and compare the development of Chl-a concentrations and their variability over time in the clusters, as shown in Fig. 4.4.

The distinction of clusters reduced the overall range of variation (STD, IQR, ΔCI95), as shown in Tab. 4.1. When averaged over the entire observational period (ca. mid-March – October), standard deviation, interquartile range and the width of the 95 % confidence interval (ΔCI95) are considerably larger for the whole region than in the cold and warm subregions. The difference in variability between the 'front' cluster and the entire area however is not as clear, with the average STD being only slightly smaller, and the IQR and ΔCI95 even larger by 0.1 $\mathrm{mg\,m^{-3}}$. The ΔCI95 normalised with the average concentration is largest in the cold cluster with 312 %, notably greater than for the 'total' area, which is potentially linked to the overall smaller average Chl-a concentration in this cluster.

The timing of the spring bloom initiation differs in the three sectors, as Fig. 4.4 clearly shows. Assuming a bloom threshold of 1 $\mathrm{mg\,m^{-3}}$ average Chl-a (Wu et al., 2007; Nöthig et al., 2015; Lampe et al., 2021), we see the earliest bloom in the front cluster, where mean concentration occasionally scratches the threshold starting with the beginning of May. Median values during this time range around 0.5 $\mathrm{mg\,m^{-3}}$. By the second half of May, mean Chl-a exceeds the threshold in the cold, Arctic-influenced cluster, reaching similar mean concentrations as in the 'front'. Following this spring bloom, mean Chl-a concentration in the cold cluster decreases drastically by the beginning of June, while this decrease is not as pronounced in the 'front'. In the front cluster, mean Chl-a drops to ca. 0.5 $\mathrm{mg\,m^{-3}}$, similar to concentrations observed in the warm cluster during this time. The spring bloom in the warm cluster initiates in the second half of June with higher intensity than the earlier blooms in the cold and front clusters, reaching average and median Chl-a concentrations of up to 4 and 2.5 $\mathrm{mg\,m^{-3}}$, respectively. Interestingly, the front

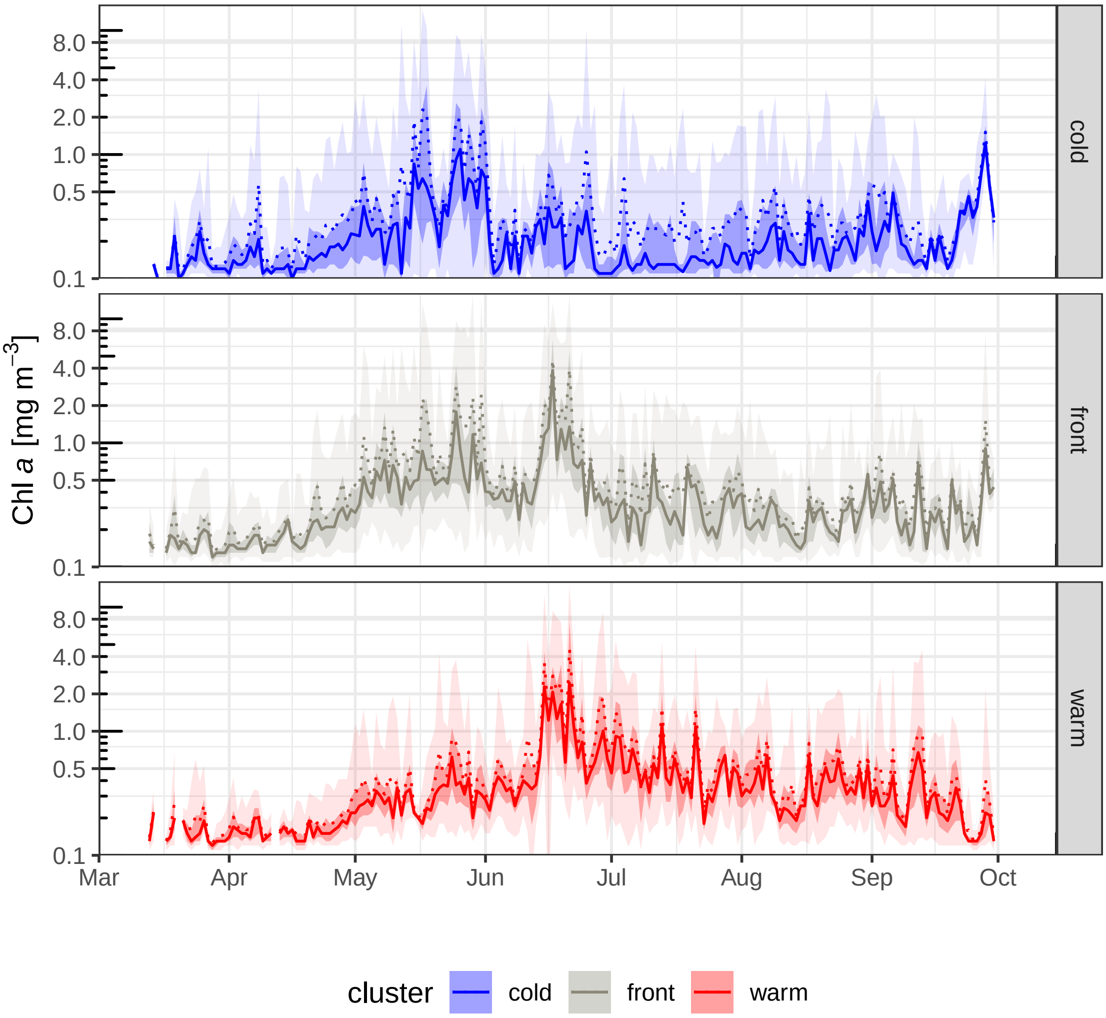

Figure 4.4: Chl-a concentrations and their variability in 2018. Daily remote sensing Chl-a concentrations were split into three regional clusters based on the SST. Solid lines represent the median, and dotted lines the mean. Darker shaded areas represent the [Q1, Q3] interval, and the lighter shaded areas indicate the 95 % confidence interval.

cluster shows a second bloom peak around the same time, indicating this cluster actually shows signals from both, the warm and the cold, regions. The bloom in the warm cluster lasts for approximately one week until concentrations decrease again. Here, post-bloom Chl-a concentrations are notably higher than in the cold and front clusters. Similar to the Chl-a time series for the entire observational region shown in Sec. 4.3.1, daily Chl-a values follow a right-skewed distribution where the means are considerably higher than median values.

Throughout the observational period, the level of variability changes. Generally, variability is higher at times Chl-a concentrations are high, as shown in Fig. 4.5(a). Observed maxima in the width of the CI95 do not differ considerably between the clusters, although their timing is associated with peaks in average Chl-a concentration, i.e. peaks in ΔCI95 occur around early and late May in the cold and front clusters, and in the second half of June in the warm and front clusters.

The relationship between the magnitude of Chl-a concentration and the asso-

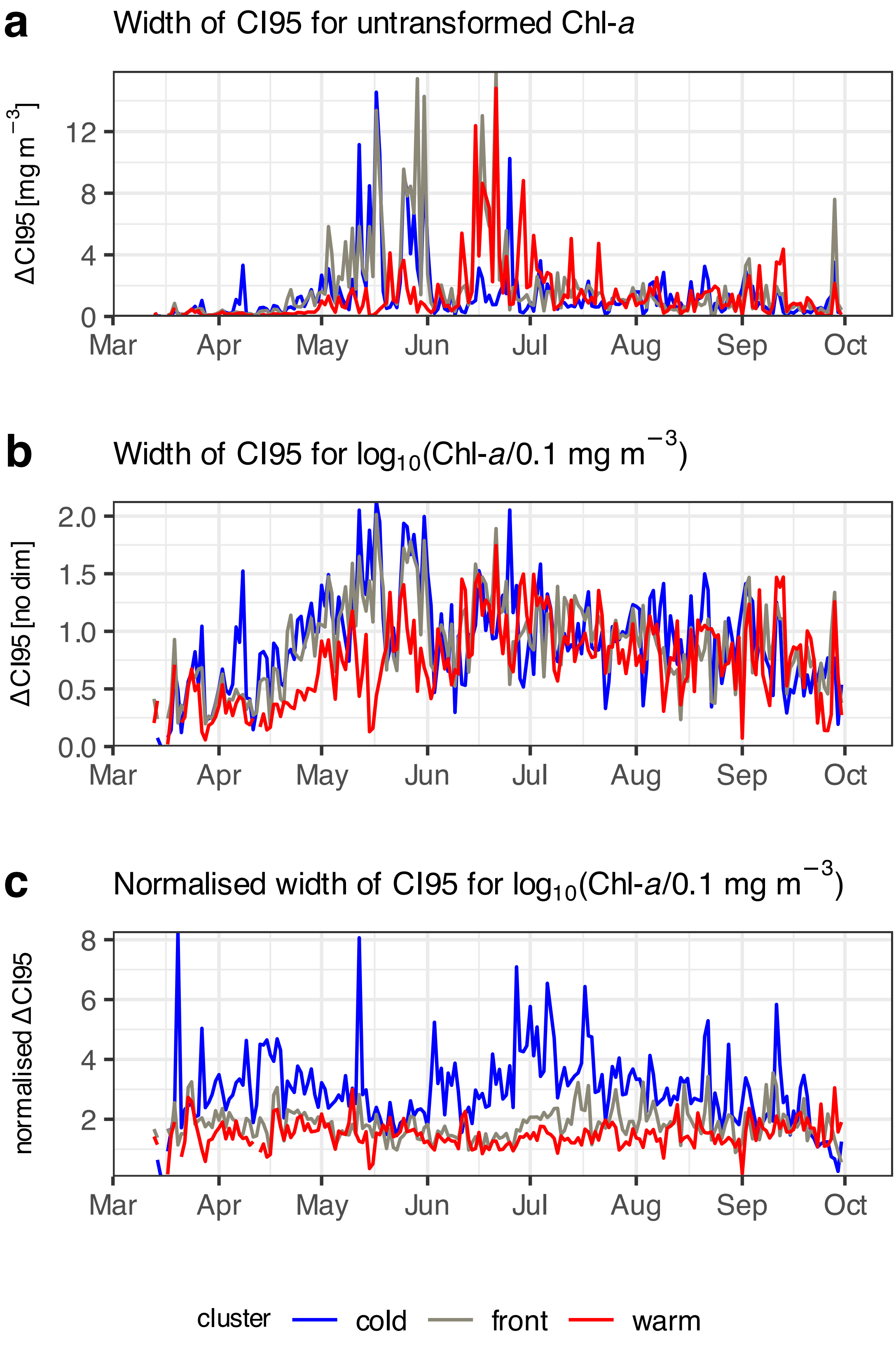

Figure 4.5: Variability of Chl-a concentrations in the identified clusters. Variability is expressed as the width of the 95 % confidence interval: $\Delta\mathrm{CI95} = Q_{0.975} - Q_{0.025}$. ΔCI95 is derived from untransformed Chl-a (a) and $\mathrm{Chl_{trans}} = \log_{10}\left(\frac{\mathrm{Chl}}{0.1\mathrm{mg\,m^{-3}}}\right)$ (b). ΔCI95 normalised by the (daily) mean($\mathrm{Chl_{trans}}$) is shown in (c).

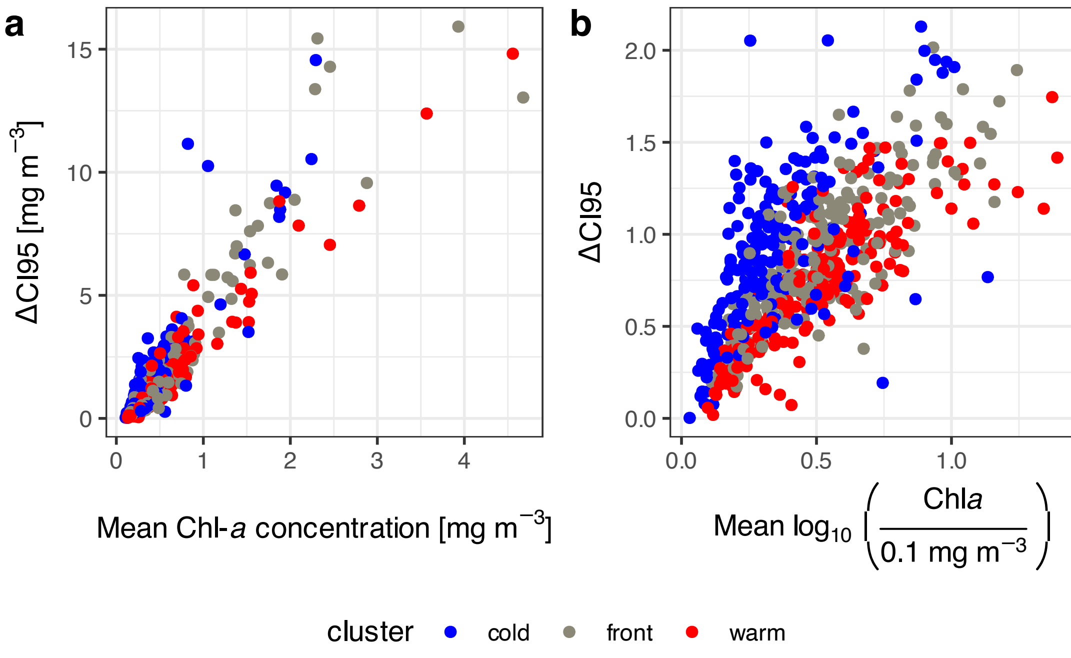

Figure 4.6: Relationship of Chl-a variability with concentration. Like in Fig. 4.5, variability is expressed as the width of the 95 % confidence interval: $Q_{0.975} - Q_{0.025}$. For (a), Chl-a was not transformed, for (b) Chl-a was transformed as $\mathrm{Chl_{trans}}=\log_{10}\left(\frac{\mathrm{Chl}}{0.1\,\mathrm{mg\,m^{-3}}}\right)$ prior to deriving means and confidence intervals.

ciated spatial variability can be best inferred from the statistics. As mentioned earlier, Chl-a concentrations in the remote sensing observations span three orders of magnitude and are right-skewed. A $\log_{10}$-transformation of normalised Chl-a concentration prior to the variability analysis reveals more uniform patterns of Chl-a variability throughout the growth period (see Fig. 4.5(b)) compared to the untransformed data, but also differences during the bloom phases between the cold and front compared to the warm sector. Between April and mid-May, ΔCI95 of $\mathrm{Chl_{trans}}$ steadily increases in all clusters. During this time, while Chl-a concentrations are increasing, ΔCI95 of $\mathrm{Chl_{trans}}$ is larger by a factor of up to 2 in the cold and front clusters, compared to the warm cluster. In the warm cluster, this increasing trend lasts until mid-June, when mean and median Chl-a concentrations in this cluster peak. From June, ΔCI95 of $\mathrm{Chl_{trans}}$ shows similar values in all clusters with a slight decreasing trend.

Further clarification is achieved by setting the ΔCI95 of $\mathrm{Chl_{trans}}$ into relation with mean $\mathrm{Chl_{trans}}$, as shown in Fig. 4.5(c), which reveals that the normalised ΔCI95 appear nearly constant throughout the observation period. This statistic is similar to a coefficient of variation and visualises well how the overall variability in the cold cluster is considerably larger than in the warm cluster. While variability is slightly larger in the front than in the warm cluster, it is notably smaller than in the cold cluster.

Overall, variability (expressed as the width of CI95, ΔCI95) is higher at high Chl-a concentrations. As Fig. 4.6(a) shows, the width of the 95 % confidence intervals increase approximately linearly with increasing average Chl-a concentration, i.e. an increase of 1 $\mathrm{mg\,m^{-3}}$ in average Chl-a concentration is accompanied with an increase in ΔCI95 of approx. 5 $\mathrm{mg\,m^{-3}}$. This relationship appears slightly steeper for the cold cluster than for the warm cluster, indicating that the effect of increasing Chl-a concentration on CI95 width is stronger in the cold cluster.

I expected a more constant relationship of variability to concentration when concentration was $\log_{10}$ transformed. However, this is not the case, as Fig. 4.6(b) shows. Also on the log scale, there appears an approximately linear increase in ΔCI95 with increasing average $\log_{10}$(Chl-a/ 0.1 mg m^{-3}). Here, the distinction between the clusters becomes more prominent than in the untransformed Chl-a, with a considerably steeper slope in the cold cluster than in the front and warm clusters. Although the warm and front clusters show a similar relationship, the slope for the front clusters appears slightly steeper.

4.3.4 Inter-annual variability in Chl-a development

To investigate whether the patterns in bloom timing, intensity, and the associated variability observed in the 2018 time series are robust features, I test whether the patterns also appear in adjacent years. Are the differences in bloom development between the regional clusters universal, or specific to 2018 and simply part of inter-annual variability? In this section, I therefore extend the analysis to the years 2016–2021, using the 8-day OC-CCI Chl-a dataset (Sathyendranath et al., 2021).

The seasonal variations in Chl-a are analysed for the individual years while distinguishing between the three regional clusters (Fig. 4.7). The figures display the median (solid lines) together with shaded areas that represent inter-quartile ranges. I chose to display the median here based on the observation that Chl-a follows a right-skewed distribution with considerably higher mean values that are influenced by extreme values, as discussed earlier. Overall, the seasonal variations observed in the 8-day-mean dataset reveal fairly robust patterns, where in all years the increase in Chl-a in spring occurs earlier in the cold (ice-influenced) cluster than in the cluster of warmer Atlantic water. The median Chl-a concentrations observed in the 8-day-mean dataset consistently appear higher than on the daily dataset used in Sect. 4.3.3. In all six years, median Chl-a begins its spring increase considerably earlier in the cold and front clusters than in the warm cluster, starting in April (2017–2021) or May (2016). Peaks in median Chl-a in the warm cluster usually happen around June, extending into July in 2016. In Sect. 4.3.3, I described how the front cluster showed the bloom features of both, the warm and the cold clusters. This pattern is also apparent when the analysis is based on 8-day-mean Chl-a data, but only for the year 2018, and to a lesser extent with a less pronounced second peak in 2019. In the years 2016, 2020, and 2021, the front cluster shows its own peak located between the earlier peak in the cold and the later peak in the warm cluster. In 2017 the first peak of the front cluster follows the one in the cold cluster, and a second peak emerges 2 weeks before Chl-a peaks in the warm cluster. Interestingly, in 2020 median Chl-a steeply increases again in late September until the end of the observation period in all clusters, a behaviour unseen in the other studied years.

Analysing the anomalies from the yearly means (difference in daily mean Chl-a concentration from the annual average), it becomes clear that timings of increased and decreased Chl-a follow similar dynamics within the clusters in the six years, but differ between the clusters. As shown in Fig. 4.8, the highest positive deviations

Table 4.2: Temporal average Chl-a concentrations over the observational periods (ca. mid-March – October) for each year in the identified clusters.

	Avg. Chl-a ($\mathrm{mg\,m^{-3}}$)					
cluster / year	2016	2017	2018	2019	2020	2021
cold	0.95	0.99	0.97	1.06	1.07	0.79
front	0.91	1.15	1.02	1.19	1.34	0.88
warm	0.92	0.91	1.22	1.10	1.04	0.85

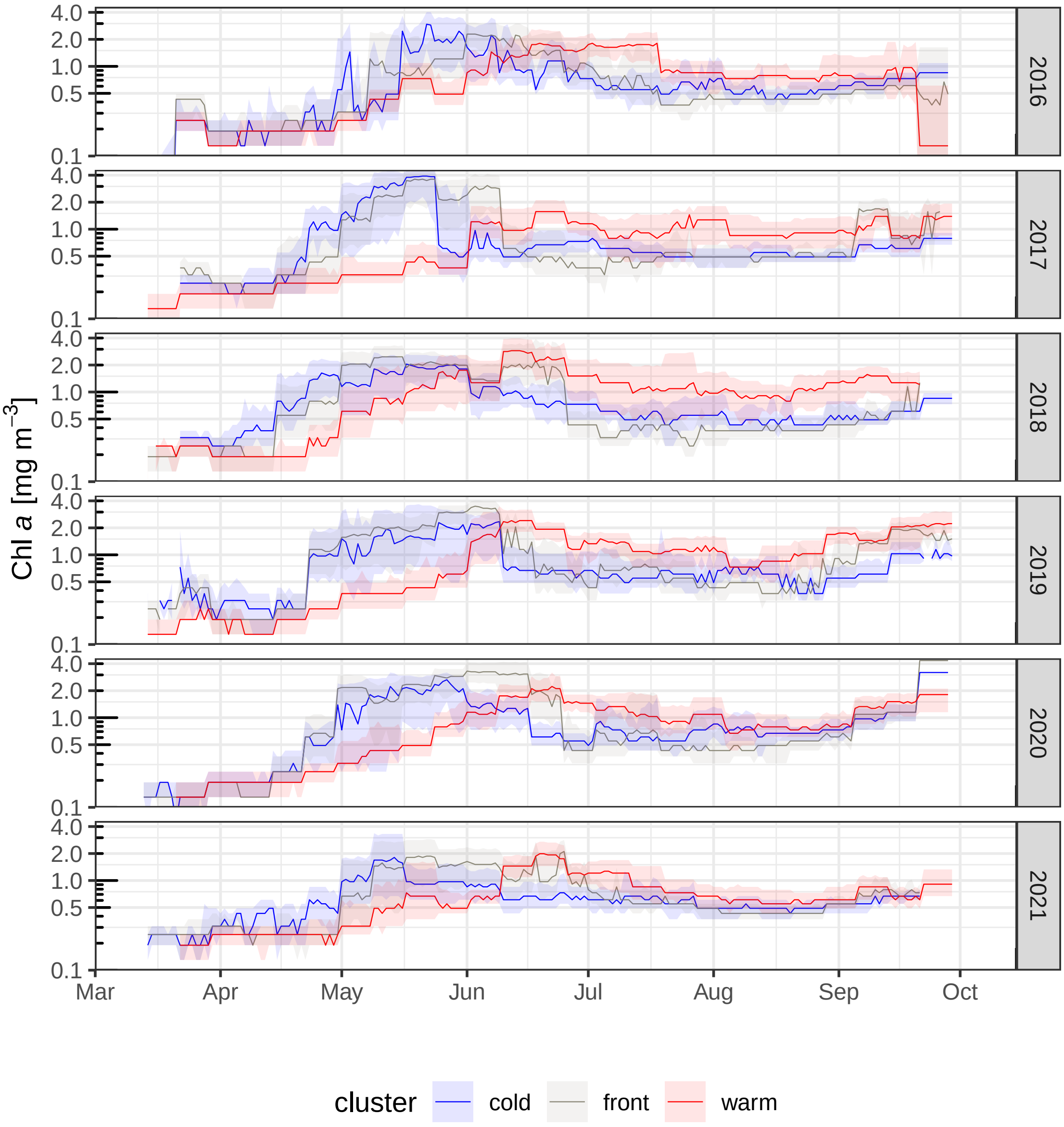

Figure 4.7: Chl-a concentrations and their variability. 8-day means of remote sensing Chl-a concentrations are split into three regional clusters based on the SST. Solid lines represent the median, and shaded areas represent the [Q1, Q3] interval.

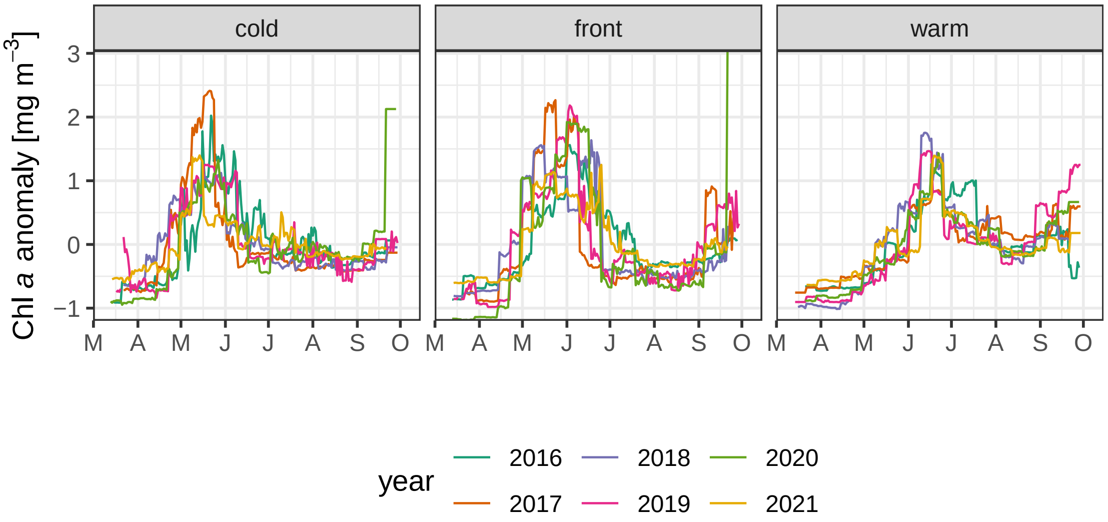

Figure 4.8: Anomalies from the average Chl-a concentration for each years observation period (ca. mid-March – October). Anomalies are calculated as the difference of daily mean Chl-a to the annual mean.

from the annual means occur first in the cold cluster, between early May in 2021 and late May in 2020. In the front cluster, the timing of large positive anomalies is more variable, reaching from the second week of May in 2018 to late June in 2021. Interestingly, the anomalies show a double peak structure for the years 2017, 2018, 2020, and 2021, which is not apparent in the median Chl-a time series shown in Fig. 4.7, except in 2018. The anomalies from the mean peak later in the warm cluster. There, the earliest peaks occur between early June (2018 and 2019) and the second half of June (2020 and 2021). Notably, the anomalies increase again in September in the front (especially 2017, 2019, and 2020) and warm cluster (2017, 2019–2022). In the cold cluster, this can be only observed in 2020.

Yearly averages of Chl-a concentrations within the clusters show no clear trends. Tab. 4.2 shows averages over the observational periods (ca. mid-March – October) of daily mean Chl-a concentrations. Values range from 0.79 mg m^{-3} to 1.34 mg m^{-3} in the cold cluster in 2021 and the front cluster in 2020, respectively.

4.4 Discussion

The results of this analysis have shown that for investigating variability in bloom development, it is meaningful to distinguish between regional (hydrographic) clusters. Apart from the transport routes along the currents, southward in the cold cluster and northward in the warm cluster, the underlying mechanisms responsible for the respective bloom development appear to be different. Intuitively, one would initially assume that the beginning of the bloom occurs earlier in the warmer, northward-moving water masses than in those areas that are influenced by much colder water masses that are strongly influenced by sea ice. In the following, I discuss the distinction that the k-means algorithm has identified based solely on SST data and ask to what extent such regional clusters are representative and can therefore be applied to analyses of data other than SST.

4.4.1 Quality of regime distinction through k-means clustering of remote sensing SST

In the past, several attempts have been made to separate the Fram Strait into meaningful hydrographic or biogeographic subregions, e.g. by a division along the 0° meridian (e.g. Nöthig et al., 2015, 2020), defining stratification regimes related to the proximity to the sea ice (i.e. meltwater vs. mixed layer regimes) (Von Appen et al., 2021), considering surface currents and bathymetry (Trudnowska et al., 2018), or defining general sea ice regimes (permanently ice-covered in the west, seasonally ice-covered in the northeast, predominantly ice-free in the east) (Soltwedel et al., 2016). Gradinger and Baumann (1991) distinguished between the East Greenland Polynya, the East Greenland Shelf, and the Marginal Ice Zone. Although some of these distinctions were rather simplistic, differences in Chl-a phenology and variability could be observed in remote sensing and *in-situ* data.

The distinction of hydrographic regime based on SST proposed by Lampe et al. (2021) was originally meant to classify the water mass properties of HAUSGARTEN *in-situ* stations when physical profiles were unavailable or ambiguous, but showed to be useful in the regionally distinctive analysis of other remote sensing data products, such as Chl-a. In the study of Lampe et al. (2021), two clusters were resolved, separating the cold EGC-influenced and warmer WSC-influenced subregions of the Fram Strait, in which the timings of bloom initiation and average Chl-a concentrations differed.

A limitation of the two-cluster separation is that it does not resolve the highly variable frontal zone. In this study, I could cleanly resolve three distinct clusters, as shown in Figs. 4.2 and 4.3, where the third cluster entails the front region with intermediate SST. Although I perform the clustering on only one single variable, SST, the cluster distinction works well in the Fram Strait as here the gradients in SST are strongly pronounced. K-means clustering is a robust and efficient machine learning algorithm, making it useful for large geospatial data sets, such as remote sensing data. This approach is particularly valuable when *in-situ* data that could be used for regime classification are sparse in time and space.

Including another clustering variable, such as e.g. sea ice cover, may improve the results further to consider its effect on the light profiles and water column stratification. It remains unclear how suitable the k-means clustering approach is for regions with less pronounced gradients in their properties, although a recent study by Mignot et al. (2023) has successfully applied a similar k-means based approach to derive global biogeochemical regions from Bio-Argo data and climatological monthly time series of 23 variables that include metrics related to carbonate chemistry, the biological carbon pump, and oxygen. The biogeochemical regions identified by Mignot et al. (2023) have coherent properties that are surprisingly similar to the biogeochemical biomes identified and proposed by Fay and McKinley (2014). These results, as well as those of my study, demonstrate the value of this machine learning algorithm for dividing oceanic areas into regions with similar characteristics.

4.4.2 Variability in Chl-a remote sensing observations

Clustering remote sensing Chl-a data into hydrographic SST regions reduces the spatial variability in the cold and warm clusters compared to the un-clustered Chl-

a data for the whole region, as demonstrated in Sect. 4.3.3, which indicates that Chl-a phenology and variability indeed differs in the two subregions. This supports the findings of Nöthig et al. (2015, 2020) and Lampe et al. (2021). The variability observed in the front cluster, however, was similar to the variability in the entire region. In this region covering parts of the marginal ice zone, the mesoscale variability is especially high, which strongly impacts phytoplankton growth (Schourup-Kristensen et al., 2021). The highest median Chl-a concentrations were observed in the front cluster (approx. 4 mg Chl m^{-3}), in line with the findings of Cherkasheva et al. (2014) who report the highest Chl-a concentrations in the marginal ice zone where melting sea ice stabilises the water column.

The strength of the variability seen in observations, and thus the level of the variances, is clearly related to the overall spatially widespread concentration of Chl-a. According to the statistics of the Chl-a concentrations within the three clusters, I learned that at times of high mean and median Chl-a concentration, variability is higher, as shown in Fig. 4.5a, and this relationship is steeper in the cold cluster (Fig. 4.6). Analysing the variability of $\text{Chl}_{\text{trans}}$ in Fig. 4.5b shows an increase of variability until the bloom peak in the respective clusters is reached, followed by a gradual gentle decrease of variability post-bloom. Pre-bloom variability however was considerably higher in the cold and front clusters. Normalising ΔCI95 by the mean $\text{Chl}_{\text{trans}}$ (Fig. 4.5c) shows, that not only the overall Chl-a concentration drives the observed variability, but also that variability is generally higher in the cold cluster compared to the other clusters. Furthermore, while the normalised variability of $\text{Chl}_{\text{trans}}$ is approximately constant in all clusters throughout the observation period, strong deviations stand out in the cold cluster that coincide with the onset of the spring bloom in May and later in July with the decline in SIC (see Fig. 4.2). These deviations indicate that SIC has a strong influence on Chl-a variability. Sea ice plays a large role in the subsurface light availability, water column stratification and thus nutrient distribution, and serves as a substrate for the growth of ice algae, all factors influencing phytoplankton growth (e.g. Castellani et al., 2022). The confidence interval of SIC (here, mean±SD) ranges between 50–100 % during the spring bloom in the cold cluster, which may allow growth in places with less ice cover, but suppress growth where SIC is high, leading to high spatial variability during this time, as the blooms turn out patchy (Trudnowska et al., 2016). During the decline of SIC in July, it drops to 25–75 % in August, indicating here the meltwater stratification increases Chl-a variability (Cherkasheva et al., 2014). Therefore, it seems likely that the large variability in SIC drives the variability in Chl-a in the front and especially in the cold cluster, as previously reported in e.g. Wu et al. (2007); Cherkasheva et al. (2014); Renner et al. (2023).

In the multi-year analysis of 2016–2021, no trends in bloom timing or overall Chl-a concentrations are apparent. The bloom threshold is reached first in the cold cluster, typically in May, and this is consistent throughout the multi-year time series, supporting the findings in Lampe et al. (2021). Although Nöthig et al. (2015) report a positive trend in average Chl-a in the WSC dominated region between 1998–2012, Nöthig et al. (2020) linked this trend to a warm anomaly lasting until 2009, after which average concentrations decreased again. Increased light availability due to earlier ice retreat and thinner ice cover may have significant effects on

Arctic PP (Castellani et al., 2022). For example, Wu et al. (2007) have shown that earlier ice retreat in the Labrador Sea causes earlier and prolonged blooms. However, in the Fram Strait, where light limitation inhibits growth before May (Cherkasheva et al., 2014), earlier ice retreat may cause mismatches between water column stratification and increasing light levels, where light is not sufficient yet at times when stratification would favour a bloom. For the whole Arctic region, trends between +30 % for the period 1998–2012 (Arrigo and van Dijken, 2015) and +4.4 % between 1998–2018 (Kulk et al., 2020) are reported from the analysis of remote sensing Chl-a data products. It remains unclear whether these reported changes are climate change induced trends or part of natural variability linked to atmospheric oscillation processes (Soltwedel et al., 2016). Henson et al. (2010) suggest that a time series of at least 40 years is needed to detect climate change signals reliably amidst the noise of natural variability.

4.4.3 Limitations and outlook

The spatial and temporal coverage of the Operational Sea Surface Temperature and Ice Analysis (OSTIA) SST data product is of remarkable usefulness, as it is a composite of satellite observations, drifters, and buoys (Good et al., 2020), on a 0.05x0.05°grid in daily time steps. It is therefore particularly suitable as a clustering variable. Unfortunately, the resolution of the Chl-a data products is considerably lower. The spatial and temporal coverage of the daily CMEMS Ocean Color data product (CMEMS and ACRI, 2023) has many gaps especially in the high latitudes due to aerosols, clouds, seasonal changes in the solar zenith (sun glint and low illumination), and sea ice cover (e.g. Cole et al., 2012; Cherkasheva et al., 2014; Kuhn et al., 2023). Especially in the cold cluster, where ice cover plays a large role, only few pixels are available on the majority of days. Such conditions may lead to estimates that are eventually biased because only those pixels with low ice cover can be considered in the variability analysis and thus may distort our measures of spread and central tendency. It remains unclear how large this effect is. Further investigations are needed in this regard. The coverage of the 8-day mean OC-CCI data product used for the multi-year analysis is slightly better but still shows considerable gaps. Cherkasheva et al. (2014) reports that even for monthly composites of the merged GlobColour data product (MERIS, MODIS, SeaWiFS), estimates for singles pixels were composed of only 2–5 days. As Comiso (1995) stated almost 3 decades ago, remote sensing data do not and may never replace surface measurements. Still, such data are a good proxy for the larger scale distributions and development of biogeochemical variables, such as Chl-a.

Finally, characterising the hydrographic regions of the Fram Strait on only one variable, SST, is although practical, likely too simplistic. It remains to be tested how the introduction of additional variables of the physical water properties, such as sea surface salinity and sea ice cover may improve the identification of ocean regions with distinctive characteristics.

4.5 Conclusion

This study utilises a machine learning approach to derive hydrographic subregions (clusters) in the Fram Strait, providing insights into, and helping to unravel, the variability of chlorophyll-a (Chl-a) concentration on both intra- and inter-annual scales. The representativeness and quality of these subregions, identified through k-means clustering of remote sensing Sea Surface Temperature (SST), are thoroughly examined. Their use seems particularly suitable for the analysis of large geospatial datasets in regions with pronounced environmental gradients.

The effectiveness of this approach in the Fram Strait, characterised by significant SST gradients, is evident. This analysis reveals clear differences in Chl-a phenology and variability within the identified hydrographic clusters:

- The cold cluster covers the permanently ice-covered region and parts of the marginal ice zone. Here, phytoplankton blooms typically start in May, and variability is driven largely by variations in sea ice cover.

- The front cluster, covering part of the marginal ice zone, exhibits high variability, influenced by mesoscale variability, the dynamic sea ice cover, and total Chl-a concentration. The timings of the peak of the bloom in this region is variable, generally closer to the timing in the cold cluster, but occasionally showing a second bloom peak associated with the later bloom in the warm cluster, or a unique peak in-between.

- The warm cluster covers the ice-free Atlantic-influenced region in the southeast. Blooms occur later compared to the cold and front clusters, typically in late June. This delay is a robust feature that occurred in all the years studied here. In this region, where no ice cover is observed, the late onset of the bloom is determined solely by the mixing and stratification conditions, which are superimposed by the seasonal change in average daylight conditions at the sea surface. Less variable growth conditions therefore cause less variability in the observed Chl-a concentration.

Despite the success of the machine learning approach, limitations arise from the lower spatial and temporal coverage of Chl-a data. Biases in variability estimates, particularly in the cold cluster with significant ice cover, highlight the need for further investigations. Future studies should explore the incorporation of other physical water properties into the clustering methodology for a more comprehensive hydrographic characterisation.

In conclusion, this research contributes valuable insights into the hydrographic variability of the Fram Strait, showcasing the efficacy of machine learning techniques in unraveling complex environmental dynamics. The identified hydrographic subregions provide a foundation for an improved understanding and interpretation of Chl-a variability, laying the groundwork for future investigations into the intricate relationships between physical properties and phytoplankton dynamics in this critical gateway to the Arctic Ocean.

4.6 Acknowledgement

I would like to express my gratitude to the PEBCAO (Plankton Ecology and Biogeochemistry in a Changing Arctic Ocean) group for their valuable comments on earlier versions of this research. Special thanks to Dr. Hongyan Xi for her assistance in interpreting remote sensing chlorophyll-a and Phytoplankton Functional Type datasets. Additionally, I thank Dr. Markus Schartau for his guidance on statistical analyses and his constructive comments, which significantly contributed to improving this manuscript. I am thankful for the proofreading and helpful comments from Dr. Tianfei Xue.

Chapter 5

Conclusion and Outlook

5.1 General conclusions

It is scientific consensus that the Arctic is undergoing significant change in terms of warming and sea ice retreat, but projections of the impacts of future climate conditions on Arctic ecosystems and the biogeochemical cycling of elements are still subject to great uncertainty. The limited availability of observational data contributes to this uncertainty surrounding the Arctic Ocean since the region is difficult to sample and even remote sensing can only provide insights to a limited extent.

The major aim of this work was to explore and understand the range and causes of spatial and temporal variability in the community size structure and abundance of Arctic protist plankton. This was achieved by combining data analyses and modelling. Different types of observational data, from microscopic measurements to remote sensing products, were used to constrain the simulation results of a Lagrangian size-based plankton ecosystem model. The individual chapters of the dissertation provide specific insights into the Arctic system in and around the Fram Strait. The individual studies are interlinked. The derivation of the plankton spectra (Chapter 2) was an important prerequisite for the modelling (Chapter 3), especially concerning the added value of how a meaningful analysis of the model solutions can be approached. Spatial separation according to k-means clustering was already part of the plankton size analyses and its elaboration in the third study (Chapter 4) not only confirmed the previous results but also extended and enhanced our understanding of spatio-temporal variations in bloom dynamics in general.

To investigate the spatio-temporal variability in the size composition of the protist plankton community, we derived continuous size spectra from highly resolved microscopic data using Kernel-Density-Estimation in **Chapter 2**. The size spectra revealed seasonal shifts in the community size composition that accompany changes in total plankton biomass, from smaller cells (< 30 µm) in summer to larger cells in autumn. Furthermore, we found deviations from the typical log-linear relationship of abundance and size that indicate size ranges of preferred grazing (negative deviations, gaps) or 'loopholes' (positive deviations, mounds), and suggest changes between the roles of bottom-up and top-down regulatory processes in the microbial food web. Notably, these size ranges appeared in both phyto- and zooplankton, emphasising the role of predation amongst ciliates of slightly different sizes (intra-guild predation) and omnivory. The separation of Arctic and Atlantic waters appeared crucial, as it revealed general similarities between the size spectra, but also differences that could be attributed to different timings in the seasonal succession of the protist plankton. Comparing the changes in the plankton community size structure and remote sensing chlorophyll-a concentrations of the polar Arctic waters in the Fram Strait with their counterparts of the northern Atlantic waters, we learned that the seasonal plankton succession in the Artic water is approximately two to three weeks ahead.

To unravel the extent to which the variability observed in HAUSGARTEN measurements of the plankton size structure, concentrations of particulate and dissolved organic matter, and rates of productivity and export can be explained by differences in the environmental conditions along the northward and southward transit of water parcels through the Fram Strait, we employed a numerical model in **Chapter 3**. In this Lagrangian modelling approach, we force a size-based (9 distinct size classes of phyto- and zooplankton) 1D ecosystem model with physical conditions that occur along trajectories tracing the major currents through the Fram Strait. The four ensembles of trajectories differ in their origin (Atlantic and Arctic) and timing of HAUSGARTEN transit (summer and autumn). The model solutions generally correspond to the observations of various types, including *in-situ* measurements of nutrient and organic matter concentrations, remote sensing estimates of phytoplankton standing stocks, and climatological nutrient concentrations. Notably, the model is able to reproduce the seasonal shift in size structure towards more larger cells ($>$ 35 µm) in the post-bloom phase, in agreement with our findings of the size spectral analyses in Chapter 2, although discrepancies between observed and simulated size spectra indicate further need to improve grazing relationships and the consideration of specific size ranges of preferential grazing. Despite using the same model parameters, the temporal development of primary production, community size structure, and export varied among the model ensembles, revealing that 10–72 % of the variability observed at HAUSGARTEN sites is driven by differences in the physical forcing prior to reaching the site. In particular, variations in the light regimes influenced the timing of blooms and the size structure of phytoplankton, and subsequently their grazers, which ultimately affected OM export. Peaks in the model's simulated productivity and vertical export occur significantly earlier and at some distance compared to the timing and location of *in-situ* sampling in the Fram Strait, which indicates that *in-situ* sampling during both, the summer and the autumn campaigns, captures snapshots of post-bloom situations that are associated to bloom events that happened outside of the HAUSGARTEN region.

For a more in-depth and comprehensive analysis and evaluation of spatial and temporal variability of phytoplankton standing stocks in the heterogeneous hydrographic subregions of the Fram Strait, I employed a machine learning clustering method on remote sensing data in **Chapter 4**. This approach extends the clustering technique described briefly in Chapter 2 and can provide a basis for comparisons of the degree of variability in phytoplankton standing stocks between the simulation results of Chapter 3 and large-scale remote sensing datasets. In contrast to resolving two regions, the warm Atlantic- and the cold Arctic-influenced sectors, I resolve a third sector that encompasses the front region with intermediate sea surface temperatures. The hydrographic sectorisation reveals differences in the phenology of chlorophyll-a concentrations within the subregions, with earlier onset of blooms in May in the Arctic region, in late June in the Atlantic region, and mixed signals in the front region. While chlorophyll-a variability was particularly high at times when its concentrations were high in all clusters, i.e. during bloom peaks, the intrinsic, concentration-normalised variability was significantly higher in the cold cluster where large variations in sea ice dynamics are observed, compared to the other clusters.

In conclusion, the distinction of water masses in the Fram Strait, realised by SST-based clustering in Chapters 2 and 4 and Lagrangian modelling in Chapter 3, revealed significant differences in the seasonal phenology of plankton standing stocks, community composition, productivity, and export rates. These differences are partly driven by differences in the characteristics of the respective water masses and the different environmental conditions they have been subject to.

5.2 Critical aspects on the comparability of community size structure representations

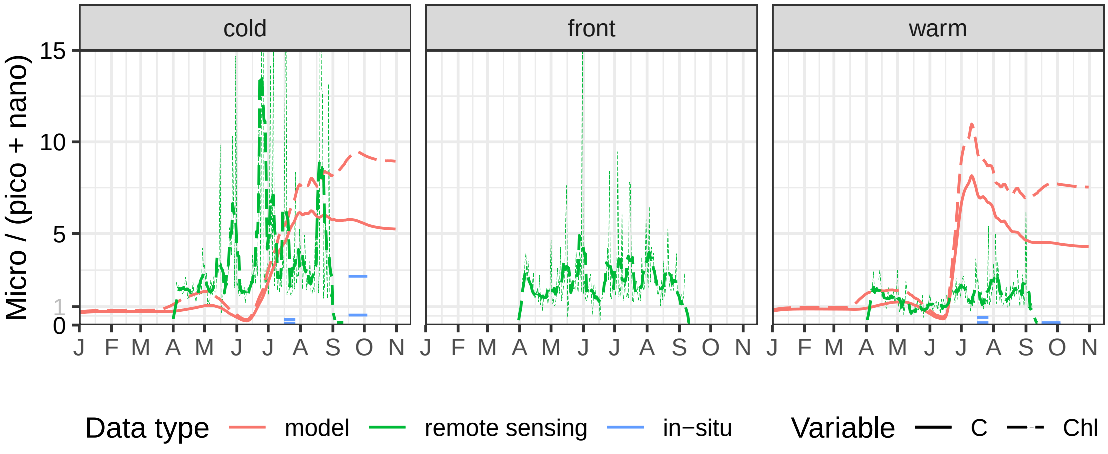

Figure 5.1: Average proportions of protist phytoplankton size classes in *in-situ* observations, model results, and remote sensing observations. Shown here is the relation of microplankton (20–200 µm) to the sum of pico- (0.2–2 µm) and nanoplankton (2–20 µm) biomass (carbon or chlorophyll).

A major advantage of continuous size spectra of the protist plankton community is that size spectra may resolve details of the community size structure that are not always recognisable when the size data are classified into discrete size bins. Furthermore, without the need to impose assumptions on size bins, continuous size spectra derived from data of various origins can be quantitatively compared by applying distance metrics. Additionally, continuous size spectra are well suited for quantitative assessments of size-based model results, as done in Chapter 3. For this, size-binned model results are simply interpolated to the discretization points used to describe the continuous plankton spectra based on observations, regardless of how many size bins the model resolves. This way, model results and observations of various size resolutions, binned or continuous, can be quantitatively compared by applying a distance metric such as the Integrated Quadratic Distance (IQD). While the size spectra derived in Chapter 2 were obtained using a Kernel Density

Estimator with Gaussian kernels, the application of Kernel Density Estimation has been further improved during the period of this thesis with the diffusion-based Kernel Density Estimator by Pelz et al. (2023), which highlights the potential for future research work.

However, as the derivation of continuous size spectra of high resolution requires considerable time effort and expertise for the microscopic analyses, such valuable data is rarely available. Therefore, one research focus has been the derivation of plankton size information from remote sensing observations (e.g. Xi et al., 2021). Although remote sensing data products typically have a much higher temporal resolution than the time intervals between *in-situ* sampling campaigns, obtaining information about the size structure of the plankton community from remote sensing is associated with large uncertainties. Therefore, some useful product could be the ratio of large (micro-, 20–200 µm) to small (nano- and pico-, 0.2–20 µm) phytoplankton biomass, which can be directly compared with counterpart ratios derived from observed or simulated size spectra, as shown in Fig. 5.1. Here, the *in-situ* data (blue) describe the ratio of large by small phytoplankton biomass, derived from the integration of biomass size spectra. Since various conversions from biovolume to carbon biomass are common in the literature (see Sect. 5.3.2), the two individual lines shown per each period denote ratios derived from size spectra of Chapter 2 that assume a steep and a more moderate carbon to biovolume relationship, respectively. The resulting ratios can differ significantly, especially when abundance is high on either side of the size spectrum, which is the case in the spectrum from the cold Arctic waters in autumn, for example. Despite the clear shift from smaller to larger plankton from summer to autumn in both Arctic and Atlantic water masses documented by the size spectra shown in Chapter 2, in the large/small plankton biomass ratio, this shift is only visible in the Arctic water and even appears reversed in the Atlantic water.

Furthermore, the variable selected as a biomass proxy appears important when comparing large/small plankton biomass ratios, as shown with the model results (red lines) that are available for carbon (solid line) and chlorophyll (dashed line) biomass, even though the units of biomass become eliminated in the fraction. Especially in the post-bloom phase, differences become large and are caused by the variable stoichiometry assumed in the model. Although the model and *in-situ* spectra show some good agreement in Chapter 3, the large/small biomass ratio representations do not align. Large/small chlorophyll-biomass ratios estimated from remote sensing (following the procedure described in Chapter 4, but using the size-binned PFT data product by CMEMS and ACRI (2023)) reveals large temporal variability in all three water masses in the daily ratios (thin green line), even when smoothed with a moving average function (thicker line). Generally, the ratios but also their variability are largest in the Arctic, intermediate in the front, and smallest in the Atlantic water masses, with no apparent trend over the growth period.

5.3 Open questions and perspectives

5.3.1 Microscopy

The size spectra presented in Chapter 2 were compiled based on microscopy observations from water samples collected *in-situ*. The data comprises size measure-

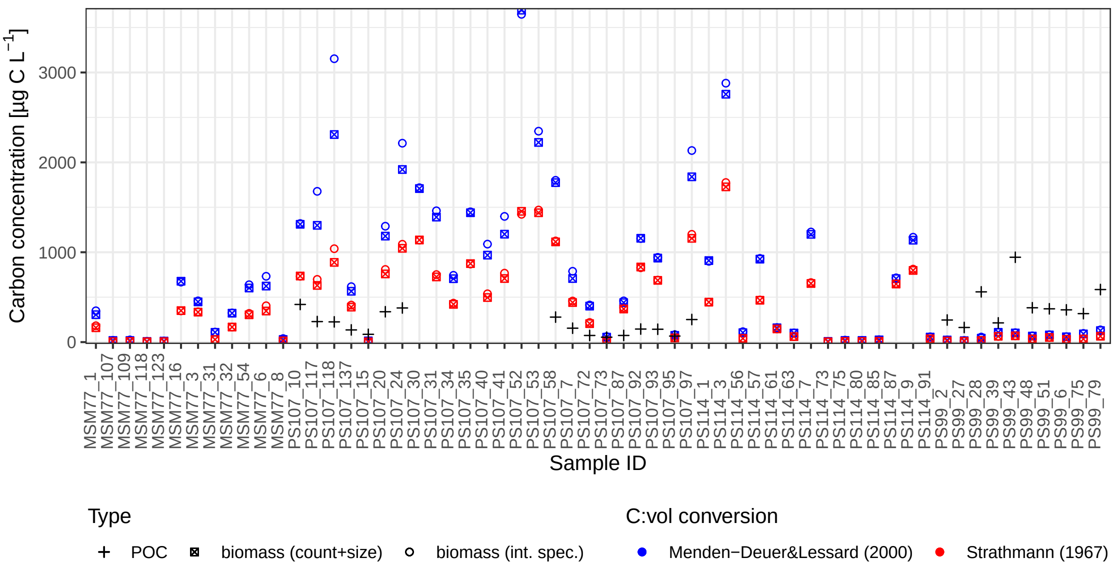

Figure 5.2: Comparison of C-biomass estimation methods, conversion factors, and total POC concentrations between different taxonomists.

ments of cell length and width, and identifications to the lowest possible taxonomic level (species, genus, or higher) for each individual cell that settled in a sedimentation chamber, thus the collection is labour-intensive and requires great expertise in plankton taxonomy. A common problem is the human factor when it comes to categorising species based on their morphological characteristics, especially since the characteristics may overlap between species. The outcome of microscopic measurements can be highly subjective with respect to the observer. For example, trained experts reach only around 43 % consensus between different people in dinoflagellate identifications, and 67–83 % self-consistency (Culverhouse et al., 2003).

As shown in Fig. 5.2, large differences arise based on the biomass estimation method (using the raw counts and size measurements versus integration of size spectra), the scaling relationship used to convert biovolume to carbon biomass (discussed in the following subsection), and, strikingly, the individual observer performing the microscopy. The data used for the analyses in Chapter 2 were collected by two student helpers (SH). Samples collected during the cruises MSM77, PS107, and PS114 were processed by SH1, and show large variation in total estimated biomass, which differs significantly by estimation methods and scaling relationships. Furthermore, the estimated biomass consistently exceeds HPLC measurements of particulate organic carbon (POC), although biomass should only be a fraction of the total POC. In contrast, samples processed by SH2 (all PS99 samples) show significantly lower estimates of biomass, with less variation and values smaller than the total POC.

By deriving confidence intervals of the size spectra through a bootstrapping approach, we attempted to explicitly take into account error sources related to the size measurements and cell counts. These explicit uncertainty considerations are obviously insufficient, as they do not account for differences between observers. However, the variability introduced by the subjectivity can be substantial, as Fig. 5.2 illustrates. Further research on how to include this kind of uncertainty into the size spectra confidence intervals and how to include the resulting confidence intervals into model evaluation metrics is warranted.

5.3.2 Abundance-to-biomass conversions

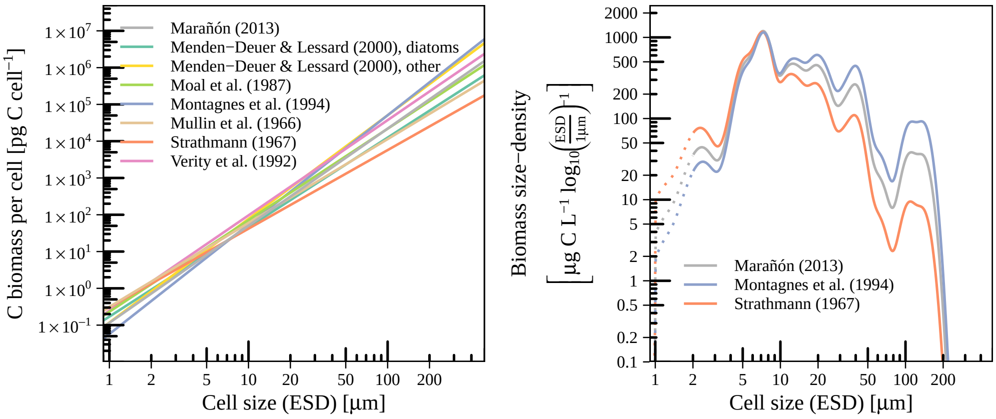

Figure 5.3: Comparison of cell volume:C biomass using different scaling relationships (left) and the resulting biomass size spectra (right), here shown for the S1 phytoplankton spectrum (summer, Atlantic waters) for the steep scaling relationship after Montagnes et al. (1994), an intermediate scaling after Marañón et al. (2013), and a more moderate scaling after Strathmann (1967).

Standing stocks of plankton are commonly expressed in units of carbon or nitrogen concentrations and represent a fundamental parameter in biogeochemical budgets and models. Plankton biomass can be estimated from microscopic measurements of abundances per cell type (species, genus, or higher taxonomic levels) and by applying constant but specific conversion factors (e.g. Smetacek, 1975). Alternatively, more sophisticated methods involve determining cellular volumes of plankton through microscopy and subsequently converting them to biomass using biomass-to-volume ratios. Here, uncertainty is introduced from the conversion of size-abundance spectra to biomass spectra. Cell volume (derived from size measurements and geometrical considerations) can be converted to carbon (or nitrogen) biomass using allometric scaling relationships. Various scaling relationships have been proposed in the literature, differing in their slopes and intercepts, as summarised in Tab. 5.1.

Depending on the C:volume scaling relationship, the carbon content per cell differs, especially in the small and large ends of the plankton size range, as illustrated in Fig. 5.3 (left). Applying such relationships to size-abundance spectra thus leads to different estimates of biomass per size class and total biomass. In Fig. 5.3 (right), the S1 phytoplankton size-abundance spectrum presented in Chapter 2 is converted to biomass using the steep C:vol scaling after Montagnes et al. (1994), an intermediate scaling after Marañón et al. (2013), and the moderate scaling after Strathmann (1967), showing similar biomass estimates in the nanoplankton size range, but considerable deviations in the pico and micro size ranges. Consequently, estimates of total biomass differ significantly, between 571, 499, and 420 $\mu g\,C\,L^{-1}$ depending on the scaling relationship applied (steep, intermediate, and moderate scalings, respectively).

This uncertainty affects data-model comparisons of the plankton size structure. In Chapter 3, we applied the Integrated Quadratic Distance (IQD) metric to compare simulated and observed plankton biovolume spectra. Here, the model output,

Table 5.1: Biomass-to-volume (C:volume) scaling relationships for carbon. Moal et al. (1987), Verity et al. (1992), Montagnes et al. (1994), and Menden-Deuer and Lessard (2000) also report N:vol relationships (not shown here).

C:vol	Reference	Comments
$\log_{10}\mathrm{C[pg]} = 0.76\log_{10} V - 0.29$ $\Rightarrow \mathrm{C[pg\ cell^{-1}]} = \frac{1}{10^{0.29}} V^{0.76} = 0.513 V^{0.76}$	Mullin et al. (1966)	Cultures of mixed plankton, incl. diatoms
$\log \mathrm{C[pg]} = -0.314 + 0.712 \log V$ $\Rightarrow \mathrm{C[pg\ cell^{-1}]} = \frac{1}{10^{0.314}} V^{0.712} = 0.485 V^{0.712}$	Strathmann (1967)	Diatoms, cultures of selected species
$\ln \mathrm{C[pg\ cell^{-1}]} = 0.829 \ln V - 0.927$ $\Rightarrow \mathrm{C[pg\ cell^{-1}]} = e^{-0.927} V^{0.829}$	Moal et al. (1987)	Batch culture of 11 species, incl. diatoms
$\log \mathrm{C[pg]} = -0.363 + 0.863 \log V$ $\Rightarrow \mathrm{C[pg\ cell^{-1}]} = \frac{1}{10^{0.363}} V^{0.863} = 0.434 V^{0.863}$	Verity et al. (1992)	Cultures of unialgal, non-diatomaceous marine plankton
$\mathrm{C\ [pg\ cell]^{-1}} = 0.109 V^{0.991}$	Montagnes et al. (1994)	Cultured species, incl. diatoms
$\mathrm{C\ [pg\ cell]^{-1}} = 0.288 V^{0.811}$	Menden-Deuer and Lessard (2000)	only diatoms
$\mathrm{C\ [pg\ cell]^{-1}} = 0.216 V^{0.939}$	Menden-Deuer and Lessard (2000)	only non-diatoms
$\mathrm{C\ [pg\ cell]^{-1}} = 10^{-0.69} V^{0.88} = 0.2042 V^{0.88}$	Marañón et al. (2013)	monocultures of 22 phytoplankton species

which is given in carbon biomass per size class, is first converted to abundance per size class and then biovolume per size class. In our model, we assume the intermediate carbon cell quota of Marañón et al. (2013) for this conversion. Further research is needed on how much differences in the assumed C:volume scaling relationships affect model representations of the community size structure, and how such uncertainty could be included in the evaluation metrics.

5.3.3 Grazing relationships

In Chapter 2, we identified specific size ranges (3–4, 8–10, 25–40, and 70–100 µm ESD) that deviate from the typical log-linear relationship of abundance and size. The presence of these deviations in both phytoplankton and zooplankton spectra reveals omnivory and size ranges of elevated abundance indicate ‘loopholes’ or niches of either reduced grazing pressure, or enhanced growth conditions, or both.

A substantial finding is that other, independently observed, size-spectra (Schartau et al., 2010) display similar patterns as those identified in this thesis, as shown in Fig. 5.4. In this comparison of size spectra of the plankton (phyto- and zooplankton combined) community observed in the Fram Strait and size spectra compiled from data collected during iron fertilisation experiments, similar patterns of positive (green background) and negative (grey background) deviations from the log-linear relationship of size and abundance are apparent. Although these specific size ranges do not show perfect agreement in both datasets, their overlap is striking, indicating the underlying mechanisms may be universal. Most interestingly, the gap observed in the 3–4 and 4–5 µm range is clearly expressed in both observations. Likewise, although not very pronounced, a step-like depression is visible in the size range between 8 and 10 µm in these spectra. Furthermore, a critical size range seems to be around 30–50 µm, where a clear trough can be identified in the Fram Strait spectrum. It is this particular size range above which a substantial increase in abundance was observed in the spectra of the iron-fertilized patch.

Our model in Chapter 3 assumes a static optimum predator-prey size ratio of $\delta_{\text{opt}} = 10$, meaning that predators reach optimal grazing rates when their prey is 10 times smaller, with decreased grazing for smaller and larger prey. However, the grazing preferences differ between plankton taxa, for example, dinoflagellates show optima at predator-prey size ratios of 1:1 and ciliates around 8:1 (Hansen et al., 1994). An important improvement in the modelling approach may be achieved by considering these size ranges of preferential grazing and 'loopholes' of reduced grazing pressure or physiologically better growth conditions for the phytoplankton. It may be worth testing different allometric relationships in combination with specific grazing kernels to clarify the details that emerge from the observed plankton size spectra.

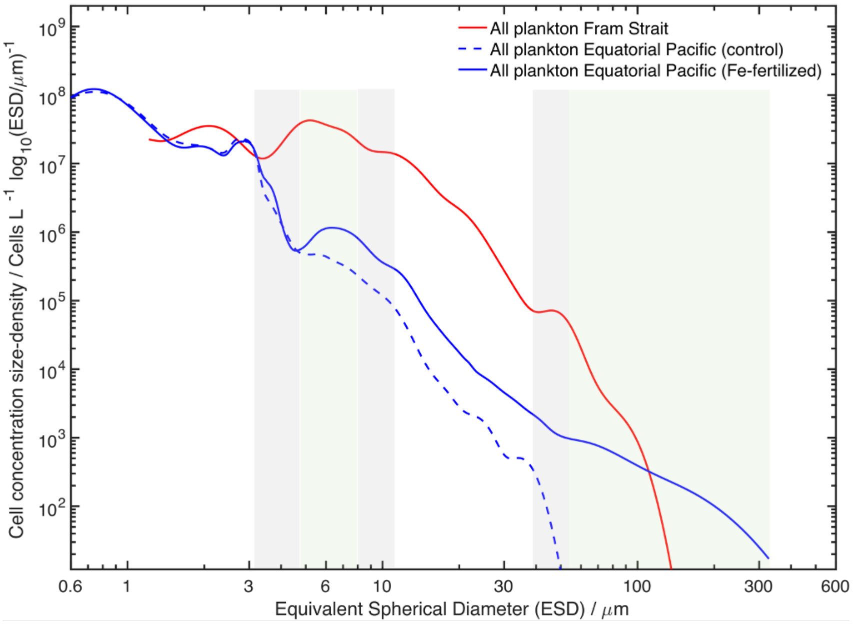

Figure 5.4: Comparison of plankton size spectra in the Fram Strait (Chapter 2, phyto- and zooplankton) to size spectra of plankton during IronEx II iron fertilisation experiments (Schartau et al., 2010). Figure kindly provided by Markus Schartau (personal communication).

A. Supporting Information for ‘Spatio-temporal variations in community size structure of Arctic protist plankton in the Fram Strait’

A.1 Resolution of *composite* and *combined* size spectra of phyto- and protozooplankton

Composite size spectra of maximum resolution can be constructed when individual size spectra of every taxonomic group are added up, i.e. j represents all taxonomic groups present in the dataset. All taxon-specific KDEs can be assembled to a *composite* size spectrum, for example of all phytoplankton or zooplankton taxa:

$$\mathrm{KDE}^{\mathrm{composite}}_{\mathrm{phy/zoo}}(s) = \sum_{j=1}^{M_{\mathrm{phy/zoo}}} \overline{\mathrm{KDE}}_j(s, h_j) \tag{A.1}$$

Here, the bandwidth parameter h_j is taxon-specific. The variability in size is typically smaller within taxa than in combined phytoplankton and microzooplankton subsets, which results in a smaller degree of smoothing (see equation 5), and thus a higher resolution in *composite* spectra, as compared to *combined* spectra.

The *composite* size spectra (Fig. A.1, left panels) therefore exhibit details with

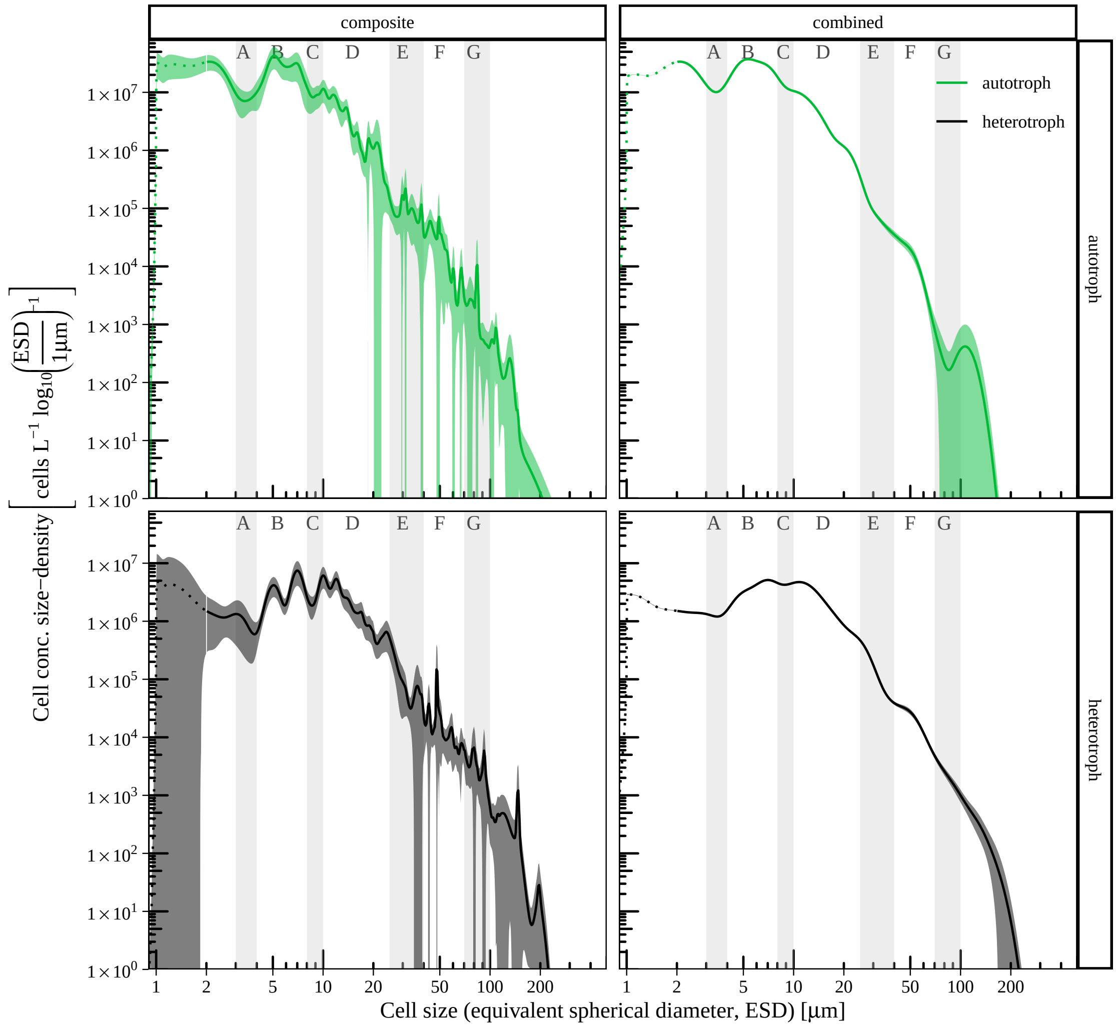

Figure A.1: *Composite* (left) and *combined* (right) size spectra for autotrophic (upper) and heterotrophic (lower) microplankton.

the highest possible resolution of the communities’ size structure. The high level of detail in the *composite* size spectra turned out to be associated with considerable uncertainties, with many narrow peaks, in particular for ESD $> 20\,\mu m$. The abundance of cells of ESD $< 20\,\mu m$ seemed less variable among taxa. The highest abundance in phytoplankton appeared in the proximity of $5\,\mu m$ and also around ESD $= 7\,\mu m$. These were mainly diatoms and prymnesiophytes. Likewise, the highest abundance of heterotrophs fell into the same size range. It is noteworthy that the distinct peaks around ESD $= 5\,\mu m$ and ESD $= 7\,\mu m$ were also apparent in the spectra of heterotrophic cells, but with an additional distinct peak in the proximity of 10–11 µm. Furthermore, heterotrophic dinoflagellates lead to an additional peak at ESD $= 200\,\mu m$.

Considering the confidence limits, it appeared difficult to unambiguously interpret ecological details of the *composite* size spectra. We found major characteristics of the *composite* size spectra to be well and consistently captured by the *combined* size spectra (Fig. A.1, right panels). Similar to the *composite* size spectra, autotrophic and heterotrophic *combined* spectra overlapped between ESD $\approx 20\,\mu m$

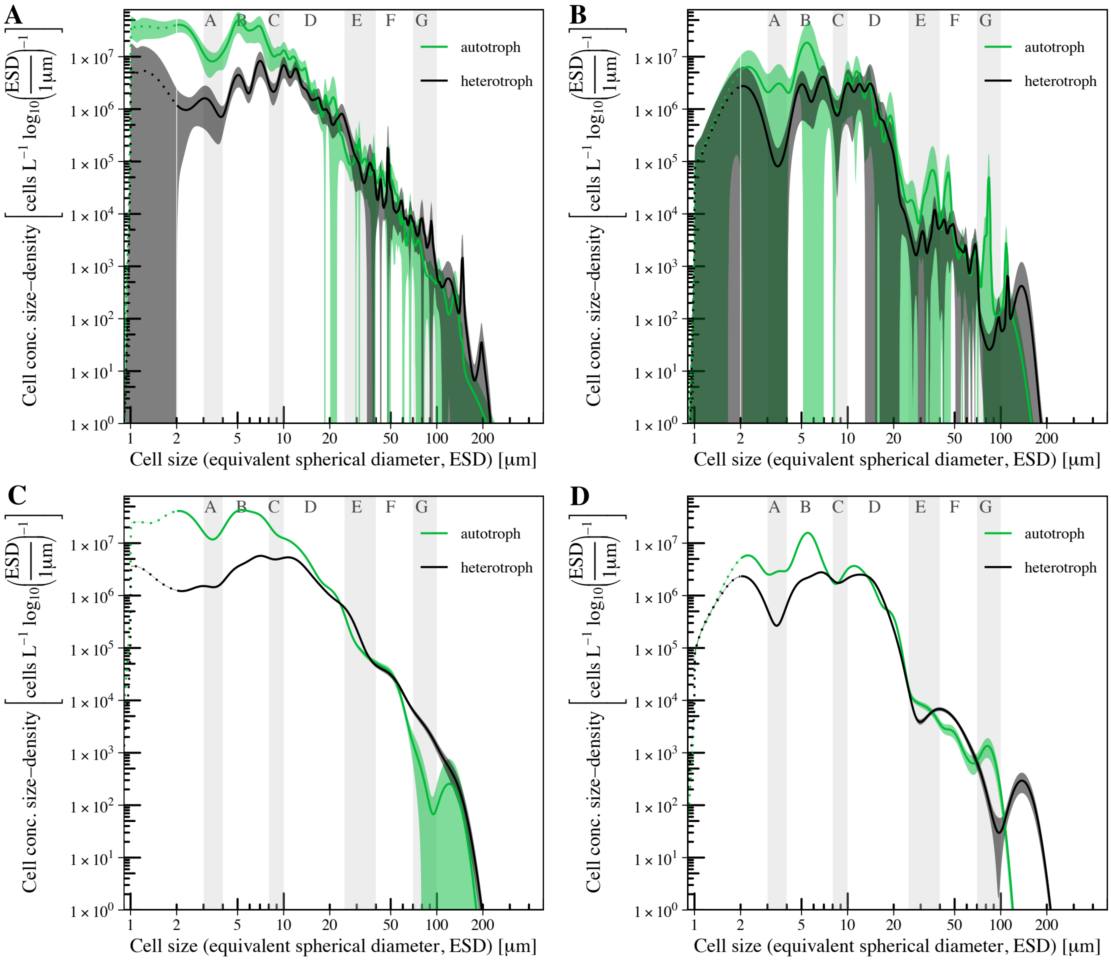

Figure A.2: *Composite* size spectra for summer (**A**) and autumn (**B**). Species-specific size spectra were summed to autotrophic and heterotrophic spectra and averaged across samples; *Combined* size spectra for summer (**C**) and autumn (**D**), derived from a combined data-set of all available data. Shaded areas mark the confidence interval ($\overline{\mathrm{KDE}}(s) \pm 1.96 \times \mathrm{SE}(s)$).

and ESD ≈ 50 µm. In size ranges ESD > 50 µm, where cell abundance decreased significantly, *combined* and *composite* size spectra differed. The largest phytoplankton in the *composite* spectrum was larger than ESD = 200 µm, while the *combined spectrum* approximated 1 cell L^{-1} s^{-1} at ESD ≈ 180 µm. Furthermore, a symmetrical peak was centred around 110 µm in the *combined* spectrum and corresponded an trough in the *composite* spectrum, where in turn a peak followed around ESD ≈ 140 µm. Heterotrophic cells covered approximately the same size range in the *composite* and *combined* spectra.

Analogously, the analysis of *composite* seasonally separated size spectra (Fig.A.2**A** and **B**) gave no clear advantage over the *combined* spectra (Fig. A.2 **C** and **D**). Many details in the *composite* size spectra are subject to considerable uncertainty, which complicates the identification and interpretation of general trends, if compared to patterns derived with the *combined* spectra. For instance, the comparison between summer (left panels of Fig. A.2) and autumn spectra (right panels) illustrates that the *combined* size spectra show only a few peaks and troughs, but total cell concentration are still in accordance with the *composite* spectra. Important and predominant features, e.g. the depression around 4 µm, the step-like drop around 30 µm, and the trough in summer and the peak in autumn of the autotrophic size spectra at 90 µm, remain well expressed in the *combined* size spectra, which also confirms the consistency and robustness of our approach.

A.2 Supplementary Tables and Figures

Table A.1: Dates and locations of sample collections. SST cluster denotes whether a sample was classified as Atlantic (warm) or Polar (cold). PS99.1–PS114 were summer cruises, MSM77 was an autumn cruise. Event labels refer to the Pangaea database.

Cruise	Event label	HG Station	Depth [m]	Date	Latitude	Longitude	SST cluster
PS99.2	PS99/041-6	S-3	28	2016-06-25	78°36’28.08"N	5°2’48.48"E	warm
PS99.2	PS99/042-11	HG-4	28.4	2016-06-27	79°3’54.72"N	4°10’22.08"E	cold
PS99.2	PS99/048-11	EG-4	23.7	2016-06-30	78°48’57.6"N	2°43’43.68"W	cold
PS99.2	PS99/048-11	EG-4	9.7	2016-06-30	78°48’57.6"N	2°43’43.68"W	cold
PS99.2	PS99/051-2	EG-1	13.4	2016-07-02	78°59’26.88"N	5°24’33.48"W	cold
PS99.2	PS99/053-2	N-5	19	2016-07-03	79°55’16.32"N	3°3’43.2"E	cold
PS99.2	PS99/054-1	N-3	10	2016-07-04	79°35’12.12"N	5°10’12"E	warm
PS99.2	PS99/055-1	N-4	21.8	2016-07-05	79°44’29.4"N	4°30’12.6"E	cold
PS99.2	PS99/065-2	SV-1	18	2016-07-09	79°1’34.68"N	11°5’33"E	warm
PS99.2	PS99/066-2	HG-1	17.2	2016-07-09	79°8’21.12"N	6°5’18.6"E	warm
PS107	PS107_2-13	S-3	35	2017-07-26	78°36’31.291"N	5°3’16.33"E	cold
PS107	PS107_2-13	S-3	10	2017-07-26	78°36’31.291"N	5°3’16.33"E	cold
PS107	PS107_6-8	HG-4	10	2017-07-28	79°3’54.288"N	4°10’5.196"E	cold
PS107	PS107_7-1	HG-5	10	2017-07-28	79°3’11.844"N	3°44’58.812"E	cold
PS107	PS107_8-1	HG-6	10	2017-07-29	79°2’46.432"N	3°36’33.077"E	cold
PS107	PS107_10-4	FS 1	20	2017-07-29	78°58’36.588"N	2°29’39.48"E	cold
PS107	PS107_10-4	FS 1	10	2017-07-29	78°58’36.588"N	2°29’39.48"E	cold
PS107	PS107_12-3	FS 2	30	2017-07-30	78°56’41.316"N	2°42’6.12"E	cold
PS107	PS107_12-3	FS 2	10	2017-07-30	78°56’41.316"N	2°42’6.12"E	cold
PS107	PS107_14-1	FS 3	30	2017-07-30	78°55’37.308"N	2°51’0.972"E	cold
PS107	PS107_14-1	FS 3	10	2017-07-30	78°55’37.308"N	2°51’0.972"E	cold
PS107	PS107_18-3	FS 5	25	2017-07-31	78°59’9.168"N	2°45’20.808"E	cold
PS107	PS107_18-3	FS 5	10	2017-07-31	78°59’9.168"N	2°45’20.808"E	cold
PS107	PS107_19-1	HG-7	10	2017-07-31	79°3’33.66"N	3°28’55.056"E	cold
PS107	PS107_22-6	EG-4	22	2017-08-03	78°49’7.716"N	2°43’0.912"W	cold
PS107	PS107_22-6	EG-4	10	2017-08-03	78°49’7.716"N	2°43’0.912"W	cold
PS107	PS107_29-1	EG-1	35	2017-08-05	78°59’41.568"N	5°28’24.636"W	cold
PS107	PS107_33-6	N-4	25	2017-08-08	79°43’37.884"N	4°30’10.512"E	cold
PS107	PS107_33-6	N-4	10	2017-08-08	79°43’37.884"N	4°30’10.512"E	cold
PS107	PS107_34-5	N-5	40	2017-08-09	80°0’1.188"N	2°56’24.828"E	cold
PS107	PS107_34-5	N-5	20	2017-08-09	80°0’1.188"N	2°56’24.828"E	cold
PS107	PS107_43-1	HG-1	20	2017-08-12	79°9’9.9"N	6°6’54.864"E	warm
PS107	PS107_43-1	HG-1	10	2017-08-12	79°9’9.9"N	6°6’54.864"E	warm
PS107	PS107_48-1	SV-1	35	2017-08-14	79°1’45.3"N	11°6’6.084"E	warm
PS114	PS114_4-1	HG-4	10	2018-07-16	79°1’24.96"N	4°20’0.6"E	warm
PS114	PS114_4-1	HG-4	34.5	2018-07-16	79°1’24.96"N	4°20’0.6"E	warm
PS114	PS114_9-1	S-3	10.1	2018-07-17	78°36’24.12"N	5°2’28.68"E	warm
PS114	PS114_9-1	S-3	29.8	2018-07-17	78°36’24.12"N	5°2’28.68"E	warm
PS114	PS114_31-1	N-5	20.4	2018-07-22	79°56’42.36"N	3°11’55.32"E	cold
PS114	PS114_31-1	N-5	10.5	2018-07-22	79°56’42.36"N	3°11’55.32"E	cold
PS114	PS114_32-2	N-4	42.8	2018-07-22	79°44’22.2"N	4°31’32.52"E	cold
PS114	PS114_32-2	N-4	10.1	2018-07-22	79°44’22.2"N	4°31’32.52"E	cold
PS114	PS114_36-2	0°-N	29.6	2018-07-24	80°51’18.72"N	0°8’24.72"W	cold
PS114	PS114_36-2	0°-N	10	2018-07-24	80°51’18.72"N	0°8’24.72"W	cold
PS114	PS114_40-3	0°- S	11.7	2018-07-25	80°9’33.12"N	0°8’19.32"E	cold
PS114	PS114_43-4	EG-4	24.5	2018-07-26	78°49’3.36"N	2°46’9.12"W	cold
PS114	PS114_43-4	EG-4	4.7	2018-07-26	78°49’3.36"N	2°46’9.12"W	cold
PS114	PS114_46-8	EG-1	15.4	2018-07-27	79°0’44.64"N	5°17’6.36"W	cold
MSM77	MSM77_3-1	S-3	7	2018-09-16	78°36’59.292"N	5°4’4.836"E	warm
MSM77	MSM77_3-1	S-3	24	2018-09-16	78°36’59.292"N	5°4’4.836"E	warm
MSM77	MSM77_4-3	HG-4	7	2018-09-17	79°3’33.08"N	4°12’0.752"E	warm
MSM77	MSM77_4-3	HG-4	27	2018-09-17	79°3’33.08"N	4°12’0.752"E	warm
MSM77	MSM77_6-1	HG-6	13	2018-09-18	79°3’36.09"N	3°34’56.669"E	warm
MSM77	MSM77_13-1	HG-1	14	2018-09-20	79°8’0.139"N	6°5’32.773"E	warm
MSM77	MSM77_13-1	HG-1	22	2018-09-20	79°8’0.139"N	6°5’32.773"E	warm
MSM77	MSM77_24-1	SV-1	17	2018-09-24	79°1’42.312"N	11°5’10.295"E	warm
MSM77	MSM77_52-1	N-5	5	2018-10-03	79°56’17.7"N	3°10’59.941"E	cold
MSM77	MSM77_52-1	N-5	31	2018-10-03	79°56’17.7"N	3°10’59.941"E	cold
MSM77	MSM77_53-3	N-4	32	2018-10-04	79°44’11.062"N	4°29’6.58"E	warm
MSM77	MSM77_54-1	N-3	34	2018-10-04	79°36’13.82"N	5°10’22.264"E	warm

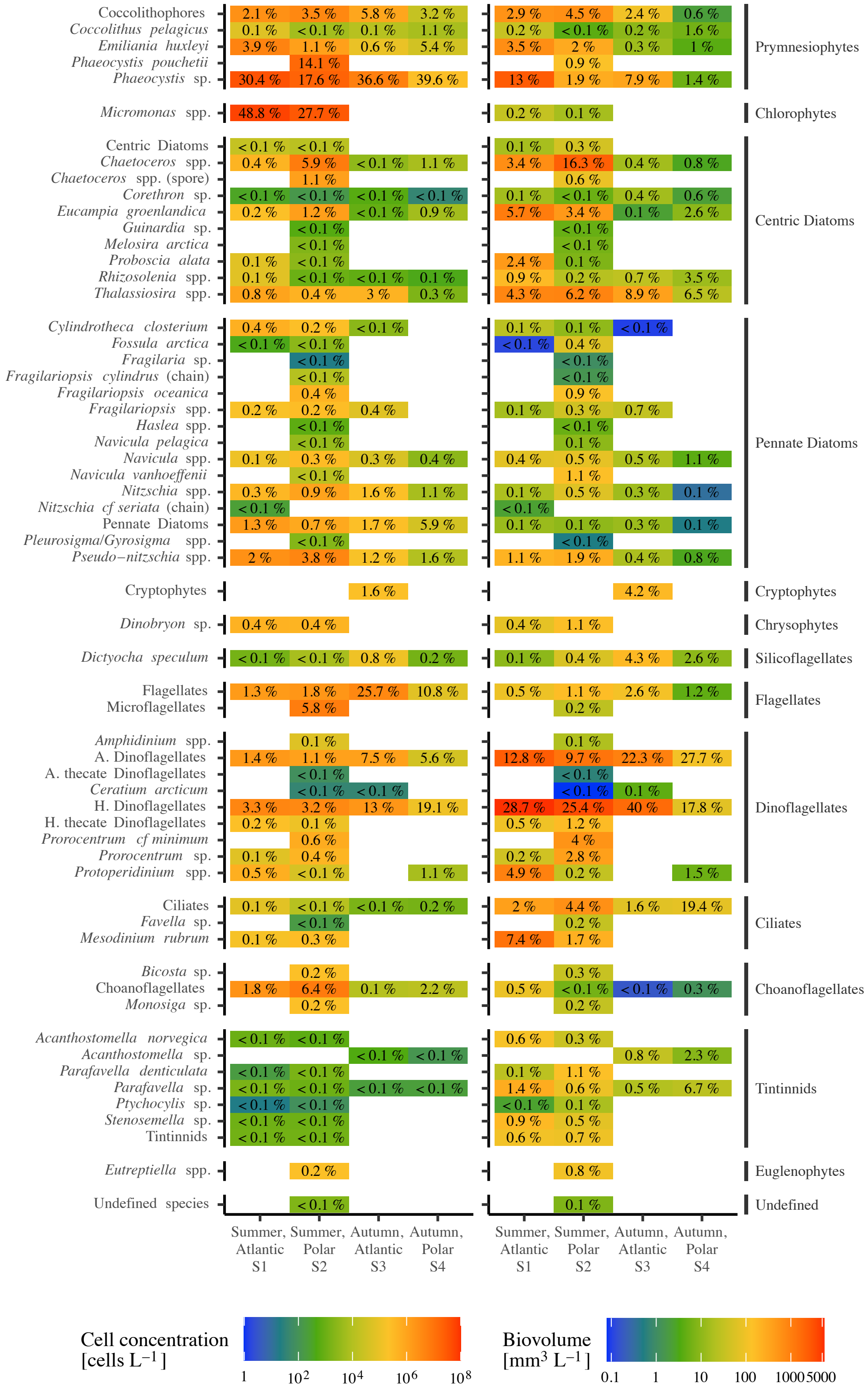

Figure A.3: Mean total cell and biovolume concentration for each identifiable group. Individual samples were grouped by season and SST region distinguishing the bloom scenarios S1–S4. Numbers represent the relative shares of the averaged total cell concentration and biovolume concentration as percentages. Respective total abundance and biovolumina are listed in Table 4.

B. Supporting Information for ‘A Lagrangian model-based analysis of protist plankton variability and its impact on organic matter dynamics along transit pathways through the Fram Strait’

B.1 Model equations

B.1.1 Cell quotas and limiting terms

Nitrogen and chlorophyll quotas are modelled as ratios with carbon:

$$Q_{i,j} = \frac{B_{i,j}}{B_{\mathrm{C},j}} \tag{B.2}$$

Nitrogen quota may lie between $Q_{\mathrm{N},j}^{\mathrm{min}}$ and $Q_{\mathrm{N},j}^{\mathrm{max}}$. These parameters correlate positively, which hinders optimisation. Therefore $\tilde{s}_{N,j}^{\mathrm{max}}$ was defined and optimised along with $Q_{\mathrm{N},j}^{\mathrm{min}}$:

$$\tilde{s}_{N,j}^{\mathrm{max}} = \frac{Q_{\mathrm{N},j}^{\mathrm{max}}}{Q_{\mathrm{N},j}^{\mathrm{max}} - Q_{\mathrm{N},j}^{\mathrm{min}}} \quad \longrightarrow \quad Q_{\mathrm{N},j}^{\mathrm{max}} = \frac{Q_{\mathrm{N},j}^{\mathrm{min}}}{1 - 1/\tilde{s}_{N,j}^{\mathrm{max}}} \tag{B.3}$$

Nutrient limitation is a linear function of nitrogen quota:

$$\gamma_{\mathrm{N},j} = \frac{Q_{\mathrm{N},j} - Q_{\mathrm{N},j}^{\mathrm{min}}}{Q_{\mathrm{N},j}^{\mathrm{max}} - Q_{\mathrm{N},j}^{\mathrm{min}}} \tag{B.4}$$

Nutrient uptake regulation term:

$$Q_{\mathrm{N},j}^{\mathrm{stat}} = 1 - \left(\frac{Q_{\mathrm{N},j} - Q_{\mathrm{N},j}^{\mathrm{min}}}{Q_{\mathrm{N},j}^{\mathrm{max}} - Q_{\mathrm{N},j}^{\mathrm{min}}} \right)^{h} \tag{B.5}$$

Temperature regulation term:

$$\gamma_T = e^{A(T - T^{\mathrm{ref}})} \tag{B.6}$$

B.1.2 Nutrient uptake rate

Michaelis-Menten function, with quota and temperature limiting terms:

$$V_{\mathrm{N},j} = \frac{v_j^{\mathrm{max}} \alpha_j N}{\alpha_j N + v_j^{\mathrm{max}}} Q_{\mathrm{N},j}^{\mathrm{stat}} \gamma_T \tag{B.7}$$

for all phytoplankton. For zooplankton, uptake rates are set to $V_{i,j_z} = 0$.

B.1.3 Photosynthesis

carbon specific light saturated photosynthetic rate:

$$P_j^{\mathrm{sat}} = P_j^{\mathrm{max}} \gamma_T \gamma_{\mathrm{N},j} \tag{B.8}$$

photosynthetic rate:

$$P_j = P_j^{\mathrm{sat}} * \gamma_{\mathrm{L},j} \tag{B.9}$$

where $\gamma_{\mathrm{L},j}$ is a light limitation term:

$$a = \frac{a_p Q_{\mathrm{Chl},j}}{P_j^{\mathrm{sat}}} \tag{B.10}$$

$$\kappa = \kappa_{\mathrm{SW}} + \kappa_{\mathrm{P}} * \int_0^{z+1} \sum_j B_{\mathrm{Chl},j} \mathrm{d}z \tag{B.11}$$

$$\gamma_{\mathrm{L},j} = 1 - \frac{Ei\left[-a * I_z\right] - Ei\left[-a * I_{z+1}\right]}{\kappa * \Delta z} \tag{B.12}$$

where $\kappa_{\mathrm{SW}} = 0.04\ \mathrm{m}^{-1}$ is the seawater attenuation coefficient (Lorenzen, 1972) and $\kappa_{\mathrm{P}} = 0.0149$ is the chlorophyll attenuation coefficient (Krause-Jensen and Sand-Jensen, 1998).

Carbon-specific production rate:

$$V_{\mathrm{C},j} = P_j - \xi V_{\mathrm{N},j} \tag{B.13}$$

Chlorophyll production rate:

$$V_{\mathrm{Chl},j} = \rho_j V_{\mathrm{N},j} \tag{B.14}$$

with

$$\rho_j = \theta \frac{P_j}{a_p Q_{\mathrm{Chl},j} I} \tag{B.15}$$

B.1.4 Predation

Grazing rate:

$$G_{\mathrm{C},j_z,j} = \gamma_T G_{j_z}^{\max} \frac{F_{\mathrm{C},j_z}}{k_G + F_{\mathrm{C},j_z}} \Phi_{j_z,j} (1 - e^{\Lambda F_{\mathrm{C},j_z}}) \tag{B.16}$$

where $\gamma_T G_{j_z}^{\max}$ denotes the maximum grazing rate, $\frac{F_{\mathrm{C},j_z}}{k_G + F_{\mathrm{C},j_z}}$ prey saturation, $\Phi_{j_z,j}$ prey switching, $(1 - e^{\Lambda F_{\mathrm{C},j_z}})$ prey refuge.

k_G is not estimated directly and the fraction of $G_a^{\max}$ and the grazing 'clearance' rate.:

$$k_G = \frac{G_{\mathrm{a}}^{\max}}{a_G} \tag{B.17}$$

Prey saturation is a Michaelis-Menten function of total prey carbon available to each predator:

$$F_{\mathrm{C},j_z} = \sum_j \phi_{j_z,j} B_{\mathrm{C},j} \tag{B.18}$$

Prey availability (availability of each prey size class j to each predator size class j_z) $\phi_{j_z,j}$ is modelled as a function of predator-prey size ratios $\delta_{j_z,j}$:

$$\phi_{j_z,j} = \exp\left[- \left(\ln \left(\frac{\delta_{j_z,j}}{\delta_{\mathrm{opt}}} \right) \right)^2 / (2\sigma^2) \right] \tag{B.19}$$

Prey switching prevents overgrazing on single size classes when other prey is more abundant (targets most abundant size class):

$$\Phi_{j_z,j} = \frac{(\phi_{j_z,j} B_{\mathrm{C},j})^2}{\sum_j (\phi_{j_z,j} B_{\mathrm{C},j})^2} \tag{B.20}$$

Grazing rates of Chl and N are the product of carbon grazing rate and cell quota:

$$G_{i,j_z,j} = Q_{i,j} G_{\mathrm{C},j_z,j} \tag{B.21}$$

Assimilation efficiency is down regulated when predator cell quotas approach their limits:

$$\lambda_{\mathrm{C},j_z} = \lambda^{\max} \gamma_{\mathrm{N},j} \tag{B.22}$$

$$\lambda_{\mathrm{N},j_z} = \lambda^{\max} Q_{\mathrm{N},j_z}^{\mathrm{stat}} \tag{B.23}$$

B.1.5 Background mortality

Size dependent mortality rate:

$$m_j = m_{\min} + (m_a - m_{\min})\mathrm{Vol}_j^{m_b} \tag{B.24}$$

$m_{\min}$ prevents m_j approaching zero as volume increases.

$$\text{background mortality} = (m_j + m_2 B_{i,j})B_{i,j} \tag{B.25}$$

B.1.6 Organic matter (detritus)

Sources of detrital organic matter are messy feeding and mortality. Cellular OM is transferred into DOM and POM upon cell death, and the proportions of POM and DOM are defined as $\beta_{j,k}$.

$$\beta_{j,\mathrm{DOM}} = \frac{b_1}{1 + e^{(x-b_3)}} + \frac{b_1 b_2}{1 + e^{(b_3-1)}} \tag{B.26}$$

$$\beta_{j,\mathrm{POM}} = 1 - \beta_{j,\mathrm{DOM}} \Rightarrow \sum_k \beta_{j,k} = 1 \tag{B.27}$$

with $x = \log_{10}(\mathrm{Vol})$.
Sources of organic matter are the sum of mortality and messy feeding:

$$\begin{aligned} S^{\mathrm{M}}_{i,k} &= \sum_j \beta_{j,k}(m_j + m_2 B_{i,j})B_{i,j} \\ &+ \sum_{j_z} B_{\mathrm{C},j_z} \sum_j \beta_{j,k}(1 - \lambda_{i,j_z})G_{i,j_z,j} \end{aligned} \tag{B.28}$$

$(1 - \lambda_{i,j_z})G_{i,j_z,j}$ are predator-specific rates of OM production through messy feeding.

B.2 Additional figures

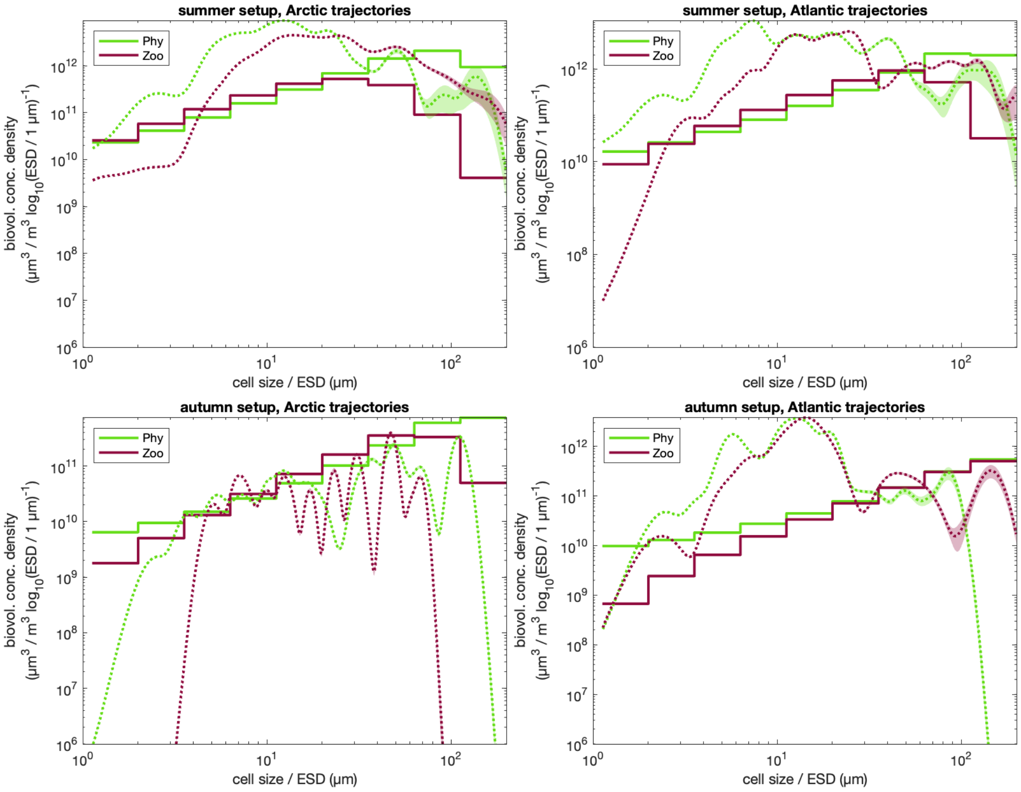

Figure B.1: Fit of simulated plankton biovolume size spectra (during sampling time frame) to observations Lampe et al. (2021). Biovolume densities are derived from abundance spectra (cell concentration density $*$ cell size) and serve as an indicator for biomass. Simulation results were extracted for the ship-sampling period ± 7 d and averaged over the upper 46 m. The lines represent the mean cell concentration densities (over trajectories) of phyto- and zooplankton respectively. Shaded areas indicate the mean± standard error. The smoother, curved graphs represent the observed plankton spectra, the stepped graphs represent the (size binned) simulations.

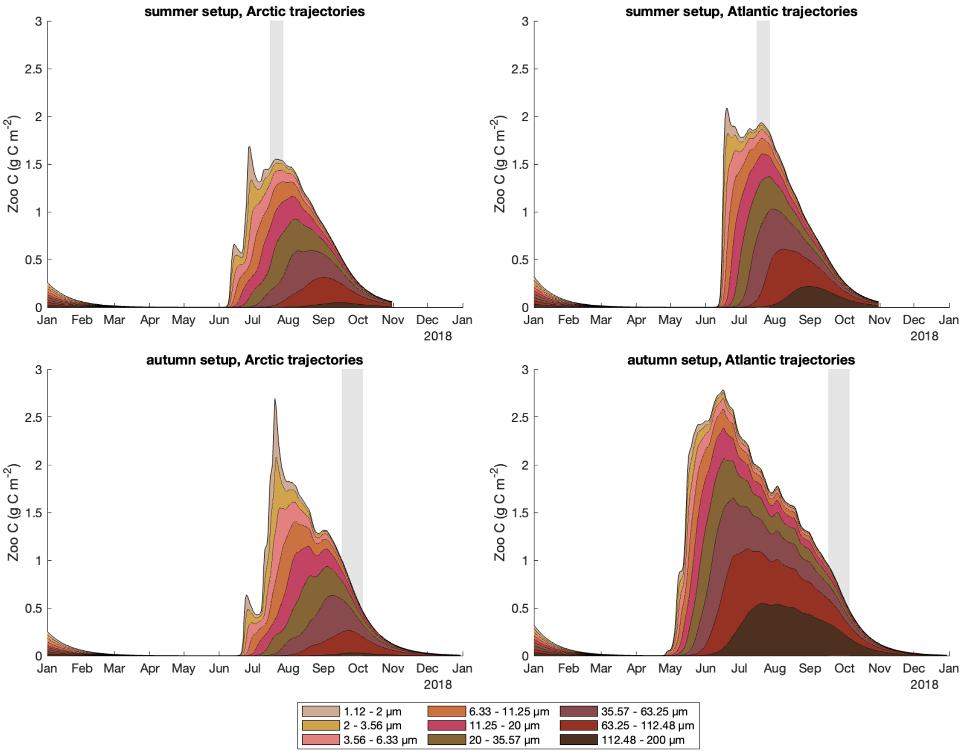

Figure B.2: Integrated zooplankton biomass per size class over time. C-biomass was integrated to 100 m depth and averaged by trajectory origin. Zooplankton size classes are represented by brown colours, and their respective sum equals total zooplankton biomass.

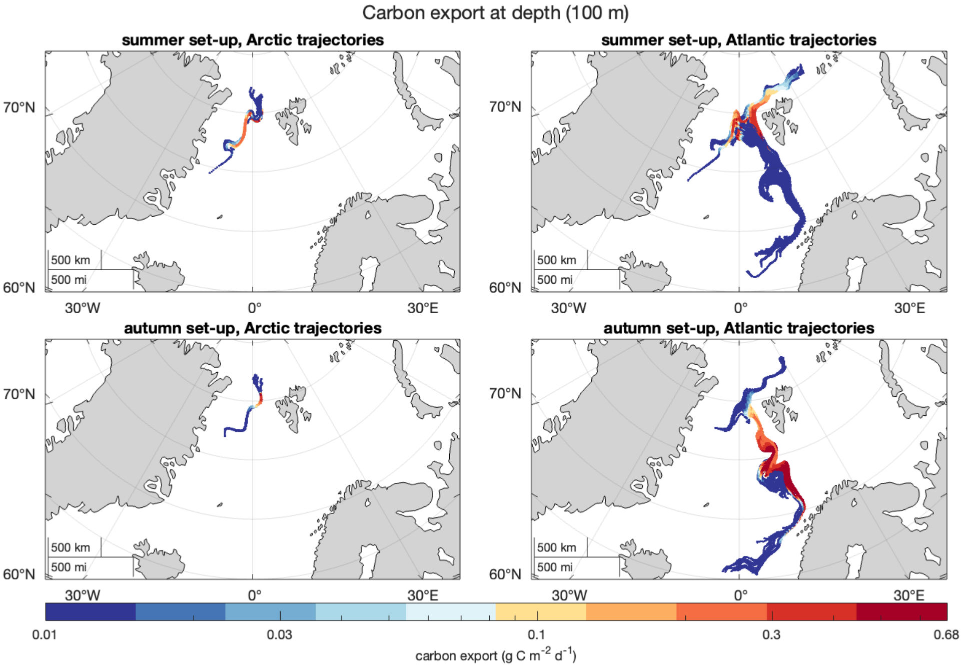

Figure B.3: Carbon export (sinking and diffusion of particulate organic carbon, including plankton and detrital matter) at 100 m depth along model trajectories. Each dot represents a export flux value of a given trajectory at a given day.

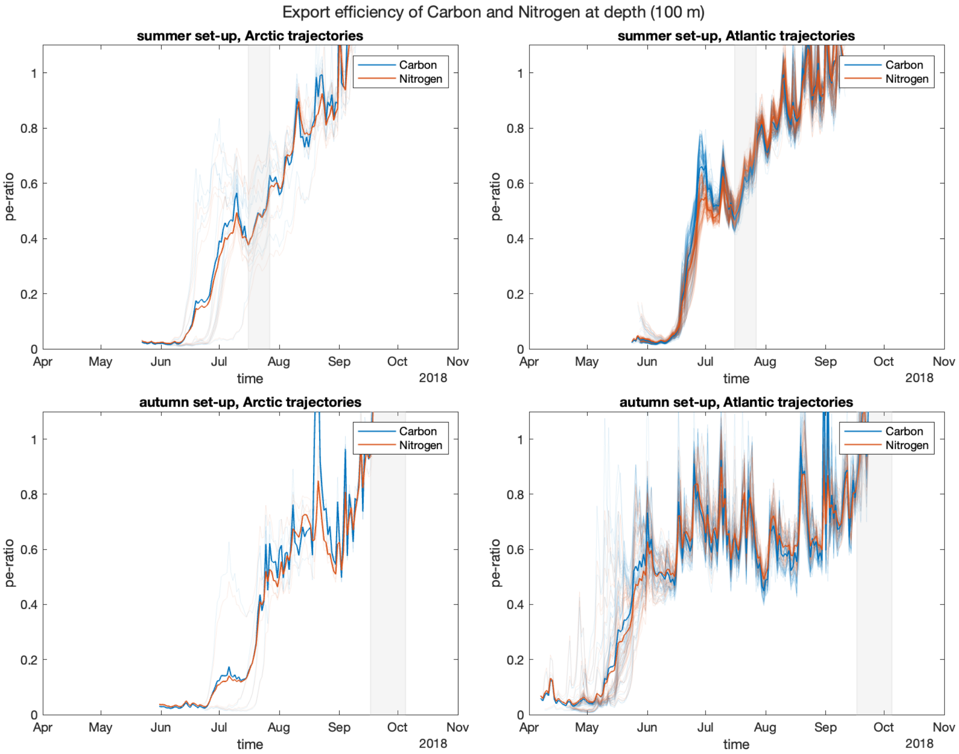

Figure B.4: Export efficiency of carbon (blue) and nitrogen (orange) for the upper 100 m. Opaque lines represent values for single trajectories, solid lines the trajectory-mean. We excluded all pe-values when the integrated daily production fell below 66.25 $\mathrm{mmol\,C\,m^{-2}\,d^{-1}}$. *In situ* sampling was conducted during the periods highlighted in grey.

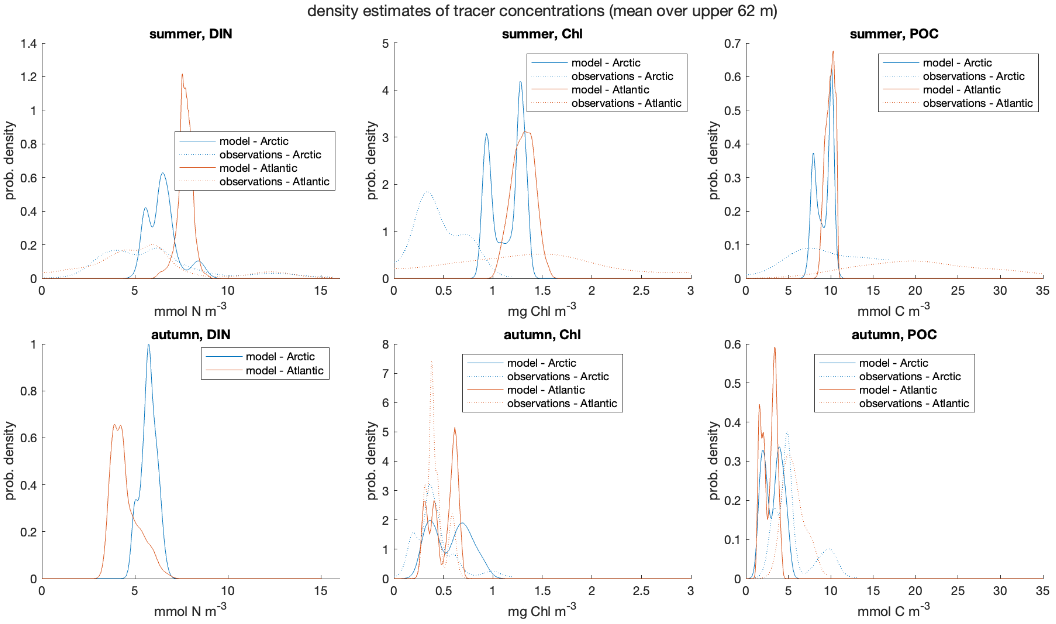

Figure B.5: Variability in the simulated (blue and orange) and observed (black) concentrations of DIN, Chlorophyll *a*, and total POC (phy + zoo + detritus) during the sampling campaigns (summer: 16–27 July 2018, upper panels; autumn: 16 Sept–4 Oct 2018, lower panels). The graphs represent the probability density distributions, as estimated with diffKDE.

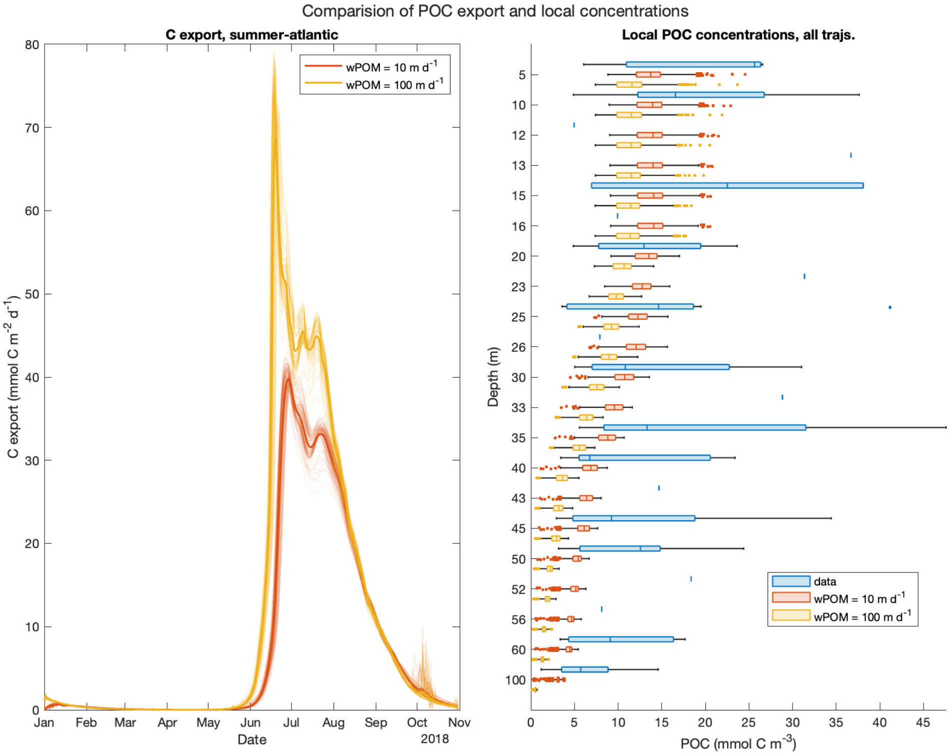

Figure B.6: Total POC export (left) and standing stocks of total POC over depth (right) for the reference solution (red) and for a simulation with increased detritus sinking speed (yellow).

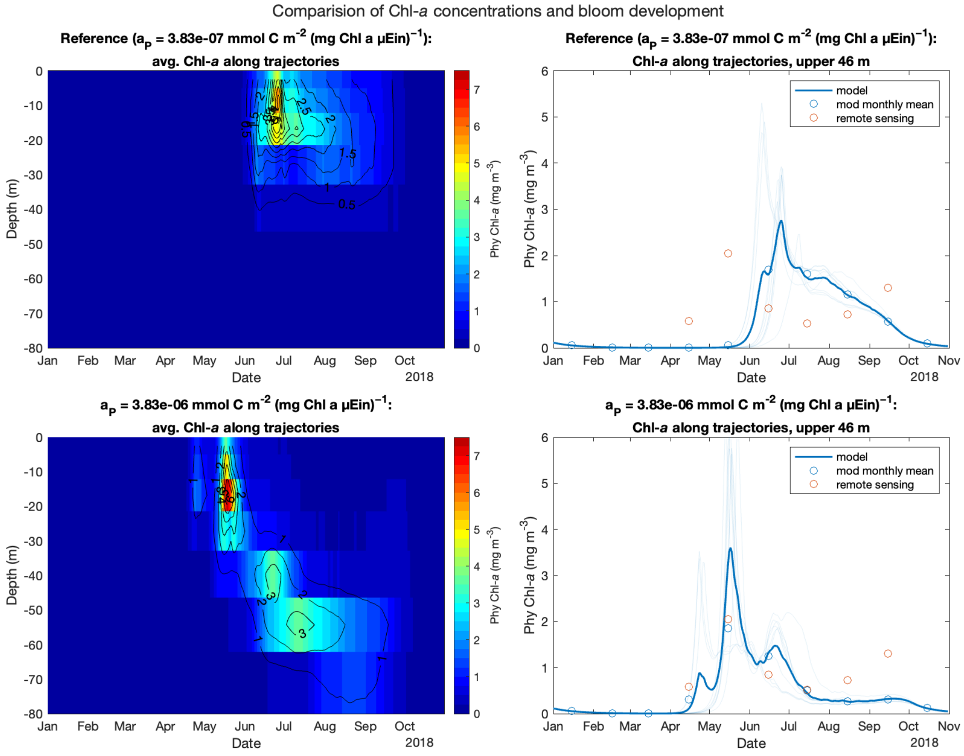

Figure B.7: Total Chl-a standing stocks (left) and depth-averaged simulated and remote sensing Chl-a (right) for the reference solution (upper) and for a simulation with increased initial slope for the PI-curve (a_P).

B.3 Additional tables

Table B.1: Root Mean Squared Deviation (RMSD), coefficient of variation (CV) and integrated quadratic distance (IQD) during sampling periods (mean over time, depth, trajectories). RMSDs are in the unit of their respective variable (DIN and PON: mmol N m^{-3}, Chl-*a*: mg Chl m^{-3}, POC: mmol C m^{-3}), CV and IQD are unit-less. *In situ* data refer to observational data collected in the Fram Strait (see Sect. 3.2.1). Climatological data data were extracted from WOA18 data along the model trajectories for each day with a 20 km radius, then averaged over trajectories and months.

Variable		Summer/ Arctic	Summer/ Atlantic	Autumn/ Arctic	Autumn/ Atlantic
***In situ* data**					
(Fram Strait, HAUSGARTEN)					
DIN	RMSD	3.4333	5.5814		
DIN	CV	0.5997	1.0478		
Chl-*a*	RMSD	1.5262	1.3254	0.4874	0.3084
Chl-*a*	CV	2.7819	0.8062	2.5122	0.8131
POC	RMSD	7.0679	20.4758	1.4249	4.793
POC	CV	0.7397	0.7849	0.4270	0.7514
PON	RMSD	0.8731	1.8388		
PON	CV	0.8272	0.6660		
Phy	IQD ($\cdot 10^3$)	13.4770	17.1693	3.3889	20.3677
Zoo	IQD ($\cdot 10^3$)	2.5540	2.8015	3.0895	18.9774
Climatological data					
(along mean trajectories)					
DIN	RMSD	2.1350	2.3497	2.0409	1.2592
DIN	CV	0.2451	0.2335	0.2150	0.1255

References

Esteban Acevedo-Trejos, Emilio Marañón, and Agostino Merico. Phytoplankton size diversity and ecosystem function relationships across oceanic regions. *Proceedings of the Royal Society B: Biological Sciences*, 285(1879), 2018. doi:10.1098/rspb.2018.0621.

D. L. Aksnes and J. K. Egge. A theoretical model for nutrient uptake in phytoplankton. *Marine Ecology Progress Series*, 70(1):65–72, 1991. doi:10.3354/meps070065.

Rainer M. W. Amon, Gereon Budéus, and Benedikt Meon. Dissolved organic carbon distribution and origin in the Nordic Seas: Exchanges with the Arctic Ocean and the North Atlantic. *Journal of Geophysical Research*, 108(C7):1–17, 2003. doi:10.1029/2002jc001594.

K.H. Andersen, T. Berge, R.J. Gonçalves, M. Hartvig, J. Heuschele, S. Hylander, N.S. Jacobsen, C. Lindemann, E.A. Martens, A.B. Neuheimer, K. Olsson, A. Palacz, A.E.F. Prowe, J. Sainmont, S.J. Traving, A.W. Visser, N. Wadhwa, and T. Kiørboe. Characteristic Sizes of Life in the Oceans, from Bacteria to Whales. *Annual Review of Marine Science*, 8(1):217–241, 2016. doi:10.1146/annurev-marine-122414-034144.

Mathieu Ardyna and Kevin Robert Arrigo. Phytoplankton dynamics in a changing Arctic Ocean. *Nature Climate Change*, 10(10):892–903, October 2020. doi:10.1038/s41558-020-0905-y.

Robert A. Armstrong. Grazing limitation and nutrient limitation in marine ecosystems: Steady state solutions of an ecosystem model with multiple food chains. *Limnology and Oceanography*, 39(3):597–608, 1994. doi:10.4319/lo.1994.39.3.0597.

Kevin R. Arrigo. The changing Arctic Ocean. *Elementa: Science of the Anthropocene*, 1:000010, January 2013. doi:10.12952/journal.elementa.000010.

Kevin R. Arrigo and Gert L. Van Dijken. Secular trends in Arctic Ocean net primary production. *Journal of Geophysical Research*, 116(C9):C09011, 2011. doi:10.1029/2011JC007151.

Kevin R. Arrigo and Gert L. van Dijken. Continued increases in Arctic Ocean primary production. *Progress in Oceanography*, 136:60–70, 2015. doi:10.1016/j.pocean.2015.05.002.

Farooq Azam, T Fenchel, John G. Field, J S Gray, L A Meyer-Reil, and F Thingstad. The Ecological Role of Water-Column Microbes in the Sea. *Marine Ecology Progress Series*, 10:257–263, 1983. doi:10.1021/acs.joc.6b00938.

Andrew Bakun and Kenneth Broad. Environmental ‘loopholes’ and fish population dynamics: Comparative pattern recognition with focus on El Niño effects in the Pacific. *Fisheries Oceanography*, 12(4-5):458–473, 2003. doi:10.1046/j.1365-2419.2003.00258.x.

Neil S. Banas. Adding complex trophic interactions to a size-spectral plankton model: Emergent diversity patterns and limits on predictability. *Ecological Modelling*, 222(15):2663–2675, 2011. doi:10.1016/j.ecolmodel.2011.05.018.

Neil S. Banas. Particulator, 2018. URL https://github.com/neilbanas/particulator. Last accessed: 2022-12-16.

Neil S. Banas, P. Sean McDonald, and David A. Armstrong. Green Crab Larval Retention in Willapa Bay, Washington: An Intensive Lagrangian Modeling Approach. *Estuaries and Coasts*, 32(5):893–905, September 2009. doi:10.1007/s12237-009-9175-7.

Neil S. Banas, Jinlun Zhang, Robert G. Campbell, Raymond N. Sambrotto, Michael W. Lomas, Evelyn Sherr, Barry Sherr, Carin Ashjian, Diane Stoecker, and Evelyn J. Lessard. Spring plankton dynamics in the Eastern Bering Sea, 1971–2050: Mechanisms of interannual variability diagnosed with a numerical model. *Journal of Geophysical Research: Oceans*, 121(2):1476–1501, February 2016. doi:10.1002/2015JC011449.

Andrew D. Barton, Andrew J. Pershing, Elena Litchman, Nicholas R. Record, Kyle F. Edwards, Zoe V. Finkel, Thomas Kiørboe, and Ben A. Ward. The biogeography of marine plankton traits. *Ecology Letters*, 16(4):522–534, 2013. doi:10.1111/ele.12063.

Benjamin I. Barton, Yueng Djern Lenn, and Camille Lique. Observed atlantification of the Barents Sea causes the Polar Front to limit the expansion of winter sea ice. *Journal of Physical Oceanography*, 48(8):1849–1866, 2018. doi:10.1175/JPO-D-18-0003.1.

Eduard Bauerfeind, Eva-Maria Nöthig, Agnieszka Beszczynska, Kirsten Fahl, Lars Kaleschke, Kathrin Kreker, Michael Klages, Thomas Soltwedel, Christiane Lorenzen, and Jan Wegner. Particle sedimentation patterns in the eastern Fram Strait during 2000–2005: Results from the Arctic long-term observatory HAUSGARTEN. *Deep Sea Research Part I: Oceanographic Research Papers*, 56(9): 1471–1487, September 2009. doi:10.1016/j.dsr.2009.04.011.

Michael J. Behrenfeld, Yongxiang Hu, Robert T. O’Malley, Emmanuel S. Boss, Chris A. Hostetler, David A. Siegel, Jorge L. Sarmiento, Jennifer Schulien, Johnathan W. Hair, Xiaomei Lu, Sharon Rodier, and Amy Jo Scarino. Annual boom-bust cycles of polar phytoplankton biomass revealed by space-based lidar. *Nature Geoscience*, 10:118–122, 2017. doi:10.1038/ngeo2861.

Agnieszka Beszczynska-Möller, E. Fahrbach, U. Schauer, and E. Hansen. Variability in Atlantic water temperature and transport at the entrance to the Arctic Ocean, 1997–2010. *ICES Journal of Marine Science (2012),*, 69(5):852–863, 2012. doi:10.1093/icesjms/fss056.

Oda Bjærke, Per R. Jonsson, Asraful Alam, and Erik Selander. Is chain length in phytoplankton regulated to evade predation? *Journal of Plankton Research*, 37 (6):1110–1119, 2015. doi:10.1093/plankt/fbv076.

Katarzyna Błachowiak-Samołyk, Józef Maria Wiktor, Else Nøst Hegseth, Anette Wold, Stig Falk-Petersen, and Anna Maria Kubiszyn. Winter Tales: The dark side of planktonic life. *Polar Biology*, 38:23–36, 2015. doi:10.1007/s00300-014-1597-4.

Julia L. Blanchard, Ryan F. Heneghan, Jason D. Everett, Rowan Trebilco, and Anthony J. Richardson. From Bacteria to Whales: Using Functional Size Spectra to Model Marine Ecosystems. *Trends in Ecology and Evolution*, 32(3):174–186, 2017. doi:10.1016/j.tree.2016.12.003.

Tim P Boyer, Hernan E Garcia, Ricardo A Locarnini, Melissa M Zweng, Alexey V Mishonov, James R Reagan, Katharine A Weathers, Olga K Baranova, Dan Seidov, and Igor V. Smolyar. World Ocean Atlas 2018, 2018. URL https://www.ncei.noaa.gov/archive/accession/NCEI-WOA18. Last accessed: 2021-08-13.

Robert J. W. Brewin, Shubha Sathyendranath, Gavin Tilstone, Priscila K. Lange, and Trevor Platt. A multicomponent model of phytoplankton size structure. *Journal of Geophysical Research: Oceans*, 119(6):3478–3496, June 2014. doi:10.1002/2014JC009859.

Kristina A Brown, Johnna M Holding, and Eddy C Carmack. Understanding Regional and Seasonal Variability Is Key to Gaining a Pan-Arctic Perspective on Arctic Ocean Freshening. *Frontiers in Marine Science*, 7(606):1–26, 2020. doi:10.3389/fmars.2020.00606.

B. B. Cael, Emma L. Cavan, and Gregory L. Britten. Reconciling the Size-Dependence of Marine Particle Sinking Speed. *Geophysical Research Letters*, 48(5):e2020GL091771, March 2021. doi:10.1029/2020GL091771.

Magda G. Cardozo-Mino, Ian Salter, Eva-Maria Nöthig, Katja Metfies, Simon Ramondenc, Claudia Wekerle, Thomas Krumpen, Antje Boetius, and Christina Bienhold. A decade of microbial community dynamics on sinking particles during high carbon export events in the eastern Fram Strait. *Frontiers in Marine Science*, 10:1173384, 2023. doi:10.3389/fmars.2023.1173384.

Giulia Castellani, Gaëlle Veyssière, Michael Karcher, Julienne Stroeve, S. Neil Banas, A. Heather Bouman, S. Andrew Brierley, Stacey Connan, Finlo Cottier, Fabian Große, Laura Hobbs, Christian Katlein, Bonnie Light, David McKee, Andrew Orkney, Roland Proud, and Vibe Schourup-Kristensen. Shine a light: Under-ice light and its ecological implications in a changing Arctic Ocean. *Ambio*, 51(2):307–317, 2022. doi:10.1007/s13280-021-01662-3.

Alexandra Cherkasheva, A. Bracher, C. Melsheimer, C. Köberle, R. Gerdes, Eva-Maria Nöthig, Eduard Bauerfeind, and Antje Boetius. Influence of the physical environment on polar phytoplankton blooms: A case study in the Fram Strait. *Journal of Marine Systems*, 132:196–207, 2014. doi:10.1016/j.jmarsys.2013.11.008.

Sallie W. Chisholm. Phytoplankton Size. In Paul G. Falkowski and Avril W. Woodhead, editors, *Primary Productivity and Biogeochemical Cycles in the Sea*, pages 213–237. Springer Science and Business Media, 1992. ISBN 978-0-306-44192-9.

CMEMS and ACRI. Global Ocean Colour (Copernicus-GlobColour), Bio-Geo-Chemical, L3 (daily) from Satellite Observations (1997-ongoing), 2023. doi:10.48670/moi-00280. Generated using CMEMS Products, production centre ACRI-ST. Last accessed: 2023-09-28.

L.A. Codispoti, V. Kelly, A. Thessen, P. Matrai, S. Suttles, V. Hill, M. Steele, and B. Light. Synthesis of primary production in the Arctic Ocean: III. Nitrate and phosphate based estimates of net community production. *Progress in Oceanography*, 110:126–150, March 2013. doi:10.1016/j.pocean.2012.11.006.

Harriet Cole, Stephanie Henson, Adrian Martin, and Andrew Yool. Mind the gap: The impact of missing data on the calculation of phytoplankton phenology metrics: IMPACT OF DATA GAPS ON PHENOLOGY METRICS. *Journal of Geophysical Research: Oceans*, 117(C8):n/a–n/a, August 2012. doi:10.1029/2012JC008249.

André M. Comeau, William K.W. Li, Jean Éric Tremblay, Eddy C. Carmack, and Connie Lovejoy. Arctic ocean microbial community structure before and after the 2007 record sea ice minimum. *PLoS ONE*, 6(11), 2011. doi:10.1371/journal.pone.0027492.

Josefino C. Comiso. Satellite remote sensing of the Arctic Ocean and adjacent seas. In Walker O. Smith and Jacqueline M. Grebmeir, editors, *Coastal and Estuarine Studies*, volume 49, pages 1–50. American Geophysical Union, Washington, D. C., 1995. ISBN 978-0-87590-263-0. doi:10.1029/CE049p0001.

Josefino C. Comiso and Dorothy K Hall. Climate trends in the Arctic as observed from space. *WIREs Climate Change*, 5:389–409, 2014. doi:10.1002/wcc.277.

Pf Culverhouse, R Williams, B Reguera, V Herry, and S González-Gil. Do experts make mistakes? A comparison of human and machine identification of dinoflagellates. *Marine Ecology Progress Series*, 247:17–25, 2003. doi:10.3354/meps247017.

L. de Steur, E. Hansen, R. Gerdes, M. Karcher, E. Fahrbach, and J. Holfort. Freshwater fluxes in the East Greenland Current: A decade of observations. *Geophysical Research Letters*, 36, 2009. doi:10.1029/2009gl041278.

Maria Degerlund and Hans Christian Eilertsen. Main Species Characteristics of Phytoplankton Spring Blooms in NE Atlantic and Arctic Waters (68–80° N). *Estuaries and Coasts*, 33(2):242–269, March 2010. doi:10.1007/s12237-009-9167-7.

Christine Dybwad, Philipp Assmy, Lasse M. Olsen, Ilka Peeken, Anna Nikolopoulos, Thomas Krumpen, Achim Randelhoff, Agnieszka Tatarek, Józef M. Wiktor, and Marit Reigstad. Carbon Export in the Seasonal Sea Ice Zone North of Svalbard From Winter to Late Summer. *Frontiers in Marine Science*, 7:525800, January 2021. doi:10.3389/fmars.2020.525800.

Lars Edler. *Recommendations on Methods for Marine Biological Studies in the Baltic Sea: Phytoplankton and Chlorophyll.* Department of Marine Botany, University of Lund, 1979. URL https://books.google.de/books?id=V1AnywAACAAJ.

Kyle F. Edwards, Mridul K. Thomas, Christopher A. Klausmeier, and Elena Litchman. Allometric scaling and taxonomic variation in nutrient utilization traits and maximum growth rate of phytoplankton. *Limnology and Oceanography*, 57 (2):554–566, 2012. doi:10.4319/lo.2012.57.2.0554.

H.C. Eilertsen, J.P. Taasen, and J.M. WesIawski. Phytoplankton studies in the fjords of West Spitzbergen: Physical environment and production in spring and summer. *Journal of Plankton Research*, 11(6):1245–1260, 1989. doi:10.1093/plankt/11.6.1245.

Anja Engel, C. Borchard, J. Piontek, K. G. Schulz, U. Riebesell, and R. Bellerby. CO2 increases 14C primary production in an Arctic plankton community. *Biogeosciences*, 10(3):1291–1308, 2013. doi:10.5194/bg-10-1291-2013.

Anja Engel, Astrid Bracher, Tilman Dinter, Sonja Endres, Julia Grosse, Katja Metfies, Ilka Peeken, Judith Piontek, Ian Salter, and Eva-Maria Nöthig. Interannual variability of organic carbon concentrations in the eastern Fram Strait during summer (2009-2017). *Frontiers in Marine Science*, 6(April):187, 2019. doi:10.3389/FMARS.2019.00187.

European Space Agency ESA. WorldView-3: Missions, March 2024. URL https://earth.esa.int/eogateway/missions/worldview-3. Last accessed: 19/03/2024.

Stig Falk-Petersen, Tore Haug, Haakon Hop, Kjell T. Nilssen, and Anette Wold. Transfer of lipids from plankton to blubber of harp and hooded seals off East Greenland. *Deep-Sea Research Part II: Topical Studies in Oceanography*, 56(21-22):2080–2086, 2009. doi:10.1016/j.dsr2.2008.11.020.

Paul G. Falkowski, Richard T. Barber, and Victor Smetacek. Biogeochemical controls and feedbacks on ocean primary production. *Science*, 281(5374):200–206, 1998. doi:10.1126/science.281.5374.200.

A. R. Fay and G. A. McKinley. Global open-ocean biomes: Mean and temporal variability. *Earth System Science Data*, 6(2):273–284, August 2014. doi:10.5194/essd-6-273-2014.

Zoe V. Finkel, John Beardall, Kevin J. Flynn, Antonietta Quigg, T. Alwyn V. Rees, and John A. Raven. Phytoplankton in a changing world: Cell size and elemental stoichiometry. *Journal of Plankton Research*, 32(1):119–137, 2010. doi:10.1093/plankt/fbp098.

Kevin J. Flynn, Diane K. Stoecker, Aditee Mitra, John A. Raven, Patricia M. Glibert, Per Juel Hansen, Edna Granéli, and Joann M. Burkholder. Misuse of the phytoplankton-zooplankton dichotomy: The need to assign organisms as mixotrophs within plankton functional types. *Journal of Plankton Research*, 35 (1):3–11, 2013. doi:10.1093/plankt/fbs062.

Alexandre Forest, Paul Wassmann, Dag Slagstad, Eduard Bauerfeind, Eva-Maria Nöthig, and Michael Klages. Relationships between primary production and vertical particle export at the Atlantic-Arctic boundary (Fram Strait, HAUSGARTEN). *Polar Biology*, 33(12):1733–1746, 2010. doi:10.1007/s00300-010-0855-3.

H. E. Garcia, T. P. Boyer, O. K. Baranova, R. A. Locarnini, A. V. Mishonov, A. Grodsky, C. R. Paver, K. W. Weathers, I. V. Smolyar, J. R. Reagan, D. Seidov, and M. M. Zweng. World Ocean Atlas 2018: Product Documentation. Technical report, NOAA, 2019a. URL https://www.ncei.noaa.gov/products/world-ocean-atlas.

Hernan E Garcia, K. W. Weathers, C. R. Paver, I Smolyar, T. P. Boyer, R. A. Locarnini, M. M. Zweng, A. V. Mishonov, O. K. Baranova, D. Seidov, and J. R. Reagan. World Ocean Atlas 2018. Vol. 4: Dissolved Inorganic Nutrients (phosphate, nitrate and nitrate+nitrite, silicate), July 2019b. URL https://www.nodc.noaa.gov/OC5/woa18/pubwoa18.html. Technical Editor: A. Mishonov. Last accessed: 13/08/2021.

S Good, E Fiedler, C Mao, M. J. Martin, A Maycock, R Reid, J Robert-Jones, T Searle, J Waters, J While, and M Worsfold. Global SST & Sea Ice Analysis, L4 OSTIA, 0.05 deg daily (METOFFICE-GLO-SST-L4-REP-OBS-SST-V2), 2020. URL https://doi.org/10.48670/moi-00168. doi:10.48670/moi-00168. Last accessed: 28/09/2023.

R. R. Gradinger and M. E.M. Baumann. Distribution of phytoplankton communities in relation to the large-scale hydrographical regime in the Fram Strait. *Marine Biology*, 111:311–321, 1991. doi:10.1007/BF01319714.

B. Hansen, F.L. Fotel, N.J. Jensen, and S.D. Madsen. Bacteria associated with a marine planktonic copepod in culture. II. Degradation of fecal pellets produced on a diatom, a nanoflagellate or a dinoflagellate diet. *Journal of Plankton Research*, 18(2):275–288, 1996. doi:10.1093/plankt/18.2.275.

Benni Hansen, Peter Koefoed Bjørnsen, and Per Juel Hansen. The size ratio between planktonic predators and their prey. *Limnology and Oceanography*, 39(2):395–403, 1994. doi:10.4319/lo.1994.39.2.0395.

E. Hansen, S. Gerland, M. A. Granskog, O. Pavlova, A. H. H. Renner, J. Haapala, T. B. Løyning, and M. Tschudi. Thinning of Arctic sea ice observed in Fram Strait: 1990-2011: Thinning of Arctic Sea Ice. *Journal of Geophysical Research: Oceans*, 118(10):5202–5221, 2013. doi:10.1002/jgrc.20393.

J. A. Hartigan and M. A. Wong. Algorithm AS 136: A K-Means Clustering Algorithm. *Applied Statistics*, 28(1):100–108, 1979. doi:10.2307/2346830.

Grethe Rytter Hasle and Berit Riddervold Heimdal. The net phytoplankton in Kongsfjorden, Svalbard, July 1988, with general remarks on species composition of Arctic phytoplankton. *Polar Research*, 17(1):31–52, January 1998. doi:10.3402/polar.v17i1.6605.

Else Nøst Hegseth and Arild Sundfjord. Intrusion and blooming of Atlantic phytoplankton species in the high Arctic. *Journal of Marine Systems*, 74(1-2):108–119, November 2008. doi:10.1016/j.jmarsys.2007.11.011.

S. A. Henson, J. L. Sarmiento, J. P. Dunne, L. Bopp, I. Lima, S. C. Doney, J. John, and C. Beaulieu. Detection of anthropogenic climate change in satellite records of ocean chlorophyll and productivity. *Biogeosciences*, 7(2):621–640, February 2010. doi:10.5194/bg-7-621-2010.

W. D. Hibler. A Dynamic Thermodynamic Sea Ice Model. *Journal of Physical Oceanography*, 9:815–846, 1979. doi:10.1175/1520-0485.

M. M. Holland and C. M. Bitz. Polar amplification of climate change in coupled models. *Climate Dynamics*, 21(3-4):221–232, 2003. doi:10.1007/s00382-003-0332-6.

Haakon Hop, Stig Falk-Petersen, Harald Svendsen, Slawek Kwasniewski, Vladimir Pavlov, Olga Pavlova, and Janne E. Søreide. Physical and biological characteristics of the pelagic system across Fram Strait to Kongsfjorden. *Progress in Oceanography*, 71(2-4):182–231, 2006. doi:10.1016/j.pocean.2006.09.007.

María Huete-Ortega, Emilio Marañón, Manuel Varela, and Antonio Bode. General patterns in the size scaling of phytoplankton abundance in coastal waters during a 10-year time series. *Journal of Plankton Research*, 32(1):1–14, 2010. doi:10.1093/plankt/fbp104.

María Huete-Ortega, Pedro Cermeño, Alejandra Calvo-Díaz, and Emilio Marañón. Isometric size-scaling of metabolic rate and the size abundance distribution of phytoplankton. *Proceedings of the Royal Society B: Biological Sciences*, 279 (1734):1815–1823, 2012. doi:10.1098/rspb.2011.2257.

E. C. Hunke and J. K. Dukowicz. An Elastic–Viscous–Plastic Model for Sea Ice Dynamics. *Journal of Physical Oceanography*, 27(9):1849–1867, 1997. doi:10.1175/1520-0485(1997)027<1849:AEVPMF>2.0.CO;2.

George L. Hunt, Kenneth O. Coyle, Lisa B. Eisner, Edward V. Farley, Ron A. Heintz, Franz Mueter, Jeffrey M. Napp, James E. Overland, Patrick H. Ressler, Sigrid Salo, and Phyllis J. Stabeno. Climate impacts on eastern Bering Sea foodwebs: A synthesis of new data and an assessment of the Oscillating Control Hypothesis. *ICES Journal of Marine Science*, 68(6):1230–1243, 2011. doi:10.1093/icesjms/fsr036.

IBCAO. International Bathymetric Chart of the Arctic Ocean (IBCAO), 2023. URL https://www.gebco.net/data_and_products/gridded_bathymetry_data/arctic_ocean/. Last accessed: 20/03/2024.

X Irigoien, K J Flynn, and R P Harris. Phytoplankton blooms: A ‘loophole’ in microzooplankton grazing impact? *Journal of Plankton Research*, 27(4):313–321, 2005. doi:10.1093/plankt/fbi011.

Morten H. Iversen. Carbon Export in the Ocean: A Biologist’s Perspective. *Annual Review of Marine Science*, 15(1):357–381, 2023. doi:10.1146/annurev-marine-032122-035153.

Hans Henrik Jakobsen, Jacob Carstensen, Paul J. Harrison, and Adriana Zingone. Estimating time series phytoplankton carbon biomass: Inter-lab comparison of species identification and comparison of volume-to-carbon scaling ratios. *Estuarine, Coastal and Shelf Science*, 162:143–150, 2015. doi:10.1016/j.ecss.2015.05.006.

Matthew Jenkins and Aiguo Dai. The Impact of Sea-Ice Loss on Arctic Climate Feedbacks and Their Role for Arctic Amplification. *Geophysical Research Letters*, 48(15):e2021GL094599, 2021. doi:10.1029/2021GL094599.

Estelle S. Kilias, Eva Maria Nöthig, Christian Wolf, and Katja Metfies. Picoeukaryote plankton composition off West Spitsbergen at the entrance to the Arctic Ocean. *The Journal of eukaryotic microbiology*, 61(6):569–579, 2014. doi:10.1111/jeu.12134.

Dorte Krause-Jensen and Kaj Sand-Jensen. Light attenuation and photosynthesis of aquatic plant communities. *Limnology and Oceanography*, 43(3):396–407, 1998. doi:10.4319/lo.1998.43.3.0396.

A.M. Kubiszyn, J.M. Wiktor, J.M. Wiktor Jr., C. Griffiths, S. Kristiansen, and T.M. Gabrielsen. The annual planktonic protist community structure in an ice-free high Arctic fjord (Adventfjorden, West Spitsbergen). *Journal of Marine Systems*, 169:61–72, 2017. doi:10.1016/j.jmarsys.2017.01.013.

Angela M. Kuhn, Matthew Mazloff, Stephanie Dutkiewicz, Oliver Jahn, Sophie Clayton, Tatiana Rynearson, and Andrew D. Barton. A Global Comparison of Marine Chlorophyll Variability Observed in Eulerian and Lagrangian Perspectives. *Journal of Geophysical Research: Oceans*, 128(7):e2023JC019801, 2023. doi:10.1029/2023JC019801.

Gemma Kulk, Trevor Platt, James Dingle, Thomas Jackson, Bror Jönsson, Heather Bouman, Marcel Babin, Robert Brewin, Martina Doblin, Marta Estrada, Francisco Figueiras, Ken Furuya, Natalia González-Benítez, Hafsteinn Gudfinnsson, Kristinn Gudmundsson, Bangqin Huang, Tomonori Isada, Žarko Kovač, Vivian Lutz, Emilio Marañón, Mini Raman, Katherine Richardson, Patrick Rozema, Willem Poll, Valeria Segura, Gavin Tilstone, Julia Uitz, Virginie Dongen-Vogels, Takashi Yoshikawa, and Shubha Sathyendranath. Primary Production, an Index of Climate Change in the Ocean: Satellite-Based Estimates over Two Decades. *Remote Sensing*, 12(5):826, 2020. doi:10.3390/rs12050826.

Vanessa Lampe, Eva-Maria Nöthig, and Markus Schartau. Spatio-Temporal Variations in Community Size Structure of Arctic Protist Plankton in the Fram Strait. *Frontiers in Marine Science*, 7:1–18, 2021. doi:10.3389/fmars.2020.579880.

M. R. Landry, M. E. Ondrusek, S. J. Tanner, S. L. Brown, J. Constantinou, R. R. Bidigare, K. H. Coale, and S. Fitzwater. Biological response to iron fertilization in the eastern equatorial Pacific (IronEx II). I. Microplankton community abundances and biomass. *Marine Ecology Progress Series*, 201:27–42, 2000. doi:10.3354/meps201027.

Aud Larsen, Jorun K. Egge, Jens C. Nejstgaard, Iole Di Capua, Runar Thyrhaug, Gunnar Bratbak, and T. Frede Thingstad. Contrasting response to nutrient manipulation in Arctic mesocosms are reproduced by a minimum microbial food web model. *Limnology and Oceanography*, 60(2):360–374, 2015. doi:10.1002/lno.10025.

E. Leu, C. J. Mundy, Philipp Assmy, K. Campbell, T. M. Gabrielsen, Michel Gosselin, T. Juul-Pedersen, and R. R. Gradinger. Arctic spring awakening - Steering principles behind the phenology of vernal ice algal blooms. *Progress in Oceanography*, 139:151–170, 2015. doi:10.1016/j.pocean.2015.07.012.

William K.W. Li, Fiona A. McLaughlin, Connie Lovejoy, and Eddy C. Carmack. Smallest algae thrive as the arctic ocean freshens. *Science*, 326(5952):539, 2009. doi:10.1126/science.1179798.

Elena Litchman and Christopher A. Klausmeier. Trait-Based Community Ecology of Phytoplankton. *Annual Review of Ecology, Evolution, and Systematics*, 39(1): 615–639, 2008. doi:10.1146/annurev.ecolsys.39.110707.173549.

Elena Litchman, Christopher A. Klausmeier, Oscar M. Schofield, and Paul G. Falkowski. The role of functional traits and trade-offs in structuring phytoplankton communities: Scaling from cellular to ecosystem level. *Ecology Letters*, 10 (12):1170–1181, 2007. doi:10.1111/j.1461-0248.2007.01117.x.

Yu Liu, Jianhui Wang, Guoqing Han, Xiayan Lin, Guijing Yang, and Qiyan Ji. Spatio-temporal analysis of east greenland polar front. *Frontiers in Marine Science*, 9:943457, 2022. doi:10.3389/fmars.2022.943457.

C. J. Lorenzen. Extinction of Light in the Ocean by Phytoplankton. *ICES Journal of Marine Science*, 34(2):262–267, 1972. doi:10.1093/icesjms/34.2.262.

Syukuro Manabe and Ronald J. Stouffer. Sensitivity of a global climate model to an increase of CO $_2$ concentration in the atmosphere. *Journal of Geophysical Research: Oceans*, 85(C10):5529–5554, 1980. doi:10.1029/JC085iC10p05529.

Emilio Marañón. Cell Size as a Key Determinant of Phytoplankton Metabolism and Community Structure. *Annual Review of Marine Science*, 7(1):241–264, 2015. doi:10.1146/annurev-marine-010814-015955.

Emilio Marañón, Pedro Cermeño, Daffne C. López-Sandoval, Tamara Rodríguez-Ramos, Cristina Sobrino, María Huete-Ortega, José María Blanco, and Jaime Rodríguez. Unimodal size scaling of phytoplankton growth and the size dependence of nutrient uptake and use. *Ecology Letters*, 16(3):371–379, 2013. doi:10.1111/ele.12052.

Walter N. Meier and Julienne Stroeve. Comparison of sea-ice extent and ice-edge location estimates from passive microwave and enhanced-resolution scatterometer data. *Annals of Glaciology*, 48:65–70, 2008. doi:10.3189/172756408784700743.

Susanne Menden-Deuer and E J Lessard. Carbon to volume relationships for dinoflagellates, diatoms, and other protist plankton. *Limnology and Oceanography*, 45(3):569–579, 2000.

Michelle Menge. *Phytoplankton succession in the eastern Fram Strait (August 2017 - July 2018) Microscopic analysis of autonomously collected water samples*. PhD thesis, Universität Bremen, Alfred-Wegener-Institut für Polar- und Meeresforschung, Bremen, 2019.

Alexandre Mignot, Hervé Claustre, Gianpiero Cossarini, Fabrizio D'Ortenzio, Elodie Gutknecht, Julien Lamouroux, Paolo Lazzari, Coralie Perruche, Stefano Salon, Raphaëlle Sauzède, Vincent Taillandier, and Anna Teruzzi. Using machine learning and Biogeochemical-Argo (BGC-Argo) floats to assess biogeochemical models and optimize observing system design. *Biogeosciences*, 20(7):1405–1422, 2023. doi:10.5194/bg-20-1405-2023.

Jeanne Moal, Véronique Martin-Jezequel, Roger P. Harris, Jean-Françios Samain, and Serge A. Poulet. Interspecific and intraspecific variability of the chemical composition of marine phytoplankton. *Oceanologica acta*, 10(3):339–346, 1987.

Coleen L. Moloney and John G. Field. General allometric equations for rates of nutrient uptake, ingestion, and respiration in plankton organisms. *Limnology and Oceanography*, 34(7):1290–1299, 1989. doi:10.4319/lo.1989.34.7.1290.

Coleen L. Moloney and John G. Field. The size-based dynamics of plankton food webs. I. A simulation model of carbon and nitrogen flows. *Journal of Plankton Research*, 13(5):1003–1038, 1991. doi:10.1093/plankt/13.5.1003.

David J. S. Montagnes, John A. Berges, Paul J. Harrison, and F. J. R. Taylor. Volume in Marine Phytoplankton. *Limnology and Oceanography*, 39(5):1044–1060, 1994.

Enrique Moreno-Ostos, José María Blanco, Susana Agustí, Luis M. Lubián, Valeriano Rodríguez, Roberto L. Palomino, Moira Llabrés, and Jaime Rodríguez. Phytoplankton biovolume is independent from the slope of the size spectrum in the oligotrophic Atlantic Ocean. *Journal of Marine Systems*, 152:42–50, 2015. doi:10.1016/j.jmarsys.2015.07.008.

M. M. Mullin, P. R. Sloan, and R. W. Eppley. Relationship Between Carbon Content, Cell Volume, and Area in Phytoplankton. *Limnology and Oceanography*, 11(2):307–311, 1966. doi:10.4319/lo.1966.11.2.0307.

Jens C. Nejstgaard, Kam W. Tang, Michael Steinke, Jörg Dutz, Marja Koski, Elvire Antajan, and Jeremy D. Long. Zooplankton grazing on Phaeocystis: A quantitative review and future challenges. *Biogeochemistry*, 83:147–172, 2007. doi:10.1007/s10533-007-9098-y.

Pia Nielsen-Englyst, Jacob L. Høyer, Wiebke M. Kolbe, Gorm Dybkjær, Thomas Lavergne, Rasmus Tage Tonboe, Sotirios Skarpalezos, and Ioanna Karagali. A combined sea and sea-ice surface temperature climate dataset of the Arctic, 1982–2021. *Remote Sensing of Environment*, 284:113331, 2023. doi:10.1016/j.rse.2022.113331.

Eva-Maria Nöthig, Astrid Bracher, Anja Engel, Katja Metfies, Barbara Niehoff, Ilka Peeken, Eduard Bauerfeind, Alexandra Cherkasheva, Steffi Gäbler-Schwarz, Kristin Hardge, Estelle Kilias, Angelina Kraft, Yohannes Mebrahtom Kidane, Catherine Lalande, Judith Piontek, Karolin Thomisch, and Mascha Wurst. Summertime plankton ecology in Fram Strait - a compilation of long- and short-term observations. *Polar Research*, 34(1):23349, 2015. doi:10.3402/polar.v34.23349.

Eva-Maria Nöthig, Simon Ramondenc, Antoine Haas, Laura Hehemann, Andreas Walter, Astrid Bracher, Catherine Lalande, Katja Metfies, Ilka Peeken, Eduard Bauerfeind, and Antje Boetius. Summertime in situ chlorophyll a and particulate organic carbon standing stocks in surface waters of the Fram Strait and the Arctic Ocean (1991 – 2015). *Frontiers in Marine Science*, 7(350), 2020. doi:10.3389/fmars.2020.00350.

Irina Olenina, Susanna Hajdu, Lars Edler, Norbert Wasmund, Susanne Busch, Jeanette Göbel, Slawomira Gromisz, Siv Huseby, Maija Huttunen, Andres Jaanus, Pirkko Kokkonen, Iveta Ledaine, and Elzbieta Niemkiewicz. Biovolumes and size-classes of phytoplankton in the Baltic Sea. *HELCOM Balt.Sea Environ. Proc.*, 106(106):144 pp, 2006. doi:HELCOM Balt.Sea Environ. Proc. No. 106, 144pp.

Maria L. Paulsen, Hugo Doré, Laurence Garczarek, Lena Seuthe, Oliver Müller, Ruth-Anne Sandaa, Gunnar Bratbak, and Aud Larsen. Synechococcus in the Atlantic Gateway to the Arctic Ocean. *Frontiers in Marine Science*, 3(October), 2016. doi:10.3389/fmars.2016.00191.

Maria-Theresia Pelz, Markus Schartau, Christopher J. Somes, Vanessa Lampe, and Thomas Slawig. A diffusion-based kernel density estimator (diffKDE, version 1) with optimal bandwidth approximation for the analysis of data in geoscience and ecological research. *Geoscientific Model Development*, 16:6609–6634, 2023. doi:10.5194/gmd-16-6609-2023.

Donald K. Perovich, Bonnie Light, Hajo Eicken, Kathleen F. Jones, Kay Runciman, and Son V. Nghiem. Increasing solar heating of the Arctic Ocean and adjacent seas, 1979–2005: Attribution and role in the ice-albedo feedback. *Geophysical Research Letters*, 34(19):2007GL031480, 2007. doi:10.1029/2007GL031480.

Felix Pithan and Thorsten Mauritsen. Arctic amplification dominated by temperature feedbacks in contemporary climate models. *Nature Geoscience*, 7(3):181–184, 2014. doi:10.1038/ngeo2071.

Igor V. Polyakov and Mark A. Johnson. Arctic decadal and interdecadal variability. *Geophysical Research Letters*, 27(24):4097–4100, 2000. doi:10.1029/2000GL011909.

Lawrence R. Pomeroy, Peter J.B. IeB. Williams, Farooq Azam, and John E. Hobbie. The microbial loop. *Oceanography*, 20(2):28–33, 2007. doi:10.5670/oceanog.2007.45.

A. E. Friederike Prowe, Bei Su, Jens C. Nejstgaard, and Markus Schartau. Food web structure and intraguild predation affect ecosystem functioning in an established plankton model. *Limnology and Oceanography*, 67(4):843–855, 2022. doi:10.1002/lno.12039.

Renato A. Quinones, Trevor Platt, and Jaime Rodríguez. Patterns of biomass-size spectra from oligotrophic waters of the Northwest Atlantic. *Progress in Oceanography*, 57(3-4):405–427, 2003. doi:10.1016/s0079-6611(03)00108-3.

R Core Team. R: A language and environment for statistical computing, 2018. URL http://www.r-project.org.

Mika Rantanen, Alexey Yu. Karpechko, Antti Lipponen, Kalle Nordling, Otto Hyvärinen, Kimmo Ruosteenoja, Timo Vihma, and Ari Laaksonen. The Arctic has warmed nearly four times faster than the globe since 1979. *Communications Earth & Environment*, 3(1):168, 2022. doi:10.1038/s43247-022-00498-3.

J. A. Raven. The twelfth Tansley Lecture. Small is beautiful: The picophytoplankton. *Functional Ecology*, 12(4):503–513, 1998. doi:10.1046/j.1365-2435.1998.00233.x.

Angelika H. H. Renner, Sebastian Gerland, Christian Haas, Gunnar Spreen, Justin F. Beckers, Edmond Hansen, Marcel Nicolaus, and Harvey Goodwin. Evidence of Arctic sea ice thinning from direct observations. *Geophysical Research Letters*, 41(14):5029–5036, 2014. doi:10.1002/2014GL060369.

Angelika H.H. Renner, Allison Bailey, Marit Reigstad, Arild Sundfjord, Melissa Chierici, and Elizabeth M. Jones. Hydrography, inorganic nutrients and chlorophyll a linked to sea ice cover in the Atlantic Water inflow region north of Svalbard. *Progress in Oceanography*, 219:103162, 2023. doi:10.1016/j.pocean.2023.103162.

A. Reul, V. Rodríguez, F. Jiménez-Gómez, J. M. Blanco, B. Bautista, T. Sarhan, F. Guerrero, J. Ruíz, and J. García-Lafuente. Variability in the spatio-temporal distribution and size-structure of phytoplankton across an upwelling area in the NW-Alboran Sea, (W-Mediterranean). *Continental Shelf Research*, 25(5-6):589–608, 2005. doi:10.1016/j.csr.2004.09.016.

Jaime Rodriguez and Michael M. Mullin. Relation between biomass and body weight of plankton in a steady state oceanic ecosystem. *Limnology and Oceanography*, 31(2):361–370, 1986. doi:10.4319/lo.1986.31.2.0361.

Jaime Rodríguez, José M. Blanco, Francisco Jiménez-Gómez, Fidel Echevarría, Julio Gil, Valeriano Rodríguez, Javier Ruiz, Begoña Bautista, and Francisco Guerrero. Patterns in the size structure of the phytoplankton community in the deep fluorescence maximum of the Alboran Sea (southwestern Mediterranean). *Deep-Sea Research Part I: Oceanographic Research Papers*, 45(10):1577–1593, 1998. doi:10.1016/S0967-0637(98)00030-2.

Véronique Rousseau, Marie Josèphe Chrétiennot-Dinet, Anita Jacobsen, Peter Verity, and Stuart Whipple. The life cycle of Phaeocystis: State of knowledge and presumptive role in ecology. *Biogeochemistry*, 83(1-3):29–47, 2007. doi:10.1007/s10533-007-9085-3.

Bert Rudels and Hans J. Friedrich. The Transformations of Atlantic Water in the Arctic Ocean and Their Significance for the Freshwater Budget. In Edward Lyn Lewis, E. Peter Jones, Peter Lemke, Terry D. Prowse, and Peter

Wadhams, editors, *The Freshwater Budget of the Arctic Ocean*, pages 503–532. Springer Netherlands, Dordrecht, 2000. ISBN 978-0-7923-6440-5 978-94-011-4132-1. doi:10.1007/978-94-011-4132-1_21. URL http://link.springer.com/10.1007/978-94-011-4132-1_21.

E. Sakshaug. Primary and Secondary Production in the Arctic Seas. In Ruediger Stein and Robie W. MacDonald, editors, *The Organic Carbon Cycle in the Arctic Ocean*, pages 57–81. Springer Berlin Heidelberg, Berlin, Heidelberg, 2004. ISBN 978-3-642-62351-6 978-3-642-18912-8. doi:10.1007/978-3-642-18912-8_3. URL http://link.springer.com/10.1007/978-3-642-18912-8_3.

I. Salter, E. Bauerfeind, K. Fahl, M. H. Iversen, C. Lalande, S. Ramondenc, W.-J. Von Appen, C. Wekerle, and E.-M. Nöthig. Interannual variability (2000–2013) of mesopelagic and bathypelagic particle fluxes in relation to variable sea ice cover in the eastern Fram Strait. *Frontiers in Earth Science*, 11:1210213, 2023. doi:10.3389/feart.2023.1210213.

S Sathyendranath, T Jackson, C Brockmann, V Brotas, B Calton, A Chuprin, O Clements, P Cipollini, O Danne, J Dingle, C Donlon, M Grant, S Groom, H Krasemann, S Lavender, C Mazeran, F Mélin, D Müller, F Steinmetz, A Valente, M Zühlke, G Feldman, B Franz, R Frouin, J Werdell, and T Platt. ESA Ocean Colour Climate Change Initiative (Ocean_Colour_cci): Version 5.0 Data., 2021. URL http://dx.doi.org/10.5285/1dbe7a109c0244aaad713e078fd3059a. doi:10.5285/1dbe7a109c0244aaad713e078fd3059a.

Markus Schartau, Michael R. Landry, and Robert A. Armstrong. Density estimation of plankton size spectra: A reanalysis of IronEx II data. *Journal of Plankton Research*, 32(8):1167–1184, 2010. doi:10.1093/plankt/fbq072.

Markus Schartau, Philip Wallhead, John Hemmings, Ulrike Löptien, Iris Kriest, Shubham Krishna, Ben A. Ward, Thomas Slawig, and Andreas Oschlies. Reviews and syntheses: Parameter identification in marine planktonic ecosystem modelling. *Biogeosciences*, 14(6):1647–1701, 2017. doi:10.5194/bg-14-1647-2017.

Vibe Schourup-Kristensen, Claudia Wekerle, Sergey Danilov, and Christoph Völker. Seasonality of Mesoscale Phytoplankton Control in Eastern Fram Strait. *Journal of Geophysical Research: Oceans*, 126(10):e2021JC017279, 2021. doi:10.1029/2021JC017279.

Enrico Ser-Giacomi, Ricardo Martinez-Garcia, Stephanie Dutkiewicz, and Michael J. Follows. A Lagrangian model for drifting ecosystems reveals heterogeneity-driven enhancement of marine plankton blooms. *Nature Communications*, 14(1):6092, 2023. doi:10.1038/s41467-023-41469-2.

Camila Serra-Pompei, Ben A. Ward, Jérôme Pinti, André W. Visser, Thomas Kiørboe, and Ken H. Andersen. Linking Plankton Size Spectra and Community Composition to Carbon Export and Its Efficiency. *Global Biogeochemical Cycles*, 36(5), 2022. doi:10.1029/2021GB007275.

R W Sheldon, A Prakash, and W H Sutcliffe. The Size Distribution of Particles in the Ocean. *Limnology and Oceanography*, 17(3):327–341, 1972.

Evelyn B. Sherr, Barry F. Sherr, Patricia A. Wheeler, and Karen Thompson. Temporal and spatial variation in stocks of autotrophic and heterotrophic microbes in the upper water column of the central Arctic Ocean. *Deep-Sea Research Part I: Oceanographic Research Papers*, 50(5):557–571, 2003. doi:10.1016/S0967-0637(03)00031-1.

B. W. Silverman. The kernel method for univariate data. In *Density Estimation for Statistics and Data Analysis*, pages 34–74. Springer US, Boston, MA, 1986. ISBN 978-0-412-24620-3. doi:10.1007/978-1-4899-3324-9_3. URL http://link.springer.com/10.1007/978-1-4899-3324-9_3.

Dag Slagstad and Thomas A. McClimans. Modeling the ecosystem dynamics of the Barents sea including the marginal ice zone: I. Physical and chemical oceanography. *Journal of Marine Systems*, 58(1-2):1–18, 2005. doi:10.1016/j.jmarsys.2005.05.005.

Dag Slagstad, Paul F. J. Wassmann, and Ingrid Ellingsen. Physical constrains and productivity in the future Arctic Ocean. *Frontiers in Marine Science*, 2, 2015. doi:10.3389/fmars.2015.00085.

Victor Smetacek. *Die Sukzession Des Phytoplanktons in Der Westlichen Kieler Bucht*. PhD thesis, Kiel University, 1975.

Walker O. Smith, M.E. Marcus E Baumann, David L Wilson, and Ludwig Aletsee. Phytoplankton Biomass and Productivity in the Marginal Ice Zone of the Fram Strait During Summer 1984. *Journal of Geophysical Research: Oceans*, 92:6777–6786, 1987.

Thomas Soltwedel, Eduard Bauerfeind, Melanie Bergmann, Nataliya Budaeva, Eveline Hoste, Nina Jaeckisch, Karen von Juterzenka, Jens Matthiesson, Vadim Mokievsky, Eva-Maria Nöthig, Nadia-Valérie Quéric, Burkhard Sablotny, Eberhard Sauter, Ingo Schewe, Barbara Urban-Malinga, Jan Wegner, Maria Włodarska-Kowalczuk, and Michael Klages. HAUSGARTEN: Multidisciplinary Investigations at a Deep-Sea, Long-Term Observatory in the Arctic Ocean. *Oceanography*, 18(3):46–61, 2005. doi:10.5670/oceanog.2005.24.

Thomas Soltwedel, Eduard Bauerfeind, Melanie Bergmann, Astrid Bracher, Nataliya Budaeva, Kathrin Busch, Alexandra Cherkasheva, Kirsten Fahl, Katarzyna Grzelak, Christiane Hasemann, Marianne Jacob, Angelina Kraft, Catherine Lalande, Katja Metfies, Eva-Maria Nöthig, Kirstin Meyer, Nadia Valérie Quéric, Ingo Schewe, Maria Włodarska-Kowalczuk, and Michael Klages. Natural variability or anthropogenically-induced variation? Insights from 15 years of multidisciplinary observations at the arctic marine LTER site HAUSGARTEN. *Ecological Indicators*, 65:89–102, 2016. doi:10.1016/j.ecolind.2015.10.001.

Janne E. Søreide, Eva V.A. Leu, Jørgen Berge, Martin Graeve, and Stig Falk-Petersen. Timing of blooms, algal food quality and Calanus glacialis reproduction and growth in a changing Arctic. *Global Change Biology*, 16:3154–3163, 2010. doi:10.1111/j.1365-2486.2010.02175.x.

Gunnar Spreen, Laura De Steur, Dmitry Divine, Sebastian Gerland, Edmond Hansen, and Ron Kwok. Arctic Sea Ice Volume Export Through Fram Strait From 1992 to 2014. *Journal of Geophysical Research: Oceans*, 125(6):e2019JC016039, 2020. doi:10.1029/2019JC016039.

William Gary Sprules and M. Munawar. Plankton size spectra in relation to ecosystem productivity, size, and perturbation. *Canadian Journal of Fisheries and Aquatic Sciences*, 43(9):1789–1794, 1986. doi:10.1139/f86-222.

John H Steele. Incorporating the microbial loop in a simple plankton model. *Proceedings of the Royal Society B: Biological Sciences*, 265:1771–1777, 1998. doi:10.1098/rspb.1998.0501.

Diane K Stoecker and Geoffry T Evans. Effects of protozoan herbivory and carnivory in a microplankton food web. *Marine Ecology Progress Series*, 25:159–167, 1985. doi:10.3354/meps025159.

Diane K. Stoecker and Peter J. Lavrentyev. Mixotrophic plankton in the polar seas: A pan-Arctic review. *Frontiers in Marine Science*, 5, 2018. doi:10.3389/fmars.2018.00292.

Richard Strathmann. Estimating the organic carbon content of phyoplankton from cell volume or plasma volume. *Limnology and Oceanography*, 12(3):411–418, 1967.

Julienne C. Stroeve, Mark C. Serreze, Marika M. Holland, Jennifer E. Kay, James Malanik, and Andrew P. Barrett. The Arctic's rapidly shrinking sea ice cover: A research synthesis. *Climatic Change*, 110:1005–1027, 2012. doi:10.1007/s10584-011-0101-1.

Arild Sundfjord, Ingrid Ellingsen, Dag Slagstad, and Harald Svendsen. Vertical mixing in the marginal ice zone of the northern Barents Sea—Results from numerical model experiments. *Deep Sea Research Part II: Topical Studies in Oceanography*, 55(20-21):2154–2168, 2008. doi:10.1016/j.dsr2.2008.05.027.

The University Centre in Svalbard UNIS. Isfjorden Adventfjorden time series, March 2024. URL https://www.unis.no/project/isa/. Last accessed: 19/03/2024.

T. F. Thingstad, R. G.J. Bellerby, G. Bratbak, K. Y. Børsheim, J. K. Egge, M. Heldal, A. Larsen, C. Neill, J. Nejstgaard, S. Norland, R. A. Sandaa, E. F. Skjoldal, T. Tanaka, R. Thyrhaug, and B. Töpper. Counterintuitive carbon-to-nutrient coupling in an Arctic pelagic ecosystem. *Nature*, 455(7211):387–390, 2008. doi:10.1038/nature07235.

Tron Frede Thingstad and L. Antonio Cuevas. Nutrient pathways through the microbial food web: Principles and predictability discussed, based on five different experiments. *Aquatic Microbial Ecology*, 61(3):249–260, 2010. doi:10.3354/ame01452.

Thordis L. Thorarinsdottir, Tilmann Gneiting, and Nadine Gissibl. Using proper divergence functions to evaluate climate models. *SIAM-ASA Journal on Uncertainty Quantification*, 1(1):522–534, 2013. doi:10.1137/130907550.

Sinhué Torres-Valdés, Annika Morische, and Laura Wischnewski. Nutrient measurements from POLARSTERN cruise PS114 (LTER HAUSGARTEN), 2019. URL https://doi.pangaea.de/10.1594/PANGAEA.907355. doi:10.1594/PANGAEA.907355.

Bryony L. Townhill, Efstathios Reppas-Chrysovitsinos, Roxana Sühring, Crispin J. Halsall, Elena Mengo, Tina Sanders, Kirsten Dähnke, Odile Crabeck, Jan Kaiser, and Silvana N. R. Birchenough. Pollution in the Arctic Ocean: An overview of multiple pressures and implications for ecosystem services. *Ambio*, 51(2):471–483, 2022. doi:10.1007/s13280-021-01657-0.

Emilia Trudnowska, Marta Gluchowska, Agnieszka Beszczynska-Möller, Katarzyna Blachowiak-Samolyk, and Slawomir Kwasniewski. Plankton patchiness in the Polar Front region of the west Spitsbergen Shelf. *Marine Ecology Progress Series*, 560(November):1–18, 2016. doi:10.3354/meps11925.

Emilia Trudnowska, S. Sagan, and K. Błachowiak-Samołyk. Spatial variability and size structure of particles and plankton in the Fram Strait. *Progress in Oceanography*, 168:1–12, 2018. doi:10.1016/j.pocean.2018.09.005.

Hans Utermöhl. Zur Vervollkommnung der quantitativen Phytoplankton-Methodik. *Internationale Vereinigung für Theoretische und Angewandte Limnologie: Mitteilungen*, 9(1):1–38, 1958. doi:10.1080/05384680.1958.11904091.

Peter G. Verity, Charles Y. Robertson, Craig R. Tronzo, Melinda G. Andrews, James R. Nelson, and Michael E. Sieracki. Relationships between cell volume and the carbon and nitrogen content of marine photosynthetic nanoplankton. *Limnology and Oceanography*, 37(7):1434–1446, 1992. doi:10.4319/lo.1992.37.7.1434.

Maria Vernet, Ingrid H. Ellingsen, Lena Seuthe, Dag Slagstad, Mattias R. Cape, and Patricia A. Matrai. Influence of Phytoplankton Advection on the Productivity Along the Atlantic Water Inflow to the Arctic Ocean. *Frontiers in Marine Science*, 6(September):1–18, 2019. doi:10.3389/fmars.2019.00583.

Maria Vernet, Ingrid Ellingsen, Christian Marchese, Simon Bélanger, Mattias Cape, Dag Slagstad, and Patricia A. Matrai. Spatial variability in rates of net primary production (NPP) and onset of the spring bloom in Greenland shelf waters. *Progress in Oceanography*, 198, 2021. doi:10.1016/j.pocean.2021.102655.

Mikko Vihtakari. ggOceanMaps: Plot Data on Oceanographic Maps using 'ggplot2', 2024. URL https://mikkovihtakari.github.io/ggOceanMaps/. R package version 2.2.0.

Wilken Jon von Appen, Ursula Schauer, Raquel Somavilla, Eduard Bauerfeind, and Agnieszka Beszczynska-Möller. Exchange of warming deep waters across Fram Strait. *Deep-Sea Research Part I: Oceanographic Research Papers*, 103:86–100, 2015. doi:10.1016/j.dsr.2015.06.003.

Wilken-Jon Von Appen, Anya M. Waite, Melanie Bergmann, Christina Bienhold, Olaf Boebel, Astrid Bracher, Boris Cisewski, Jonas Hagemann, Mario Hoppema, Morten H. Iversen, Christian Konrad, Thomas Krumpen, Normen

Lochthofen, Katja Metfies, Barbara Niehoff, Eva-Maria Nöthig, Autun Purser, Ian Salter, Matthias Schaber, Daniel Scholz, Thomas Soltwedel, Sinhue Torres-Valdes, Claudia Wekerle, Frank Wenzhöfer, Matthias Wietz, and Antje Boetius. Sea-ice derived meltwater stratification slows the biological carbon pump: Results from continuous observations. *Nature Communications*, 12(1):7309, 2021. doi:10.1038/s41467-021-26943-z.

Wilken-Jon Von Appen, Till Baumann, Markus Janout, Nikolay Koldunov, Yueng-Djern Lenn, Robert Pickart, Robert Scott, and Qiang Wang. Eddies and the Distribution of Eddy Kinetic Energy in the Arctic Ocean. *Oceanography*, 35(3-4), 2022. doi:10.5670/oceanog.2022.122.

Anabel von Jackowski, Julia Grosse, Eva Maria Nöthig, and Anja Engel. Dynamics of organic matter and bacterial activity in the Fram Strait during summer and autumn. *Philosophical transactions. Series A, Mathematical, physical, and engineering sciences*, 378(2181):20190366, 2020a. doi:10.1098/rsta.2019.0366.

Anabel von Jackowski, Julia Grosse, Eva-Maria Nöthig, and Anja Engel. Organic matter and bacteria measurements of POLARSTERN cruise PS114 and Maria S. Merian cruise MSM77, 2020b. doi:10.1594/PANGAEA.915751.

Anabel von Jackowski, Kevin W. Becker, Matthias Wietz, Christina Bienhold, Birthe Zäncker, Eva Maria Nöthig, and Anja Engel. Variations of microbial communities and substrate regimes in the eastern Fram Strait between summer and fall. *Environmental Microbiology*, 24(9):4124–4136, September 2022. doi:10.1111/1462-2920.16036.

Qiang Wang, Claudia Wekerle, Xuezhu Wang, Sergey Danilov, Nikolay Koldunov, Dmitry Sein, Dmitry Sidorenko, Wilken Jon von Appen, and Thomas Jung. Intensification of the Atlantic Water Supply to the Arctic Ocean Through Fram Strait Induced by Arctic Sea Ice Decline. *Geophysical Research Letters*, 47(3), 2020. doi:10.1029/2019GL086682.

Ben A. Ward and Michael J. Follows. Marine mixotrophy increases trophic transfer efficiency, mean organism size, and vertical carbon flux. *Proceedings of the National Academy of Sciences of the United States of America*, 113(11):2958–2963, 2016. doi:10.1073/pnas.1517118113.

Ben A. Ward, Stephanie Dutkiewicz, O. Jahn, and Michael J. Follows. A size-structured food-web model for the global ocean. *Limnology and Oceanography*, 57(6):1877–1891, 2012. doi:10.4319/lo.2012.57.6.1877.

Ben A. Ward, Stephanie Dutkiewicz, and Michael J. Follows. Modelling spatial and temporal patterns in size-structured marine plankton communities: Top-down and bottom-up controls. *Journal of Plankton Research*, 36(1):31–47, 2014. doi:10.1093/plankt/fbt097.

Ben A. Ward, Emilio Marañón, Boris Sauterey, Jonathan Rault, and David Claessen. The Size Dependence of Phytoplankton Growth Rates: A Trade-Off between Nutrient Uptake and Metabolism. *The American Naturalist*, 189(2): 170–177, 2017. doi:10.1086/689992.

Paul Wassmann. Arctic marine ecosystems in an era of rapid climate change. *Progress in Oceanography*, 90(1-4):1–17, 2011. doi:10.1016/j.pocean.2011.02.002.

Paul Wassmann and Marit Reigstad. Future Arctic Ocean Seasonal Ice Zones and Implications for Pelagic-Benthic Coupling. *Oceanography*, 24(3):220–231, 2011. doi:10.5670/oceanog.2011.74.

Paul Wassmann, Dag Slagstad, Christian Wexels Riser, and Marit Reigstad. Modelling the ecosystem dynamics of the Barents Sea including the marginal ice zone: II. Carbon flux and interannual variability. *Journal of Marine Systems*, 59(1-2): 1–24, 2006. doi:10.1016/j.jmarsys.2005.05.006.

Paul Wassmann, Dag Slagstad, and Ingrid Ellingsen. Primary production and climatic variability in the European sector of the Arctic Ocean prior to 2007: Preliminary results. *Polar Biology*, 33:1641–1650, 2010. doi:10.1007/s00300-010-0839-3.

Paul Wassmann, Carlos M. Duarte, Susana Agustí, and Mikael K. Sejr. Footprints of climate change in the Arctic marine ecosystem. *Global Change Biology*, 17(2): 1235–1249, 2011. doi:10.1111/j.1365-2486.2010.02311.x.

Matthias Wietz, Christina Bienhold, Katja Metfies, Sinhué Torres-Valdés, Wilken-Jon von Appen, Ian Salter, and Antje Boetius. The polar night shift: Seasonal dynamics and drivers of Arctic Ocean microbiomes revealed by autonomous sampling. *ISME Communications*, 1(1):76, 2021. doi:10.1038/s43705-021-00074-4.

Chris Wilson, Yevgeny Aksenov, Stefanie Rynders, Stephen J. Kelly, Thomas Krumpen, and Andrew C. Coward. Significant variability of structure and predictability of Arctic Ocean surface pathways affects basin-wide connectivity. *Communications Earth & Environment*, 2(1):164, 2021. doi:10.1038/s43247-021-00237-0.

Yongsheng Wu, Ingrid K. Peterson, Charles C.L. Tang, Trevor Platt, Shubha Sathyendranath, and César Fuentes-Yaco. The impact of sea ice on the initiation of the spring bloom on the Newfoundland and Labrador Shelves. *Journal of Plankton Research*, 29(6):509–514, 2007. doi:10.1093/plankt/fbm035.

Hongyan Xi, Svetlana N. Losa, Antoine Mangin, Philippe Garnesson, Marine Bretagnon, Julien Demaria, Mariana A. Soppa, Odile Hembise Fanton d'Andon, and Astrid Bracher. Global Chlorophyll *a* Concentrations of Phytoplankton Functional Types With Detailed Uncertainty Assessment Using Multisensor Ocean Color and Sea Surface Temperature Satellite Products. *Journal of Geophysical Research: Oceans*, 126(5):e2020JC017127, 2021. doi:10.1029/2020JC017127.

Victor Zhurbas, Dmitry Lyzhkov, and Natalia Kuzmina. Drifter-derived estimates of lateral eddy diffusivity in the World Ocean with emphasis on the Indian Ocean and problems of parameterisation. *Deep Sea Research Part I: Oceanographic Research Papers*, 83:1–11, 2014. doi:10.1016/j.dsr.2013.09.001.

List of Figures

List of Tables

Acknowledgements

I am deeply grateful to Prof. Dr. **Andreas Oschlies** for providing me with the opportunity to pursue my PhD in the GEOMAR Biogeochemical Modelling group. His guidance and support have been invaluable throughout my academic journey.

I extend my sincere appreciation to Prof. Dr. **Anja Engel** for generously dedicating her time to serve as the second examiner for my thesis and contributing to the academic rigor of my work.

I owe a debt of gratitude to Dr. **Markus Schartau** for his unwavering supervision and support throughout this project. I am deeply thankful for his mentorship and for teaching me to become a researcher. His valuable tips, suggestions, and constructive criticism have significantly contributed to improving this thesis. Thank you for not letting me give up.

Special thanks to the members of the BMBF NERC Changing Arctic Ocean microARC project, particularly my 'Doktorschwester' Dr. **Anabel von Jackowski**, for her support and friendship during this journey. I also express my gratitude to Dr. **Eva-Maria Nöthig** for her invaluable assistance in understanding the Excel sheets of plankton size data with their obscurities and their implications and her words of encouragement.

I am thankful to the GEOMAR Biogeochemical Modelling group for their constructive feedback during group meetings and seminars, and enjoyable conversations during lunch breaks and group retreats. In particular, I thank Dr. **Tianfei Xue** and **Neha Mehendale** for their support and their proofreading of parts of my thesis. The countless walks with Dr. **Maria-Theresia Pelz** and her encouragement truly helped me keep up a good spirit. I extend my gratitude to **Monika Peschke** for her assistance with administrative matters.

I am deeply indebted to my family for their steadfast patience and belief in me. Special thanks to **Ties** for his constant support, motivation, and always having my back.

I am thankful to all my friends, family, and colleagues who have supported me throughout this journey, even if I couldn't name each one individually. Your encouragement has been invaluable to me.

Finally, I would like to acknowledge the funding of large parts of this research provided by the Helmholtz Association and the German Federal Ministry of Education and Research (BMBF) as a contribution to the microARC project (03F0802A). MicroARC was part of the Changing Arctic Ocean programme, jointly funded by the UKRI Natural Environment Research Council (NERC) and BMBF.

Erklärung

Hiermit erkläre ich, dass die vorliegende Arbeit mit dem Titel **‘Linking observations and modelling to advance our understanding of spatio-temporal variations in structure and productivity of Arctic protist plankton’**

1. nach Inhalt und Form von mir selbst verfasst ist, und abgesehen von der Beratung durch den Betreuer keine Hilfsmittel verwendet wurden;
2. unter Einhaltung der Regeln guter wissenschaftlicher Praxis der Deutschen Forschungsgemeinschaft entstanden ist;
3. weder im Ganzen noch in Teilen schon einer anderen Stelle im Rahmen eines Prüfungsverfahrens vorgelegen hat.

Veröffentlichte oder zur Veröffentlichung eingereichte Manuskripte wurden kenntlich gemacht.
Es wurde kein akademischer Grad entzogen.

Kiel, April 2024
Vanessa Lampe